



The
University
Of
Sheffield.

Machining strategies for distortion control during high speed machining

By:

Ravi Bilkhu

A thesis submitted in partial fulfilment of the requirements for the degree of
Doctor of Philosophy

The University of Sheffield
Faculty of Engineering
Department of Advanced Manufacturing Research Centre

04/06/2020

Acknowledgements

I would firstly like to thank my supervisor Dr. Christophe Pinna and Dr. Sabino Ayvar for their suggestions and guidance in this thesis. I also would like to thank Dr. James Castle (The Boeing Company) for his support and guidance for the development for this research. I would also like to thank Professor Anish Roy and Dr. Mahmoud Mousavi for their research enlightenment, feedback and help throughout the Viva; this has helped me with the final version of the thesis. I would also like to thank Professor Matt Carre for facilitating this.

I would also like to thank the AMRC with Boeing and the Board members for their financial support throughout this study.

I am also very grateful for the support of Dr's Shu Yan Zhang, Joe Kelleher, Saurabh Kabra (Engin-X) and the patience and optimism of Dr. Anna Paradowska (ANSTO) all who made it possible for residual stress measurements using Neutron Diffraction to be performed. I would also like to say thank you to Dr Mike Prime for his advice on the contour method, I really appreciated it! I would also like to thanks James Farrar and his team in Wilde Group for their continued support using DEFORM throughout the whole program.

A massive thank you to all my colleagues and friends at the AMRC with Boeing, the Machining Group, the Machine shop floor, the metrology group for their help and their machining expertise, especially Ignacio Blanco, Paul Ridgen, Garry Hibbert, Chris Depledge, Richard Salmon, Adam Wiles, Dr's Peace Onawumi, Kartik Chandrashekar, Javier Caballero and Meurig Thomas Professor Brad Wayne (Material Department, University of Sheffield). I would also like to thank Dr's. Chris Tyler and Sebastian Nervi from The Boeing Company on their support when I needed!

Most importantly, I would like to thank my wife Suman for her patience and support especially in the final stages, my grandmother Mira, Aunt Papinder, my sisters Sonia and Sunita, my two brothers Ajay and Arjun for all their tireless support and motivating me from the beginning.

Finally, I would like to express my gratitude to Mama Maria and Mungu Baba for giving me everything I have and walking with me throughout this all whole journey always.

It has been a journey and I have met and worked with so many wonderful people throughout and I want to thank all those who I have not mentioned but have really helped me! Thank you!

Abstract

Airframe structural components that are machined from aluminium forgings or plate stock represent a significant contribution to the cost of both military and commercial aircraft. These components tend to distort due to heat treating induced bulk stresses and machining. Correcting these distortions increase costs and manufacturing lead times, especially for a high-volume, high-quality production company. In addition to this, variation in the residual stress profile from component to component is common due to variation in the condition of supply state. There is therefore a need to understand and model the effects of heat-treating and machining strategies on distortion and to predict, minimize, and control these distortions. This thesis addresses the modeling, data acquisition, and validation of residual stress and distortion models using different aluminium test cases. The project is divided into five technical studies to build the modeling capability:

In the first study, aluminium 7050 material data and heat transfer coefficients were experimentally acquired. This data was to be used as an input to demonstrate the capability of Finite Element (FE) modelling as the main tool to predict and design robust strategies in the presence of residual stress variation due to processing or geometric differences. In the second study, the simulation study was performed to improve the machining distortion by using finite element (FE) modelling on symmetric and asymmetric residual stress profiles of aluminium coupons. In the third study, the popular aluminium tool path strategies were simulated using FE modelling. The fourth study, aimed to investigate the effect of a pocketing sequence, billet orientation and part location in a representative aluminium structure, on machining distortion. Finally, utilizing the knowledge acquired from the validated finite element simulation of these different studies, a machining process strategy for distortion control was proposed which reduced the distortion further by around 20%.

Table of Contents

Table of Contents

Acknowledgements.....	i
Abstract.....	ii
Table of Contents.....	iii
Table of Figures.....	vii
Table of Tables.....	xvii
Table of Equations.....	xviii
1 Introduction.....	1
Production demands in aerospace industry.....	1
Manufacturing demands in Aerospace.....	4
1.1 Aim and Objectives.....	7
1.2 Dissertation organization.....	8
2 Residual stress evolution within manufacturing of aerospace components.....	10
2.1 Introduction.....	10
2.2 Material processing and demand.....	10
2.3 Residual stress influence during aluminium processing.....	12
2.4 Effect of heat treatment on residual stress.....	14
2.5 Effect of machining on residual stress and distortion.....	21
2.5.1 Motivation of reducing distortion in machining.....	22
2.5.2 Residual stress-induced machining distortion.....	22
2.5.3 Justification of influence of residual stress from the quenching operation on machining distortions.....	25
2.5.4 Different factors influencing machining distortions.....	26
2.6 Summary and discussion.....	30
3 Measurement techniques.....	31

Table of Contents

3.1	Residual Stress measurements	31
3.1.1	Bulk residual stress measurements	32
3.2	Distortion measurement techniques.....	36
3.2.1	Contact measurement techniques.....	37
3.2.2	Optical 3D coordinate measuring machines	38
3.3	Strain measurements in machining	40
3.4	Summary and conclusion.....	41
4	Modelling of residual stress and machining distortions.....	42
4.1	Analytical models	42
4.1.1	Bending moment theory	43
4.1.2	Strain energy density relaxation theory	45
4.2	Numerical modelling	47
4.2.1	Simulation requirements	49
4.2.2	Quenching simulation	52
4.2.3	Machining distortion simulation software.....	53
4.3	Model validation.....	62
4.4	Summary and conclusion.....	63
5	Finite element modelling methodology	64
5.1	Finite element development.....	64
5.1.1	Model formulation	65
5.1.2	Model assumption.....	78
5.1.3	Numerically prediction of residual stress during heat treatment process	78
5.1.4	Numerical simulation of the machining process	105
5.2	Summary and discussion.....	137
6	Experimental methodology.....	139
6.1	Flow stress calculation.....	139

Table of Contents

6.2	Elastic material data.....	145
6.3	Heat treatment experimental set up	146
6.3.1	Thermocouple set up	146
6.3.2	Solution heat treatment and quenching set up	147
6.4	Residual stress measurements.....	155
6.4.1	Contour measurements	155
6.4.2	Neutron diffraction	158
6.5	Strain measurements using strain gauges	164
6.6	Machining trials.....	165
6.6.1	Machining trial set up for symmetric and asymmetric coupons.....	165
6.6.2	Experiment: tool path layout trials	166
6.6.3	Machining trial set up for representative part	167
6.7	Summary	170
7	Residual stress and distortion analysis	171
7.1	Residual stress analysis.....	171
7.1.1	Residual stress analysis on rectangular coupons.....	171
7.1.2	Residual stress analysis for symmetric and asymmetric RS on coupons	180
7.1.3	Residual stress measurement on rectangular blocks	187
7.1.4	Residual stress measurement on representative part	188
7.1.5	Effect of part offset on representative part	191
7.2	Strain measurements during machining of coupons.....	193
7.3	Distortion analysis.....	194
7.3.1	Distortion analysis on rectangular coupons.....	194
7.3.2	Distortion analysis during machining of symmetric and asymmetric RS on coupons 198	
7.3.3	Distortion analysis on tool path strategy.....	204
7.3.4	Distortion analysis due to the varying billet orientation	210

Table of Contents

7.3.5	Distortion analysis on varying part location	214
8	Machining Process Strategy for Distortion Mitigation from Bulk Residual Stress	217
9	Final conclusion	222
10	Future work	224
11	References.....	225
	Appendix A: Residual stress simulation of pocketing strategies	242

Table of Figures

Table of Figures

Figure 1-1: Boeing aircraft demand predictions from 2018 – 2037 [1] .	1
Figure 1-2: Airbus aircraft demand predictions from 2018 – 2037 [2].	2
Figure 1-3: Next generation aircraft demand prediction and range.	2
Figure 1-4: Percentage weight distribution of different materials in both Airbus A350 XWD [7] and Boeing 787 Dreamliner [8].	3
Figure 1-5: Aerospace material outlook [9].	4
Figure 1-6: Conversion of an aluminium structure; (a) Assembled structure, (b) Monolithic structure.	5
Figure 1-7: Machining generated distortion on aerospace components [21].	6
Figure 2-1: Production history of aluminium alloys in the aerospace industry [10].	10
Figure 2-2: Use of forming processes on (a) Airbus fleet, (b) Boeing fleet.	11
Figure 2-3: The coupling of temperature, stress and metallurgical changes [44].	12
Figure 2-4: (a) Cracking in a cast aluminium ingot due to excessive residual stresses [15], (b) Thin wall-floor aluminium component [45].	13
Figure 2-5: Schematic of potential causes of distortion and residual stresses during fabrication of a steel component [46].	13
Figure 2-6: Generation of residual stresses during quenching: (a) The external region and the internal region are in plastic state, (b) The external region is shrinking and in elastic state while the inner region is still in plastic state, and (d) Both layers are in elastic state.	14
Figure 2-7: Axial residual strain relief as a function of time (in-situ) during solution heat treatment of Al engine blocks [54].	15
Figure 2-8: Residual stress measurements in real time [70].	17
Figure 2-9: Residual stress profile of a heat treated aluminium 7050 T74 alloy [78].	19
Figure 2-10: Residual stress measurements across the length of a T-section beam in flange-out case [80].	20
Figure 2-11: Effect of stress relieving and distortion [84].	21
Figure 2-12 – Effects of high speed machining on: (a) cutting force (radial and thrust) for aluminium alloys [85] (b) temperature [86].	21
Figure 2-13: Relationship between quench residual stress, machine induced stresses and machining distortion [32].	22
Figure 2-14: Residual stress profile in pre stretched material [99].	23

Table of Figures

Figure 2-15: Machining induced residual stress on; (a) Measurements on rib section, (b) Measurements on web section, (c) Measurement locations [101].	24
Figure 2-16: Source of machining distortion related to the machining of parts [106].	24
Figure 2-17: Illustration of the position of the final part within the initial part [11].	27
Figure 2-18: Effect of machining tool path strategies [123].	29
Figure 3-1: Current residual stress measurement techniques [15].	32
Figure 3-2: Superposition principle of the contour method [128]: (a) Original Stress in the component, (b) Part is cut in two, distorting the cut surface, (c) Cut surface is forced back to its original position.	33
Figure 3-3: Residual stress measurements due to diffraction.	35
Figure 3-4: Attenuation length against X-ray energy for various aerospace material.	35
Figure 3-5: GOM Triple Scan 3D-Scanner with blue light technology [149], Scanning at different angles [150].	38
Figure 3-6: Example of an optical displacement scan of: (a) Machined aerospace frame component, (b) Scan result [157].	40
Figure 4-1: Distortion generation due to residual stress distribution [99].	43
Figure 4-2: Integration of bending moment and strain energy density [184].	45
Figure 4-3: Stored elastic energy and machining distortion [84].	46
Figure 4-4: Advantages of finite element predictions of an aerospace rib component; (a) Numerical model set up, (b) Actual distorted component [45].	47
Figure 4-5: Element and node discretization in FEA.	48
Figure 4-6: Flow stress input example in DEFORM [196] as a function of Temperature, Strain rate and Strain.	50
Figure 4-7: Tetrahedral and hexahedral elements and their local coordinate system [225].	52
Figure 4-8: Thermal, metallurgical, and mechanical couplings in heat treatment [196].	52
Figure 4-9: One-step machining distortion simulation: (a) Pre heat treatment geometry, (b) Final part geometry with distortion.	56
Figure 4-10: Multi step machining distortion geometry at different stages: (a) Pre heat treatment, (b) Post heat treatment, (c) First material removal, (d) Second material removal, (e) Third material removal, (f) Final geometry.	56
Figure 4-11: Multi step with path dependency machining distortion simulation: (a) Pre heat treatment, (b) First material removal, (c) Second material removal, (d) Third material removal, (d) Fourth material removal, (e) Final geometry unconstrained.	57
Figure 4-12: Element deactivation technique at different regions for rib component [143].	58

Table of Figures

Figure 4-13: Interpolation of cutting forces on a pocket geometry [108], (b) hybrid model incorporating thermos-mechanical behaviour [171].	59
Figure 4-14: Comparison between Boolean operation and element deactivation [91].	59
Figure 4-15: Boolean operation with local remeshing [45].	60
Figure 4-16: Boolean illustration [11].	61
Figure 5-1: Hardening function determination from true stress with plastic strain in tension test.	68
Figure 5-2: Different hardening mechanisms:(a) isotropic hardening, (b) Kinematic hardening, (c) Combined iso-kinematic hardening, (d) Resulting stress–strain curves showing different yield stress in compression [251].	69
Figure 5-3: (a) DEFORM's interpolation, (b) Extrapolation rule for flow stress [196].	70
Figure 5-4: Kinematics of finite incremental deformation with Ω_0 is the deformed configuration at a current time t and a Ω_t deformed configuration at an incremental time $t + \Delta t$ [11] [250].	71
Figure 5-5: Redistribution and transfer of element data during remeshing [11].	73
Figure 5-6: Comparison of using conjugate gradient and sparse solvers as a function of elements for: (a) Relative time, (b) Relative memory.	73
Figure 5-7: Newton Raphson iteration method [258].	74
Figure 5-8: 2D to 3D conversion in DEFORM: (a) 2D FE model, (b) 3D FE model.	77
Figure 5-9: Automated symmetry plane assignment to die/ workpiece geometry and boundary code assignment for mesh [196].	77
Figure 5-10: Literature Block Configuration [28].	79
Figure 5-11: Traction free boundary conditions in: (a) σ_{XX} , (b) σ_{YY} , (c) σ_{ZZ} .	80
Figure 5-12: Sensitivity analysis of mesh elements on residual stress prediction in σ_{ZZ} .	81
Figure 5-13: Sensitivity analysis of Temperature change per step on residual stress in σ_{YY} .	82
Figure 5-14: Sensitivity analysis of Time change per step on residual stress in σ_{YY} .	82
Figure 5-15: Sensitivity analysis for convection coefficient on residual stress in σ_{YY} .	83
Figure 5-16: RS simulation using Koc et al stress in; (a) σ_{XX} and (b) σ_{YY} stress component.	84
Figure 5-17: RS simulation using Koc et al Stress in the σ_{ZZ} .	85
Figure 5-18: Test Block Selected for Experiments: (a) Block geometry, (b) Heat transfer boundary conditions.	86
Figure 5-19: Cooling Rates Sensitivity to Heat Transfer Coefficient point locations (P1, P2).	86
Figure 5-20: Cooling Rates Sensitivity to Heat Transfer Coefficient: (a) Surface region (P1), (b) Core region (P2).	87
Figure 5-21: Virtual Cooling Experiment to Select Thermocouple Locations.	88

Table of Figures

Figure 5-22: Experimental quench tests thermocouple data.....	89
Figure 5-23: Overall inverse optimization process [261].	91
Figure 5-24: Comparison between experimental thermal data and FEM [261].	92
Figure 5-25: Heat transfer coefficient for: (a) Face 1, (b) Face 2.	92
Figure 5-26: Heat transfer coefficient for: (a) Face 3, (b) Face 4, (c) Face 5, (d) Face 6.	93
Figure 5-27: HTC values at different temperatures for the rectangular coupon.....	93
Figure 5-28: Heat treatment process: a) Heat treatment process diagram, b) Heat transfer coefficient, (c) Application of convection coefficient (shaded) on all surfaces.	94
Figure 5-29: Rigid body motion nodal constraints during quenching, (b) Fixing of nodes in X, Y and Z direction.	96
Figure 5-30: Residual stress contour for the rectangular coupon.	96
Figure 5-31: Heat transfer coefficient profiles used during the quenching simulation.....	97
Figure 5-32: FEA process route.	98
Figure 5-33: Asymmetric FE model: (a) Inter-object relationship to join the two workpieces, (b) Temperature prediction, (c) Longitudinal Stress Prediction.	99
Figure 5-34: Heat treatment on aluminium 7050 slab.	100
Figure 5-35: Heat treatment longitudinal residual stress prediction.	101
Figure 5-36: (a) Rectangular pocket geometry dimensions top view, (b) Rectangular pocket geometry dimensions top view.	101
Figure 5-37: (a) rigid body motion boundary conditions, (b) Core section stress prediction.	102
Figure 5-38: Boundary condition used for the model.	102
Figure 5-39: Graphic illustration of the T74 heat treatment condition.....	104
Figure 5-40: 2D to 3D FE model conversion to confirm successful data interpolation and mesh type sensitivity at the mid width line in the σ_{XX} direction.....	104
Figure 5-41: 2D to 3D FE model conversion to confirm successful data interpolation and mesh type sensitivity at the mid width line in the σ_{YY} directions.	105
Figure 5-42: Comparison of DEFORM model with analytical, numerical formula from Shin [204].	106
Figure 5-43: Tool path optimization strategies: (a) Strategy one, (b) Strategy two, (c) Strategy three.	107
Figure 5-44: Residual stress redistribution due to material removal (fixed condition): (a) Residual stress before material removal, (b) Residual stress after material removal ((fixed condition)...	108
Figure 5-45: Residual stress redistribution due to material removal (unconstrained condition).	109

Table of Figures

Figure 5-46: Distortion mode in (a) Z direction, (b) X direction.	109
Figure 5-47: Distortion mode in (a) Y direction, (b) Twisting.	110
Figure 5-48: Post machining distortion influence of the rigid body motion constraint: (a) Constraint in the centre of the model, (b) Constraint in the end of the model.....	110
Figure 5-49: Post machining distortion influence of the rigid body motion constraint: (a) Constraint in the center of the model, (b) Constraint in the end of the model.....	111
Figure 5-50: Longitudinal stress profile and distortion measurements following material removal at the bottom (a) before taking second cut, (b) 3 mm axial material removal, (c) 1 mm axial material removal.	112
Figure 5-51: Influence of material removal on stress profile variation in the X-Z plane at different depths of cut carried out on a low compression gradient.....	113
Figure 5-52: Machining distortion model set up: (a) Boundary constraint applied in <i>X, Y and Z</i> direction, (b) Boundary constraint applied in Z direction only, (c) Material removal volume on workpiece.....	116
Figure 5-53: Initial material removal based on Stress Profile: a) Low RS profile, b) Medium RS profile, c) High RS profile.	117
Figure 5-54: Fixture release modelling: (a) Applied rigid boundary motion conditions, (b) Measurement locations.	118
Figure 5-55: Residual stress redistribution and distortion against depth of cut.	119
Figure 5-56: Schematic of the machined block; (a) Isometric view, (b) Top view, (c) Front view, (d) Machining FE model with boundary condition (highlighted in red).	120
Figure 5-57: Two widely used tool paths for machining aluminium alloys: (a) Zig-Zag layout, (b) Helical layout.	121
Figure 5-58: Residual stress evolution between helical and zig-zag tool path: (a) 2 mm depth of cut helical, (b) 2 mm depth of cut zig-zag, (c) 35 mm depth of cut helical, (d) 35 mm depth of cut zig-zag, (e) 70 mm depth of cut helical, (f) 70 mm depth of cut zig-zag.	122
Figure 5-59: Different tool entry angles on machining of aluminium pockets: (a) Helical ramping (3°), (b) Helical ramping (7°), (c) Helical tool path.	124
Figure 5-60: Radial depth of cut simulation (<i>ae</i>) : (a) Residual stress contour integration with tool path using <i>ae</i> = 14 mm, (b) Residual stress contour integration with tool path using <i>ae</i> = 5 mm.	125
Figure 5-61: Process flow chart of the development of the model for pocketing strategies.....	127
Figure 5-62: Boundary condition model set up for machining distortion simulation (a) Movement constraints in X, Y axis (b) Movement constraints in Z axis.	128

Table of Figures

Figure 5-63: Positioning of the machined workpiece in the forged billet (dimensions in mm)...	129
Figure 5-64: Section billet illustrating the axial part offset variation; (a) Billet 1, (b) Billet 2, (c) Billet 3.....	130
Figure 5-65: FE model comparison: (a) comparison of on machine inspection data, (b) FE model 2 stress profile (FE model 1 rotated 180° in the X axis), (c) Residual stress profile on FE model 1, (d) Residual stress on FE model 2, (e) Residual stress prediction across the thickness.....	132
Figure 5-66: Residual stress redistribution rate during volume removal of pockets 1-9.	133
Figure 5-67: Pocket removal analysis; (a) Pocket numbers, (b) Measurement locations, (c) Sequence displacement range comparison.....	135
Figure 6-1: (a) Experimental test machine, (b) coupon for material characterization tests.	140
Figure 6-2: Illustration of the test specimen geometry employed for the on-cooling tensile tests.	140
Figure 6-3: Temperature-time plot during testing of the coupon during: (a) On-heating and (b) On-cooling.	141
Figure 6-4: Aluminium 7050 True Stress Strain in as Forged Condition.	142
Figure 6-5: Strain rate sensitivity for aluminium 7050 Material data from the forged condition.	143
Figure 6-6: Aluminium 7050 Material data from the solution heat-treated and water quench condition.	143
Figure 6-7: Strain Rate Sensitivity in aluminium 7050 Material data from the solution heat-treated and water quench condition.	144
Figure 6-8: Integrated Flow stress calculation from [268] and Experimental results from Sheffield University Materials department with strain rates for 0.1.	144
Figure 6-9: Flow stress calculation from [268] and Experimental results from Sheffield University Materials department with strain rates for 0.01.....	145
Figure 6-10: Material input data for quenching simulation; (a) Elastic modulus, (b) Poisson's ratio.	145
Figure 6-11: Material input data for quenching simulation; (a) Thermal expansion, (b) Heat Capacity, (c) Thermal Conductivity.....	146
Figure 6-12: Thermocouple location on AA7050 block.	147
Figure 6-13: Heating up and holding temperature measurements for typical thermocouple. ...	148
Figure 6-14: Experimental during solution heat treatment.	148
Figure 6-15: Experimental set up for: (a) Quench tank (b) Top view of the AA7050 block in quench tank, (c) Post quenched block with thermocouples [13] inserted in coupon.	149

Table of Figures

Figure 6-16: Experimental set up for: (a) Symmetrical rectangular coupon, (b) Asymmetrical rectangular coupon.	150
Figure 6-17: Quench of the asymmetrical block.	151
Figure 6-18: Heat treatment set up for rectangular coupons: (a) Blocks set up (b) Thermocouple on blocks, (c) Air transfer of blocks, (d) Quenching of blocks.	152
Figure 6-19: Graphic illustration of the solution heat treatment condition.....	153
Figure 6-20: Process flow chart of the development of the model for pocketing strategies.	154
Figure 6-21: Contour measurement set up: (a) Wire EDM machine, (b) Surface roughness measurements.	156
Figure 6-22: Contour measurement set up: (a) 3D displacement measurements, (b) Data handing in MATLAB, (c) Residual Stress Contour.	157
Figure 6-23: Slitting the billet into sections A1 and A2 using wire EDM.	157
Figure 6-24: Residual stress measurement carried out using Neutron diffraction showing (a) Block fixturing (b) Measurement strategy.....	160
Figure 6-25: Block orientations for residual stress measurements.....	161
Figure 6-26: Measurement locations using neutron diffraction for the coupons: a) Mid width line direction, (b) Mid length line direction. Note that dimensions in the figures are in mm.	162
Figure 6-27: Measurement locations using neutron diffraction for the coupons: a) Mid width line direction, (b) Mid length line direction. Note that dimensions in the figures are in mm.	163
Figure 6-28: Measurement locations using neutron diffraction; (a) Mid width line direction, (b) Mid length line direction.	163
Figure 6-29: Measurement locations using neutron diffraction: (a) Thickness direction, (b) Set up. Note that dimensions in the figures are in mm.....	164
Figure 6-30: Strain measurements using strain gauges with (a) Strain gauge mounting on blocks, (b) Strain gauge locations.	164
Figure 6-31: Strain measurements using strain gauges.	165
Figure 6-32: Experimental set up.	166
Figure 6-33: Set up for blocking up the billet. Faces 2, 4 and 6 are in the opposite face.	168
Figure 6-34: Experimental set up for pocketing trials.....	168
Figure 7-1: σ_{XX} stress measurements in the X-Z plane for blocks 1, 2 and 3 after quenching.	171
Figure 7-2: σ_{XX} stress measurements in the Y-Z plane for blocks 1, 2 and 3 after quenching.	172
Figure 7-3: Data from the thermocouple mounted on the surface of all the quenched blocks. .	172
Figure 7-4: FE model comparison with experimental RS measurements in σ_{YY}	173

Table of Figures

Figure 7-5: σ_{XX} comparison of residual stress measurements on the mid thickness of the X-Z plane length.	174
Figure 7-6: σ_{XX} comparison between experimental stress data and numerical analysis for non-improved tool path in the X-Z plane.....	175
Figure 7-7: σ_{XX} comparison between experimental stress data and numerical analysis for improved tool path in the X-Z plane.....	176
Figure 7-8: σ_{XX} comparison between the robust process validation in mid thickness section of the block.	177
Figure 7-9: σ_{XX} contour measurement comparison along the block length (white line) between the (a) AMRC with Boeing and (b) Hill Engineering.	178
Figure 7-10: σ_{XX} symmetric residual stress measurements compared with FE models.	180
Figure 7-11: σ_{XX} residual stress measurements compared with FE models.	181
Figure 7-12: Crack across coupon caused due to excessive residual stresses generated during the quenching process.	182
Figure 7-13: σ_{XX} residual stress profile after machining the top face: (a) Coupon 1, (b) Coupon 2; (c) Coupon 3 (Coupon 4), (d) Measurement locations across coupon thickness.	183
Figure 7-14: σ_{XX} residual stress profile after machining the top face: (a) Coupon 1, (b) Coupon 2, (c) Measurement locations across coupon thickness.	184
Figure 7-15: σ_{XX} residual stress profile after machining the bottom face:(a) Coupon 1, (b) Coupon 2, (c) coupon 4, (d) Measurement locations across coupon thickness.....	185
Figure 7-16: Residual stress profile after machining the bottom face: (a) Coupon 1, (b) Coupon 2, (c) Measurement locations across coupon thickness.	186
Figure 7-17: σ_{XX} residual stress comparison with FE Model across the transverse direction..	187
Figure 7-18: σ_{XX} residual stress comparison with FE Model across the thickness.....	188
Figure 7-19: Measurement locations: (a) Across the width, (b) Across the thickness.	189
Figure 7-20: Residual stresses in the mid width line of the billet in σ_{XX}	189
Figure 7-21: Residual stresses in the mid width line of the billet in σ_{YY}	190
Figure 7-22: Residual stresses in the mid width line of the billet; (a) in σ_{XX} ,(b) in σ_{YY}	191
Figure 7-23: Residual stresses measurements in the mid width line of the billet; (a) σ_{XX} ,(b) σ_{YY}	192
Figure 7-24: σ_{XX} residual stresses comparison in the mid width line for: (a) Billet 1, (b) Billet 2.	193
Figure 7-25: Influence of improved cut 11 on strain.....	194

Table of Figures

Figure 7-26: Different stages of material removal; (a) Initial stage, (b) Machined top face, (c) Machined bottom face.....	195
Figure 7-27: Comparison of experimental distortion data with numerical simulation for machining strategy A (non-improved tool path).	195
Figure 7-28: Comparison between experimental distortion data and numerical analysis for machining strategy B (Improved tool path).	196
Figure 7-29: Comparison between experimental distortion data and numerical analysis for robust selection process.	197
Figure 7-30: Distortion comparison between non-improved tool path (A) and improved tool path (B).....	197
Figure 7-31: Second cut analysis for symmetric residual stress coupons: (a) Coupon 1, (b) Coupon 2, (c) Coupon 3, (d) Coupon 4.	199
Figure 7-32: Second cut analysis for symmetric residual stress coupons: (a) Coupon 1, (b) Coupon 2.	199
Figure 7-33: Effect of Tool Path Strategy on machining Distortion Machining distortion comparison with experimental data for the symmetric RS coupon 1.....	200
Figure 7-34: Effect of Tool Path Strategy on machining Distortion Machining distortion comparison with experimental data for the symmetric RS coupons: (a) Coupon 4, (b) Coupon 5.	201
Figure 7-35: Effect of Tool Path Strategy on machining Distortion Machining distortion comparison with experimental data for the asymmetric RS coupons: (a) Coupon 1, (b) Coupon 2.	202
Figure 7-36: FE model comparison with post machining distortion for the symmetric RS coupons: (a) Coupon 1, (b) Coupon 2.	202
Figure 7-37: FE model comparison with post machining distortion for the symmetric RS coupon 4.....	203
Figure 7-38: FE model comparison with post machining distortion for the asymmetric RS coupons: (a) Coupon 1, (b) Coupon 2.	203
Figure 7-39: Post machining distortion comparison between tool path strategies used for pocketing operation.....	204
Figure 7-40: FE Model comparison with On Machine Inspection for: (a) Zig-Zag tool path, (b) Helical tool path.	205
Figure 7-41: Effect of Neutral Axis on machining distortion.	206
Figure 7-42: FE comparison with post machining distortion data for zig-zag tool path.....	206
Figure 7-43: FE comparison with post machining distortion data for helical tool path.	207
Figure 7-44: Post machining distortion comparison for helical ramp angles.	207

Table of Figures

Figure 7-45: FE model comparison with CMM for 3 ° ramp angle.....	208
Figure 7-46: FE model comparison with CMM for 7 ° ramp angle.....	209
Figure 7-47: FE model comparison with CMM for 3 ° ramp angle.....	209
Figure 7-48: 3D displacement scanning for billets: (a) Convex, (b) Concave.....	210
Figure 7-49: 3D displacement scanning for billets: (a) Convex, (b) Concave.....	211
Figure 7-50: 3D scanning repeatability assessment.	211
Figure 7-51: FE model comparison with CMM for effect of pocketing sequence on machining distortion.	212
Figure 7-52: FE model comparison with CMM for effect of billet orientation on machining distortion.	212
Figure 7-53: FE model comparison with CMM and 3D displacement scanner for pocketing using sequence A.....	213
Figure 7-54: FE model comparison with CMM for effect of billet orientation and pocketing sequence.	214
Figure 7-55: FE model comparison with CMM for effect of billet orientation.	215
Figure 7-56: FE model comparison with CMM for effect of billet orientation.	215
Figure 8-1: Production manufacturing strategy flow chart.....	217
Figure 8-2: Positioning of the machined workpiece in the forged billet (dimensions in mm).....	218
Figure 8-3: Part offset in the width direction.	219
Figure 8-4: Residual stress variation across the longitudinal direction.....	220
Figure 8-5: Part offset in the longitudinal direction.....	220
Figure 8-6: Post machining distortion comparison between current MoM and Proposed MoM.	221
Figure A-1: Bulk residual stress redistribution during pocketing sequence: (a) Quench residual stress condition of the billet, (b) Pocket 1, (c), Pocket 2, (d) Pocket 3.	242
Figure A-2: Bulk residual stress redistribution during pocketing sequence: (a) Pocket 4, (b) Pocket 5, (c) Pocket 6, (d) Pocket 7.....	243
Figure A-3: Bulk residual stress redistribution during pocketing sequence: (a) Pocket 8, (b) Pocket 9, (c) Fixture release.	244
Figure A-4: Bulk residual stress redistribution during pocketing sequence: (a) Quench residual stress condition of the billet, (b) Pocket 1, (c) Pocket 2, (d) Pocket 3, (e) Pocket 4, (f) Pocket 5.	245
Figure A-5: Bulk residual stress redistribution during pocketing sequence: (a) Pocket 6, (b) Pocket 7, (c) Pocket 8, (d) Pocket 9, (e) Sequence 2 fixture release.....	246

Table of Tables

Table 4-1: Quenching simulation software capabilities [67].	53
Table 4-2: Comparison between ABAQUS and DEFORM for machining distortion simulations.	55
Table 5-1: Heat treatment FE model input parameters.	95
Table 5-2: 2D Heat treatment FE model input parameters.	103
Table 5-3: T74 process information.	103
Table 5-4: Machining distortion FE input parameters.	108
Table 5-5: Tool path strategy.	115
Table 5-6: Axial depth of cuts of the symmetric stress profile.	118
Table 5-7: Axial depth of cuts of the asymmetric stress profile.	118
Table 5-8 - Tool path layout durations in Siemens NX 7.	123
Table 5-9: Machining distortion FE input parameters.	129
Table 5-10: Axial material removal.	131
Table 5-11: Pocket sequence.	136
Table 6-1: Experimental Matrix.	142
Table 6-2: Solution heat treatment process.	153
Table 6-3: Heat treatment procedure for representative part.	154
Table 6-4: Contour measurements performed by different centers.	155
Table 6-5: Neutron diffraction measurements performed by different centers.	158
Table 6-6: Diffraction parameters performed by different centers.	162
Table 6-7: Machining parameters.	166
Table 6-8 - Machining parameters.	167
Table 6-9: Tap test information.	169
Table 6-10: Machining parameters.	169

Table of Equations

Equation 3-1: Bueckner's superposition principle	33
Equation 3-2: Bragg's law.	34
Equation 4-1: Relationship between the curvature and the bending moment	44
Equation 4-2: Strain energy density.	46
Equation 4-3: Distortion as a function of strain energy density.	46
Equation 4-4: Stress range as a function of strain energy density and distortion.	46
Equation 4-5: Flow Stress Formulation.	50
Equation 4-6: Element stress equation.....	57
Equation 4-7: Material matrix.	58
Equation 4-8: Boolean subtraction definition [240].	60
Equation 5-1: Stress Tensor as function of Hydrostatic and Deviatoric Parts.	65
Equation 5-2: Equivalent von Mises stress.....	65
Equation 5-3: Initial yielding condition.	66
Equation 5-4: Incremental linear strain tensor.	66
Equation 5-5: Law of strain additivity from the Prandtl-Reuss theory.....	66
Equation 5-6: Effective strain rate as a function of the plastic strain.	66
Equation 5-7: Effective strain as a function of the effective strain rate.....	66
Equation 5-8: Stress-strain relations in x y z coordination system.	67
Equation 5-9: Stress-strain relations in tensor notation for isotropic materials.	67
Equation 5-10: Associated flow rule.	67
Equation 5-11: The associated flow rule in relation to the von Mises criterion.	67
Equation 5-12: Yield stress as a function of hardening function, plastic strain and true stress...68	
Equation 5-13: Isotropic hardening rule as a function of equivalent stress and plastic strain.69	
Equation 5-14: Equivalent stress as a function of plastic strain, strain rate and temperature.....70	
Equation 5-15: Position vector of a material location.	71
Equation 5-16: Langrangian displacement.	71
Equation 5-17: Modified Langrangian method for small time increments.....71	
Equation 5-18: Equilibrium condition.	75
Equation 5-19: Jacobian stiffness matrix.....	75
Equation 5-20: Change of incremental displacement as a function of incremental displacements for the <i>ith</i> iteration.	75

Table of Equations

Equation 5-21: Explicit method formulation.	76
Equation 5-22: Velocity convergence error limit.	76
Equation 5-23: Force convergence error limit.	76
Equation 5-24: Traction free boundary conditions.	80
Equation 5-25: Evaluation of the objective function.	91
Equation 5-26: Evaluation of the objective function with respect to nodal temperature and FEM.	92
Equation 5-27: Relationship between the residual stress redistribution ratio and distortion.	119
Equation 5-28: Residual stress redistribution ratio.	119
Equation 5-29: Coulomb friction law.	128
Equation 5-30: Residual stress redistribution relationship during material removal.	137
Equation 5-31: Residual stress redistribution relationship during material removal.	138
Equation 6-1: Stress calculation in X, Y and Z directions.	159
Equation 6-2: Strain calculation in X, Y and Z directions.	159
Equation 7-1: Cumulative error in FE modelling of residual stresses.	184
Equation 8-1: Part offset relationship with tri-axial stresses.	220

1 Introduction

Production demands in aerospace industry

Passenger traffic continues to show impressive expansion on a global scale. According to studies done in 2018 by the Boeing company [1] has predicted deliveries of 42,730 planes (Figure 1-1) with a market value of \$6.3 trillion from 2018 – 2037 regardless of increased air travel and airport restrictions. This led the Boeing Company to commence manufacturing the next generation Boeing 777 X aircraft, building on the success of 777 and the 787 Dreamliner families. Similarly, Airbus group [2] have similarly predicted an increase of demand for over 47990 new fleets (Figure 1-2) with an estimated market value of \$4.6 trillion. According to both companies, there is a popular demand mainly in Asia pacific countries for the single aisle planes from both companies (70% increase).

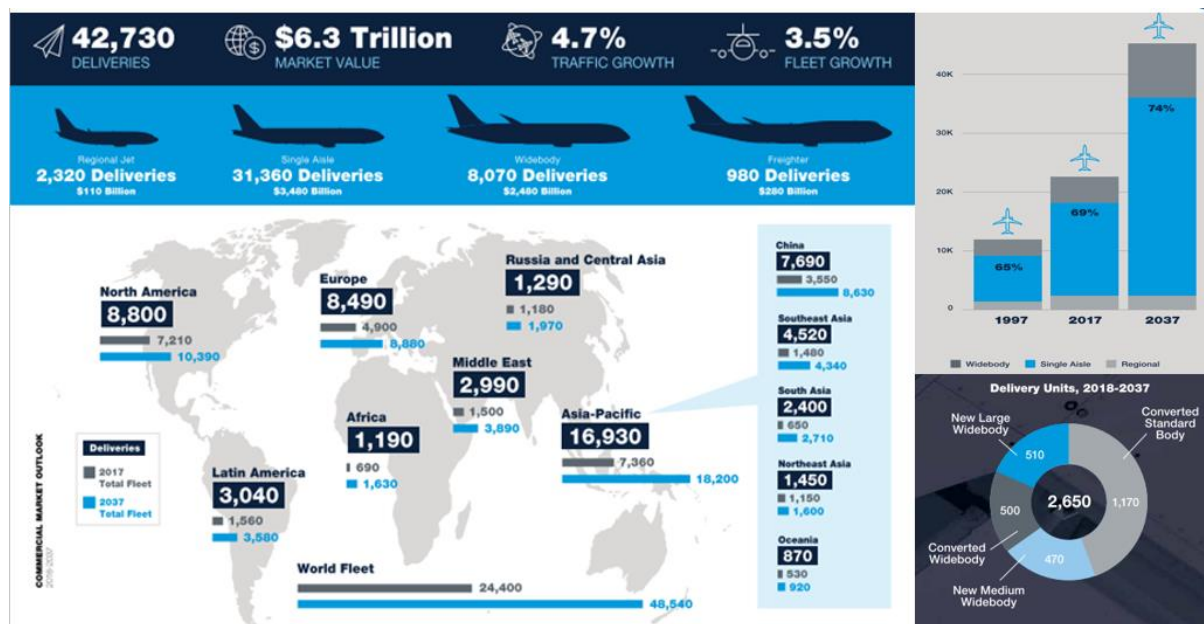


Figure 1-1: Boeing aircraft demand predictions from 2018 – 2037 [1] .

Chapter 1: Introduction

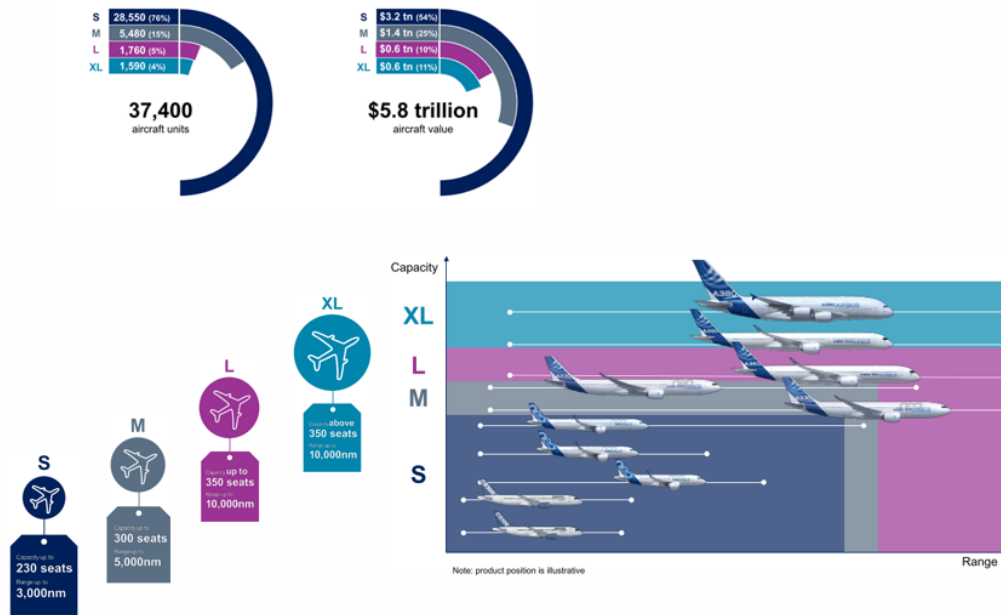


Figure 1-2: Airbus aircraft demand predictions from 2018 – 2037 [2].

With these demand forecasts for the next 19 years, the industry is facing many challenges to increase nautical range and passenger seats for the next generation aircraft (Figure 1-3) while producing further efficient parts with reduced lead times, using the most advanced materials and manufacturing technologies with passengers benefit from an increased level of comfort [1] [2].

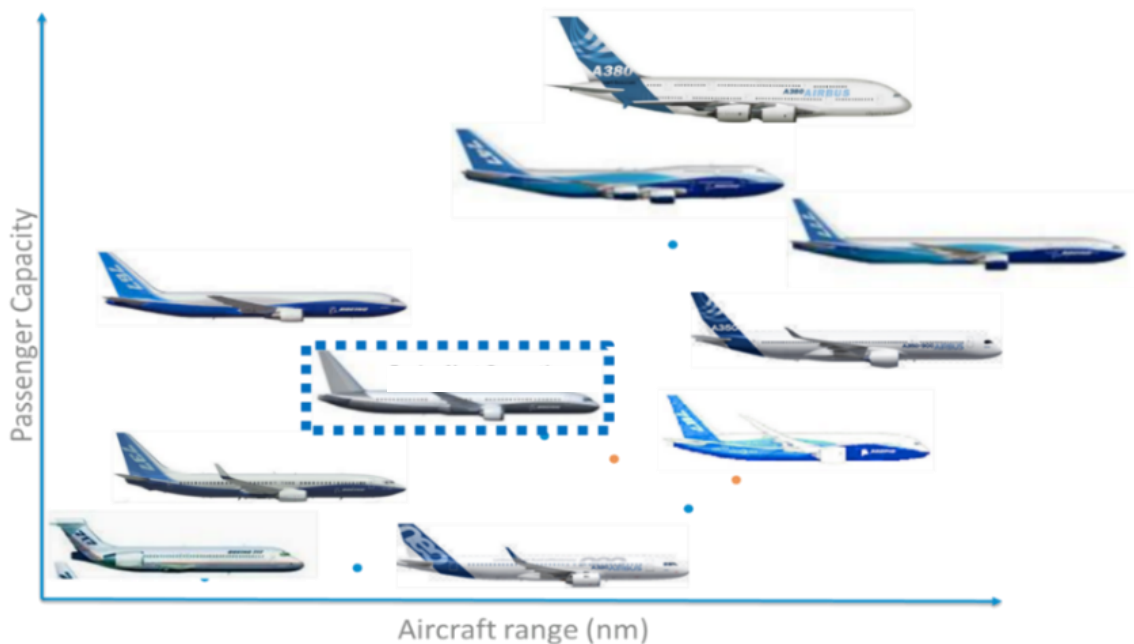


Figure 1-3: Next generation aircraft demand prediction and range.

Chapter 1: Introduction

One way to attain this industry objective of efficient and effective production is through the manufacturing of lightweight components to save on the airline's fuel cost which is the largest cost incurred by airlines [3]. The other factor that the industry is aiming to achieve competent and valuable production is via designing aircraft components with optimized mechanical properties using the least amount of resources and waste (material, energy) possible to produce them within the intended or expected result [4]. Both the development of advances in materials and the optimization of the manufacturing processes are therefore solutions.

This need has already led to an increase in the use of percentage weight of composite materials for aircraft construction as shown in Figure 1-4. Although Figure 1-4 illustrates an increase in the use of percentage weight composites, according to Alcoa, aluminium alloys will still remain a material of choice in the manufacture of airframe components [5] [6] especially on parts with a complex form or with significant mechanical loading in flight. A study was done by economic & financial analysis (Figure 1-5) on the aerospace supply chain and material outlook until 2024 found that there is a 48% material demand for aluminium only in comparison to a combination of demand from other metal alloys (48%) or composite materials (4%). The study also highlighted that between 30% and 36% demand for the aluminium alloys is coming from Boeing and Airbus respectively.

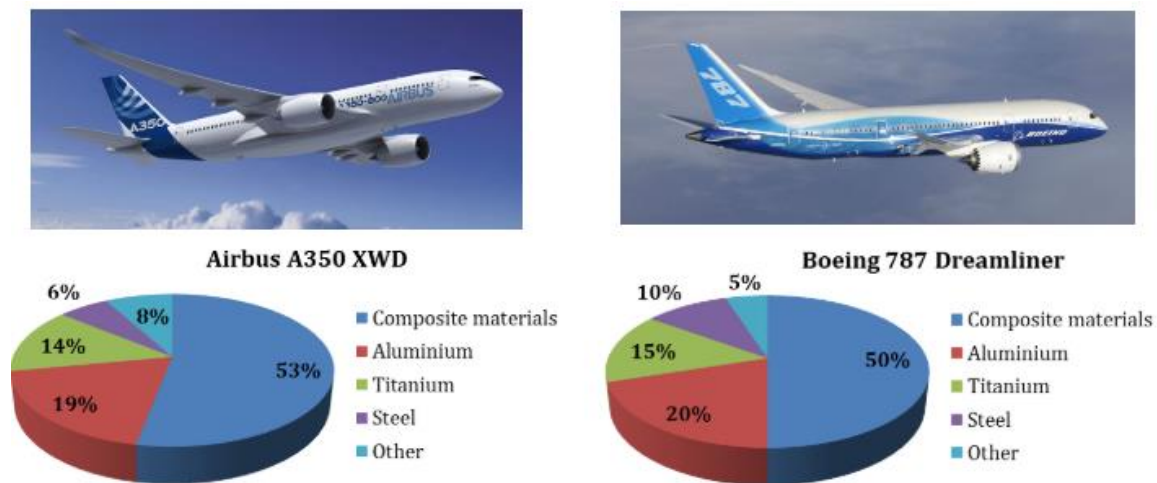


Figure 1-4: Percentage weight distribution of different materials in both Airbus A350 XWD [7] and Boeing 787 Dreamliner [8].

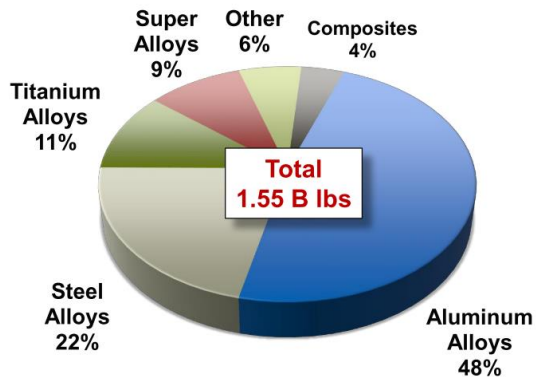


Figure 1-5: Aerospace material outlook [9].

Manufacturing demands in Aerospace

With the use of aluminium to reduce weight in aircraft components by using the appropriate material or design, a further initiative was made to reduce weight by reducing the part inventory in the aircraft.

This led to a drive to manufacture components from a single structure (monolithic), functionally equivalent to its assembly counterpart, rather than manufacturing smaller multiple parts assembled into the same designed structure for example; fittings, bulkheads, wing ribs, and beams [10]. With the number of parts (Figure 1-6) reduced, this produced effective benefits of the reduction in the aircraft weight, overall part cost [3] [11].

With the advantages of monolithic components, manufacturing these parts using the appropriate parameters is vital. Manufacturing delays slowing down the delivery of the aircraft often have severe consequences (for example penalties of around \$5.1 Billion) can damage the reputation of the aircraft company [12], therefore production times are important to be reduced.

Machining is often the final step of the manufacturing process, therefore, a critical operation in the overall manufacturing of aerospace components. With the development in high performance computer numeric control (CNC) machines and advanced cutting tools, extraordinary material removal rates can be attained making high performance milling (HPM) an efficient solution to the manufacturing of monolithic aerospace components within the given time scale [5].

Chapter 1: Introduction

During the manufacturing of monolithic components, 90% of material is machined away to obtain the final part. Unfortunately, the large volumes of material removed at a phenomenal rate lead to an increased non-conformance rate due to machining distortions resulting from the residual stresses imbalance within the billet, a phenomenon that is yet to be subjugated up to date.

Part distortion is a common problem in the manufacturing life cycle and is defined as the deviation of part shape when compared to its nominal design dimensions. The larger the deviation, the larger the non-conformance. Machining distortion has been identified as one of the main causes of geometric error and scrap parts [13] hence the importance to understand and overcome this phenomenon.

(a)



(b)

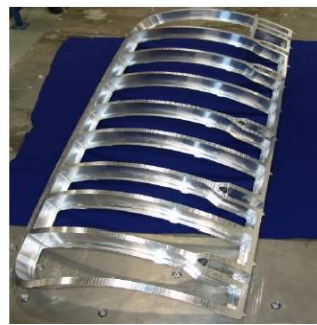


Figure 1-6: Conversion of an aluminium structure; (a) Assembled structure, (b) Monolithic structure.

Residual stress and machining distortion importance

Aerospace components especially aluminium alloys when compared with other alloys present a strong state of residual stresses due to the primary process (casting, forging, quenching), which results in undesired distortions after machining [14]. Residual stresses (RS) are defined as stresses which are in a material generated due to misfits either thermal-mechanical loads or microstructural [15] [16]. These stresses can either be beneficial or detrimental on the part for example, a particular machining process imparting stresses on the surface or sub surface residual stress on the part can extend or shorted the fatigue life of the component [17].

Chapter 1: Introduction

In the context of machining, when a layer is machined away from a material, the equilibrium of the stresses within the material is broken and the residual stresses would need to equilibrate to give a final residual stress profile. During this re-equilibration process, the part distorts. The distortion magnitude and direction would depend on the part rigidity, geometry and the residual stress magnitude prior to the removal of the layer.

Part distortion (Figure 1-7) due to inherent residual stresses has resulted in recurring concession, rework and incurred part rejection costs [18] in some cases worth millions during the aircraft development and manufacturing program. A study done by Boeing in 2001 estimated that the rework and scrap costs related to distortion, based on four aircraft programs, was in excess of 290 million dollars [19]. Furthermore, it is estimated that distortion generated during heat treatment create an economic loss in Germany for machine tool, automotive and power transmission industries costing an economic loss of €850 million [20] .



Figure 1-7: Machining generated distortion on aerospace components [21].

The choice of machining process plan is based on years of experience and expertise generated by trial and error philosophy of both the manufacturing engineers, machine operators and tooling and fixture suppliers. It is difficult for the manufacturing engineer to be able to quantify the distortion of a part according to the proposed operation. There is therefore almost no understanding and contradictions available based on scientific analysis in the definition of machining process plans. A lapse that is recurring constantly in the machining process plan is the exclusion of the residual stresses from the primary process of the initial workpiece. This can be due to either the limitations of the CAD/CAM software, lack of information from the material suppliers or both factors combined. There is therefore a requirement for a more systematic and scientific approach for machining distortion control and optimization.

Due to these restrictions in industry to control machining distortions due to trial error, there is a requirement to reduce the experimental work and generate a method of understanding the method of residual stress redistribution and its relation with machining distortions.

1.1 Aim and Objectives

Previous scientific research has attempted to diminish distortion in various ways. One of the most popular methodologies and oldest is by controlling the residual stresses generated from the heat treatment process. These stresses are found to be the main contributor of machining distortion in aluminium alloys [14] therefore different attempts have been made to reduce these stresses by utilizing different quenching strategies [16] [22] [24] [25] or ageing.

An alternative approach and is implemented universally by aluminium producers is to mechanically stress relieve the part after heat treatment. This methodology has been proven to reduce further the residual stresses after the heat treatment process between 70 – 80% [26] [27] [28]. Other researchers have attempted to employ vibration to stress relieve aluminium components [29] [30]. Regardless of their attractiveness and promises, some of these techniques are limited to simple geometries or dimensions. Additionally, machining the stress relieved components clearly exhibit distortion issues especially in thin walled / floor aluminium components [31]. This has led researchers to segment their approach on different machining strategies on areas including:

- Machining tool path strategy [11] [32] [33]
- Work holding [11] [34]
- Machining sequence [11] [35]
- Cutting parameters [11] [36] [37] [38]

Regardless of all the efforts to mitigate machining distortion, majority of these studies have shown a limitation in their strategy to impede distortion by either using trial and error or working on simple geometries, which lacks on providing an explanation of how to mitigate machining distortions using practical, cost effective and time saving approaches.

Therefore, the study in this thesis aims to overcome the current limitations by creating a methodology to control machining distortion due to the residual stresses.

Chapter 1: Introduction

This is done in the fulfilling five objectives:

- Simulate residual stresses from the quenching process for different case studies. The models will then be validated using two widely used residual experimental techniques: contour technique and neutron diffraction.
- Once the heat treatment model is validated, different machining strategies and their effects on distortion will be simulated. These case studies will then be validated by performing machining trials and validating the distortions using experimental measurement techniques. This objective demonstrates the novelty of this thesis.
- Neutron diffraction residual stresses will be performed on a case study to understand the evolution of residual stresses during the machining process. Similarly, the measurement of the residual stress redistribution during different machining process demonstrates the novelty of this thesis.
- Once the underlying principles of machining distortion is appreciated, an experimental machining solution will be proposed based on a sequential arrangement of the machining operations depending on the findings from the finite element simulations.

Therefore, this research overcomes current knowledge gaps by provides a methodical and satisfying the economical demand for truculent machining distortion concerns.

1.2 Dissertation organization

Chapter 2 embodies a review of literature presented constituting the backbone for the whole dissertation. This chapter discusses residual stresses development during the manufacturing process, measurement techniques employed to quantify these stresses and consequent distortions. Finally, numerical models developed to simulate the machining are revised.

Chapter 3 is dedicated to the finite element methodology used in this study. This chapter will include simulating the quench residual stress from the heat treatment process. An in depth analysis will then carried out on the machining strategies of first order (factors with the biggest influence) from simple coupons to machining of complex industrial parts. This will lead to determining a set of rules to ensure part conformance.

In chapter 4, the experimental work will be presented and discussed to allow experimental validation of the numerical tool.

Chapter 1: Introduction

This will include the material characterization set up, the heat treatment, machining trials and both the residual stress and machining distortion measurements on both the coupons and a representative part.

In chapter 5, in order to validate our hypothesis, the simulated finite element models are to be compared with the post machining distortion and residual stress measurement results to provide a better understanding of the machining process and the possibility to optimize the machining process plan to ensure the accuracy and quality aimed.

Following the validation of the hypothesis from this research, a machining process strategy for machining distortion mitigation will be presented in chapter 6. This will present a machining process plan to help avoid the rejection of parts due to the non-conformity with dimensional and geometrical specifications as well as the realization of extra-conforming steps to decrease the post-machining distortions and to make the part compliant with the tolerance specifications.

Following on from this, Chapter 7 consists of a general discussion and conclusion of this thesis and recommendations for some improvements that can be made to the FE models that were presented in this thesis and other related work that would be relevant for the continuation to that which had been achieved so far.

2 Residual stress evolution within manufacturing of aerospace components

2.1 Introduction

For a better apprehension of residual stresses, an introduction of their origins and influences is discussed further in this chapter. This section is dedicated to a complete review of literature on the effect of the manufacturing processes on the residual stress (RS) evolution on machining distortion, especially for aluminium alloys.

2.2 Material processing and demand

Aluminium is the most heavily consumed non-ferrous metal in the world due to its attractive cost of production, density and elastic modulus ratio [26]. Aluminium alloys (2XXX series) have been the material of choice in the aerospace industry since the 1920's (Figure 2-1). The increased requirement of strength, damage tolerance, and corrosion resistance, necessary to enable optimized structural performance saw the introduction of 7XXX series for thicker and upper section of the wings in the 1950's. Further development in the 1970's saw the development of aluminium 7050 first used on the Grumman A-6 Intruder twin jet aircraft. This alloy is considered the workhorse of high-strength aluminium alloys, due to its good balance of strength, stress corrosion cracking (SCC) resistance and toughness [39] and was less quench sensitive than most aerospace aluminium alloys at that time. Typical applications for aluminium 7050 plates include wing skins applications, fuselage frames and bulkheads where section thicknesses are 50–152 mm.

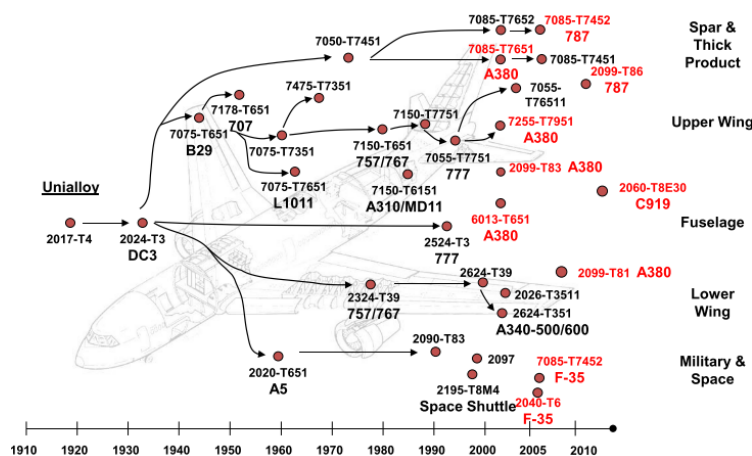


Figure 2-1: Production history of aluminium alloys in the aerospace industry [10].

Chapter 2: Residual stress evolution within manufacturing of aerospace components

Aluminium thick aerospace structural components [40] processing begins with forgings due to their high property retention [26] [41]. The forging process begins where the cast ingot is shaped using an upper (male) and lower die (female). The male die applies a large force (a punch / blow) on the cast ingot / billet forming it according to the semblance of the female die geometry. Unlike other material processing techniques, the grain structure formed in forgings is multi-directional and refined therefore producing homogenous material properties [41] [42]. It has also been found that forging or cold compression (T7452) has an advantage in terms of fatigue life [41], residual stress and machining in comparison to its stretched equivalent (T7451). The interactions of different aluminium processing techniques is shown in Figure 2-2. From Figure 2-2 (a) Boeing fleet has a large number of forged products (18%) in comparison to Airbus's fleet (5%), as also found in Figure 2-2 (b). It has also been reported that on the Airbus A380, around 1000 parts were forged [43].

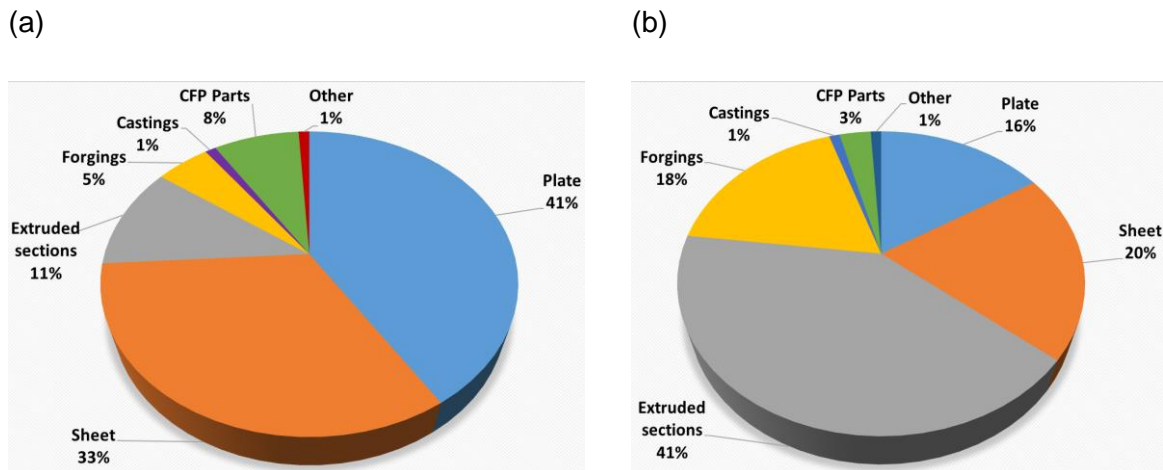


Figure 2-2: Use of forming processes on (a) Airbus fleet, (b) Boeing fleet.

Following the forging process, the mechanical properties are obtained during the solution heat (SHT) treatment and quenching process. The alloy is held at solution temperature for a certain amount of time to obtain a solid solution at equilibrium. This amount of time at the solution temperature assures that sufficient diffusion has occurred to allow complete solution of the alloying elements. The temperature is held just below the eutectic melting point to maximize diffusion rate and solubility. Quenching aims at cooling the material to room temperature as fast as possible to obtain a state as close as possible to solid solution at equilibrium before quenching. Quenching is fast in order to avoid or limit precipitation. In general, these aluminium-processing routes are beneficial to create the required properties but they can also act as an inconvenience.

This is due to these processes individually inducing large non-uniform plastic deformations, generate rapid temperature changes during cooling, phase transformations in the production process, and are often the main source of generation for residual stresses.

2.3 Residual stress influence during aluminium processing

In order to understand the residual stresses in the manufacturing process, it is important first to perform a global study on the origins of these stresses in the manufacturing process. Residual stresses are generated due to a coupling relationship between temperature, thermal stress and microstructure during manufacturing as shown in Figure 2-3. The processes responsible for producing residual stresses in aluminium alloys are due to:

1. Non-uniform plastic deformation due to processes like forgings, rolling or extrusions.
2. Large non-homogenous thermal gradients caused by quenching, precipitation hardening, additive manufacturing, welding or casting.
3. Manufacturing processes for example, milling, turning, grinding or shot peening.

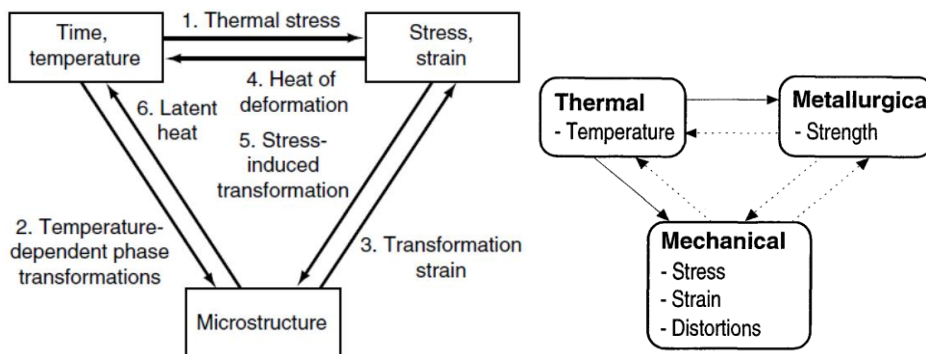


Figure 2-3: The coupling of temperature, stress and metallurgical changes [44].

Regardless of their extensive existence in everyday components, residual stresses are often overlooked during the design stage mainly due to their nature of existing without the need of external loads [15] and is often seen as a conundrum. This omission can have severe risk since RS can have a large influence on the material strength, distortion and service life of a component. For example, RS alone or in combination of other factors, can cause the failure of aircraft components (Figure 2-4) often with substantial loss of life and part distortion. Thus, it is deemed important to quantify these stresses to ensure integrity of structures when deployed to the working environment.

(a)



(b)



Figure 2-4: (a) Cracking in a cast aluminium ingot due to excessive residual stresses [15], (b) Thin wall-floor aluminium component [45].

To emphasize this further, a cause and effect diagram (Ishikawa diagram) is shown in Figure 2-5 to show the different factors that influence the residual stress and distortions from the heat treatment to the machining process. From this diagram, the design of the geometry, the material properties, the quenching environment and the machining operation are named to have an influence on residual stresses therefore on machining distortions.

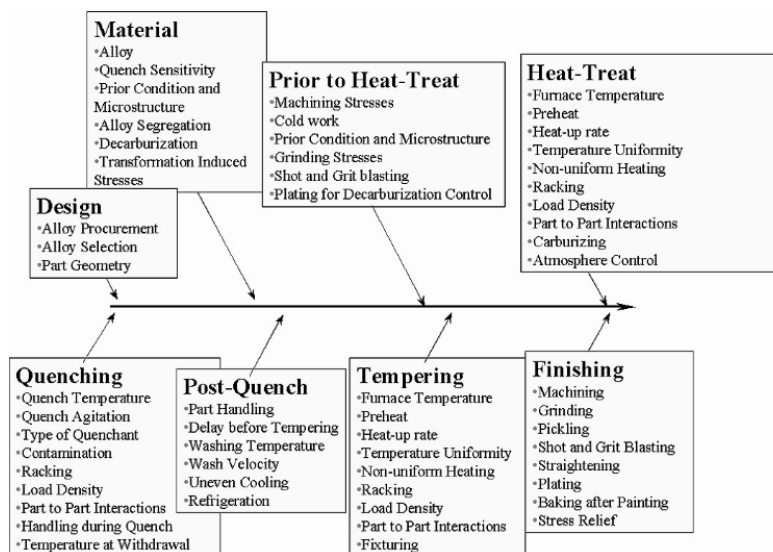


Figure 2-5: Schematic of potential causes of distortion and residual stresses during fabrication of a steel component [46].

2.4 Effect of heat treatment on residual stress

The residual stresses are generated when the block is immersed in a quenched bath and the surface region contract at a higher rate due to the cooling than the core region (Figure 2-6 (a)). During this process, the core regions begins to deform plastically so that it can adjust to the already contracted surface region (Figure 2-6 (b)). At this stage, the surface region has already cooled and restricts the interior region to contract further (Figure 2-6 (c)). This creates a misfit between the two regions and generates tensile stresses as a result in the core region and these stresses are equilibrated with compressive stresses near the surface [47].

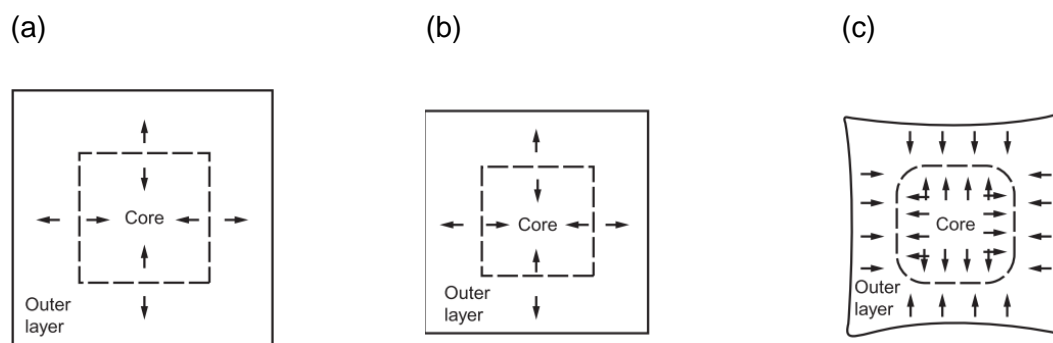


Figure 2-6: Generation of residual stresses during quenching: (a) The external region and the internal region are in plastic state, (b) The external region is shrinking and in elastic state while the inner region is still in plastic state, and (d) Both layers are in elastic state.

The amount of published work on residual stress effects in aluminium confirm that residual stresses in this alloy is a matter of concern, making it the most non-ferrous alloy investigated in published research. Davis [48] in his book on Aluminium alloys mentions that the solution heat treatment and quenching are the most critical processes since this is the stage where the required mechanical properties are generated but with a penalty of the residual stresses. Residual stresses generated in the quenching process have been found to have a critical influence in the subsequent manufacturing process of aluminium alloys [22]. Among the leading researchers studying the effect of residual stress in aluminium alloys, Robinson and Truman [49] have been publishing work for over 18 years. In his research, the residual stresses from the heat treatment were simulated and compared with experimental measurements in aluminium 7010. In another study, Robinson et al. [50] two forgings of aluminium 7010 and 7075 were quenched and residual stress measurements were performed to understand their influence of quench sensitivity.

Chapter 2: Residual stress evolution within manufacturing of aerospace components

In this study, it was found that aluminium 7010 was less quench sensitive than aluminium 7075 therefore the residual stresses were higher.

In another study, the residual stresses on Aluminium 7449 were immersed quenched and measured using neutron diffraction [51]. Although the work done was in aluminium 7075, the data is relevant to aluminium 7050 as both materials have similar material properties due to their chemical composition as stated by The Aluminum Association [52].

The generation of residual stresses during the heat treatment process in aluminium alloys has been studied in extent by Chobaut [53] in this thesis on the modelling and measurements of residual stresses during quenching. In this thesis, three different aluminium alloys (2618, 7040, and 7449) were studied and their residual stresses measured. It was also highlighted that this heat treatment stage that the residual stresses generated from the forging process (or any other forming process) are completely relieved during the solution heat treatment soaking time.. Lombardi et al. [54] demonstrated by a pioneering study done as shown in Figure 2-7 where residual stresses were measured in-situ during the heat treatment process. In this study, the residual micro strain shows that during the soaking time, the residual stress decrease. Additionally, this figure shows that the higher the solution temperature, the smaller the micro strain. The soaking times for most aluminium alloys are proposed as per the Aerospace Material Standard (AMS) and its highly recommended to use this standard as a guidance [26] [55].

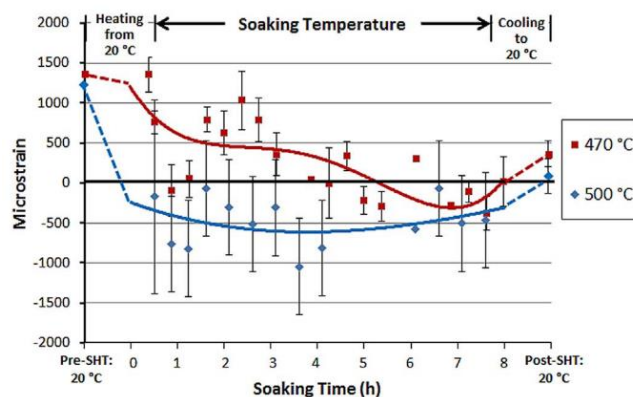


Figure 2-7: Axial residual strain relief as a function of time (in-situ) during solution heat treatment of Al engine blocks [54].

Once the part is soaked for the required durations, it is cooled after solution heat treatment in a quenchant. A quenchant is a medium that cools the workpiece, at different rates [56] creating the desired mechanical properties.

Chapter 2: Residual stress evolution within manufacturing of aerospace components

During the quenching of aluminium alloys, the material is plastically deformed at low strain rates, the rate of quenching determines the final magnitude of residual stress [50].

The common quenchants used in aluminium cooling is cold or warm water. Totten in his book [57] [58] stated that age hardened alloys (aluminium 2024, 2219, 7075, 7050 and 6061) are normally quenched in water. Similarly, Robinson et al. [59] quenched an Aluminium 7050 forging in four different quenchants which included warm water (60 °C), boiling water, molten salt (200°C) and uphill quenching (-196°C). From this study, it was found that quenching into boiling water and salt at 200°C did substantially reduce the residual stress and had only a small detrimental effect on the majority of the properties measured. In another study Tanner et al. [60] performed a study on the effect of quenching using warm water (60°C) and boiling water on residual stresses. In this study, it was concluded that quenching with boiling water reduces the stresses although with a penalty on the mechanical properties. Fontecchio et al [61] used distilled water for quenching aluminium 6061. Yang et al. [62] studied the effect of three different quenchants; water, machine oil and 5%-UCON quenchant A . In this study it was found that machine oil produced the lowest stresses, followed by the 5%-UCON quenchant and water caused the highest residual stresses due to the quench rate [63]. Zhang et al. [64] studied the effect of water and polyalkylene glycol solution on residual stresses during the quenching of aluminium 2024 blocks of different thicknesses from 20 to 50 mm.

From this study, it was concluded that residual stresses in polyalkylene glycol quench conditions were proved to cause lower levels of residual stress than water quench for blocks between 20 and 30 mm block thickness. Masoudi et al. [65] studies the effect of different quenchants (water, uphill quenching and polymer). The conclusion from this study showed that the water quenching had increased the distortion by three times in comparison to a part of the same geometry and material quenched using uphill or polymer quenching. Finally, the study concluded by stating that there was no recrystallization in the part quenched with water but this was not the case with uphill or polymer quenching, due to the slow quench rate.

The heat transfer coefficient ($W.m^{-2}.K^{-1}$) is identified as an important factor that need to be captured for accurate residual stress prediction. In 1964, Stolz [66] pioneered the method in which the heat transfer coefficient (HTC) can be calculated by simply comparing the measured temperature against the calculated temperature field. Osman et al. [25] later developed a method called the inverse heat transfer coefficient method using thermocouple data mounted internal of a workpiece.

Chapter 2: Residual stress evolution within manufacturing of aerospace components

Buczek et al. [63] found that during quenching, due to the rapid changing heat flux transferred to the coolant with time, the HTC cannot be calculated directly and required the use of a numerical method for this. The requirements of capturing the heat transfer coefficient accurately using thermocouples have been defined in detail by Bozidar [67].

Becker [68] in this simulation study found that by changing the elastic properties and thermal expansion coefficient in the material model made little difference in comparison to changing the heat transfer coefficient. Furthermore, three different regimes during the quenching process operate successively as shown in Figure 2-8 (a). These zones define how the HTC graph is as shown in Figure 2-8 (b).

- The convective cooling zone (room temperature ~100°C) - the water flow will increase the heat transfer capability since convection and radiation are the main heat transfer process in these zones.
- The nucleate boiling zone (100°C~200°C) - In the nucleate boiling zone, the water flow will decrease the heat transfer capability of the nucleate boiling. It is at this stage that the residual stress formation is critical and changes from compression to tension in the bulk of the material (Figure 2-8 (c)). The heat transfer coefficients in the range of 100°C ~200°C have a great influence on the quenching residual stresses, especially for the heat transfer coefficient near 150°C [69].
- The vapor blanket zone (above 200°C) - the water flow increases the heat transfer capability since convection and radiation are the main heat transfer processes in these zones.

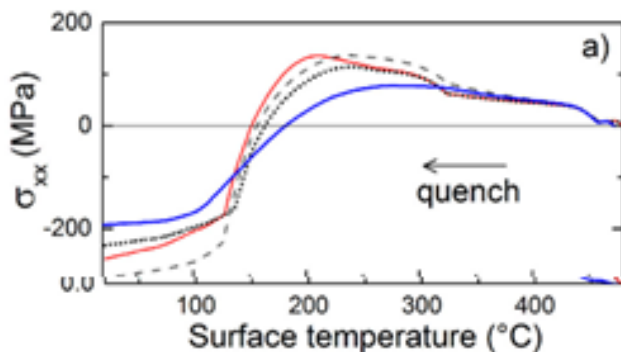


Figure 2-8: Residual stress measurements in real time [70].

From work done in Dong et al. [71] on the calculation of HTC values for different quenchants and different thermocouple locations in a 2XXX series aluminium block, it was found that the maximum HTC values varied between 15 – 20. Similarly, values of HTC was found by Koc et al. [28] on aluminium 7075 alloy and Li et al. [69] done on aluminium 7055 alloy therefore it can be concluded that the maximum HTC values are around 20 for water. It was also found that the HTC varies with the component surface as shown by Hall et al [72]. In this study, an L shaped component was quenched and temperature data was recorded across the different regions. It was concluded the temperature varies across the component due to the varying HTC. A similar conclusion was found by Campos et al [22] on an aluminium impeller. Although Urresti et al. [73] stated that with lack of HTC data across the surface, it is possible to assume the HTC is equal across the surfaces. Koc et al. [28] highlighted that a non-symmetric stress profile could be due to a non-uniform and non-symmetric quenching orientation of the part which would affect the symmetry of the residual stresses in the part due to the different heat transfer coefficient of the interface. Kopun [74] found that by quenching a part on the thicker section first, the residual stresses are lower than quenching the thinner region. From these studies, the two main factors that affect the HTC are the quenchant temperature and the rate of cooling between the workpiece and the quenchant [75]. Understanding the generation of the thermal gradient leads to a better understanding of the formation of residual stresses in four stages:

1. When there is an initial contact between the workpiece and the quenchant, there is an instantaneous non-homogeneous cooling of the formed component when the heated region makes contact with the quenching medium [61]. This non-homogeneous cooling creates a thermal gradient between the core and the bulk of the component.
2. This thermal gradient creates an elastic-plastic condition where the yielding of the material causes plastic deformation. During this rapid cooling, the plastically deformed region expands due to the tension.
3. At this stage now, the bulk of the component has a higher temperature than the outer region and begins to start cooling. Due to the temperature difference between the two areas, it begins to contract.
4. As the component continues to cool further, compressive stresses begin to develop on the surface while tensile stresses counteract the compressive stresses in the bulk, developing the common “bell shape” residual stress profile (Figure 2-9).

Chapter 2: Residual stress evolution within manufacturing of aerospace components

This profile is the conception of the profile that would evolve throughout the manufacturing process; therefore, it is critical to control this profile.

From Figure 2-9, the residual stress profile begins with low compressive stresses at the surface, which progressively increase in magnitude up to around 5 mm below the surface. Then compressive stresses tend to decrease (also known as edge effect [76]) down to zero in an area known as the 'neutral-stress area' [77].

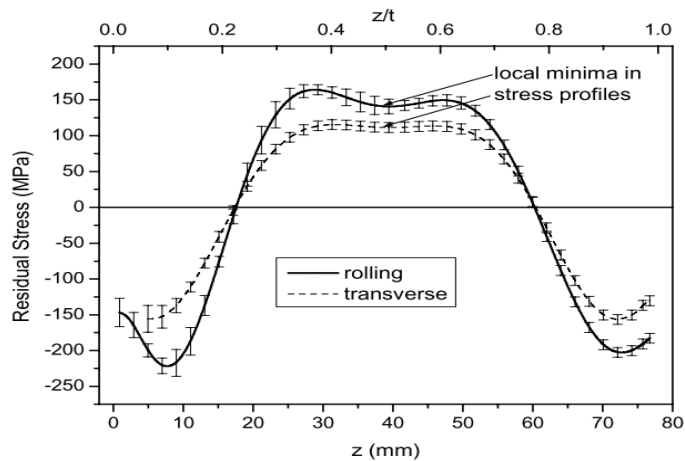


Figure 2-9: Residual stress profile of a heat treated aluminium 7050 T74 alloy [78].

In an extensive study of residual stresses and machining distortion, Robinson [51] concluded that a symmetrical residual stress profile from quenching is unlikely in cold water quenching. This is due to local variations of the heat transfer coefficient caused by surface finish variations and chaotic variations in convection. Another study by Ahmad [79] supports this observation by stating that residual stresses vary with each surface and there is no guaranteed repeatability of the residual stress profile during the quenching process.

Other factors that affect the residual stress profile is the component geometry. Zhang et al. [80] highlighted a non-symmetrical quenched part would produce a non-symmetrical residual stress profile which would create post machining distortion problems. This was illustrated where multiple residual stress measurements using the contour method was performed on a T-section beam aluminium 2662 aerospace component (Figure 2-11). In this study, it was found the residual stresses across the length of the beam was asymmetrical. In another study, Zhang et al. [81] performed contour measurements on an aluminium 7050 die forging that was quenched. The residual stresses across the thickness and length was asymmetrical which would similarly produce undesired post machining distortions.

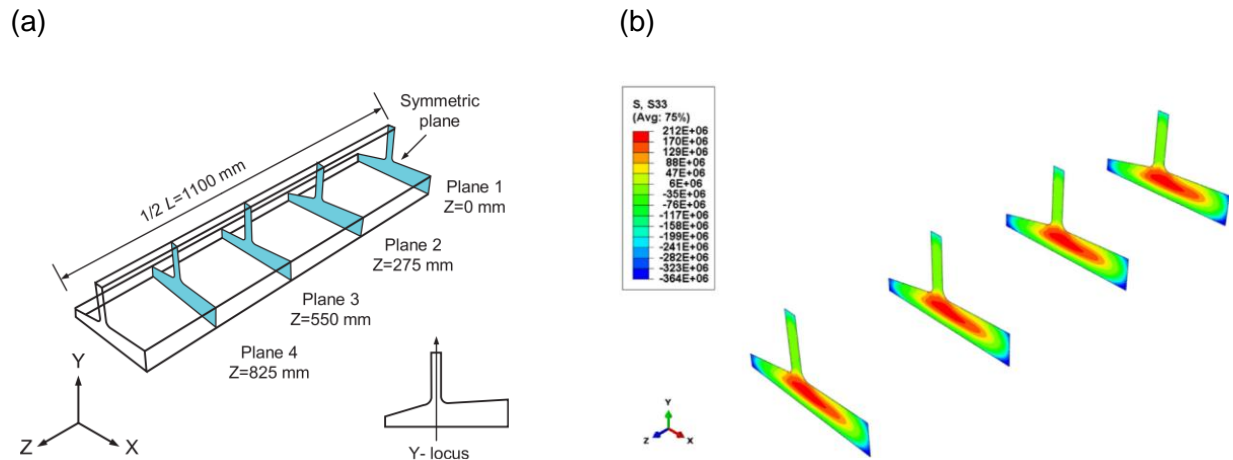


Figure 2-10: Residual stress measurements across the length of a T-section beam in flange-out case [80].

Other factors the quench induced residual stresses are the material properties [24], quench tank arrangement (i.e. (vertical or horizontal) [16] [22] [26]. Following the quenching process, the ageing process is performed. This process has been documented to relieve the quenching stresses by 20% [51].

Further stress relieving initiatives led in conjunction by both aircraft manufacturers and aluminium producers have been employed due to the high residual stresses developed during the quenching process of aluminium alloys. This led the aluminium manufacturers to develop tempers to stress relieved aluminium alloys [82] mainly for the aerospace industry. This is in order to control the distortion in the consequent manufacturing operations (for example machining) as shown in Figure 2-11. Majority of the stresses that have undergone using these tempers are either within the magnitudes of ± 30 MPa or below as shown by Prime et al. [78]. However, these stress relieving techniques either cannot be applied to complex geometries or influence the material properties [83]. Regardless of these limitations, it is currently the preferred industrial method to use. Despite this endeavor to control distortion using stress-relieving techniques, machining distortion effects are still evident and further research is required to better understand and control this phenomenon.

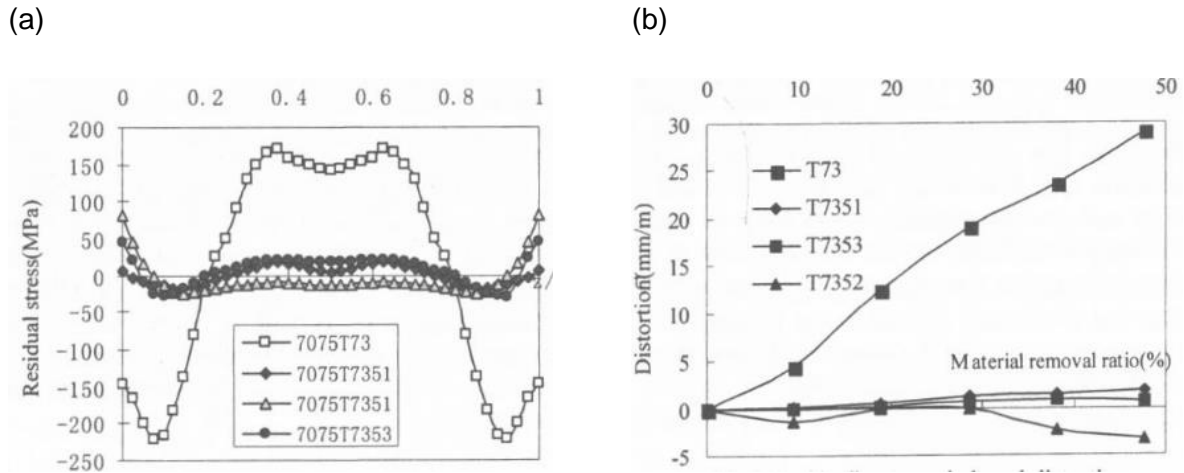


Figure 2-11: Effect of stress relieving and distortion [84].

2.5 Effect of machining on residual stress and distortion

Many researchers have covered the advantages of high speed machining of aluminium alloys, but apart from the obvious faster material removal rate, it is shown to offer reduced cutting forces (radial and thrust forces, Figure 2-12 (a)) and heat generation, (Figure 2-12 (b)).

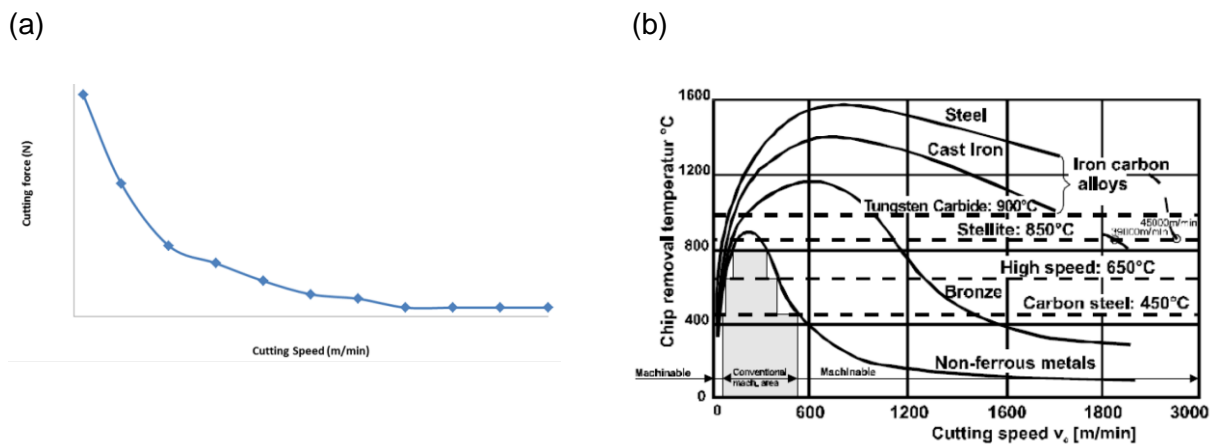


Figure 2-12 – Effects of high speed machining on: (a) cutting force (radial and thrust) for aluminium alloys [85] (b) temperature [86].

2.5.1 Motivation of reducing distortion in machining.

Regardless of the advantages of high speed machining of aluminium alloys, part distortion during the manufacturing has been an unsolved issue since the 1960's. Further, on the years, substantial amount of work was done in this area with research programs supported by government funding in conjunction with both automotive and aerospace companies to understand, control and optimize distortions in manufacturing [19] [45] [87].

The push from industry comes from a study which found that 95% of the cost of producing an aircraft is spend on manufacturing [88], with the issue of part distortion costing the manufacturing industry hundreds of millions of pounds according to studies done by Boeing [19] and Airbus [87]. Another research has found that although 95% of material volume is removed, it is only after around 60% of material removal that distortion begins to appear. Other research found that distortion-related costs are due to scrap (£10k to over 100k [89]), remanufacturing (re-machining) and quality related problems during component assembly costs [19]. Machining distortion has therefore been the subject of many research initiatives especially in aluminium alloys in comparison to other alloys such as Steel and Titanium alloys [90]. Majority of the aluminium alloy studied was aluminium 7050 T7451.

2.5.2 Residual stress-induced machining distortion

Inherent residual stresses from primary processes remain in equilibrium before machining [83] [91] [92]. Therefore during material removal (Figure 2-13), the machining process interferes with the inherent residual stress equilibrium leading to the redistribution of the residual stresses to achieve a new equilibrium. The remaining material now has a reduced stiffness to resist any deformation, therefore distorting during this redistribution process [93] [94] [95].

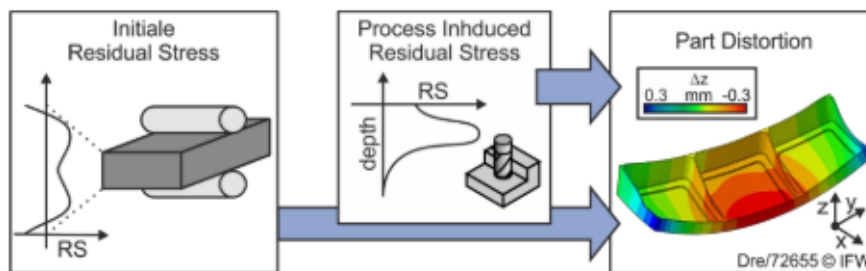


Figure 2-13: Relationship between quench residual stress, machine induced stresses and machining distortion [32].

Treuting and Read [17] (Figure 2-14) established a relationship, between stress and curvature by removing sheet material layer by layer, paving the way for analysis of the redistribution of residual stress and distortion [96], which has been used widely by many authors [97] [98]. The length and the width of the billet are usually larger than the thickness therefore residual stresses are assumed to be distributed uniformly along the length and the width of the billet and only change along the thickness.

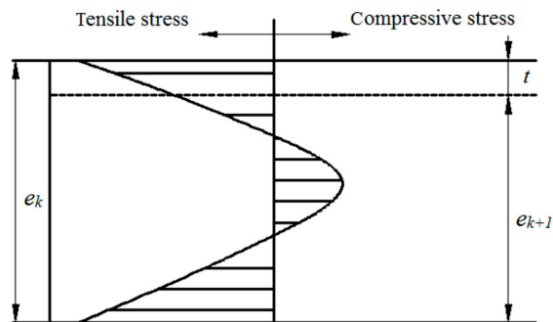


Figure 2-14: Residual stress profile in pre stretched material [99].

The machining process induced stresses act locally and can be due to the clamping load, cutting forces or temperatures [100]. These machining-induced stresses are caused during the separation of workpiece and chip, the friction between the tool and workpiece interface, and the compression of flank face on the machined surface due to the easy springback of aluminium alloy materials, leading to the generation of mechanical stresses in the cutting process. Typical cutting forces during the machining roughing operation of aluminium has been reported to be between 1000 – 3000 N [101] [102]. These forces induce compressive stresses in the workpiece.

Concurrently, the plastic deformation and the friction between the tool / chip and tool / workpiece produce large amounts of cutting heat resulting in uneven temperature distributions between the surface and the subsurface of the workpiece, which leads to the generation of thermal stresses which induce tensile stresses [103] [104] [105]. An example of the resulting machining-induced residual stress profile is given by Figure 2-15. From this figure, it is shown that the greater the depth below the machined surface, the lesser the amount of plastic deformation. In another study, Zhang et al. [80] highlighted that web section endures more stress than the flange during the bending process.

Chapter 2: Residual stress evolution within manufacturing of aerospace components

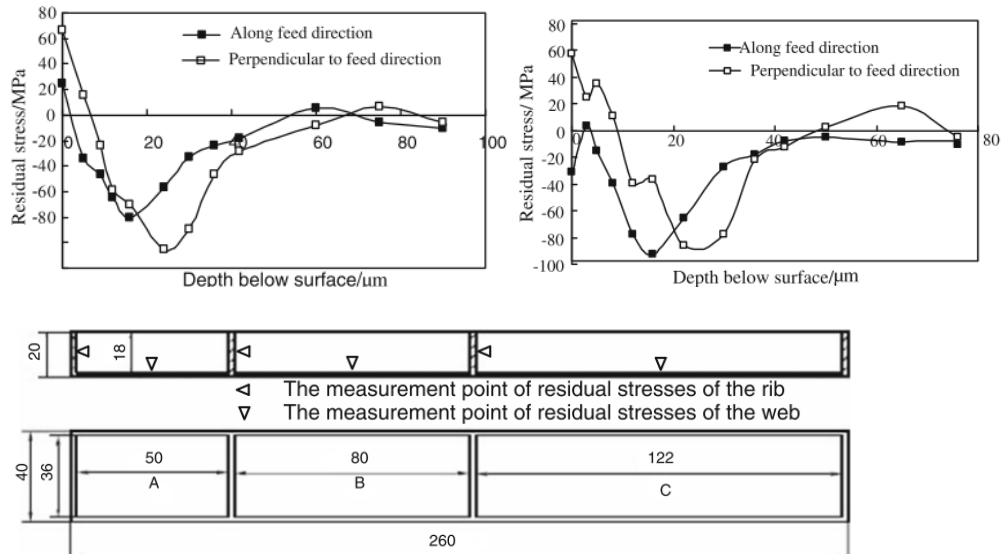


Figure 2-15: Machining induced residual stress on; (a) Measurements on rib section, (b) Measurements on web section, (c) Measurement locations [101].

A summary of the different factors influencing machining distortion is shown in Figure 2-16. From this figure, it can be seen that the machining conditions, tool type, machining strategies, design, alloy composition and the workpiece processing all contribute to distortion. However, it is crucial to identify what factors play the most important influence on machining distortion.

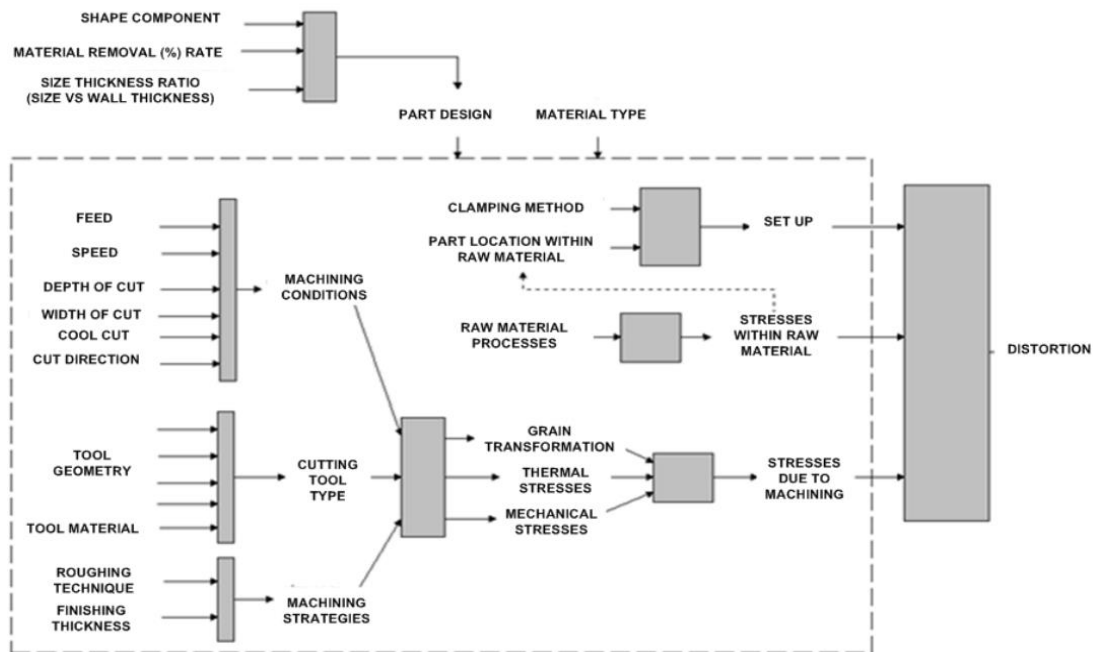


Figure 2-16: Source of machining distortion related to the machining of parts [106].

2.5.3 Justification of influence of residual stress from the quenching operation on machining distortions

Regarding to what has the prominent influence on machining distortion, Brinksmeier et al [107], among other prominent researchers in this field have attributed the effect of the quench residual stresses to machining distortion in comparison to the process induced stresses. Li et al. [91] in his in depth study on the advances on machining distortions concluded that regardless of thickness of the walls of the component, the bulk stresses should not be ignored and has to be considered for distortion analysis in aluminium alloys. In another study, Hussain et al. [108] found the influence of elastic stress on machining distortion is 75% more than the plastic stress. Other studies show that the effect of machining-induced stresses on distortion is between 9 [109] – 30% [104] and the rest from the bulk stresses. Huang [110] estimated that 10% of the total distortion was caused by machining-induced stresses while quench residual stresses accounted for 90%. Guo et al. [111] accounted for the influence of machining- induced stresses to be around 3% in comparison to bulk stresses.

Yang et al. [14] in this pioneering work highlighted that in order to control distortion in aluminium alloys, its critical to understand the quench residual stresses. Jiang et al. [97] studied on the effect of varying the residual stresses from the heat treatment process. It was found that there is a linear relationship between the residual stress magnitude and the machining distortion, therefore the quench residual stresses are critical to control to reduce the effect of machining distortion in comparison to other factors. Zhang et al. [112] reinforced this and added that increased distortion increases with machining asymmetry [113] [114].

Yang et al. [115] in the study on the machining distortion influences on an aluminium 7050 T7451 rib component, found that that the quench residual stress magnitude has the highest influence in the machining distortion, therefore decreasing the residual stress magnitude and the part position in the billet has an influence on the machining distortion. Finally, Gao et al. [93] in this extensive research looked into the effect of five different residual stress profiles on machining distortion. In this study, it was found that by varying the quench residual stress profile can reduce the distortion by 63%.

In an extensive study of residual stresses and machining distortion, Gao et al. [100] stated that machining-induced residual stresses are not a major factor to consider in the distortion due to their influencing layer depth if less than 200 μm .

Cerutti [11] finally concluded the machining parameters have an influence on the cutting temperature but only the sub surface region is affected. In this work, it was mentioned, that the machining induced stresses have a bigger effect on their performance and fatigue strength. With these statements, it is still unclear on the impact of machining induced residual stresses on distortion. Robinson et al. [51] in this in depth study quenched aluminium alloys followed by machining, and concluded that machining induced residual stresses could have an impact on thin walled components (2 mm) but not on thick components.

In general, although differences of opinion still exist on the influence of the machine-induced stresses on machining distortion, there appears to be agreement that the quench residual stresses cannot be ignored.

2.5.4 Different factors influencing machining distortions

2.5.4.1 Part geometry and bending stiffness

The part geometry is one of the most important factors that affect the machining distortion as it involves, the pocket dimensions, wall thickness and the bending stiffness. Hussain [108] in his thesis found that during the measurement of distortion across the whole rib structure, pockets with a larger surface area had a higher distortion than pockets of a smaller surface area of the same geometry.

Gao et al. [98] looked extensively into creating a semi-analytical machining distortion model for aluminium 7075 T6 thin walled pocket parts in incorporating the bending stiffness and the effect of biaxial stresses which other authors failed to incorporate. Based on seven case studies, he concluded that by improving the bending stiffness and the pocket geometry, the machining distortions could be reduced by around 75%. Although this research is quite informative, the spindle speeds, feeds and depths of cut used in this research are not practical in a production environment.

A similar finding was found by Bianhong et al. [109] highlighted the influence of bending stiffness on distortions. It was found that as the bending stiffness increased, the distortions decreased. Therefore, to optimize for the distortions, increasing the wall thickness in an area of a suspected high distortion is beneficial. This is because the machining distortion is proportional to the moment and inverse proportional to the inertia moment of the workpiece.

Chen et al. [116] in this study on the effect of machining a single sided against a double sided components found that the distortion reduced by 35% during the simulation modelling of aluminium 7050 T7351.

2.5.4.2 Part offset

Part offset is the location of the final machined geometry within the initial workpiece which can either be the distance between the top or bottom surface of the machined part and the one of the initial workpiece as demonstrated by Cerutti [11] and Denkena et al. [117]. Figure 2-17 shows the offset value represents the distance between the bottom surface of the machined part and the initial workpiece. Additionally, it can also be seen that with a varying part location, the residual stresses also vary. In this study, it was found by choosing the correct part location in the initial workpiece; the distortion can be optimized by 124%. This work generated a set of rules for locating the final geometry in the workpiece to control distortion however these set of rules have been contradicted by work done by other authors and have not been validated by experimental trials. Zhang [112] controlled the machining distortion by varying the part offset and found it to decrease the distortion by 83%. In another work partly funded by the European Commission with Airbus (COMPACT) [118] concluded that selection of the appropriate part offset is dominant for controlling machining distortions in aluminium aerospace components. Yang et al. [115] concluded that at the neutral axes of the workpiece, the distortions is improved by 88% and the optimum machining distortion was found due to its low quench residual stresses and due to the less residual stress variation across the thickness. It was found in this research; part offset played the biggest factor in machining distortion, followed by tool path strategy.

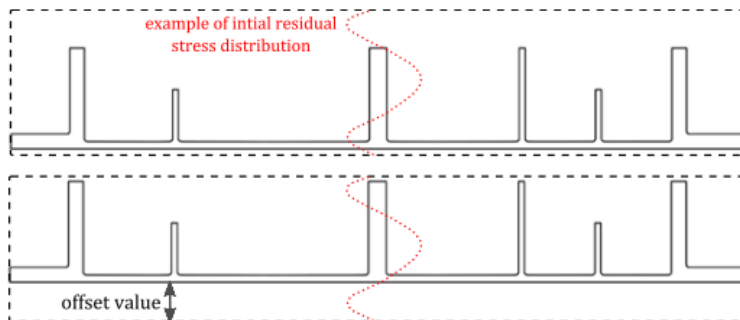


Figure 2-17: Illustration of the position of the final part within the initial part [11].

In this intensive study on analytical modelling of machining distortion, Gao et al. [100] looked at influence of part offset on machining distortion by machining three different strategies on a 25 mm thick rectangular block to a final thickness of 5 mm. The machining strategies uses were; symmetric (machining equal amounts of material from both ends), asymmetrical (machining unequal material from both ends) and a semi asymmetric machining (machining only one side of the block). It was found that symmetrical machining was a more effective machining strategy, controlling the distortion by 75% and it was concluded that the effect of part location has a large influence on the consequent machining distortion. Although symmetric machining lowers the distortion, it may increase the machining time due to set up times for each section, therefore hinder production. In this study as well, there was no detailed explanation as to why part location is effective. Regardless of the studies performed the effect of varying the part location in the thickness direction, but presently, there has been no work to look into varying the part in the width and the length of the billet.

2.5.4.3 Axial depth of cut

Cerutti [11] among other authors found that the axial depth of cut has the second highest contribution to machining distortion (~56%) in comparison to the other factors. In this work, it was concluded that the final depths of cut have a large influence on the machining distortion. Liu et al. [119] on his research of the machining distortions made from aluminium alloy 7085 found that after removal of 60%, the machining distortions doesn't increase much. Beizhi et al. [120] found that increasing the axial depth of cut, increases the residual stresses therefore the machining distortion. This research concluded by stating that by carefully selecting the axial depth of cut that exceeds the prior depth of the maximum compressive residual stress, the distortion can be reduced by 34%. Although it was found the importance of the depth of cut during machining, the parameters used, was not practical (between 0.025 – 0.5 mm). Finally, extensive work was done by Rai et al. [121] on integrating the machining tool paths with machining distortion. In this study, it was found that the final axial depth cuts have a large influence on controlling the distortion.

2.5.4.4 Machining sequence

The machining sequence is defined as the procedure in which the parts are going to be machined. Urresti [73] also looked at three machining sequences on aerospace turbine discs during the roughing and finishing stages. In this study, it was found that the final machining distortion was improved three times by simply changing the machining sequence.

Jiang [97] study also looked into six pocketing sequence was compared. The ideal pocketing sequence was based on comparing the workpiece stiffness or rigidity evolution during the pocketing process. The distortion was improved by 34% by changing the machining sequence. However, in this study, the rigidity of all the pocketing strategies had a similar value; therefore, this theory is not strong enough. Chen [116] found that the pocketing sequence can either be beneficial or detrimental for the machining distortion. In this work, it was found that the distortion could be reduced by 30% when using the correct pocketing sequence. Finally, Cerutti [11] looked into the sequential pocketing of different rib structures. In this study, pocketing sequence was applied in both the roughing and finishing stages. However, no justification of the pocketing sequence was provided.

2.5.4.5 Tool path strategy

The tool path is defined as the strategy on how the part will be machined. In this study for different tool paths, Denkena [32] studied the effect of two tool paths (spiral outwards and zig only) on machining distortion. In this study it was found that using a zig pocketing strategy had decreased the distortion by 34% although in practicality this tool path is never used due to the machining time incurred.

In another study by Dreier [123], three popular tool paths as shown in Figure 2-18 (spiral outwards, zig across, zig vertical) were used during the machining of a rib geometry and it was found that the spiral outward had decreased the distortion by 32%. A recent study conducted by Jiang [97] on the effect of different tool paths on controlling distortion on thin walled components showed that Spiral inward, zig machining and zig-zag machining produced an increased distortion of 10%, 35% and 17% respectively and that the best tool path was Spiral outward.

It was concluded this was due to the stress distribution shows that the spiral outward tool path generated a more uniform residual stress profile during the machining simulation. Additionally, from these measurements, it can be found that as the depth of cut increases, the maximum compressive stresses also increase similar to findings by [120].

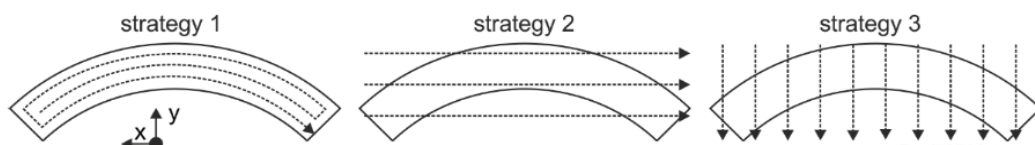


Figure 2-18: Effect of machining tool path strategies [123].

2.6 Summary and discussion

From the literature review, it has been shown that during the quenching operation, the desired mechanical properties are generated although so are undesired large residual stress magnitudes. While during material removal, the residual stresses re-equilibrate within the part causing distorting of the component. In the order of relevance, below are a list of the factors that influence distortion:

1. Quenching rates of the part
2. Uni-axial part location in the workpiece
3. Axial depth of cut
4. Machining sequence
5. Tool path

Although, the previous research work provides an extensive insight on the different influencing factors on machining distortion, some of the theories either provided contradicting theories or cannot be utilized in a practical machining environment. Furthermore, little or no work have looked into the effect of the following on distortion:

1. Controlling of residual stresses with varying residual stress input conditions
2. Tri-axiality of the part location within the billet
3. Machining strategy
 - a. Effect of the tool entry
 - b. Effect of the radial depth of cut
 - c. Zig-Zag tool path
4. Effect of intermittent fixture release during machining

Therefore, this research study seeks to obtain better understanding to address the knowledge gap listed above, with the aim of providing solutions to the challenges associated with the distortion of machined parts. A new approach combining carefully designed machining trials, state-of-the-art residual stress and distortion measurements and finite element modelling will be developed to generate in-depth understanding of part distortion caused by machining under industry-relevant practical conditions. A robust methodology for controlling machining distortion will then be developed.

3 Measurement techniques

3.1 Residual Stress measurements

In general, using more than one experimental technique each with well-defined error/validity ranges [40] are required for the validation of numerical models. Residual stress measurements is vital to capture the stresses that within a component. These stresses can either be beneficial in terms of extending the service life of a high performance component or detrimental on the part in terms of the effect of machining distortions [17].

Due to the advancements of alloy material and measurement requirements, residual stress measurement methods need to be distinguished in terms of resolution, portability and penetration depth. These measurements from a machining perspective are critical tools to understanding the magnitudes and variation of stresses within the initial and final machined part. More importantly useful in the validation of the finite element model which will be used in the development of optimization strategies.

Common residual stress measurement methods are distinguished by three main factors; measurement depth, the method of analysis i.e. destructive or non-destructive and cost of analysis as illustrated in Figure 3-1. The measurement depth can be further divided as macro (Type I) and micro or intergranular (Type II) or atomic (Type III) stresses. Macro stresses are normally larger than a few mm and vary across different grains within the material [15] while micro stresses occur within the micron level between the material grains and the atomic stresses are limited to the dislocations and crystal interfaces [124]. Ideally, measurement of a part is recommended using two independent techniques (destructive or non-destructive) as defined by the Structural Integrity Assessment due to the different characteristics deeming the measurements authentic and reliable [125].

Chapter 3: Measurement techniques

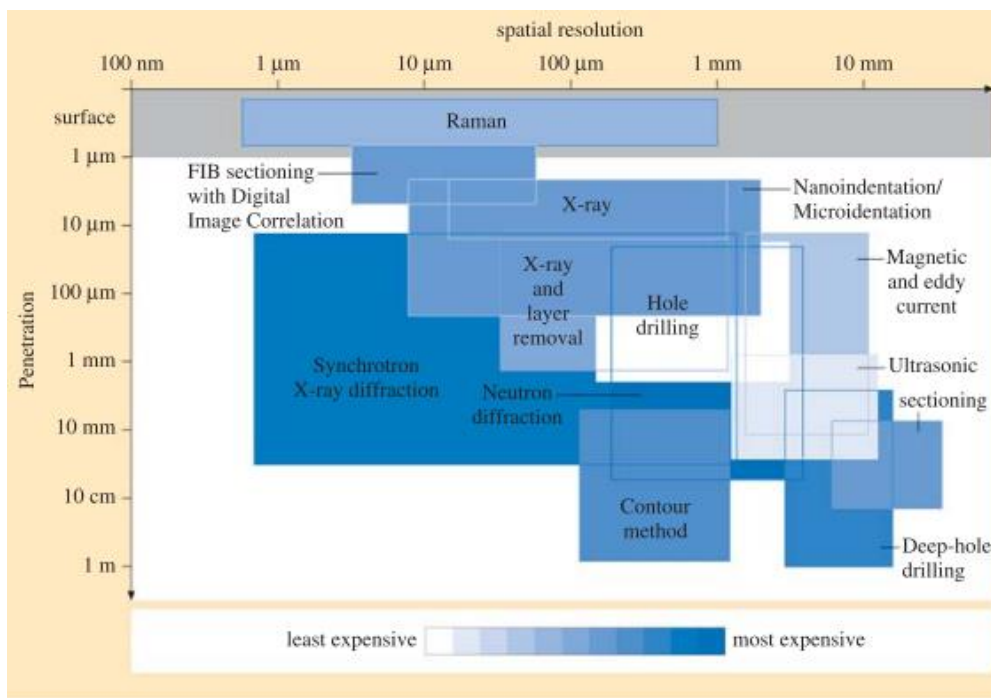


Figure 3-1: Current residual stress measurement techniques [15].

3.1.1 Bulk residual stress measurements

As highlighted in the literature review, capturing the residual stress magnitude from the heat treatment is critical due to its documented influence in machining distortion for aluminium alloys. Among the many techniques listed in Figure 3-1, the two widely used residual stress techniques for the bulk of the part are contour [140] and neutron diffraction [62]. These methods have been used by many authors to complement each other [141] [142] [18].

3.1.1.1 Contour method

The contour method, is the most recent technique for bulk residual stress measurements developed by Mike Prime [126] utilizing Bueckner's superposition principle [127]. The technique is performed by slitting a specimen in two ((Figure 3-2 (a)). This slitting operation is performed using a Wire EDM ideally since it doesn't induce any plastic deformations i.e. the deformations coming from the cut is assumed to be purely elastic [126]. Once the cut has been performed, the specimen is unclamped and the distortions on the normal to the cut surfaces are measured ((Figure 3-2 (b)). The displacements from the normal surface are critical as the accuracy of this provides confidence of the calculated normal stresses.

Chapter 3: Measurement techniques

The displacement contour of the two cut surfaces are then averaged in order to eliminate the effects of the transverse displacement and the shear stresses. A finite element model of the cut geometry is then constructed. The final step ((Figure 3-2 (c)). is the interpolating the averaged displacement contour normal to the plane of cut. This interpolation on the normal surface calculates the resulting residual stresses normal to the cut plane. The calculation of the residual stresses can be defined using Bueckner's superposition principle as shown in Equation 3-1, where σ refers to the complete stress tensor and $\sigma^a, \sigma^b, \sigma^c$ represent the original residual stresses in the component prior to cutting. σ^b are the stresses normal to the cut surface and are zero as the normal surface has no distortion, this principle determines the original residual stresses on the part prior to slitting. σ^c are the stresses calculated from the distortion from the normal surface after the cut that are forced back.

$$\sigma^a(x, y, z) = \sigma^b(x, y, z) + \sigma^c(x, y, z)$$

Equation 3-1: Bueckner's superposition principle

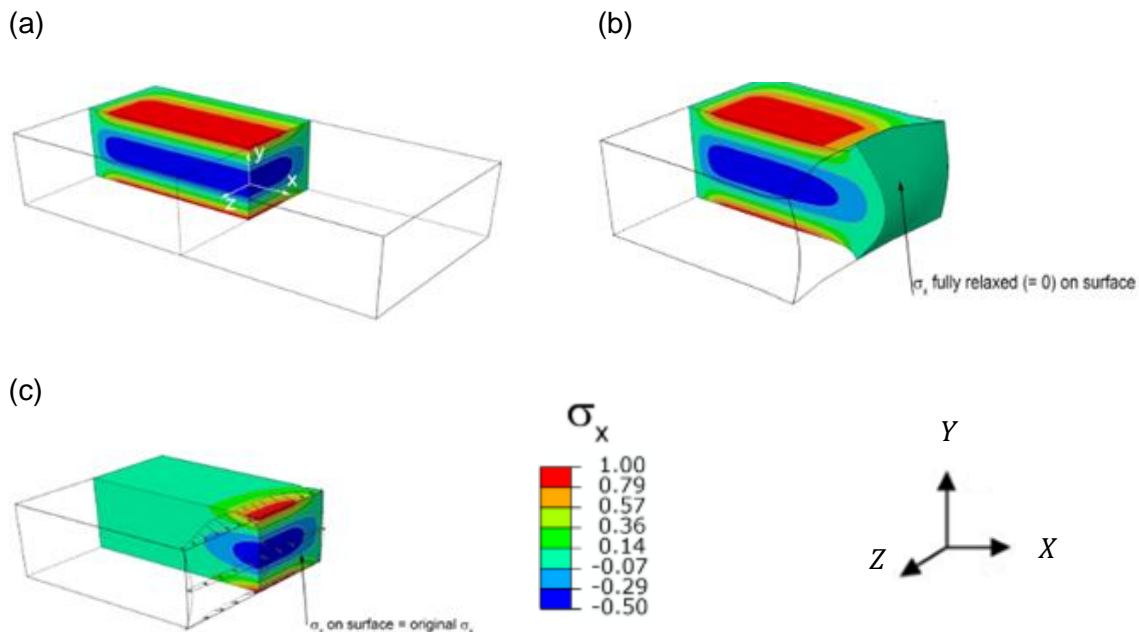


Figure 3-2: Superposition principle of the contour method [128]: (a) Original Stress in the component, (b) Part is cut in two, distorting the cut surface, (c) Cut surface is forced back to its original position.

Chapter 3: Measurement techniques

The accuracy and uncertainties have been published to be as low as 10% [129] and work published by Hill [130] on five aluminium 7050 coupons with different heat treatments show good repeatability of being less than 10 MPa, which is similar or better than other measurement techniques [130]. Prime et al [126] states although this method has been proven to be reliable, its accuracy depends on the sectioning procedure in order to control of plasticity during the cut. This statement has similarly been mentioned by and Hosseinzadeh et al. [131]. Additionally, this method requires a surface roughness value between 10 to 100 μm peak to valley variation [15] [129].

This technique is attractive to machine shops over other residual techniques as it simply utilizes equipment within the machine shop and metrology department. Residual stress measurements have been performed on quenched aluminium blocks using this technique by several authors and compared with finite element simulation and other bulk residual stress measurement techniques. One of the most in depth on this technique was performed by Johnson [132] in his thesis. Zhang et al. [81] used contour method to measure the residual stresses in an aluminium 7050-T7452 alloy forging using the contour method.

3.1.1.2 Neutron diffraction

Another popular bulk measurement technique is the neutron diffraction technique. This technique exploits the use of penetrating radiation to measure the distance between the nucleus of the atomic planes within crystalline materials. When a material is deformed, the crystal structure within the material is reoriented and during measurements, the radiation is absorbed and diffracted with an intense emanation at certain angle orientations and weak in others. The angles with the strong emissions is defined by Bragg's Law (Equation 3-2) (Figure 3-3): where n is an integer, λ is the wavelength of the electromagnetic radiation, d is the distance between the diffracting planes (inter-atomic lattice spacing) and θ is the Bragg angle. The Bragg angle (θ) is defined as the angle, which produces the highest radiation from a range of angles that are scanned by the diffraction technique.

An increase in the compressive stresses will give an increase in the diffraction angle and likewise an increase in the tensile stresses will give a decrease in the diffraction angle.

$$n\lambda = 2d \sin\theta$$

Equation 3-2: Bragg's law.

Chapter 3: Measurement techniques

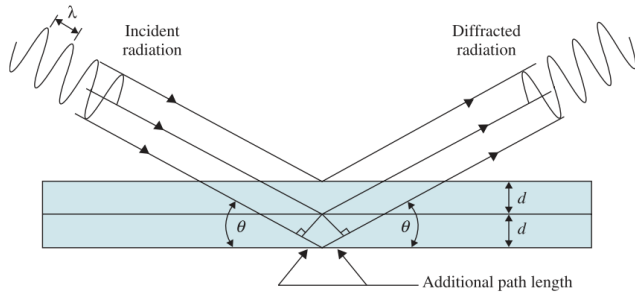


Figure 3-3: Residual stress measurements due to diffraction.

Unlike other diffraction techniques, neutron diffraction shows a much higher penetration depth than other diffraction techniques (Figure 3-4), measuring up to thicknesses between a range of 0.1 – 1.5 m with a spatial resolution of 1 mm [15].

Importantly, this technique is attractive for aluminium alloys because of its relatively low absorption characteristic and has four to ten times the penetration depth in comparison to other aerospace alloys like Steel [133] or Nickel, Titanium, and Stainless Steel [15] [134].

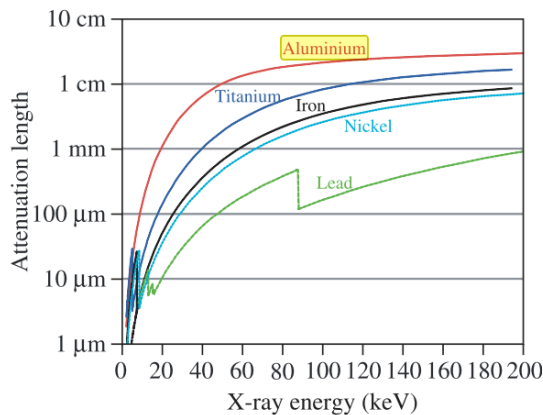


Figure 3-4: Attenuation length against X-ray energy for various aerospace material.

The main disadvantage of neutron diffraction is:

- The high cost associated with the use of the equipment
- Measurement time
- Limited to certain dimensions due to the space of the measurement equipment,
- Dependent on material measured
- Works on an assumption that the rate of change of stress is linear across a section.

Chapter 3: Measurement techniques

A study done by Robinson [51], noted that the distributions determined by neutron diffraction were found to be in equilibrium (typically always within 14% of being balanced). Regardless of these limitations, this technique has been widely employed by researchers in their study to understand the effect of residual stresses on machining distortion in aluminium alloys. Pan et al. [76] studies the effect of thermal residual stress relaxation during cold rolling. Whereas Drezet et al. [135] used this technique to measure the residual stresses in quenched aluminium test samples[136]. Chobaut et al. used this technique to validate quench aluminium alloy 2618 FE model [137]. Lalonde [138] used this technique to measure the residual stresses from the quenching process to a final machine aluminium component. Summary and conclusion

To achieve a good understanding of the magnitude of impact of the residual stresses on machining distortion, the methodology employed in a machining environment have been identified in residual stress measurement. These techniques varies depending on the type of residual stresses and their geometrical restrictions, therefore, these measurement techniques proposed have to be adapted to the requirements.

From the literature review, there is still a major gap in the measurement of quench residual stresses evolution in machining processes. This still causes limited understanding on the impact of residual stresses in manufacturing. Residual stress measurements by various authors have adapted the methodology of measuring before and after the machining processes but nothing in-between the manufacturing process, as a result a major knowledge gap is generated. Therefore, this research aims to overcome this gap and provide a deeper understanding of the residual stress redistribution at different critical stages within the manufacturing process. This will be achieved by taking measurement of the heat-treated component using two independent techniques such as contour and neutron diffraction for bulk residual stresses. Furthermore, neutron diffraction technique will be used to measure the residual stresses through the manufacturing process, which has not been utilized before in any manufacturing environment.

3.2 Distortion measurement techniques

In order to qualify the machining quality of a component, the use of metrological equipment is required. Geometrical conformance is one the factors used to decide the machining quality of the component [139], therefore it is critical to inspect the machined component for conformance according to the design criteria. Unlike residual stress measurement techniques, distortion measurement techniques in thin walled components has not been documented well enough.

In this study, two widely used technologies, applying different principles, will be presented and discussed.

3.2.1 Contact measurement techniques

One of the tools used to characterize this conformance is the computer coordinate machine (CMM) [45]. This is a point based measurement system using a stylus, a laser or ultrasound [140] where the displacement is calculated from a nominal value set by the operator. The CMM is considered an approved universal measuring machine and a report by the National Physical Laboratory shows that products worth over £100M was inspected by using CMM [141]. The CMM has the capability of dimensional evaluations in three dimensions, two dimensional (planar) or one dimensional (linear) [139]. The mechanism by which the CMM works is when there is a physical contact between the workpiece and the touch trigger probe.

The opto-electric system using glass scales gives the probe location which is combined with machine coordinates to locate the surface [24]. This method is accurate, reliable and widely used especially in the measurement of machining distortion in large aluminium thin walled components [11][108] [142] [143]. The CMM is usually performed in a temperature controlled environment to ensure repeatability in the measurements and is defined in the ISO10360 measurement standard [144]. For further reading on the use of CMM, the reader is recommended to refer to the NPL (National Physical Laboratories) guide [141] which advises the user to follow the following guidelines to always make an informed measurement:

- Selection of the features on the workpiece to be measured to decide whether using a CMM is practical or cost effective.
- Definition the workpiece datum feature(s) to be used within the co-ordinate system.
- Selection of the workpiece orientation.
- Selection of the workpiece holding method.
- Stylus system qualification.
- Definition of the probing strategy.
- Programming of the CMM and assessment information recording

Although, CMM has its advantages, it is rendered powerless during measurement of thin walled components [145].

3.2.2 Optical 3D coordinate measuring machines

Another widely used displacement measurement method for industrial applications is by using an optical 3D scanner (Figure 3-5). A 3D scanner is a powerful apparatus combines structured light and photogrammetry [146] and depending on the volume of the lens used, can take over 7 million points per scan [147] and transforms a real object into a digital form [148].

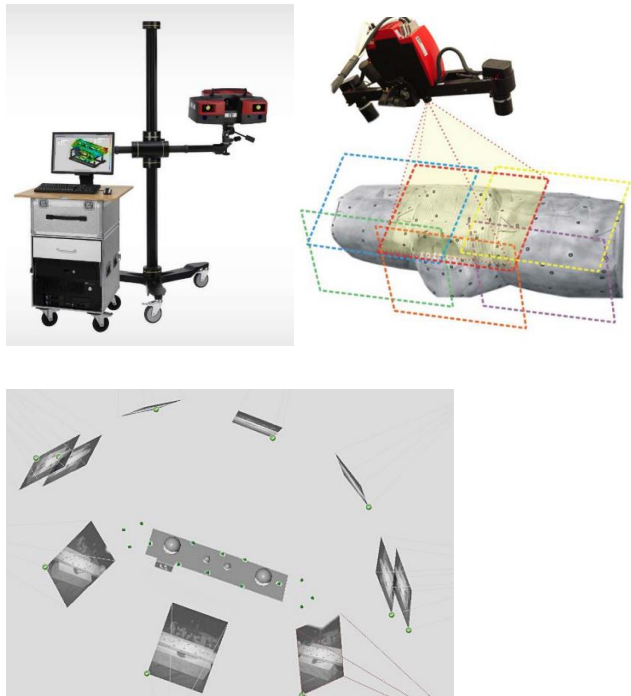


Figure 3-5: GOM Triple Scan 3D-Scanner with blue light technology [149], Scanning at different angles [150].

The advantages that cannot be offered by any other technique as Ma (10) stated are:

- Measurements can be performed on complex geometries [150]
- Rapid measurements (40% measurement time saved for Rolls Royce Holdings plc [147])
- Capture of large density data
- Measurements are independent of the part's rigidity which is critical for thin walled aerospace aluminium components [150],
- Measurements can be reversed engineered to produce an accurate geometry volume of the component to be machined, capturing variation, rather than using a nominal CAD geometry.

The technique works in the following way [148] [149]:

- Eclipse Markers are placed on the object to act as a reference to be located by the 3D scanners
- Anti-reflective coating is then sprayed on the object for the scanner to reduce the object reflection [148] (most importantly on machined aluminium objects [151]).
- Different arrays of light are projected onto an object and the scanner records where and how the object distorts the light arrays.
- Through simple trigonometry, the distance and location of thousands of data points where the light pattern hits the object are calculated.
- The location of these points on the object's surface are triangulated, using the projector and cameras as reference points.
- A point cloud representing the geometry the object is created and edited
- The data is then exported in a triangular mesh

Unlike the CMM or contact metrology inspection methods, the optical systems do not follow an international standard of procedure. However, in 1996, The German Society for Photogrammetry and Remote Sensing (DGPF) and the working group "Co-ordinate measuring machines" of the German Society for Measurement and Automatic Control (VDI/VDE-GMA) developed a standard guideline for acceptance and verification of optical 3-D measuring systems (VDI/VDE 2634). This specification is used widely [152] [153] and defines the calibration specimen, characteristic values, measurement conditions and the evaluation method [153].

3.2.2.1 Sources of error in optical scanning

Barbero [154] calculated the uncertainty of the scanner by measurement of different specimens and found it to be 25 μm . In addition to this, he found that the ATOS scanner had a 15% difference with CMM. Mendricky [150] compared the GOM ATOS scanner with this specification and determined the device calibration was the most critical factor followed by the anti-reflection coating. In addition to this, the red or blue [155] structured light has been identified to increase the accuracy of the optical scanner than white light [147] [156]. This is because white light is easier to distort and scatter. In addition to this, scanners that use white light are susceptible to internal heat generated from the equipment as they are largely influenced by ambient light.

3.2.2.2 Use of optical scanners in a machining environment

Dreier [123] among other researchers [157] [158] [159] have used optical distortion measurement techniques to quantify the machining distortion (Figure 3-6). Furthermore, Stephenson [160] defined a methodology of using either the CMM or an optical scanner for the measurement of machining error during machining and combining this with a mathematical transformation can amend the NC part program to correct for these errors. Achouri [161] concluded by using a 3D scanner, an accurate estimation of the displacements generated through slitting a part.

Michalowska [162] performed measurements using an optical scanner and a digital sensor and found both to be congenial and captured the distortion trend accurately. However, these techniques have less accuracy than their contact based counterparts [163].

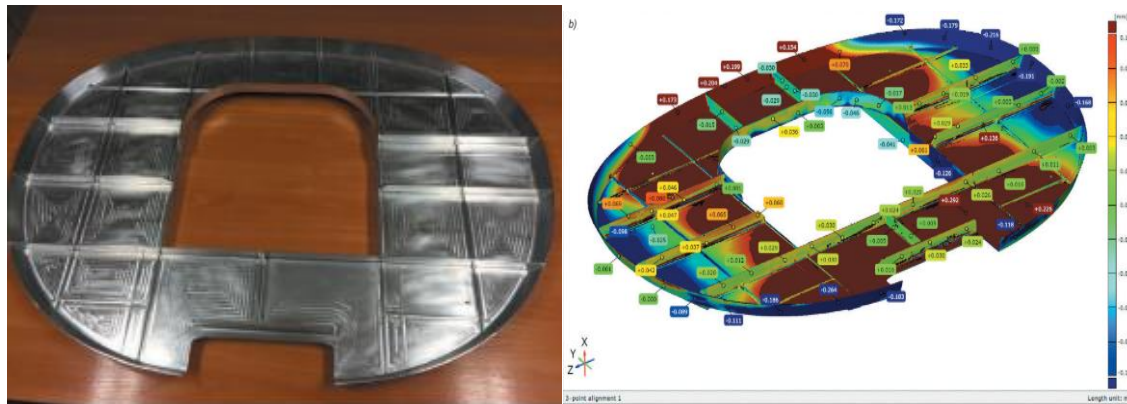


Figure 3-6: Example of an optical displacement scan of: (a) Machined aerospace frame component, (b) Scan result [157].

3.3 Strain measurements in machining

Strain gauges are the most widely used surface strain measurement technique due to its cost benefits. A strain gauge consists of a long strip of conducting metal foil, which changes the electrical resistance when the length of this foils changes; this is later converted to strain with mathematical calculations. There are different types of strain gauges and the choice depends mainly on the desired application.

Factors to consider when selecting a strain gauge are; a) type of material to be mounted on, b) gauge length, c) application. These can be further sub divided by a) which rosette type is suitable (rectangular, tee or delta) and b) rosette construction (single or layered).

The tee rosette is used when the principle strains are known but there is a large error in readings due to influences from geometrical tolerances and strains in other directions. In general, a rectangular or delta rosette is used to overcome the errors experienced with tee rosettes. There is little comparison between the delta rosettes and rectangular although rectangular was a popular choice in the past due to their ease of use and fast data capture but with recent advances in data processing tools, the delta rosettes is increasing its popularity. Due to their accuracy, strain gauges will be utilized in the monitoring the strain response during machining.

3.4 Summary and conclusion

From the literature presented, CMM is an established and unquestionable measurement technique for post machining distortion inspection. Furthermore, 3D optical scanners are progressively being exploited for post machining distortion measurements.

However, there is a void on utilizing the 3D optical scanner technology to assist in the regulation machining distortion. Therefore, this research aims to integrate this technology by providing:

1. A profound understanding of the variation of component geometry (representative part) to the nominal CAD model prior to machining.
2. Capture the component form and orientate the component at different positions on the machine bed. The component will then be machined and the post machining distortion assessed.
3. Comparison of the optical scan result against the FE model prediction and CMM in a machining environment.

4 Modelling of residual stress and machining distortions

The prediction of machining distortions have been a major considerations in modelling [164]. A model (either analytical or numerical) is defined as a well-constructed mathematical calculation that should provide predictions of events or states of systems that can be confirmed consistently by physical observations [124] [165]. Accurate simulations of the machining process can solve economic and scientific problems by generating distortion control or optimization solutions by developing new processes, saving scrap costs. A study done by Hornbach et al. [89] highlighted that modelling the machining process can help tackle the problems of distortions especially for non-symmetric residual stress profiles. Volk [166] suggested that using the a validated model can save a manufacturing company around 54% of the cost incurred.

For the modelling of part distortion after machining, there are three kinds of effective methodologies used; analytical [167], numerical [91] [167] and hybrid models [168]. The choice of a particular model depends on the information desired, the required accuracy of this information, and the available computational resources. Lutervelt et al [169] was among the first authors to define the different mathematical models in a metal cutting perspective. In this work, he defined the advantages and disadvantages of analytical models to predict cutting forces, chip geometries, strain and stresses and concluded that this technique is fast, but is limited to the application. Umbrello et al [164] similarly compared and contrasted different machining modeling methods for surface integrity showing the advantages and disadvantages of each modelling methodology.

4.1 Analytical models

Analytical models are preferred in comparison to numerical models due to their quick analysis and attractiveness of reduced license fees [83] especially for small and mid-sized manufacturing companies which has increased the use of open source FEM software [20] [170]. Majority of the programming language is Matlab [171], C++, Python and Visual basic.

Regardless of their advantages, there is a reduced number of analytical models for predicting the residual stresses during quenching, although the earliest attempt to model this was by Askel et al. [172] using a simple beam model. Apart from this work, analytical solution is not utilized for these mathematical models.

This is because of the highly coupled and non-linear nature of the problem, and their solution relies on the application of numerical methods such as the finite difference method (FDM), finite volume method (FVM), and finite element method (FEM) [173], where the latter is the most widely used in numerical analysis.

Rather, to avoid numerically modelling residual stresses from the heat treatment process, researchers have opted to experimentally measure the residual stresses and interpolate them onto the workpiece mesh element prepared for machining distortion simulations. This methodology was applied in recent studies by Cerutti [11], Guo [100], Sim [118], Zhang [174] and Ma [102]. The disadvantage of this methodology, where the numerical model has dominance, is that in order to capture the tri-axiality of residual stresses, additional residual stress measurements would need to be performed [175] and interpolated onto the workpiece mesh element. Despite the fact much work has been published for analytical modeling for surface integrity in machining, there is limited work in the study of machining distortion.

4.1.1 Bending moment theory

The first analytical model for the calculation of machining distortion incorporating the initial residual stresses was done by Shin [176]. In this work, a concise formulation was presented to calculate the distortion using the bending moment theory. The longitudinal stresses were considered in the calculation due to their influence on distortion in comparison to tangential stresses [167]. When material is removed in milling, the initial residual stress equilibration is disturbed (Figure 4-1). The residual stress redistributes to achieve equilibrium and in the process distorts.

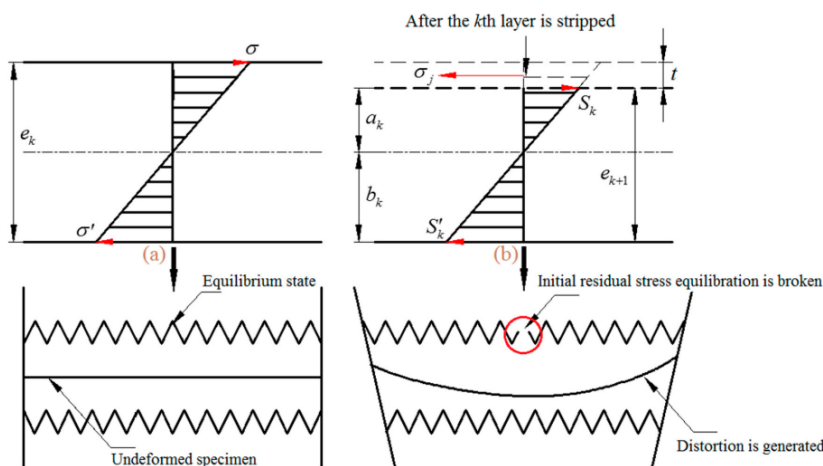


Figure 4-1: Distortion generation due to residual stress distribution [99].

Chapter 4: Modelling of residual stress and machining distortions

The initial residual stress prior to any material removal in the part is in equilibrium as the resultant force. When materials are removed in milling, the initial residual stress equilibration is broken. To re-equilibrate it, the residual stress is redistributed, and the distortion of the plate is generated at the same time. The curvature relation of the workpiece before and after milling a layer is as Equation 4-1, where k is the number of the layer, R_k and R_{k+1} are the curvature radius before and after the k_{th} layer is stripped, e_k and e_{k+1} are the thickness of workpiece before and after the k_{th} layer is stripped, σ_j is the stress before the k_{th} layer is stripped, and E is the elastic modulus. After the k_{th} layer is stripped, a_k and b_k are the distance from upper surface and lower surface to the neutral plane, respectively

$$\frac{1}{R_k} - \frac{1}{R_{k+1}} = \frac{6te_k\sigma_j}{E(e_k + 1)^3}$$
$$e_k = a_k + b_k$$

Equation 4-1: Relationship between the curvature and the bending moment .

A similar theory was proven by Madariaga [177], when relating the bending moment with the distortion, found that the level of distortion increases parallel to the level of bending moment. Wu [178] used a finite different method (FDM) to calculate the machining distortion. This study used the bending moment theory in two axes to calculate the resulting machining distortion. He additionally used FDM to compare with FEM and experimental trials and found that the difference was 22%. Unlike previous work, Jiang calculated the machining distortion purely from the machine induced stress [83]. This was done by assuming the machined induced residual stress profile as a polynomial function. A similar approach was applied by Omar [179] predicting the machining distortion using the machine induced stress from the cutting forces generated by the tool geometry. Gao [98] in this extensive analysis on a comparison between a semi analytical model (hybrid model) with FEM and experimental data for different pocket geometries shows the accuracy and the robustness of the semi analytical model in predicting the distortion. Additionally to this, the hybrid model simulated the distortion. In recent work, Llanos [180] predicted the machining distortion of a rib component by analytical calculating the inherent residual stresses from the workpiece. The rib geometry was then simplified to an “equivalent” geometry. By neglecting the stress components in the transverse and depth directions (Y and Z directions) due to their influence in the bending of the machined component, the whole geometry was representative by the cross section for that geometry.

4.1.2 Strain energy density relaxation theory

The other theory that has been widely used is by Strain energy density relaxation theory. This was first introduced by Euler in 1744 [181]. Wang [167] and Pidaparti [182] state that during material removal, the release of the elastic strain energy leads to the strain redistribution and therefore part distortion until an equilibrium is reached [183].

Therefore, he concluded, the storage and release of strain energy are the root causes of the deformation of workpieces due to residual stresses. In that research, the machining process was optimized by 34% simply by changing the machining sequence directed by optimizing the strain energy density.

Additionally, Wang in a pioneering work combined both the effect of the bending moment and strain energy density for the prediction of machining distortion (Figure 4-2).

Additionally FEM and analytical models were compared and found to be similar in terms of prediction with a difference of 6.4% and 26.4% when compared to experimental results although these models neglected factors of cutting loads, clamping forces and vibration.

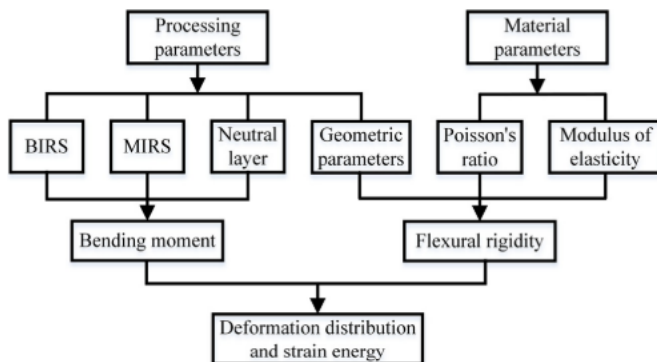


Figure 4-2: Integration of bending moment and strain energy density [184].

The strain energy density or the mean stored elastic energy (strain energy) per unit volume (kJ/m^3) provides an indication of the distortion after machining. This theory was developed by Heymes [84] and is shown in Equation 4-2. Where W is strain energy density, t is plate thickness, E is Young's Modulus, σ_{RD} , σ_{TD} are the directional stresses in the rolling and transverse direction respectively and z is through thickness coordinate.

Chapter 4: Modelling of residual stress and machining distortions

$$W = \frac{1}{t} \int_0^t \frac{\sigma_{RD}^2 - 2\nu\sigma_{RD}\sigma_{TD} + \sigma_{TD}^2}{2E} dz$$

Equation 4-2: Strain energy density.

From this study, Heymes stated that the axial depth of cut has a large effect on the machining distortion. Additionally, as shown in Figure 4-3, that no significant distortion should be expected if the strain energy density is less than 1 kJ/m^3 , a risk of significant distortion with values larger than 2 kJ/m^3 and large distortions can be observed with values over 4 kJ/m^3 .

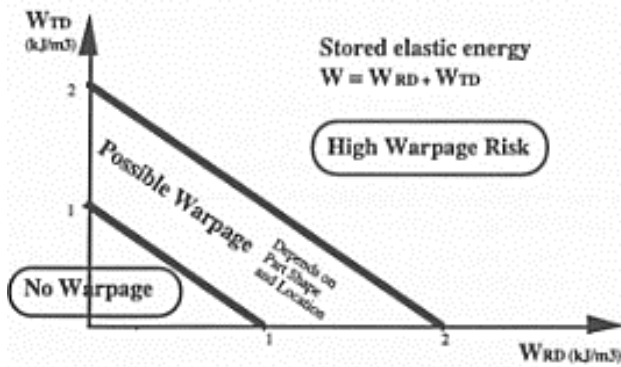


Figure 4-3: Stored elastic energy and machining distortion [84].

This methodology has been used by other authors [11] [185] [186] to provide a quick indication of the consequent machining distortion. Robinson [51] compared calculated elastic strain energy density from Hooke's law with the numerical simulation on a machined specimen.

Schultz [186] took the strain energy density theory further and concluded that the strain energy density is proportional to the machining distortion (Equation 4-3). It was further stated that the stress range ($\Delta \sigma$), the difference between the maximum and minimum stress has a linear relationship with the square root of the strain energy density (Equation 4-4). A similar conclusion was found by Nurhaniza using a numerical simulation [187], although the equations look promising, they don't agree with findings by Heymes [84], Wu [185] or Robinson [51].

$$distortion \propto \sqrt{W}$$

Equation 4-3: Distortion as a function of strain energy density.

$$\Delta \sigma = \sigma_{maximum} - \sigma_{minimum}$$

Equation 4-4: Stress range as a function of strain energy density and distortion.

Chapter 4: Modelling of residual stress and machining distortions

Although calculating strain energy density to control distortion sound promising, the calculation does not take into consideration the original stress distribution, shape of the final part location in the original workpiece and machining induced stresses therefore it should only be used as an indication.

Other analytical methodologies for calculating machining distortion was developed by Nervi [188]. In this work, a mathematical model was established to predict the machining distortion by solving the Navier-Lame equations [189], a linear elastic model. The methodology uses experimentally measured bi-axial residual stress as an input and the consequent machining distortions are predicted well without considering the machining induced residual stresses.

Regardless of their advantages of being direct and simple, analytical models are limited to their specific application this is due to the following factors:

1. There is a deviance from the experimental measurements due to the three dimensional spatial distribution of residual stresses [91]
2. Exclusion of the machining induced residual stresses [188].
3. Omission of workholding effects

4.2 Numerical modelling

Numerical models are the most widely used models for both the heat treatment (quenching and ageing) and machining distortion simulations. This is due to their advantage of flexibility, ease of use and opportunities that finite element modelling present by generating a deeper understanding on various influencing factors influencing residual stress and machining distortion.

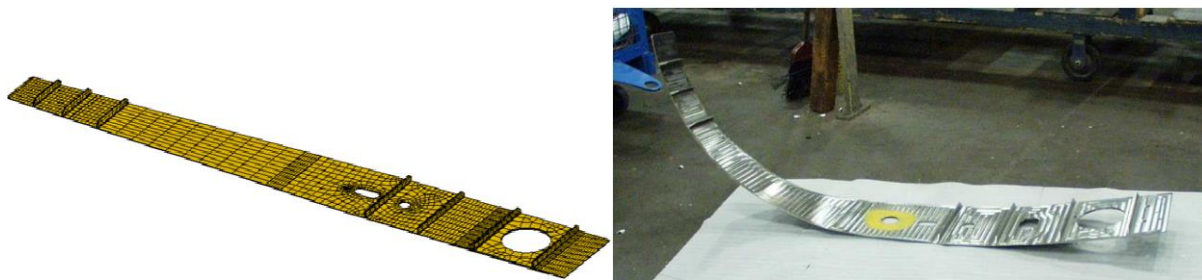


Figure 4-4: Advantages of finite element predictions of an aerospace rib component; (a) Numerical model set up, (b) Actual distorted component [45].

Chapter 4: Modelling of residual stress and machining distortions

To overcome the limitations of analytical models in heat treatment and machining distortion simulations, numerical models are utilized. The most widely used numerical models for machining distortion analysis is finite element analysis or method (FEA or FEM).

FEA is a numerical model that divides a complex structure into a smaller sections or elements. The performance of each element is connected further by nodes, which connect each section of the element together within the structure (Figure 4-5).

The reconnection of these elements produces a set of simultaneous algebraic equations. More often, a large complicated model would have a great number of such equations, and a high performance computer must then be employed in solving them [190].

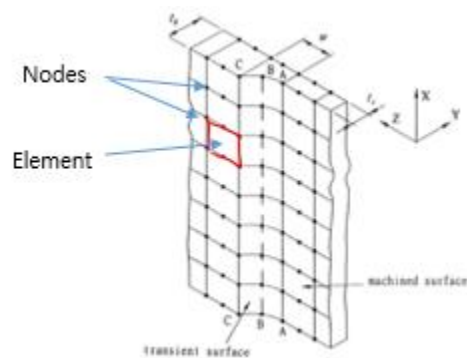


Figure 4-5: Element and node discretization in FEA.

The main factors as defined by Koc et al. [28], Ma et al. [45], Awan et al. [143], Davim [191] and Markopoulos et al [192], that influence the residual stresses and machining distortion predictions are (in order of their importance):

- Material model which is acquired by experimental trials
 - Flow Stress material data (on cooling tensile tests)
 - Stress Relaxation/Creep Tests
 - Thermo-Physical Property Tests
- Heat transfer coefficient calculations
- Machining boundary conditions
- Mesh generation as the simulation convergence highly depend on this

The importance of heat transfer coefficients acquired by thermocouple test has already been covered in the previous section. The following are other critical factors for residual stress modelling, especially in the heat treatment process.

4.2.1 Simulation requirements

4.2.1.1 Material properties

While most simulation packages predict the trend accurately, there is still a limitation on software to predict the magnitude accurately due to lack of material data [193].

The NPL Good Practice Guide [194] and other authors have highlighted that the key to any successful modelling prediction has been accounted to the use of realistic properties tested from room temperature to the solution temperature at different strains and strains as an input to the model [45] [67] [72] [195] [196] [197] [198] [199] [200] [201]. Robinson [202] stated that the material property governs the residual stress magnitude and distortion due to its resistance to plastic deformation during and after quenching.

During milling, the material removal is performed by moving a rotating cutter in either 3 or 5 axis against a workpiece. Aluminium is considered to be the most machinable alloy compared to other lower density alloys like titanium or magnesium [85]. The removal of material in milling aluminium alloys generate high levels of strains and strain rates. The impact of the high strains or strain rates increase the cutting forces and temperatures [203]. The strain rates that occur in the high speed machining of aluminium 7050 can be as high as $10^4 s^{-1}$ [203] [204] [205]. For the simulation of chip formation analysis in aluminium alloys, it is justifiable to calculate the strain rates to a minimum of $10^3 s^{-1}$. These tests can be acquired using a high impact test machine like the Klosky bar or the Split Hopkinson Pressure Bar. Since the simulations in this study have low strain rates (for the quenching) and the machining distortion, simulation considers an elastic model (the distortions are purely from an elastic relaxation). This data is therefore not required for the case studies.

Reich [197] stated that simulation for residual stress in aluminium alloys is rarely used due to the lack of accurate elastic-plastic material data. Rate-independent Elastic-plastic material models widely used for finite element simulation need a yield function, a flow stress rule and strain softening or hardening law.

The hardening law mostly used is the isotropic hardening law [27] [206]. Other authors have used kinematic hardening [207] while other have utilized both [16] and seen an accurate prediction of residual stresses.

Chapter 4: Modelling of residual stress and machining distortions

The flow stress data is one of the most important inputs in the material model and the accuracy of this data will impact the accuracy of the machining model [196]. The flow stress is defined as the yield stress of a metal under uniaxial conditions [208]. The most versatile flow stress [196] [208] calculation is expressed as in Equation 4-5 where the flow stress (σ) is expressed as a function of strain (ε), the strain rate ($\dot{\varepsilon}$) and Temperature (T) and is input in a FE software as shown in Figure 4-6.

$$\sigma = f(T, \varepsilon, \dot{\varepsilon})$$

Equation 4-5: Flow Stress Formulation.

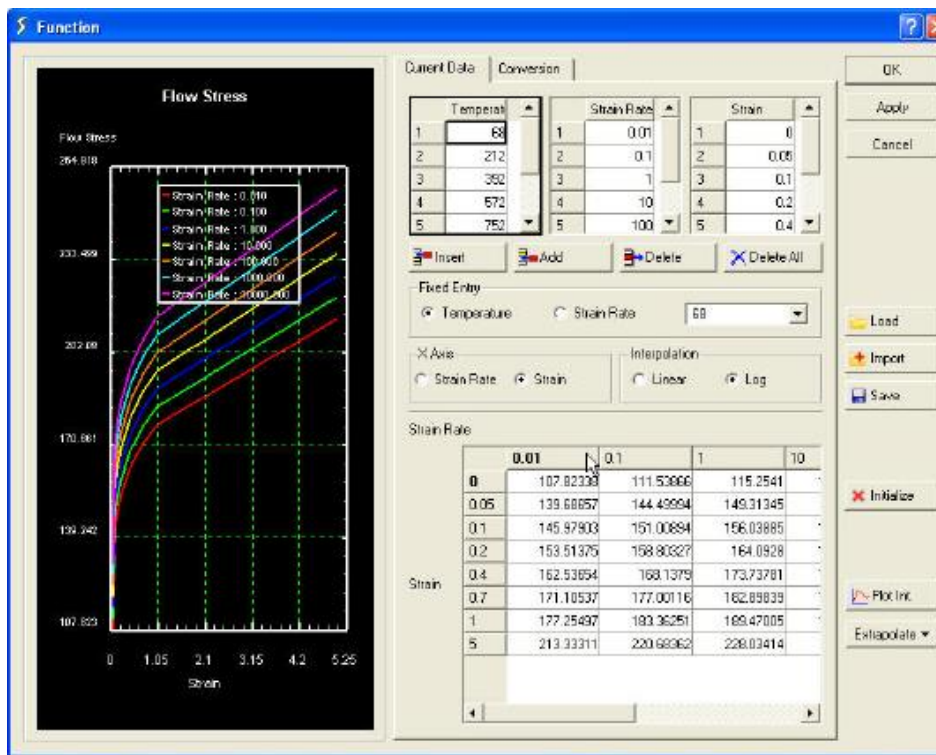


Figure 4-6: Flow stress input example in DEFORM [196] as a function of Temperature, Strain rate and Strain.

This data can be acquired from experimental tests [208] [209] [210] [211] [212] [213]. Tensile tests are used to determine the mechanical properties of metals at low strain rates. The tests involve a metal bar which undergoes uniaxial tension up to fracture and the process of performing tensile tests for simulation of residual stresses and machining distortion is defined by Ma [45] and ASTM standard [214]. This technique is applicable for the simulation of machining distortions and residual stresses due to their low strains.

The other alternative is compression tests [208] [215] [216] [217] which are used to determine mechanical properties under large strains as defined by the ASTM standard [218]. Other tests used for the calculation of material properties are Gleeble tests [135] [208] or torsion test [208] [219] as a function of strain, strain rate and temperature [28] [137] [197]. In addition to these tests, the Young Modulus, yield stress, ultimate tensile stress, and uniform elongation, total elongation can be determined using tensile test can also be acquired. For the accuracy of the simulation, these coupons should be taken from the same material specimen [210].

In other studies, Chobout found that the effect of precipitation has been found to influence the residual stress and distortion for 75 mm thick plates [70]. A similar finding has been found by Denis [220]. In addition to this, the effect of phase changes are not usually considered in the simulation of aluminium alloys [172] [221].

If there is no route to gather experimental data, the material data can be acquired from commercial software like JMAT Pro [193] [222] [223], a Java-based Materials Property simulation software or Thermo-calc [224]. In this study, JMAT Pro will be used to acquire the elastic material properties.

4.2.1.2 Element type

Although much work is done on the different software and methodologies, not much work has been done on the effect of element type on machining distortion. Young [21] stated the machining prediction can change by around 50% due to the remeshing process, to avoid this, the correct mesh would need to be used initially. Cerutti [11] additionally stated that the accuracy of the finite element model strongly depends on the mesh quality.

In another recent study done by [225] compared and contrasted the different elements for machining distortion (Figure 4-7). The two main element types used in the 3D simulation of machining distortion are hexahedral elements and tetrahedral elements [11] [32] [142] [226] [227]. In general, a hexahedral mesh is better than a tetrahedral mesh of the same number of nodes [45]. For the interpolation of material data (residual stress, thermal data, and cutting forces) onto the mesh, the hexahedral mesh has preference.

When compared with each other for simple bending moment calculations, it was found that both the tetrahedral and hexahedral elements produced acceptable results [228]. In another study on the simulation of deflection on an engine component, a 10 node tetrahedral mesh element was found to be closer to the experimental measurements than a 8 node hexahedral mesh [229].

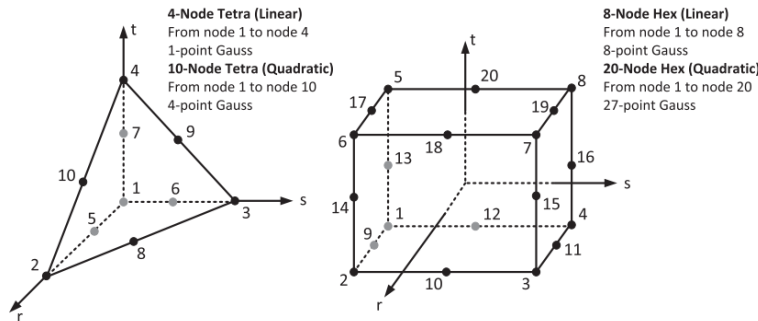


Figure 4-7: Tetrahedral and hexahedral elements and their local coordinate system [225].

For machining distortion simulation, the preferred tetrahedral element is the linear tetrahedral element (one integration point) [225].

4.2.2 Quenching simulation

The simulation software used for heat treatment simulation are well established since the 1970's. Quenching is a multi-physics process involving a complex coupling between different physical events such as heat transfer, phase transformations, and stress evolution (Figure 4-8). The coupling from the mechanical to the thermal part can be neglected, since during cooling, the thermally induced deformations are small, so the heat generation due to plastic dissipation is negligible [221]. With these assumptions, the only remaining couplings are those from the thermal part to the metallurgical part and to the mechanical part.

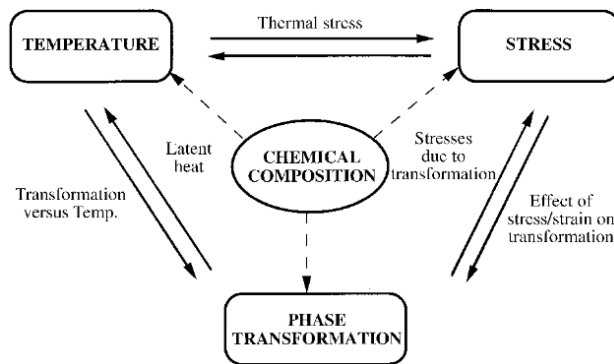


Figure 4-8: Thermal, metallurgical, and mechanical couplings in heat treatment [196].


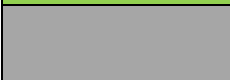
Liscic [67] and other authors [206] stated the FEM is the most acceptable method of simulating quenching residual stress in comparison to Finite Difference Method or Finite Volume Method and summarized the software employed for heat treatment simulation as shown in Table 4-1.

Chapter 4: Modelling of residual stress and machining distortions

As shown in this table, SYSWELD, FORGE and DEFORM are cable of modelling the thermo-metallurgical- mechanical coupling than the other software.

Table 4-1: Quenching simulation software capabilities [67].

Code	2D/3D	Phase Transformation	Mechanical Model		Coupling
			Elastic / Plastic	Elastic Viscoplastic	
SYSWELD	Capable of simulating	Capable of simulating	Capable of simulating	Capable of simulating	T-S T-M S-M
FORGE	Capable of simulating	Capable of simulating	Capable of simulating	Capable of simulating	T-S T-M S-M
ANSYS	Capable of simulating	Not capable of simulating	Capable of simulating	Capable of simulating	T-S
ABAQUS	Capable of simulating	Capable of simulating	Capable of simulating	Capable of simulating	T-S
MSC MARC	Capable of simulating	Capable of simulating	Capable of simulating	Capable of simulating	T-S
DEFORM	Capable of simulating	Capable of simulating	Capable of simulating	Capable of simulating	T-S T-M S-M

	Capable of simulating
	Not capable of simulating

4.2.3 Machining distortion simulation software

One of the critical modelling requirements in machining process is the capability to model part distortions [164]. In modelling of machining distortions, two consecutive analysis steps are performed: a material removal modelling step and a redistribution step [230]. The software that are widely used for machining distortion simulation most recently are ABAQUS [96].

Chapter 4: Modelling of residual stress and machining distortions

Other authors have used ANSYS [184], MSC Marc [225], DEFORM [35], Thirdwave's Advantedge [231], CALCULIX [20] and company specific software SC03 [73]. Most recently a software that was previously used for forging simulation [232] is now increasingly being used for the simulation of machining distortion simulation is FORGE [233].

To incorporate the machine induced stresses, Rakshi et al. [234] incorporated the machine induced stresses simulated using AdvantEdge. These stresses were then incorporated with quench residual stresses from literature into an Airbus group component. Similarly, Wu et al used DEFORM [235] to model the machine induced stresses and incorporate into ABAQUS to model the machining distortion.

The choice of software purely depends on the user requirements and outcome. A comparison between different machining software for chip formation analysis have preferred DEFORM to other FE software [236] [237] [238] [239] but there is currently no work to compare simulation tools for machining distortion.

Chapter 4: Modelling of residual stress and machining distortions

Table 4-2: Comparison between ABAQUS and DEFORM for machining distortion simulations.

	ABAQUS CAE 3D FEA	DEFORM-3D FEA
General overview	<ul style="list-style-type: none"> -General purpose finite element software. -Need previous experience to learn 	<ul style="list-style-type: none"> -Specially designed for forming operations
Machining distortion simulation	<ul style="list-style-type: none"> - User can design or import workpiece, fixtures. - Lengthy process to perform material removal operation - No interactive user interface - Higher meshing capability incorporating either hexahedron or tetrahedron elements or even both. 	<ul style="list-style-type: none"> - User can design or import workpiece, fixtures. - Practical amount of set up time using the interactive graphical user interface. - Reduced meshing capability due to use of tetrahedral mesh elements.
Material library	<ul style="list-style-type: none"> -No built in material library, user needs to manually input the data 	<ul style="list-style-type: none"> -User can input material model -Extensive material library from experiments or literature -Comprehensive material models
Remeshing capabilities	<ul style="list-style-type: none"> -ALE adaptive meshing for mesh distortion reduction - Adaptive remeshing for increasing accuracy -Mesh to mesh solution mapping 	<ul style="list-style-type: none"> -ALE adaptive meshing for mesh distortion reduction - Adaptive remeshing for increasing accuracy -Mesh to mesh solution mapping
Solver type	<ul style="list-style-type: none"> -Direct Sparse Solver -Iterative Linear Equation Solver 	<ul style="list-style-type: none"> -Direct Sparse Solver -Iterative Linear Equation Solver
Iteration method	<ul style="list-style-type: none"> -Direct -Iterative 	<ul style="list-style-type: none"> -Direct -Iterative

4.2.3.1 Modelling techniques

Ma [45] in this extensive analysis on the modelling of machining distortions, defined three different methodologies for modelling of machining distortion. The first procedure defined as the one-step procedure interpolates the residual stresses from the initial geometry (Figure 4-9 (a)) directly onto the machined geometry (Figure 4-9 (b)). This methodology is fast, predicted the distortion trends and avoids the issues and delays associated with remeshing [11] [226] but has an accuracy penalty.



Figure 4-9: One-step machining distortion simulation: (a) Pre heat treatment geometry, (b) Final part geometry with distortion.

The second procedure defined by Ma [45] is the multi-step procedure with pre-determined material removal which is based on a machining paths as used in the machining process (Figure 4-10). The layers are coloured to illustrate the different layers to be removed incrementally where orange represents the first layer to be removed, brown represents the second layer, red represents the third layer and finally green represents the fourth layer.

This methodology models the machining process better than the one step procedure although if there are any changes in the machining paths, the model has to be remeshed from the initial stage [11].

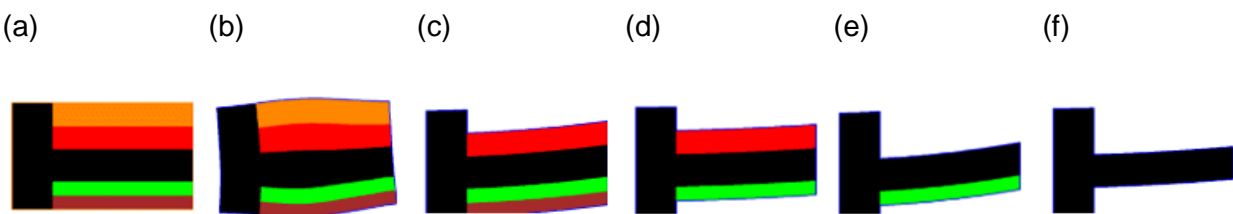


Figure 4-10: Multi step machining distortion geometry at different stages: (a) Pre heat treatment, (b) Post heat treatment, (c) First material removal, (d) Second material removal, (e) Third material removal, (f) Final geometry.

Chapter 4: Modelling of residual stress and machining distortions

The third and final procedure is the multi-step procedure with a path-dependent material removal models the machining process more closely to the experimental trials since it incorporates the machining paths and fixture interactions (Figure 4-11) unlike the other two procedures defined by Ma [45]. Figure 4-11 (a) shows the pre heat treatment geometry. Figure 4-11 (b) shows the distorted post heat treatment geometry with first material removal and boundary conditions. Figure 4-11 (c) shows the distorted geometry with second material removal and additional boundary conditions. Figure 4-11(d) shows the distorted geometry with the modified boundary conditions. Figure 4-11(e) shows the distorted geometry with the modified boundary conditions and finally Figure 4-11 (e) shows the model in an unconstrained state.

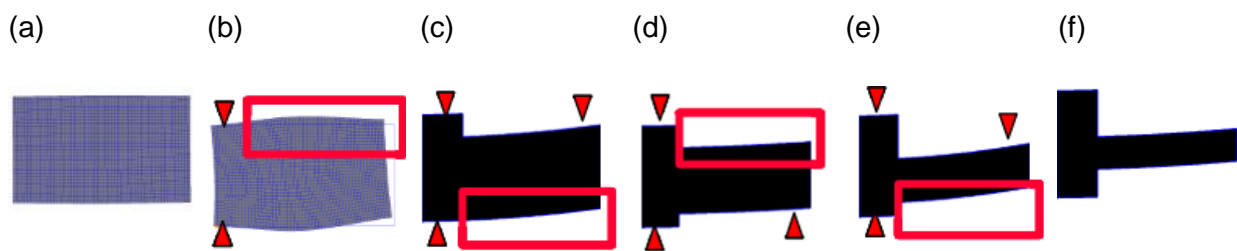


Figure 4-11: Multi step with path dependency machining distortion simulation: (a) Pre heat treatment, (b) First material removal, (c) Second material removal, (d) Third material removal, (d) Fourth material removal, (e) Final geometry unconstrained.

The multi-step procedure can be further divided into various techniques for numerical material removal. Three types of methods can be distinguished:

1. The deactivation or "death & birth" method
2. The massive removal approach
3. Level-set method.

Deactivation technique

To model machining distortion, a technique known as element deactivation (element birth and death) would need to be applied in regions of the machining tool path. This is done by deactivating (or reducing) the element (mainly using hexahedral mesh elements) stiffness matrix to 10^{-6} . This is explained in Equation 4-6. The Element stress $\{\sigma\}$ can be represented by the matrix $[D]$, $[B]$ the shape function matrix and the displacement vector $\{u\}$ as follows:

$$\{\sigma\} = [D][B]\{u\}$$

Equation 4-6: Element stress equation.

Chapter 4: Modelling of residual stress and machining distortions

In plane stress, the matrix [D] is defined in Equation 4-7 where [D] is material matrix, E is modulus of elasticity and ν is Poisson's ratio.

$$[D] = \frac{E}{1-\nu^2} \begin{bmatrix} 1 & \nu & 0 \\ \nu & 1 & 0 \\ 0 & 0 & \frac{1-\nu}{2} \end{bmatrix}$$

Equation 4-7: Material matrix.

Therefore, if the assumed modulus of elasticity of the removed element is around zero, the matrix [D] in Equation 4-6 and Equation 4-7, while the element stresses $\{\sigma\}$ in Equation 4-6 will be zero. In other words, the corresponding properties and parameters (applied loading, initial stress, temperature loads, specific heat, etc.) linked to all these elements are zeroed out [143].

In order to compute redistributed stresses and displacements due to the removal of elements, nodal forces, $\{F\}$, from the initial residual stresses should be first calculated. Assuming $E \cong 0$ in all of the elements being removed, the stresses and displacements were calculated by applying negative nodal forces, $-\{F\}$. The stresses in the remaining (active) elements were then used to determine distortion and the redistribution of original residual stress distributions in remaining materials [185].

An example of the elements to be deactivation is shown in Figure 4-12 [143]. Simulation steps 1 to 5 follow the material removal (elements deactivated one by one) entirely from top face layer then inside pockets, middle pockets, side pockets, and finally the bottom face.

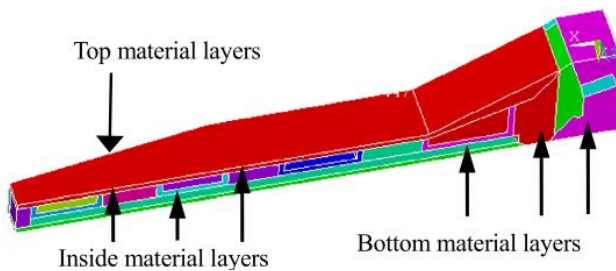


Figure 4-12: Element deactivation technique at different regions for rib component [143].

This technique was first utilized for machining distortion analysis by Wang [14] and has been used most recently by different authors [93] [143].

To overcome the simulation time limitations of numerical models and the simplified assumptions of analytical models, a methodology to calculate either the temperature, cutting forces or the

induced machining residual stress can be integrated to the numerical model as shown in Figure 4-13.

In this research, Hussain [108] adopted a new method to apply analytically obtained thermo-mechanical loads to the relevant nodes in the model. In this model, he used hexahedral mesh elements.

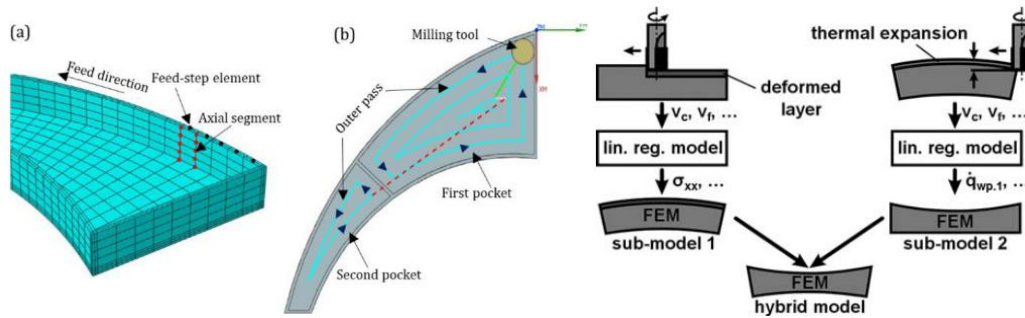


Figure 4-13: Interpolation of cutting forces on a pocket geometry [108], (b) hybrid model incorporating thermos-mechanical behaviour [171].

Although this technique is the most widely used, it is difficult to be applied on parts with irregular machining features (i.e. non rectangular) or with complex initial geometries[11] [91]. This is due to the structured mesh being defined by the cutting parameters i.e. depth of cut and machining tool path [11] [121] [190]. Furthermore, the user would need to pre-define the tool path, which is not practical in a fast-paced manufacturing environment.

Boolean method

The Boolean method is similar to the deactivation technique with the only major difference being the Boolean method removes a larger amount of volume [11] is easily adaptive to the tool path as shown in Figure 4-14.

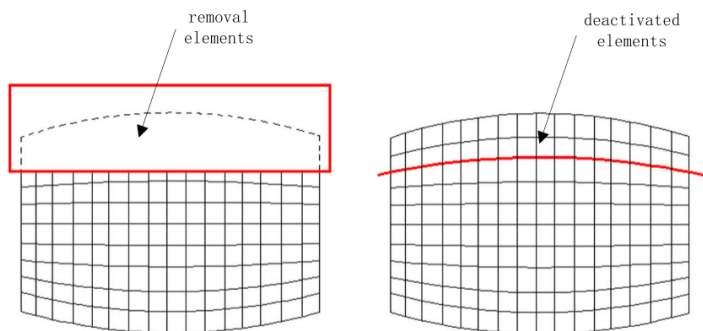
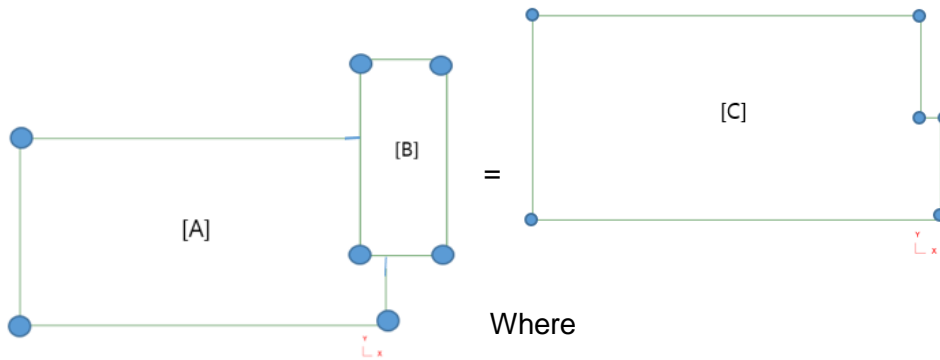


Figure 4-14: Comparison between Boolean operation and element deactivation [91].

Chapter 4: Modelling of residual stress and machining distortions

This methodology consists of subtracting an unwanted volume from the mesh of the workpiece from the machine path geometry. Figure 4-15 and Equation 4-8 define this, where C represents the machined workpiece matrix, B represents the tool path volume matrix and A is the workpiece volume matrix. From this example, the regions of geometry B that lie inside the geometry of A and the regions that intersection of A and B are saved. All the points are then subtracted.



Where

$$[C] = [A] - [B]$$

$$[A] = \begin{bmatrix} 0 & 0 \\ 20 & 0 \\ 20 & 10 \\ 0 & 10 \\ 0 & 0 \end{bmatrix}, [B] = \begin{bmatrix} 8 & 5 \\ 12 & 5 \\ 12 & 14 \\ 8 & 14 \\ 8 & 5 \end{bmatrix}, [C] = \begin{bmatrix} 0 & 0 \\ 20 & 0 \\ 20 & 5 \\ 19 & 5 \\ 19 & 10 \\ 0 & 10 \\ 0 & 0 \end{bmatrix},$$

Equation 4-8: Boolean subtraction definition [240].

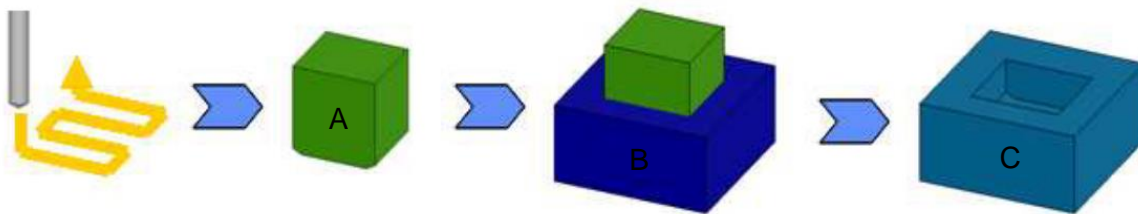


Figure 4-15: Boolean operation with local remeshing [45].

Chapter 4: Modelling of residual stress and machining distortions

The Boolean operation process in the following sequence (Figure 4-16) as defined by Bilkhu et al. [241], Madenci et al. [242] and Pidarpart et al. [182] and Ma et al. [45] Cerutti [11], Prete et al. [199], Rai et al. [243] in their research work:

- The first step is aligning the volume to subtract onto the initial mesh.
- Depending on the sign of distance, the nodes (elements) are either kept or removed.
- If the distance is positive or zero, the node is therefore not on the machining path and has to be kept
- If the distance is negative the node is in the machining area (material removal area) and has to be removed
- When an element has nodes that should be removed and kept, the element crosses the machining surface and has to be cut.

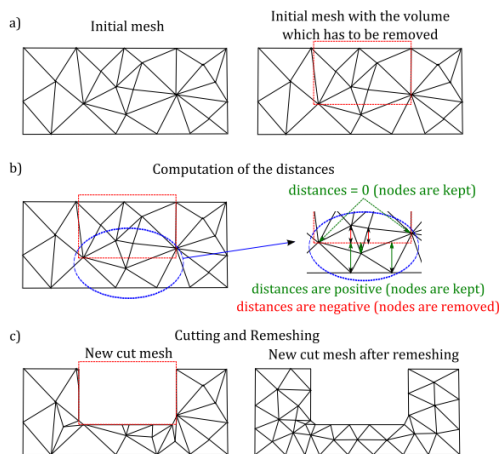


Figure 4-16: Boolean illustration [11].

In the case of the boundary condition being removed in the Boolean region, software like DEFORM have the advantage of automatically applying a boundary condition when the Boolean operation removes a constrained node, ensuring that the model is not left unconstrained [196]. The Boolean technique has been widely used recently by Prete et al. [244] for the simulation of machining distortion for both simple and complex geometry and has been found to be adaptive and a suitable technique from an industrial perspective.

4.3 Model validation

Model validation is usually the final step in every simulation. This is done by correlating the model prediction with experimental results. A validated model can be seen as a very powerful tool that can be easily adapted for prediction of different processes in the context of prediction of machining distortions and residual stresses. Kleijnen [245] defined model validation as determining whether the simulation model is an acceptable representation of the real system.

It is important to highlight that quenching or machining distortion validations become successful only if the correct methodology is performed from the initial conception i.e. the careful selection and justification of the material model and boundary conditions. Ideally, the constructed model should be validated against a similar experimental machining condition. It is noted that not only is there an accuracy limit with the model code but it is widely accepted in industry and academia that there is a large variation in both the workpiece (residual stresses) [180], machining experimental trials and measurements [45] [124] [191] [246].

Nervi [188] and Davim [247] identified four sources of errors in modelling of machining distortions:

1. Errors in the residual stresses
2. Variation in the material properties
3. Variation in the thickness
4. Errors in measurements

Furthermore, Astakov [191] and Nervi [188] states that there is always a need to remodel by adjusting the set up used in the construction of the first model including the boundary conditions, the mesh element and in some cases the material model [166]. Therefore, the model is firstly created and used for calibration with experimental results, it is then validated [22] [188] [166]. Ma [45] in order to create a reasonable model prediction and overcome any modelling errors, intentionally generated large residual stress which produced large distortions for measurement accuracy avoiding large experimental errors.

It was further suggested that to overcome the global model validation, it is better to validate the model at each incremental step in order to save time and isolate the shortcomings of the model. Finally, Ma also found that the residual stresses were different when compared with the simulation by 150%. These variations were attributed to the inverse method of calculating the residual stress from the measured strain, leading to large errors.

Additionally, it was stated that small distortions are likely to generate noise in the data making such data unsuitable for model validation. It has been found that machining simulations of complex aerospace parts can commonly generate a difference of around 50% from the experimental results, with simple geometries showing around 19%-40% error [248].

4.4 Summary and conclusion

Modelling methods, most especially numerical models, have been identified as a powerful tool in predicting and optimizing the manufacturing process to control distortion.

Advantages and disadvantages of each modeling methodology in an industrial perspective has been described. Finally, a simulation requirement has been drafted to assist in accurately simulating quenching and machining distortion simulations. From the current literature review, the following are identified gaps in simulation of manufacturing process:

1. There is no literature identified where both operations (heat treatment and machining distortion) have been simulated using a single software.
2. Although DEFORM has been found to be adaptable for modelling the heat treatment and for metal cutting simulations, there is a substantial gap for its use on modelling of machining distortion on aerospace aluminium structural components (wing ribs, skins, stringers etc.).

Therefore, this research aims to overcome these gaps by exploiting DEFORM's capability for the simulation of the complete manufacturing process i.e. heat treatment and machining distortion simulations. This is done by simulating machining distortion for different machining scenarios on small coupons in order to provide a deeper understand on the effect of material removal strategies influences on machining distortion. These simulations then will be validated using experimental residual stress and post machining distortion measurements. Once an understanding of the factors influencing distortion during material removal has been developed, knowledge of this will then be applied to a representative part. As a conclusion to this study, an effective industrial manufacturing plan will be developed to inhibit machining distortions.

5 Finite element modelling methodology

5.1 Finite element development

In this section, the FE model to be used for the distortion and stress prediction is introduced. Design Environment for Forming (DEFORM) is a multi-functional Finite Element Analysis (FEA) software based process simulation system designed to analyze various forming and heat treatment processes used by metal forming and related industries [196]. DEFORM was developed at Battelle Columbus Laboratories as an initial collaboration between the US Air Force and rigid–plastic FEM, conducted by the University of California Berkeley [249]. DEFORM is considered a leader in the generation of adaptive meshes (AMG) and remeshing complex geometry making it attractive for simulation of machining operations. Additionally, it has been proved to provide simulation advantages that decrease experimental trials which incur large costs and time and labour [227].

In summary, DEFORM simulates the machining distortion in three stages:

1. Material removal simulation
2. The workpiece is allowed to spring back while still constrained on the fixture
3. The workpiece is finally allowed to springback from the fixture

Prior to any modelling activities, it is essential to generate the representative input. As emphasized in the literature review, the material properties and the heat transfer coefficient are integral in the prediction of residual stresses during the heat treatment process. Therefore, the first section will initially define the experimental process and results to develop the material data. This will be followed by the model formulation for both the heat treatment and the machining simulation.

In the final section, the methodology for different machining factors will be simulated to control machining distortion simulation will be presented. These main factors normally considered by manufacturing engineers include:

- The machining parameters:
 - The radial depth of cut
 - The axial depth of cut
- The tool path strategy
- The tool entry strategy
 - The ramp angle
 - The tool entry location
- Pocketing strategy

5.1.1 Model formulation

5.1.1.1 Material model

Plastic deformation definition

The yield or plastic flow data (flow stress) is fundamental to heat treatment and machining distortion simulations since it governs deformation and flow behavior. Out of the two popular yield criteria, the von Mises yield criterion is considered closer to reality than the Tresca criterion.

The plastic flow defined by the von Mises yield criterion and the data required for deformation relates the equivalent von Mises stress (σ_{eq}) as a function of the effective strain (ε_{eq}), effective strain rate ($\dot{\varepsilon}_{eq}$) and temperature (T). The von Mises yield criterion is calculated from the deviatoric part of the stress tensor as shown in Equation 5-1.

$$\sigma = \left(\frac{1}{3} \text{tr}\sigma'\right) 1 + \sigma' \quad \text{where } \left(\frac{1}{3} \text{tr}\sigma'\right) = 0;$$

Equation 5-1: Stress Tensor as function of Hydrostatic and Deviatoric Parts.

Therefore, the equivalent von Mises stress (σ_{eq}) is given by Equation 5-2.

$$\sigma_{eq} = \left(\frac{3}{2} \sigma'_{ij} \sigma'_{ij}\right)^{\frac{1}{2}}$$

Equation 5-2: Equivalent von Mises stress.

Since, at the initial yielding σ is equal to σ_Y , the Mises criterion in terms of σ_{eq} is shown in Equation 5-3.

$$\sigma_{eq} - \sigma_Y = f$$

Equation 5-3: Initial yielding condition.

One of the ways of calculating the plastic deformation is incrementally; usually adopted for Lagrangian simulations. This is shown in Equation 5-4 where $d\varepsilon$ is both the elastic and plastic strain, du is the current incremental displacement, $\nabla(du)$ measure of the deformation incrementally. $d\varepsilon$ is the incremental linear strain tensor.

$$d\varepsilon = \frac{1}{2} (\nabla(du) + (\nabla(du))^T)$$

Equation 5-4: Incremental linear strain tensor.

The elastic and plastic components can be separated as shown in Equation 5-5 and the effective strain and strain rate can be calculated as shown in Equation 5-6 and Equation 5-7.

$$d\varepsilon_{ij} = d\varepsilon_{ij}^e + d\varepsilon_{ij}^p$$

Equation 5-5: Law of strain additivity from the Prandtl-Reuss theory.

$$\dot{\varepsilon}_{eq}^p = \left(\frac{2}{3} \varepsilon_{ij}^p \dot{\varepsilon}_{ij}^p \right)^{\frac{1}{2}}$$

Equation 5-6: Effective strain rate as a function of the plastic strain.

$$\varepsilon_{eq}^p = \int \dot{\varepsilon}_{eq}^p dt$$

Equation 5-7: Effective strain as a function of the effective strain rate.

Elastic Plastic flow definition

During the simulation of machining distortion, majority of the strains usually remain within the elastic region. If there is some yielding during the simulation, this could be due to a high residual stress redistribution level or the use of an unsuitable fixture [11]. Therefore, an elastic-plastic constitutive model is considered this work.

For the simulations of quenching and machining distortions, a linear relationship between each stress tensor component (σ_{ij}) with the elasticity tensor (C_{ijkl}) and the linear strain tensor (ε_{kl}) is shown in Equation 5-8.

$$\sigma_{ij} = C_{ijkl}\varepsilon_{kl}$$

Equation 5-8: Stress-strain relations in x y z coordination system.

The elasticity tensor (C_{ijkl}) can be modified as shown in Equation 5-9 where the constants λ and μ are known as the Lamé's constants, E the Elastic modulus (GPa) and ν the Poisson's ratio.

$$\sigma = \lambda(tr\varepsilon)1 + 2\mu\varepsilon$$

$$\lambda = \frac{E\nu}{(1 + \nu)(1 - 2\nu)}$$

$$\mu = \frac{E}{2(1 + \nu)}$$

Equation 5-9: Stress-strain relations in tensor notation for isotropic materials.

The Prandtl-Reuss model (Equation 5-10) can be used to determine the stress-strain relationship for an elastic- plastic material where (f) the yield function is and where $d\lambda$ is a scalar plastic multiplier. Prakash [250] stated that the this value is a function of three factors; the stress increment, the hardening relation and the stress state.

$$d\varepsilon_{ij}^p = d\lambda \frac{\partial f}{\partial \sigma_{ij}}$$

Equation 5-10: Associated flow rule.

The von Mises criterion (Equation 5-2) can be related to the flow rule (Equation 5-10) as shown in Equation 5-11.

$$d\varepsilon_{ij}^p = d\lambda \sigma'_{ij}$$

Equation 5-11: The associated flow rule in relation to the von Mises criterion.

Hardening rule

Hardening is another factor that is used to determine the level of plastic deformation. Hardening is useful to define the subsequent yielding that occurs with the level of changing plastic deformation. This is shown in Figure 5-1 where the criterion for subsequent yielding is defined by Equation 5-12 where h is the hardening function, ε^p is the plastic strain, σ is the true stress.

Chapter 5: Finite element modelling methodology

When ε^p is zero, the hardening function is equal to the yield stress (σ_y). The hardening function (h) depends on the material.

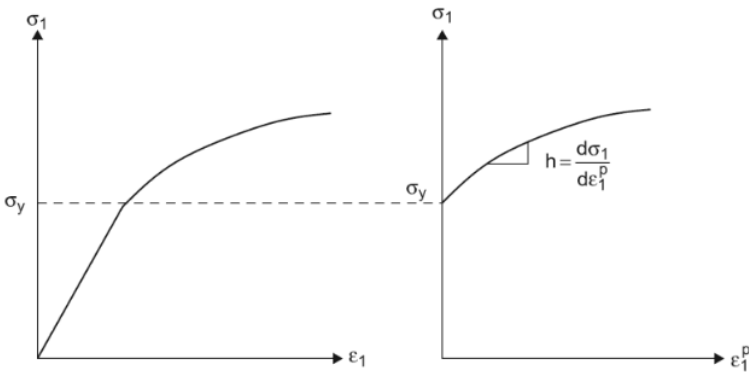


Figure 5-1: Hardening function determination from true stress with plastic strain in tension test.

$$\sigma - h(\varepsilon^p) = 0$$

Equation 5-12: Yield stress as a function of hardening function, plastic strain and true stress.

There are two popular hardening mechanisms used; isotropic hardening and kinematic hardening. The assumption made by the isotropic hardening rule is that the von Mises yield surface equally expands as the material enters into the plastic regime (Figure 5-2 (a)) [196]. In contrast, the assumption made by the kinematic hardening is that the von Mises yield surface is translated from the origin of the Von Mises yield circle (Figure 5-2 (b)) [196]. The combination of both the isotropic and kinematic hardening showing the expansion and translation of the yield surface with plastic strain is shown in Figure 5-2 (c). The consequence of the three hardening mechanisms on the compression yield stress is shown in Figure 5-2 (d), where point C – is the kinematic hardening, D is the mixed hardening, and E is the isotropic hardening.

Chapter 5: Finite element modelling methodology

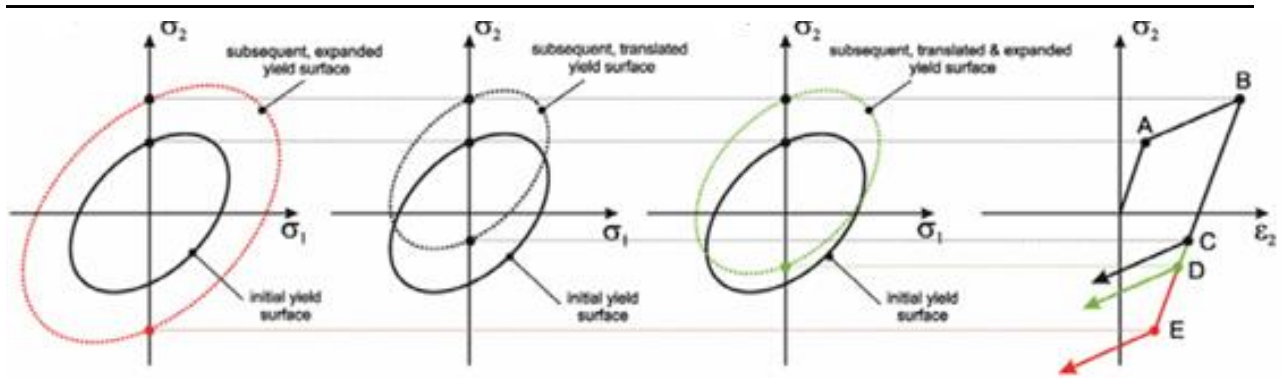


Figure 5-2: Different hardening mechanisms:(a) isotropic hardening, (b) Kinematic hardening, (c) Combined iso-kinematic hardening, (d) Resulting stress–strain curves showing different yield stress in compression [251].

For the quenching simulations used in this study, an isotropic hardening rule is used as is recommended due to its low strain rates [196]. Chobaut [252] justified neglecting kinematic hardening and using isotropic hardening for quenching simulations for Aluminium 7040 and 7449 due to the low plastic strains and low Bauschinger effect. In another study, Chobout et al. [253] concluded in that the Bauschinger effect can be neglected in the case of residual stress generation during quenching for aluminium 7040. Similarly, Bovin et al [27] compared both hardening models during quenching of Aluminium 7075 and validated the models with experimental residual stress measurements. From this research, it was found that the isotropic hardening model predicted closely with the experimental results than the kinematic model. Bellini et al [254] used the isotropic hardening for the simulation of quenching of Aluminium cast parts. With these justifications, the use of isotropic hardening was used in this study. Muránsky et al. [251] mathematically expresses the isotropic hardening rule as shown in Equation 5-13 where σ^0 is the equivalent (uniaxial) stress.

$$f(\sigma) = \sigma^0(\varepsilon_{eq}^p, \theta)$$

Equation 5-13: Isotropic hardening rule as a function of equivalent stress and plastic strain.

Therefore, assuming an isotropic hardening mechanism, the equivalent stress (σ_{eq}) can be determined as a function of the equivalent plastic strain (ε_{eq}^p), equivalent plastic strain rate ($\dot{\varepsilon}_{eq}^p$) and temperature (T) (Equation 5-14). In DEFORM, the hardening rule (H) is incorporated in the flow stress curves, in the tabulated format.

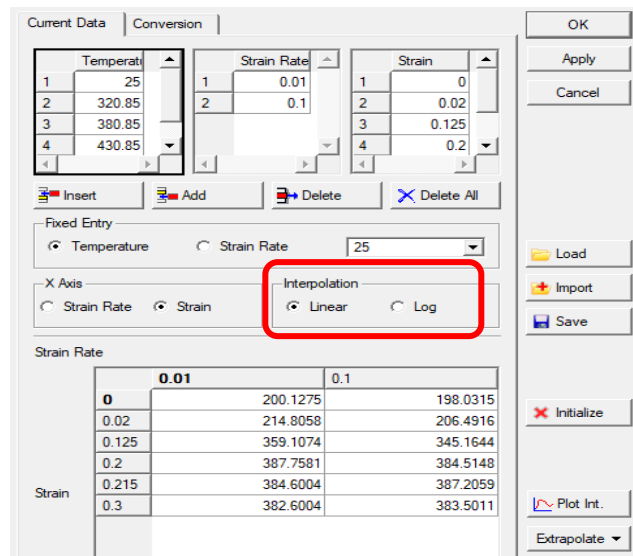
Chapter 5: Finite element modelling methodology

$$\sigma_{eq} = H(\varepsilon_{eq}^p, \dot{\varepsilon}_{eq}^p, T)$$

Equation 5-14: Equivalent stress as a function of plastic strain, strain rate and temperature.

When a simulation undergoes a plastic strain or strain rate that is within the specified data range, DEFORM interpolates this data either linearly or the log interpolate (Figure 5-3 (a)). If the data is not within the specified data range, DEFORM extrapolates the data linearly to determine the corresponding data, as shown in Figure 5-3 (b).

(a)



(b)

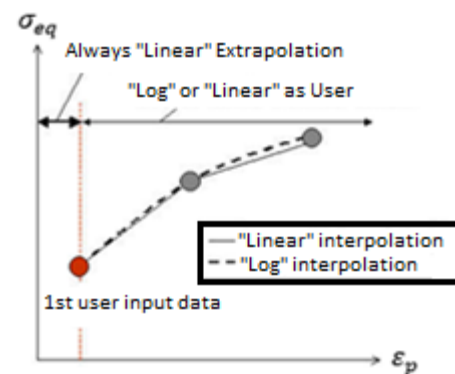


Figure 5-3: (a) DEFORM's interpolation, (b) Extrapolation rule for flow stress [196].

5.1.1.2 Lagrangian Incremental simulation

There are three common measures of plastic deformation; the incremental linear strain tensor, strain rate tensor or a combination of both. The incremental linear strain tensor is effective for deformation occurring in small incremental steps normally associated with heat treatment, machining distortion, forgings and bending simulations [250]. These deformations are liable to incremental formulation also known as the incremental Lagrangian formulation.

In order to calculate the incremental displacements, incremental strains and incremental stresses in a deformable body, three sets of incremental equations need to be solved [250]. In DEFORM, the elastic-plastic, Lagrangian Incremental simulation for heat treatment and machining simulations is solved by creating solutions at discrete time increments.

Chapter 5: Finite element modelling methodology

At each individual time increment of each node, key variables such as the temperature and velocity are calculated based on factors such as the boundary conditions applied, material properties of the work piece materials. The Lagrangian approach calculates the evolution of each point of the material with time from the initial position to the current one where the mesh node points move with corresponding material points (Figure 5-4).

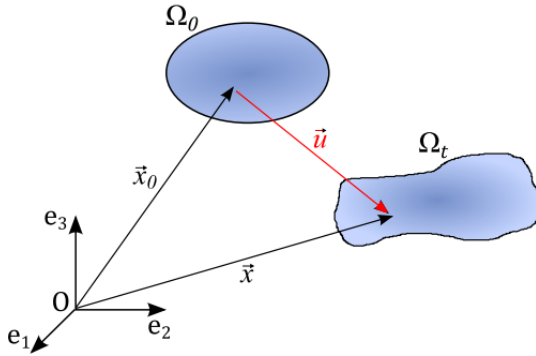


Figure 5-4: Kinematics of finite incremental deformation with Ω_0 is the deformed configuration at a current time t and a Ω_t deformed configuration at an incremental time $t + \Delta t$ [11] [250].

The Lagrangian displacement during deformations of solids (for both rotations and translation) (\vec{u}) is defined from Equation 5-15 to Equation 5-17. When deformation occurs on a material, the position vector (\vec{x}) at the current time of an arbitrary location on the material can be related by the initial position \vec{x}_0 of the material point at time t_0 by a function (φ). In DEFORM, an updated Lagrangian formulation is applied, which is a slight modification of Equation 5-15 where the position is defined for each time interval by a function (φ^t) and at smaller time increments of Δt to be able to capture the smaller deformations.

$$\vec{x} = \varphi(\vec{x}_0, t)$$

Equation 5-15: Position vector of a material location.

$$\vec{u} = \vec{x} - \vec{x}_0 = \varphi(\vec{x}_0, t) - \vec{x}_0$$

Equation 5-16: Lagrangian displacement.

$$\vec{x}_{t+\Delta t} = \varphi^t(\vec{x}_t, t + \Delta t)$$

Equation 5-17: Modified Lagrangian method for small time increments.

Langrangian formulation is mostly used in machining simulations [255] and most recently in the simulation of machining distortion simulations [11]. This is due to its advantage of providing better simulation cycle times. Additionally, the main advantage of a Langrangian formulation is that when a simulation has stopped unexpectedly, the simulation can recommence at the last step where the simulation stopped.

5.1.1.3 Adaptive mesh generation (AMG)

In addition to this, due to the issues associated with element distortions in Langrangian formulations [11], DEFORM [196] uses the Adaptive (automated) Mesh Generator (AMG) function developed by Wu in this thesis [256]. AMG works by taking value specified in the initial mesh density specified by the user and prior to remeshing generates approximately the same number of elements. The simulation alters the mesh without the user intervention that makes this software a step ahead over its competitors.

The process at which AMG is applied in simulations is as follows:

1. When elements are distorted (due to large time steps [196]) during deformation simulations, the AMG is activated.
2. The simulation is interrupted due to these element distortions. The mesh is then redistributed, using the similar global element numbers as the previous mesh and then applied onto the geometry (Figure 5-5).
3. The process variables are then interpolated from the old mesh to the new mesh.

This is in order to facilitate the enhanced resolution of part features [196]. The adaptive meshing tool is a powerful tool that during remesh, local elements are used at regions of higher strain rates and lesser elements at lower deformations for accuracy of solution. The main advantages of the AMG function is to enhanced resolution of part features that can maintain a good control of the overall problem size and computing requirements. In addition, a flexible user- defined control of local mesh density provides a better analysis to meet specific conditions [227].

Furthermore, the remeshing can be triggered on the number of defined increments and the mesh quality. Once the remeshing step is completed, the state variable fields have to be transported into the new mesh.

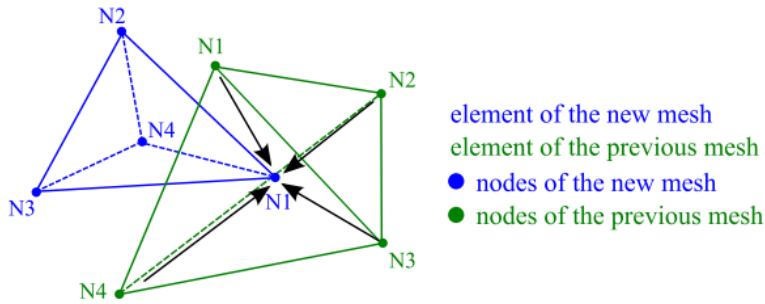


Figure 5-5: Redistribution and transfer of element data during remeshing [11].

5.1.1.4 Deformation solvers

There are two main iterative solvers used in DEFORM; a) Conjugate Gradient, b) Sparse. The sparse solver is a direct solution that makes use of the “sparseness” of FEM formulation to increase speed while the conjugate gradient solver uses an approximate iterative approach. In some cases it is better to simulate using a Sparse solver under specific conditions (for example with poor initial boundary conditions in a forging simulation).

The conjugate gradient is (Figure 5-5) mostly useful in demanding simulations although this solver has convergence problems in “large rigid body motions”, undergoing light deformation or bending simulations, therefore it is better to use the Sparse solver [257].

Regardless of this limitation, advantages of the conjugate solver over sparse is simulation time is decreased by five times as shown in Figure 5-6 [196]. DEFORM has another advantage if the conjugate-gradient solver cannot successfully converge, the simulation will revert to the sparse solver.

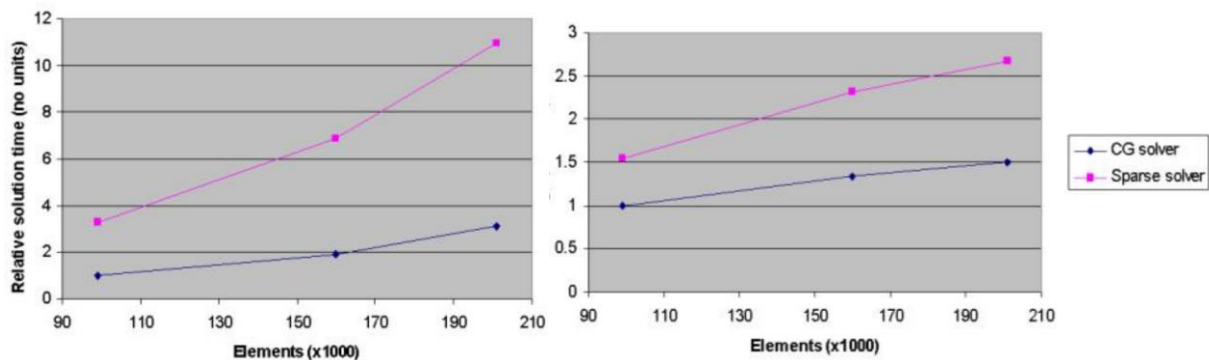


Figure 5-6: Comparison of using conjugate gradient and sparse solvers as a function of elements for: (a) Relative time, (b) Relative memory.

5.1.1.5 Iteration methodologies

Heat treatment and machining distortion simulations are non-linear system to solve. The Newton-Raphson method transforms a non-linear problem into a series of linear problems [11] [257]. The Newton-Raphson method is widely used for the simulation of heat treatment [22] and machining distortion simulations [11]. The Newton-Raphson method is recommended for most problems because it generally converges in fewer iterations than the other available methods. For each linear iteration, the Newton-Raphson solution improves the solution until a satisfactory result is found.

Deformation iteration is assumed to have converged when the velocity and force error limits have been satisfied i.e. the change in both the nodal velocity norm and the nodal force norm is below the specified value (Figure 5-7).

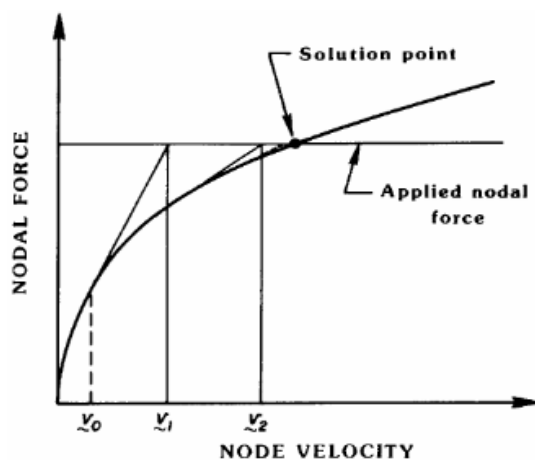


Figure 5-7: Newton Raphson iteration method [258].

The quenching and machining distortion simulation requires a time integration calculation. The two time integration formulations used are the implicit and explicit methods. The implicit method solves a series of simultaneous equations using information at a time $(t + \Delta t)$ and at a state of increment of time $(t + \Delta t)$ [259] until the solution has converged. This formulation is used to simulate problems where the effects of strain rate are low such as quenching and machining distortion simulation. The implicit method iterations using the Newton Raphson Method [191] and iterates until the solver will find the lowest error solution to the numerical problem..

Chapter 5: Finite element modelling methodology

In contrast, the explicit method simulates without iterations and utilizes a central difference rule to integrate the equations of motion through time i.e. solves the state of a finite element model at time $(t + \Delta t)$ based on data at time (t) .

Mathematically these two equations can be defined as shown in Equation 5-18 where (P) , is the external applied force, (I) is the internal forces, (\ddot{u}) is the nodal accelerations and (M) is the mass matrix. The significant difference between the explicit and implicit method is in on how the nodal acceleration (\ddot{u}) are calculated.

$$M\ddot{u} = P - I$$

Equation 5-18: Equilibrium condition.

Using Taylor series Equation 5-18 can be further rewritten as Equation 5-19 where K is the Jacobian Matrix (or the global stiffness matrix) and Δu_{i+1} is the change in incremental displacements. The incremental displacements for the i th iteration is therefore updated at $t + \Delta t$ as shown in Equation 5-20. In order to solve for Δu_{i+1} , the Jacobian matrix is inverted.

$$K_{i+1}\Delta u_{i+1} = P - I;$$

$$K = \frac{\partial I}{\partial u} - \frac{\partial P}{\partial u}$$

Equation 5-19: Jacobian stiffness matrix.

$$u_{i+1}^{t+\Delta t} - u_i^{t+\Delta t} = \Delta u_{i+1}$$

Equation 5-20: Change of incremental displacement as a function of incremental displacements for the i th iteration.

Inversely, the explicit method determines the solution the nodal acceleration (\ddot{u}) as shown in Equation 5-21 Equation 5-21. Unlike the implicit method where the Jacobian matrix (K) is inverted, the Mass Matrix (M) for the explicit method has been inverted (M^{-1}) to increase its efficiency. To prevent any instability of the solution due to the time increment (Δt) , an estimate of the time increment stability is shown in Equation 5-21 where L^e is the characteristic length, c^d is the dilation wave speed of the material, λ , μ are Lamé's constants and ρ is the material density.

$$\ddot{u} = M^{-1}(P - I)$$

$$\Delta t = \min\left(\frac{L^e}{c^d}\right);$$

$$c^d = \sqrt{\frac{\lambda + 2\mu}{\rho}}$$

Equation 5-21: Explicit method formulation.

In DEFORM [196], the convergence for each simulation step is defined by both the velocity and force convergence error limits. The assumed convergence for the velocity error limit is shown in Equation 5-22 are satisfied where $\|u\|$ is the Euclidean norm of nodal velocity at current iteration and $\|\Delta u\|$ is the Euclidean norm of the different between the nodal velocity at the current iteration and nodal velocity at the start of the iteration.

$$\left\|\frac{\Delta u}{u}\right\| \leq v_{elerr}$$

Equation 5-22: Velocity convergence error limit.

Similarly, the assumed force convergence error limits can be represented as Equation 5-23, where $\|f\|$ is the norm of nodal velocity at current iteration and $\|\Delta f\|$ is the norm of the different between the nodal velocity at the current iteration and nodal velocity at the start of the iteration.

$$\left\|\frac{\Delta f}{f}\right\| \leq v_{elerr}$$

Equation 5-23: Force convergence error limit.

In DEFORM, the convergence limit for the nodal velocity 0.001 and the force limit is 0.01, therefore the nodal and velocity and forces will be updated until the solution is reached. If the solution does not converge in the specified number of iterations, and with automatic step size reduction that follows, the simulation will terminate.

5.1.1.6 2D to 3D Model conversion tool

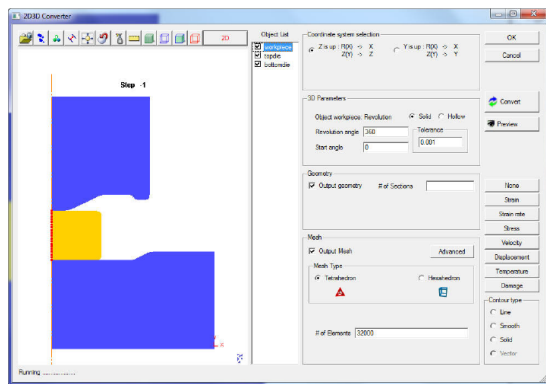
DEFORM has a tool that converts a 2D FE model into a 3D FE model (Figure 5-8). The tool uses the advanced geometry option where the following steps are applied:

Chapter 5: Finite element modelling methodology

- The user can input a 2D cross section geometry and specify the revolution angle (for 2D axisymmetric models) or the extrusion length (for 2D plane stress or strain models) to a 3D FE model.
- Select the orientation of the converted 3D workpiece
- The number of geometry sections is then defined.
- Finally, the number of mesh sections and element number is then specified for 3D model conversion.

This methodology is useful as it overcomes the simulation cycle time constraints that is associated with heat treatment simulations. In addition to this, an improved mesh can be generated in the 2D to 3D conversion tool. There is no current published information of utilizing this tool for machining distortion simulations.

(a)



(b)

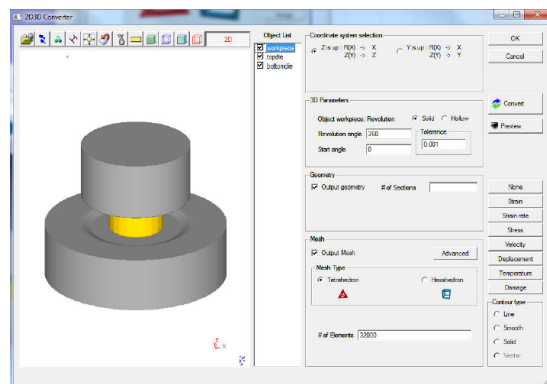


Figure 5-8: 2D to 3D conversion in DEFORM: (a) 2D FE model, (b) 3D FE model.

When the model is converted from 2D to 3D the symmetry plane, BCC assignments and materials are assigned automatically to the respective objects (Figure 5-9).

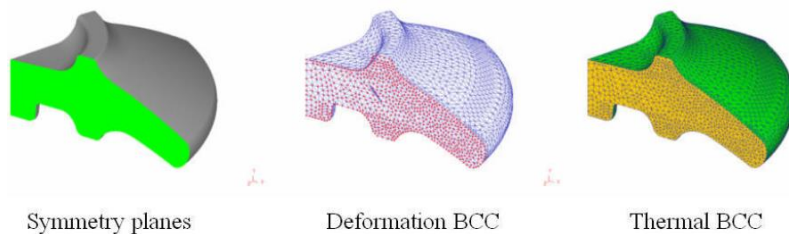


Figure 5-9: Automated symmetry plane assignment to die/ workpiece geometry and boundary code assignment for mesh [196].

5.1.2 Model assumption

Based on the literature review on the effect of residual stresses on distortion presented in section 2.5.3 , the following assumptions can be made:

- No actual machining operation is simulated; only an elastic model which predicts the distortions by mimicking the machining material removal process by deleting the volume removed instantaneously and predicting the distortions due to the residual stress redistribution, therefore the effect of high strain rates are not considered in this simulation. This strategy has been performed widely by many authors including Cerutti et al. [11], Ma et al [45], Bilkhu et al.[241].
- There are no stresses at the beginning of the case studies since they was heated and held at 477°C above the recrystallization temperature as defined by the ASM Handbook [75].
- The residual stresses from the quenching process and not the machining induced stresses are the main reason for machining distortion for these case studies. This is due the effect of the machine induced stresses acting to a maximum depth of 250 μm [260] and its influence to up to 3 mm wall and floor thickness [11].
- During the quenching simulation, the influence of microstructure and phase changes on residual stress magnitude are not considered in the simulation. This has been defined by Denis et al. [220] stating that although important these effects have a smaller influence to the overall residual stresses.
- The post machining distortion would be used to validate the FE model in most of the finite element models. If the case study has been fully constrained and then released post machining, the residual stress redistributes at a higher magnitude to achieve equilibrium, therefore distorting more.
- The gravitational and inertial forces are neglected in this simulation due to the thickness of the final machined parts. A similar assumption was made by Cerutti [11].

5.1.3 Numerically prediction of residual stress during heat treatment process

The first area of development consisted of quenching and heat-transfer modelling of aluminium Alloy 7050 (AA7050) block. Successful modelling enables to capture the correct transient time and temperature data during the rapid cooling process during water quenching.

This transient process provides the non-uniform thermal loading that imparts the quench residual stresses into the work piece. The aim was also to simulate large residual stresses. These large stresses are beneficial in validation of finite element models as once the blocks are machined, the bulk stresses would redistribute hence distorting the part with a large magnitude which are higher than errors from measurement equipments.

5.1.3.1 Modeling and Simulation of Reference Case

The conceptual step was development of the modeling methods necessary to accurately model residual stresses induced by quenching. This consisted of modeling studies to verify the numerical solution for proper convergence. Secondly, it consisted of validation against experimental measurements using a literature reference from Koc et al. [28] to demonstrate that the verified solution was accurate in addition to being converged. The block dimension used for this validation was 124 mm x 127 mm x 340 mm as shown in Figure 5-10. In addition to this, the material properties (Elastic Modulus, yield stress-strain, density, thermal expansion, Poisons ratio from room temperature and different temperatures) used in the simulation from Koc et al. [28] was used as an input.

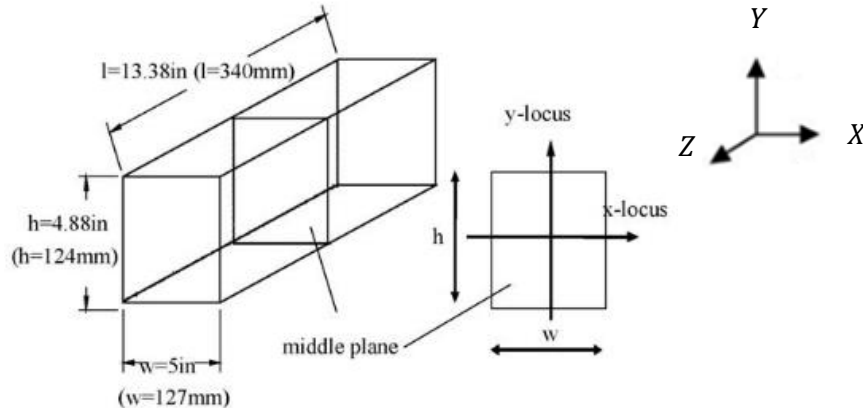


Figure 5-10: Literature Block Configuration [28].

As an initial model verification, the residual stress simulation was checked to see if it satisfies the traction-free boundary conditions in Equation 5-24 where n_j denotes the surface normal. From Figure 5-11, it can be seen that the X , Y and Z stresses normal to the corresponding surfaces are zero or close to zero.

$$\sigma_{ij} \cdot n_j = 0$$

Equation 5-24: Traction free boundary conditions.

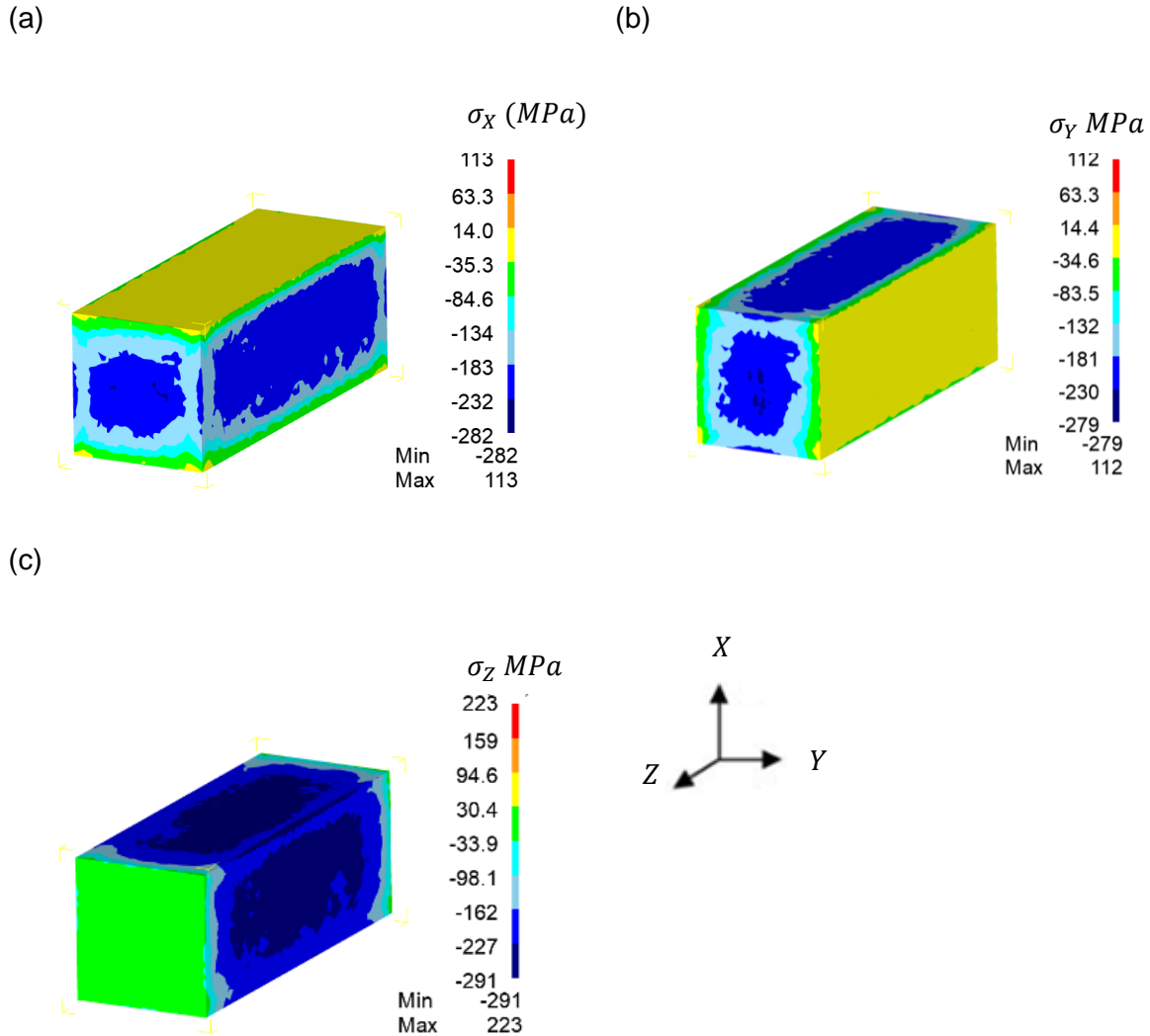


Figure 5-11: Traction free boundary conditions in: (a) σ_{xx} , (b) σ_{yy} , (c) σ_{zz}

To verify convergence, it is first necessary to demonstrate that the numerical solution is not affected by the mesh. To achieve this, this solution was run using a progressive refinement of the mesh until the numerical solution remains constant between two successive refinements.

As can be seen in Figure 5-12, this numerical convergence due to mesh density was seen at a 75000 element mesh, as the answer remained similar for the 100000 element mesh. The stress distributions obtained from the experimental measurements are not exactly symmetric.

Chapter 5: Finite element modelling methodology

The reason for the non-symmetry in the Neutron diffraction data from Koc et al could be due to three causes:

- The block was not entirely stress-free before it was heated
- There might have been deviations during measurements
- A non-uniform and non-symmetric quenching process might be caused by slow immersion into the quenchant

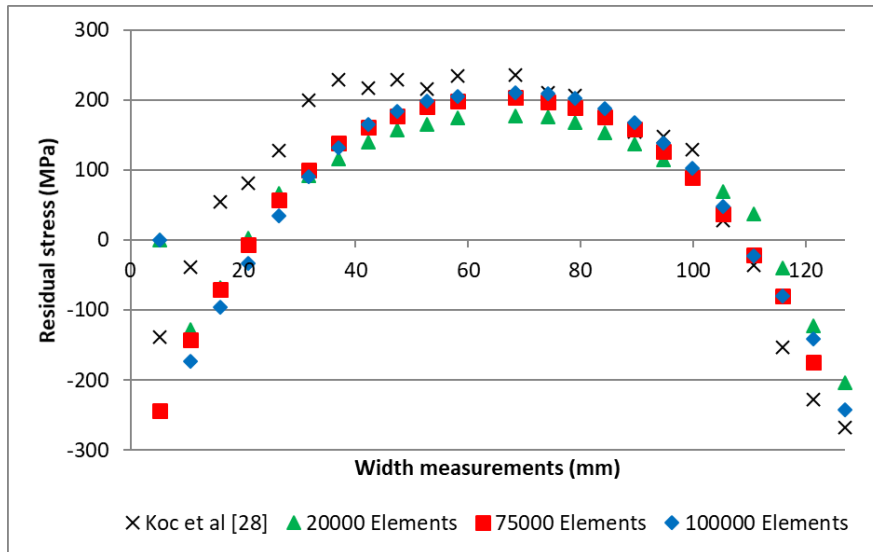


Figure 5-12: Sensitivity analysis of mesh elements on residual stress prediction in σ_{zz} .

Having established the necessary mesh refinement, the next step was to identify the numerically stable solution parameters. The first is the maximum temperature change per solution step. The maximum temperature change increment limits the amount that the temperature of any node can change during one time step. In Figure 5-13 the sensitivity of temperature change per step is analyzed for 5, 10, and 15 degrees/step. Despite the longer solution times, 5 degrees was chosen as the preferred step due to the nature of the transient problem and the sensitivity study.

Chapter 5: Finite element modelling methodology

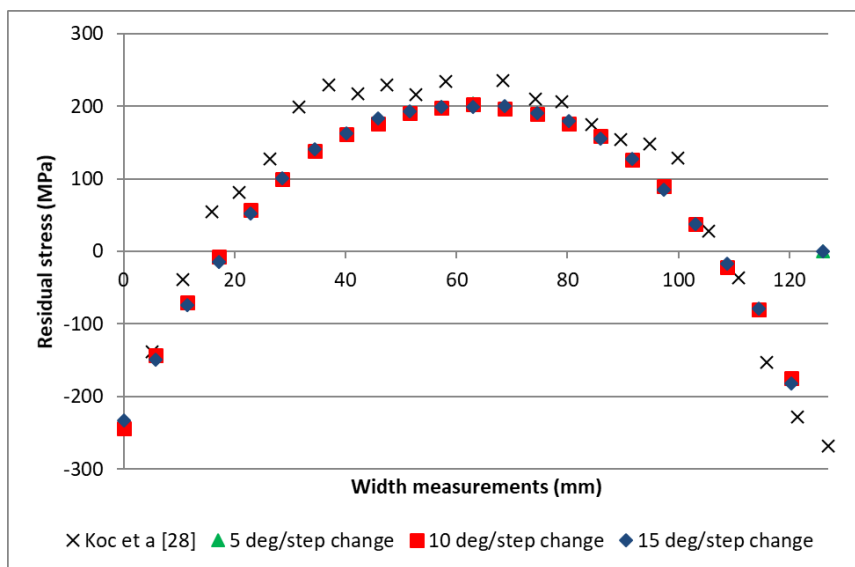


Figure 5-13: Sensitivity analysis of Temperature change per step on residual stress in σ_{YY} .

The alternative solution parameter is to identify a maximum number of seconds per step change in the iterative solver. The user defines the time step and smaller time steps are often employed to assist the code in finding a convergent solution. In a quenching problem, the larger the time step, the larger the thermal gradient across an element. A greater thermal gradient will result in an increased elastic strain across the element, which may lead to local yielding and the development of larger residual stresses. In Figure 5-14 below, it can be seen that varying the time per step change had a strong impact on the repeatability of the solution and it was determined that that temperature iteration method was better suited for the problem.

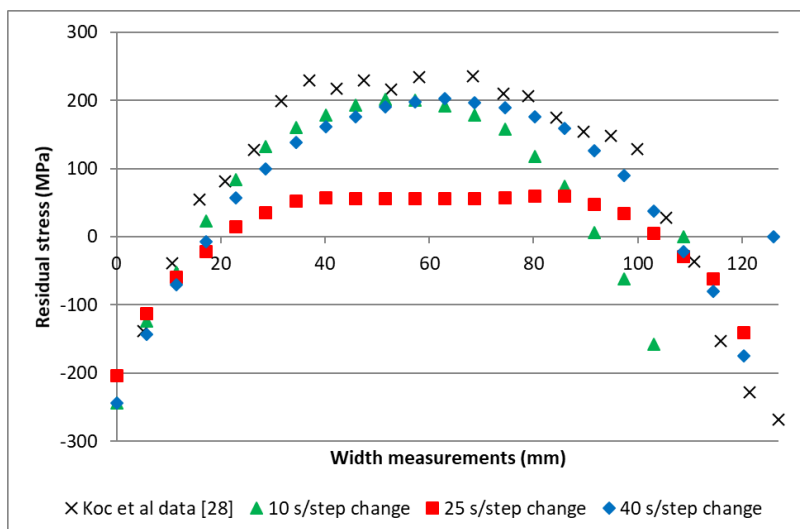


Figure 5-14: Sensitivity analysis of Time change per step on residual stress in σ_{YY} .

Chapter 5: Finite element modelling methodology

Having verified the proper mesh and iteration technique to ensure a converged numerical solution, the next step was to assess the sensitivity of the problem to the key inputs. For the quenching problem, the key driver is the heat transfer coefficient (Figure 5-15). Using the heat transfer coefficients generated in [28] as a reference, they were scaled either double or halved. As can be seen, in Figure 5-15 below, varying the heat transfer coefficient +/-50% produces different residual stresses, but they are still within a reasonable range.

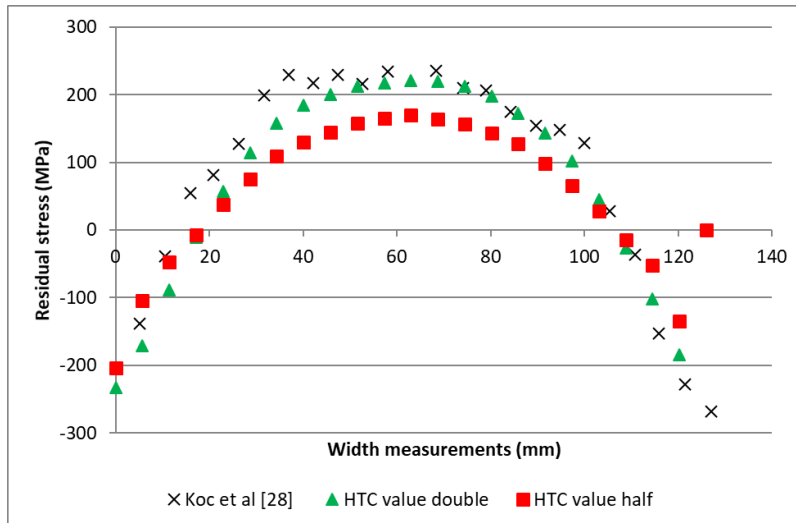
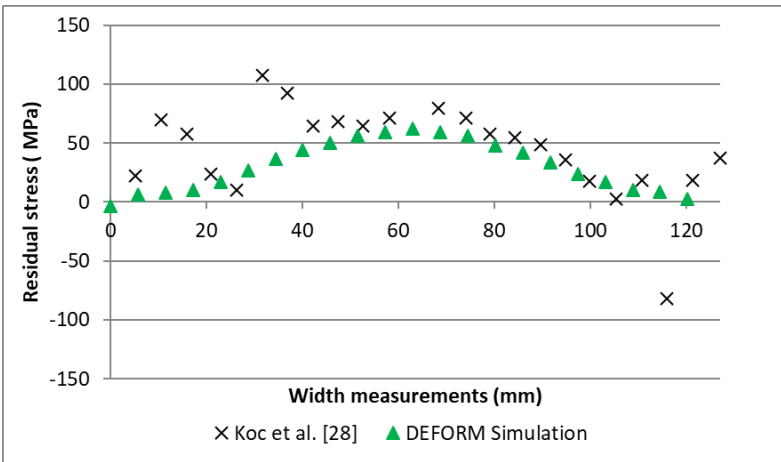


Figure 5-15: Sensitivity analysis for convection coefficient on residual stress in σ_{YY} .

Finally, having verified the numerical solution, the parameters were applied to model the literature reference block from Koc et al. [28].

Comparison stress line plots are provided in Figure 5-16 and Figure 5-17 respectively for the X, Y and Z directions. The Z and Y directions correlate well indicating consistency with the reference. In the X direction, the correlation is not as good; however, where they deviate is where the reference stress solution diverges from what is statically possible indicating an error in the reference. This can be inferred because by static equilibrium, the tensile and compressive stresses should be symmetric and the reference condition is not.

(a)



(b)

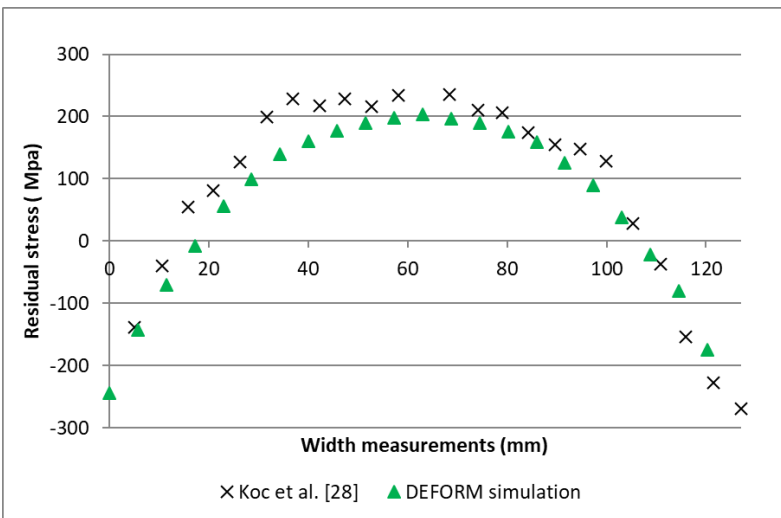


Figure 5-16: RS simulation using Koc et al stress in; (a) σ_{XX} and (b) σ_{YY} stress component.

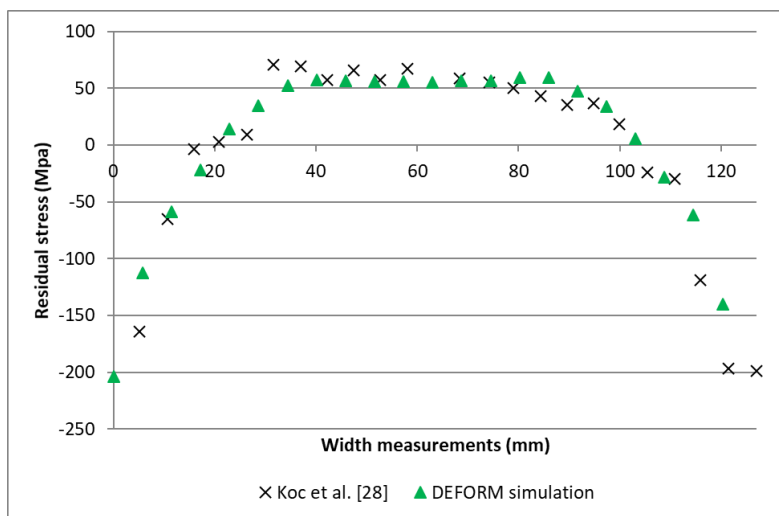


Figure 5-17: RS simulation using Koc et al Stress in the σ_{ZZ} .

5.1.3.2 Heat transfer calculation

Following verification and validation of the model, the next step was to perform a virtual simulation study on the proposed experiment to allow proper design of the experiment. To simulate accurately both the thermal history and the residual stresses in the quenching process, thermal expansion, and elastic modulus of the actual material data in section 6.1 and 6.2. The flow stress properties used for this simulation is shown in Figure 6-8 and Figure 6-9.

The primary objective of these simulations was to determine the theoretical cooling rates at potential thermocouple locations. From these cooling curves, the thermocouple locations were chosen so that there was a measureable difference between adjoining thermocouples and appropriate numbers and spacing of thermocouples were chosen. The first step was to determine the size of the test part. For this experiment being performed at the University of Sheffield's materials department, the limiting factors were furnace size, quench tank size, and the mass of the specimen, since it needed to be manipulated by hand. An aluminium block size was chosen of the dimensions 50 mm x 100 mm x 250 mm as shown below in Figure 5-18. The dimensions were selected to provide the opportunity for variations due to the geometry. Aluminium 7050 hand forgings in the "as forged" condition were sourced for the experiment.

Chapter 5: Finite element modelling methodology

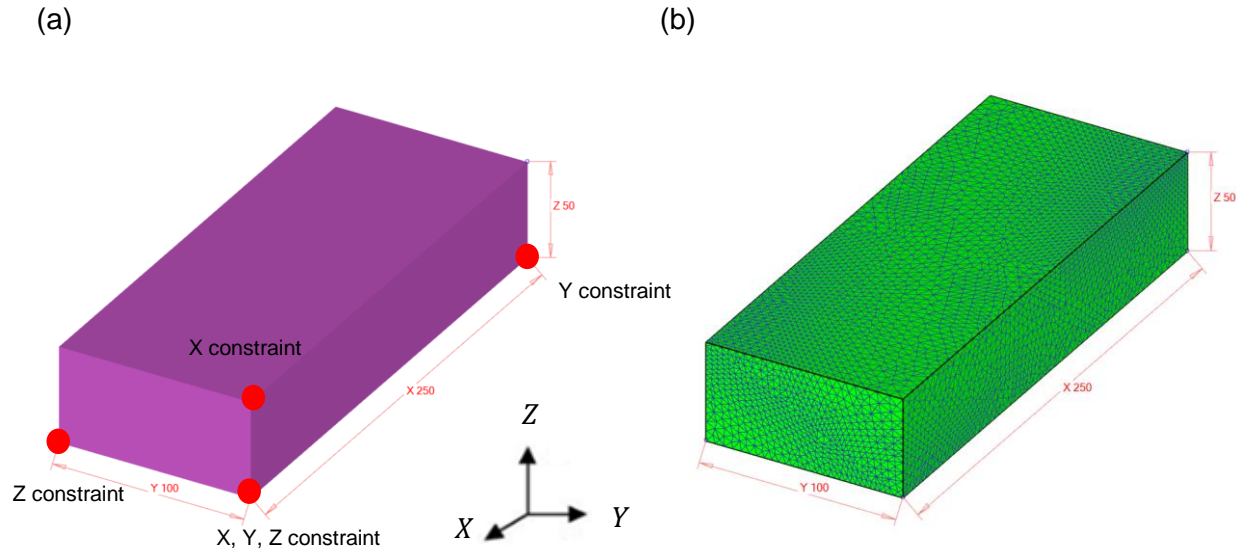


Figure 5-18: Test Block Selected for Experiments: (a) Block geometry, (b) Heat transfer boundary conditions.

To enable selection of thermocouple locations, first the sensitivity of the cooling curves to a constant initial heat transfer coefficient was assessed. This provided a family of cooling curves based on location and heat transfer coefficient. The results, shown in Figure 5-20, were stable and consistent allowing points to be assessed in the next step.

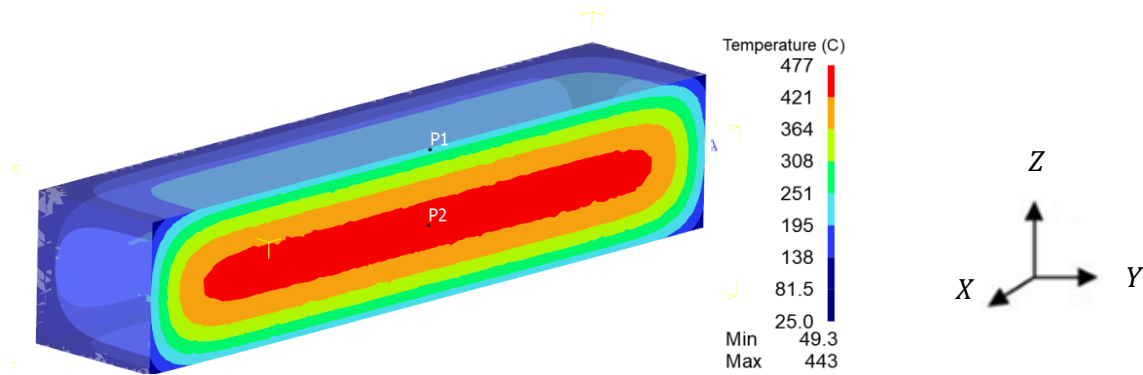
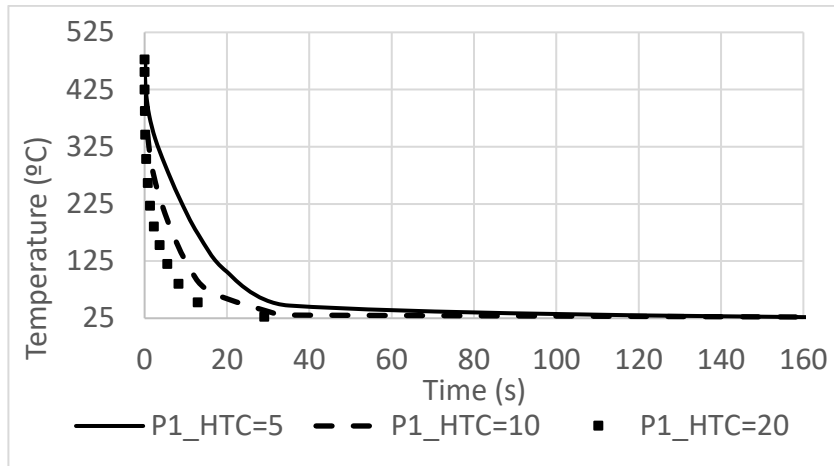


Figure 5-19: Cooling Rates Sensitivity to Heat Transfer Coefficient point locations (P1, P2).

(a)



(b)

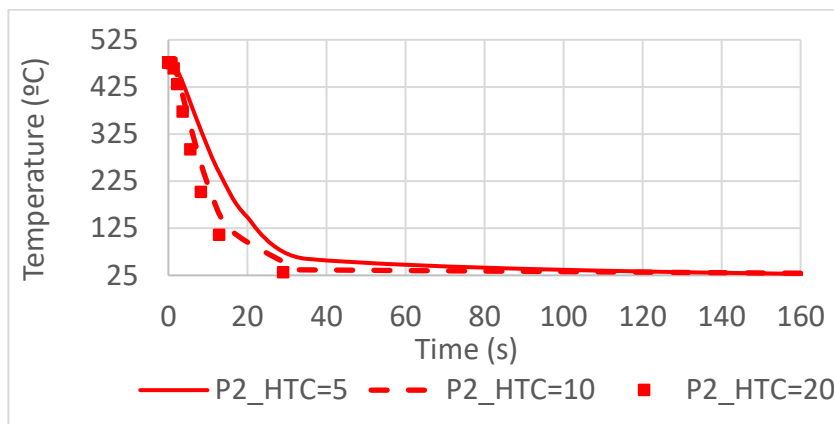


Figure 5-20: Cooling Rates Sensitivity to Heat Transfer Coefficient: (a) Surface region (P1), (b) Core region (P2).

Points were extracted from the cooling simulation of proposed thermocouple locations (Figure 5-21). Families of location specific curves were then generated and from these points the non-linear spacing in the locations necessary to provide an even solution space was found.

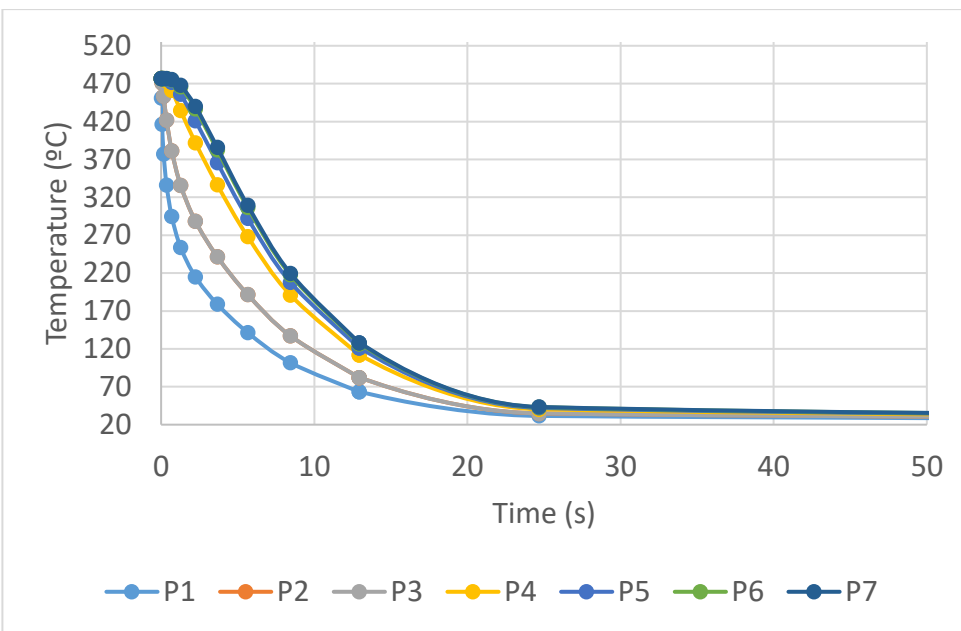
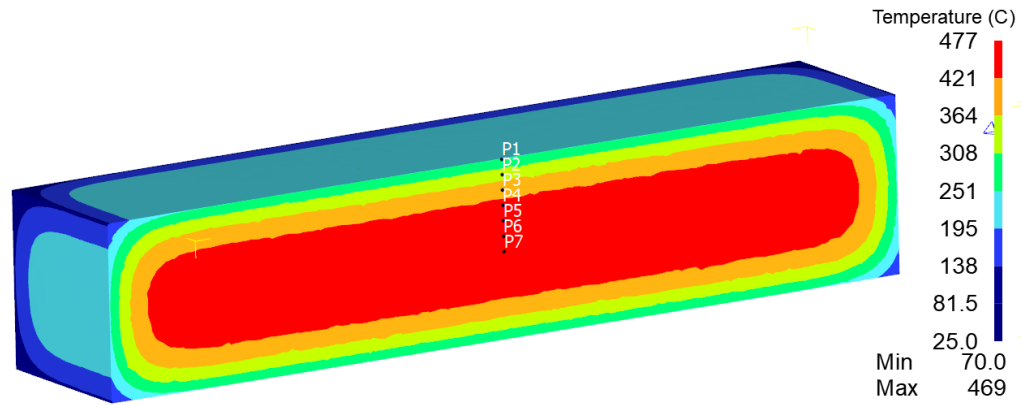


Figure 5-21: Virtual Cooling Experiment to Select Thermocouple Locations.

Upon quenching, the part cooled rapidly and the temperature was captured by the thermocouples. This test was repeated four times on different quench blocks of the same dimensions and average value from these four measurements is shown in Figure 5-22. The locations of these points are shown in Figure 6-12.

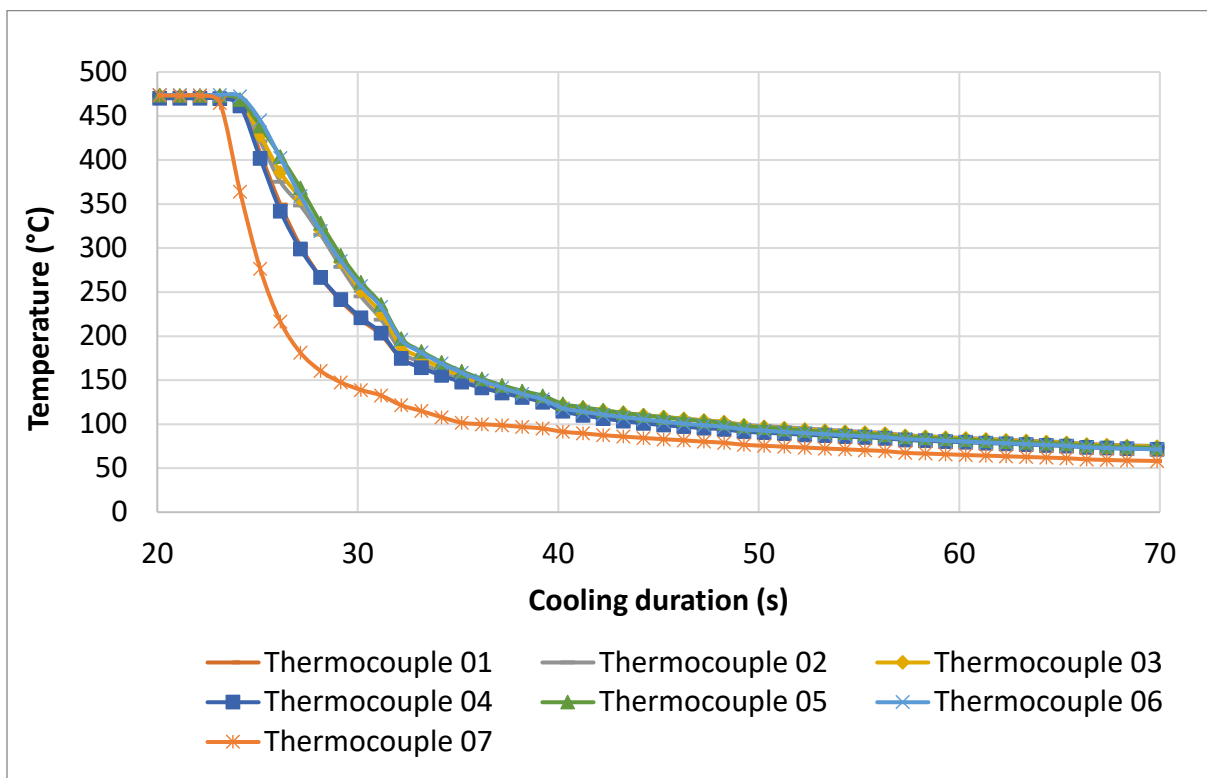


Figure 5-22: Experimental quench tests thermocouple data.

Upon capture of the cooling curves, these temperature measurements must be used to estimate the convection heat transfer coefficient on each surface as a function of temperature. This is an inverse problem which is solved by iterating heat transfer coefficients on the surfaces using experimental cooling rate data and comparing them with predicted cooling rates until they are matched. DEFORM provides a sub-routine to perform this inverse analysis. DEFORM begins by initially simulating a quench process using an estimated heat transfer coefficients. DEFORM then runs using an optimization algorithm (Equation 5-25 and Equation 5-26 [261]) which would then compare the simulated thermal results with the experimental thermal results and would modify the heat transfer coefficients until an acceptable agreement is attained. In addition to this, DEFORM can run the Broyden–Fletcher–Goldfarb–Shanno algorithm (BFGS) and further information can be found in the DEFORM system manual [196].

Chapter 5: Finite element modelling methodology

The inverse heat transfer coefficient procedure is defined as follows (Figure 5-23) as defined by [261].

- Start $k=0$,
- Evaluate the objective function $f(P^{(k)})$, which is the difference between model's prediction and experimental temperature,
- Calculate the gradient of objective function $\nabla f(P^{(k)})$,
- Determine a search direction ($d^{(k)}$),
- Perform a one-dimensional search to reduce the objective function as much as possible to find α ,
- Check for convergence to the optimum. If satisfied, exit,
- Update the heat transfer coefficient, $P^{(k+1)} = P^{(k)} + \alpha d^{(k)}$,
- $k=k+1$, Go to step 2.

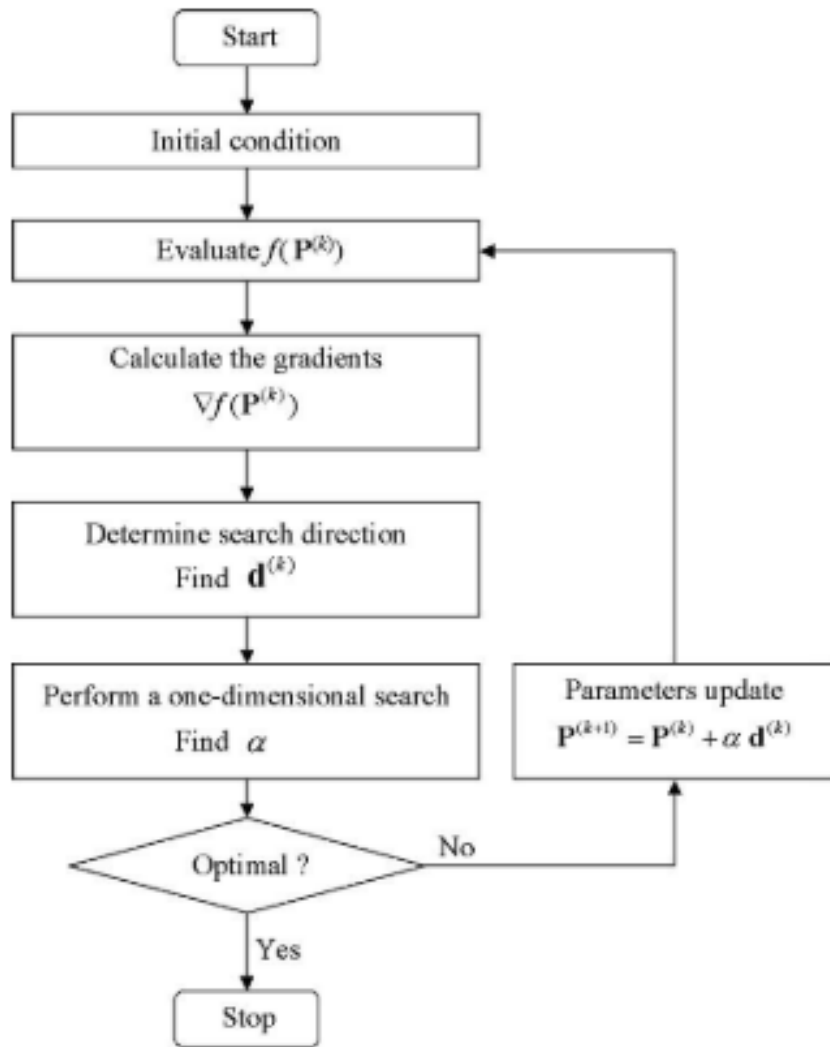


Figure 5-23: Overall inverse optimization process [261].

Figure 5-24 shows the measured temperature-time curve and predicted temperature-time curve at the thermocouple point. The objective function $f(P)$, which will be minimized during inverse optimization process, and its gradient are defined as follows where T_{exp} is the measured temperature, T_{fem} is predicted temperature, N_{data} is the total number of sampling points, and the P is the heat transfer coefficient. The derivative of nodal temperature and the FEM ($\frac{\partial T_{FEM}}{\partial p}$) will be calculated during the DEFORM simulation.

$$f(P) = \frac{1}{N_{data}} \sum (T_{exp} - T_{FEM})^2$$

Equation 5-25: Evaluation of the objective function.

Chapter 5: Finite element modelling methodology

$$\nabla f(P) = -\frac{1}{N_{data}} 2 \sum (T_{exp} - T_{FEM}) \frac{\partial T_{FEM}}{\partial p}$$

Equation 5-26: Evaluation of the objective function with respect to nodal temperature and FEM.

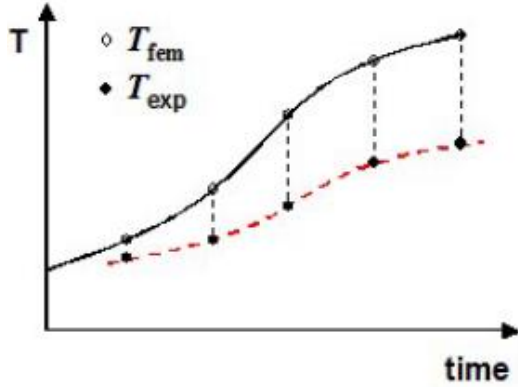
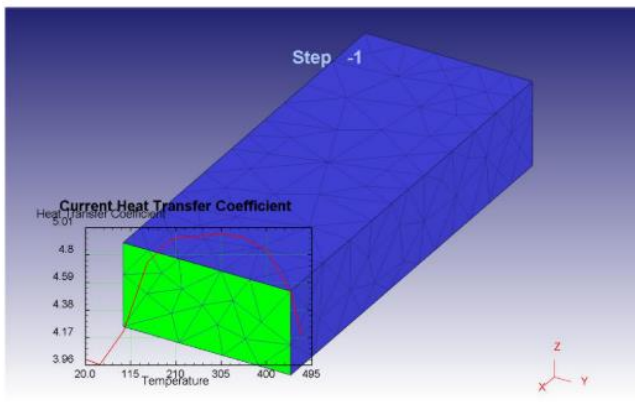


Figure 5-24: Comparison between experimental thermal data and FEM [261].

Applying this technique for the block, the heat transfer coefficient solutions for face 1 - 6 of the block as an example are shown in Figure 5-25 and Figure 5-26. From these figures, it is clear that the heat transfer coefficient varies with each face of the block as highlighted in literature. This variation is due to the cooling rate variation of each block face. The average heat transfer coefficients is shown in Figure 5-27. The profile is similar to the block references by Koc et al. [28].

(a)



(b)

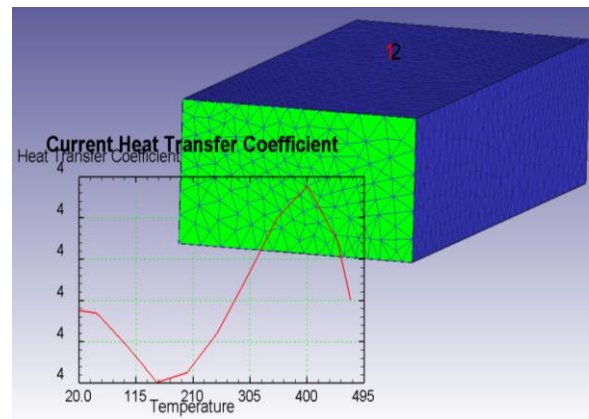
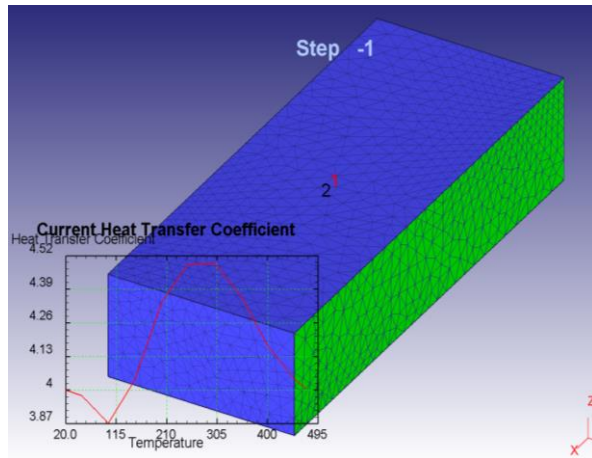


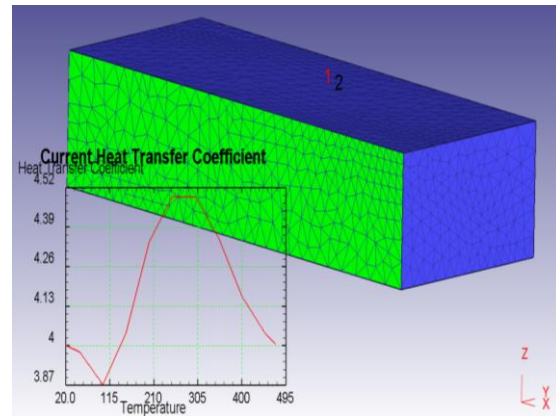
Figure 5-25: Heat transfer coefficient for: (a) Face 1, (b) Face 2.

Chapter 5: Finite element modelling methodology

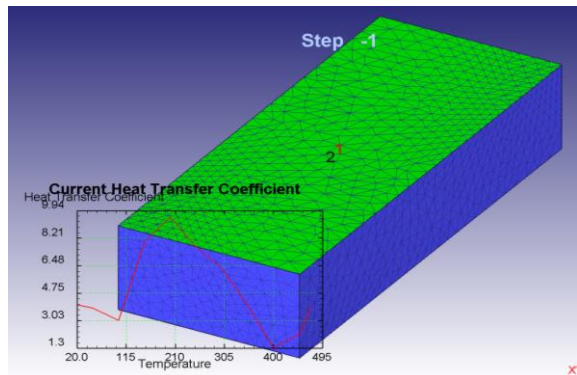
(a)



(b)



(c)



(d)

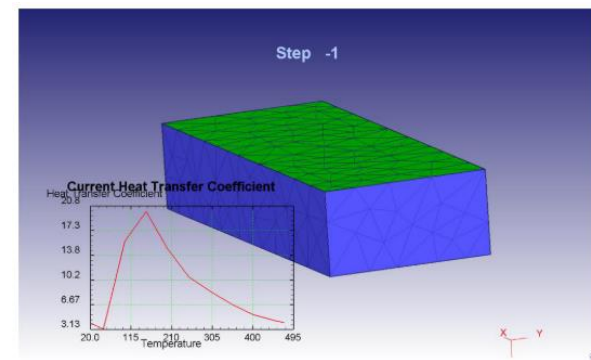


Figure 5-26: Heat transfer coefficient for: (a) Face 3, (b) Face 4, (c) Face 5, (d) Face 6.

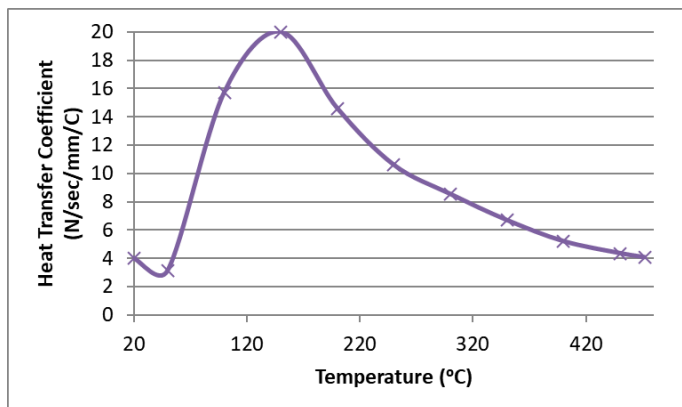
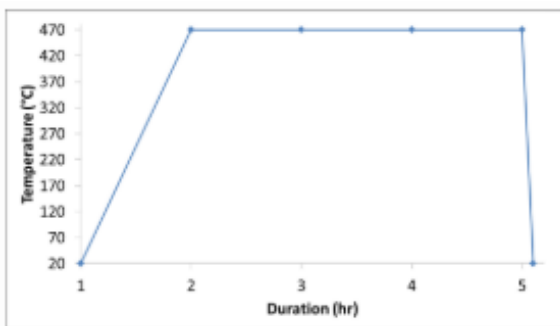


Figure 5-27: HTC values at different temperatures for the rectangular coupon.

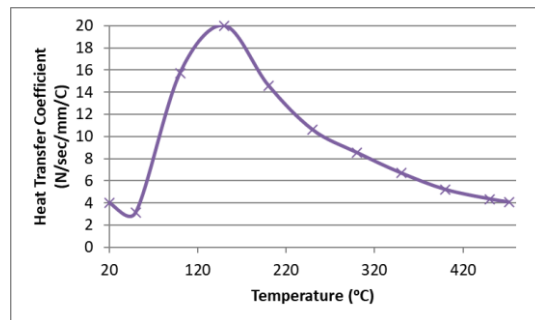
5.1.3.3 Heat treatment simulation for rectangular coupons.

For the heat treatment model, an elastic-plastic, Newton-Raphson iteration, Lagrangian incremental model was simulated. The solver used for the temperature measurements was conjugate gradient. Using the heat treatment temperatures and durations from the AMS standard [262], the heating up of the coupon was simulated from room temperature to solution temperature (477 °C) over a period of 3 hours, and the quench process was modelled using a convection coefficient and material data generated previously as shown in Figure 5-28 (a). The convection coefficient was applied on all surfaces for the generation of regular residual stress as per Figure 5-28 (b).

(a)



(b)



(c)

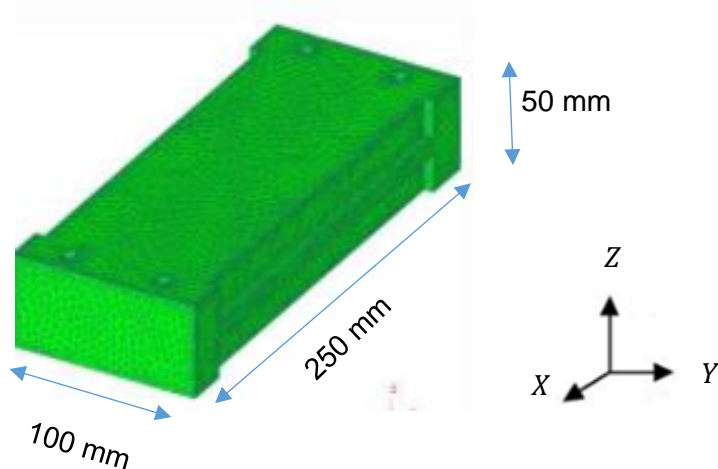


Figure 5-28: Heat treatment process: a) Heat treatment process diagram, b) Heat transfer coefficient, (c) Application of convection coefficient (shaded) on all surfaces.

Chapter 5: Finite element modelling methodology

The FE model parameters of the heat treatment are provided in Table 5-1.

Table 5-1: Heat treatment FE model input parameters.

Parameter	Value
Object	Elastic-Plastic
Material	Aluminium 7050
Tetrahedral Mesh	75000 elements
Temperature change per step	25 °C/ Step
Environment temperature	20 °C
Solution temperature	477 °C
Heat transfer coefficient	Figure 5-28 (b)

In order to constrain the simulation without influencing the prediction result, a free distortion boundary condition was applied (Figure 5-29). The procedure for applying free distortion boundary condition [196] [35] to prevent translation, one node was fixed in X, Y, Z direction to remove the three-degree of freedom in translation. In order to prevent rotation, the following procedure is followed:

- To prevent rotation in X direction, a node is picked which is at the similar X and Z position but different Y is fixed in the Z direction.
- To prevent rotation in the Y direction, a node is picked which is at the similar Y and X position but different Z is fixed in the X direction.
- To prevent rotation in the Z direction, a node is picked which is in a similar Z and Y position but different X is fixed in the Y direction.

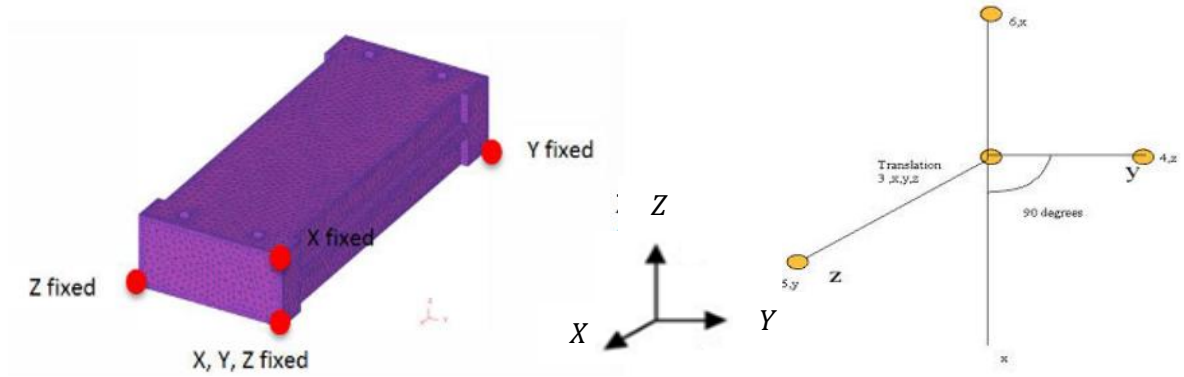


Figure 5-29: Rigid body motion nodal constraints during quenching, (b) Fixing of nodes in X, Y and Z direction.

The residual stress prediction contour in the X-axis is shown in Figure 5-30. From the prediction, the prediction matches with what is presented in literature [263]. In addition to this, the simulation as also compared with two experimental bulk residual stress measurements techniques to validate the model.

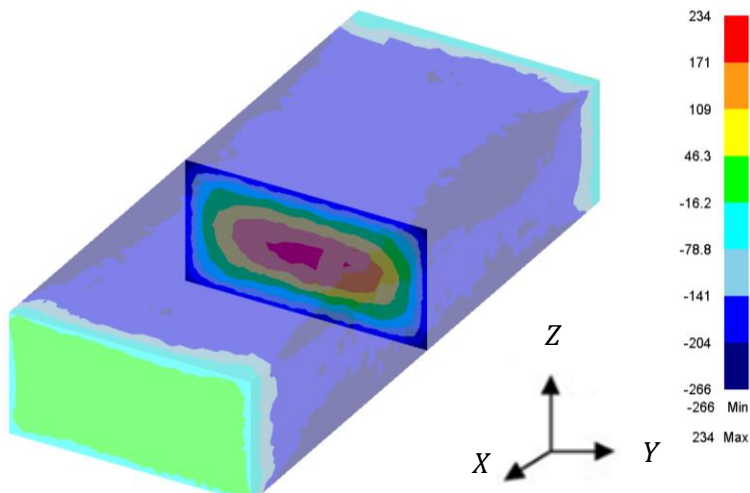


Figure 5-30: Residual stress contour for the rectangular coupon.

5.1.3.4 Heat treatment simulation for symmetrical and asymmetrical (S&A) residual stress

This research aimed to understand the effects of symmetric and asymmetric residual stress (RS) profiles, and residual stress redistribution during the machining cycle and fixture release.

Three different heat transfer coefficients: Low, Medium and High (Figure 5-31) were created to simulate three possible residual stress profiles to capture any bulk stress variations in the coupons which are normally experienced in industry. The medium HTC was generated by using experimental thermal measurements in the section 5.1.3.2 and using an inverse formulation to generate the appropriate HTC for this material. The low and high HTC profiles were generated by applying a scale factor of 3.2 and 1.6 respectively to generate residual stress profiles within a range of experimental stress profiles found in literature [128]. The heat treatment procedure is shown in Figure 5-32.

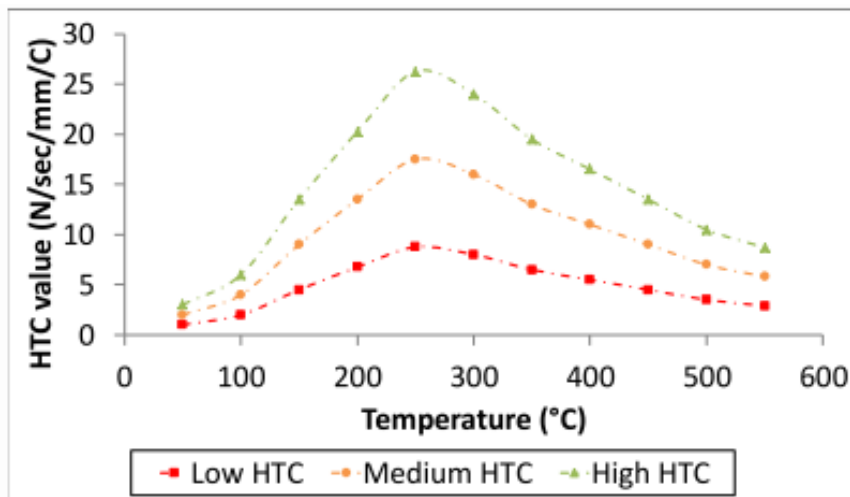


Figure 5-31: Heat transfer coefficient profiles used during the quenching simulation.

The heating up, quenching and boundary conditions for these simulations was similar with the boundary conditions similar to Figure 5-29. The results of the symmetrical residual stress simulation for the heat treatment of this coupon was similar to Figure 5-30. For the heat treatment simulation to generate an asymmetric stress profile, an inter-object relationship was set up for the two workpieces joined (Figure 5-33).

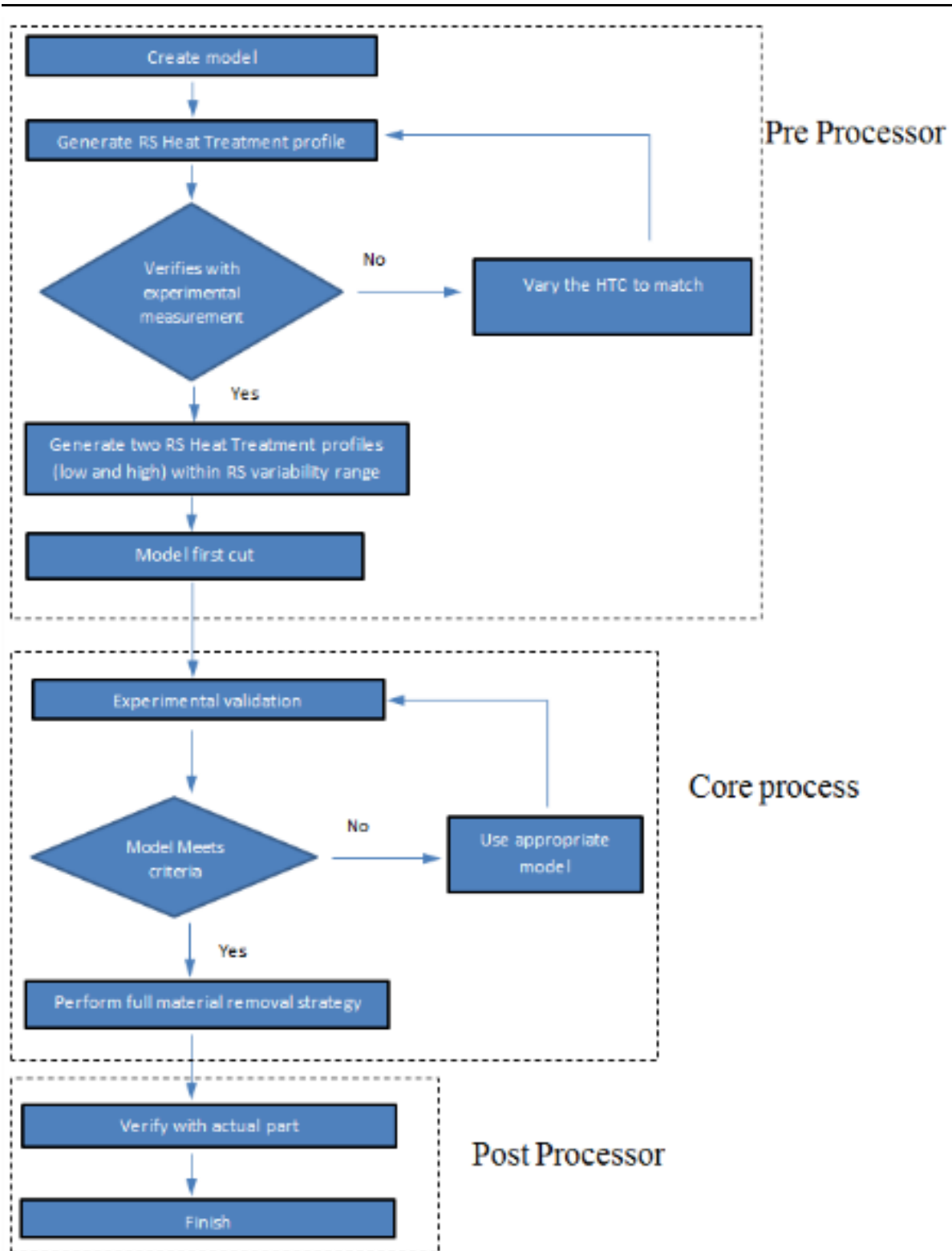


Figure 5-32: FEA process route.

Chapter 5: Finite element modelling methodology

In order to generate an asymmetric residual stress profile, the heat convection coefficients were applied on the external faces of both parts except where the two coupons are in contact with each other. From Figure 5-33 (b), it can be seen that the temperature distribution is stabilized for both blocks; although Figure 5-33 (c) illustrates that, the residual stress profile is varying, accomplishing the target of the simulation. The HTC used was generated by recording the temperature within the coupon on the surface, the middle thickness and the bottom surface using thermocouples and converting this to the heat transfer coefficient using an inverse formulation within the FE software to generate the appropriate HTC for this material.

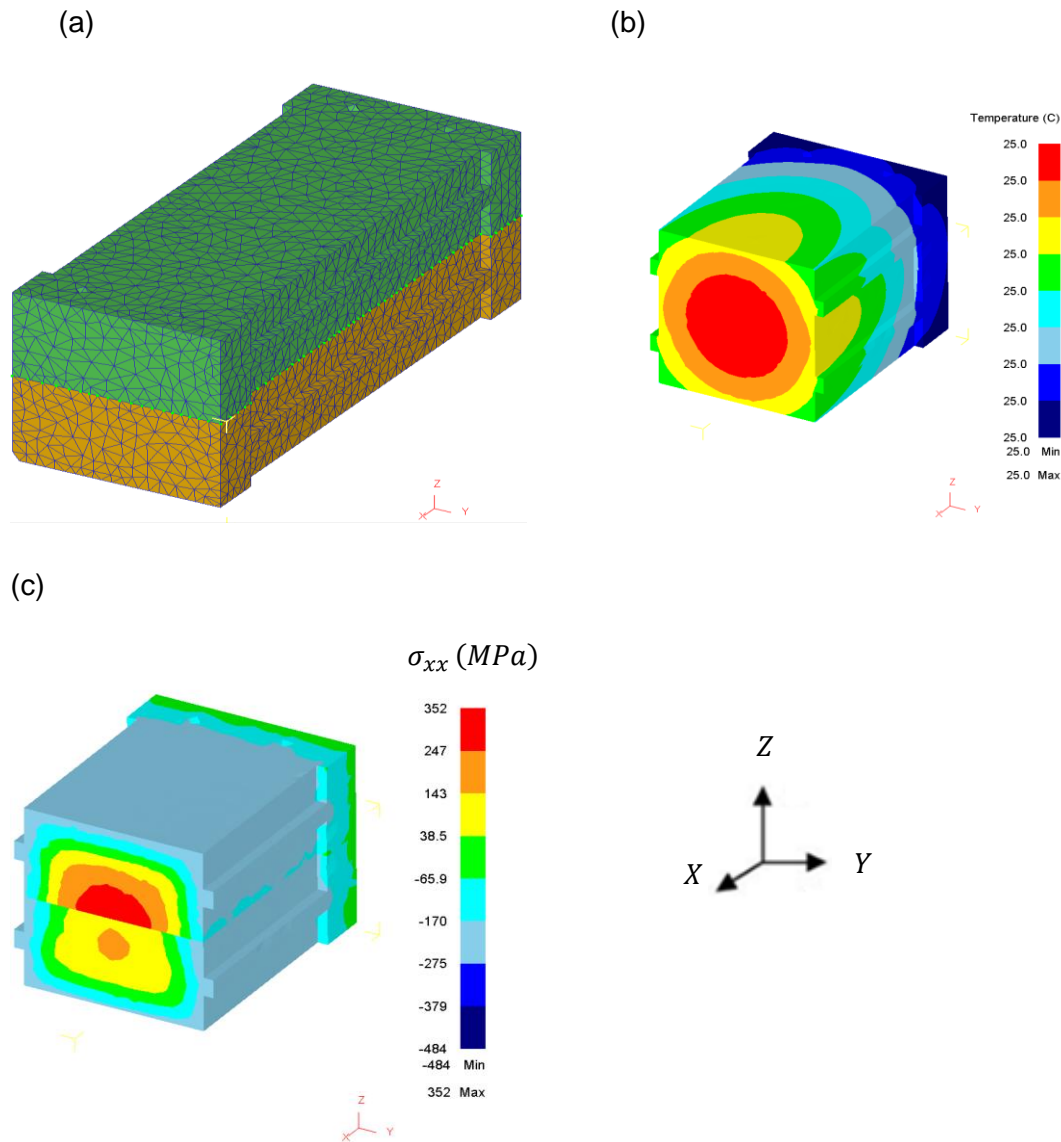


Figure 5-33: Asymmetric FE model: (a) Inter-object relationship to join the two workpieces, (b) Temperature prediction, (c) Longitudinal Stress Prediction.

5.1.3.5 Heat treatment simulation for the rectangular pocket geometry

Unlike the other two previous simulation trials, the rectangular pocket geometry was machined off from a large rectangular aluminium 7050 slab as shown in Figure 5-35 (a) with dimensions of 3660 mm (length) X 1250 mm (width) X 76.2 mm (height). In order to understand the residual stresses on the parent material, a simulation was run following the actual heat treatment process. Once the simulation had concluded, the residual stresses from the slab were interpolated at geometries at each of the positions defined in Figure 5-34. A similar strategy has been proposed by Cerutti [11] and Ma [45]. This task was to understand the variation of residual stresses depending on the location of where the target part is machined. The simulation result from the residual stress interpolation is shown in Figure 5-35.

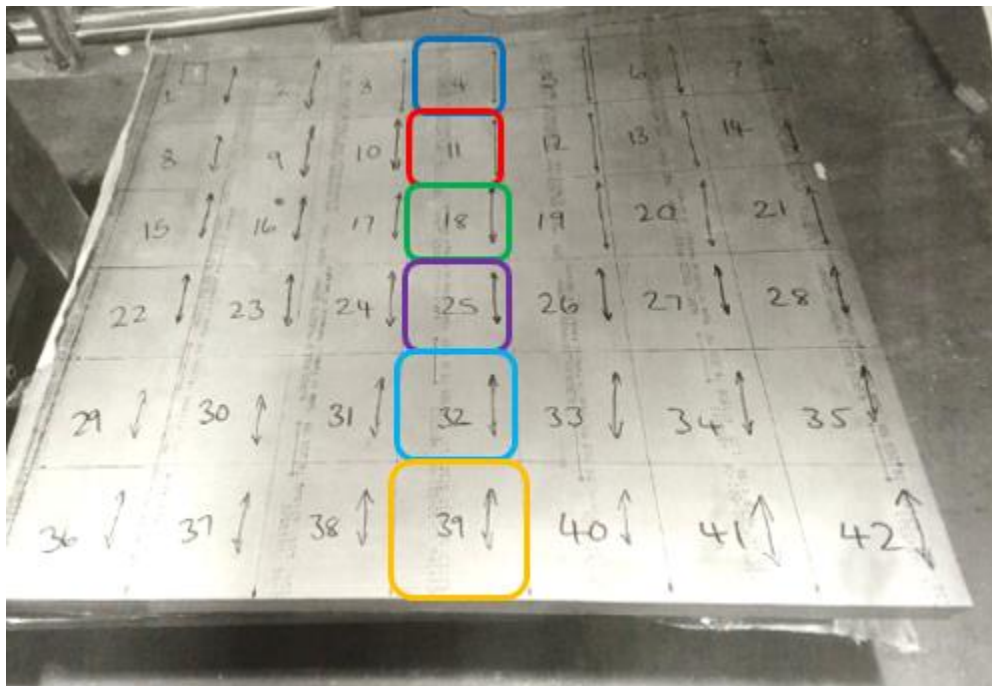


Figure 5-34: Heat treatment on aluminium 7050 slab.

From the simulation, it was found that there was a variation of the heat treatment residual stress across each region. The residual stresses also were low, therefore to understand the effect of different machining strategies on distortion would not be large.

Chapter 5: Finite element modelling methodology

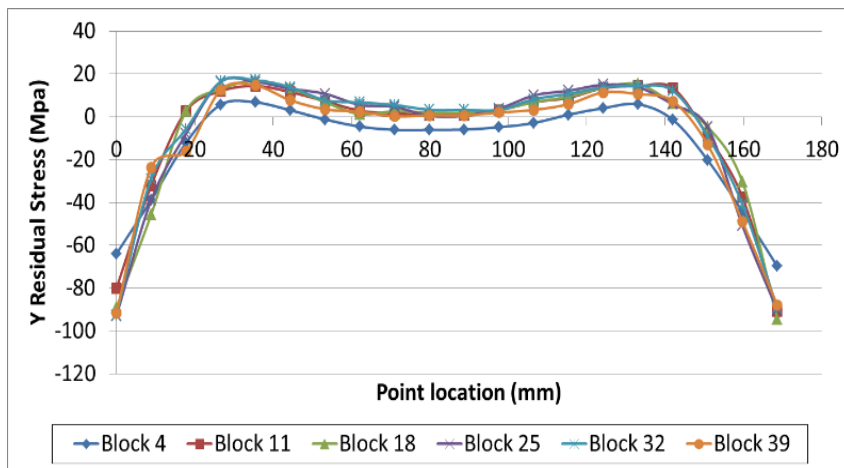


Figure 5-35: Heat treatment longitudinal residual stress prediction.

Therefore, to create a similar residual stress profile for each of the blocks, the individual blocks (4, 11, 18, 25, 32, and 39) were re heat treated and quenched. Prior to this, the blocks were machined to create the ridges on the sides of the block where the clamps will be applied during machining as shown in Figure 5-36 and Figure 5-37. A quench simulation was then generated. The boundary conditions for the quench FE model is shown in Figure 5-37 (a). The simulation input used is defined in Table 5-1. In addition to this, the simulation as also compared with bulk residual stress measurements techniques from two sources to validate the model as described in section 6.4.

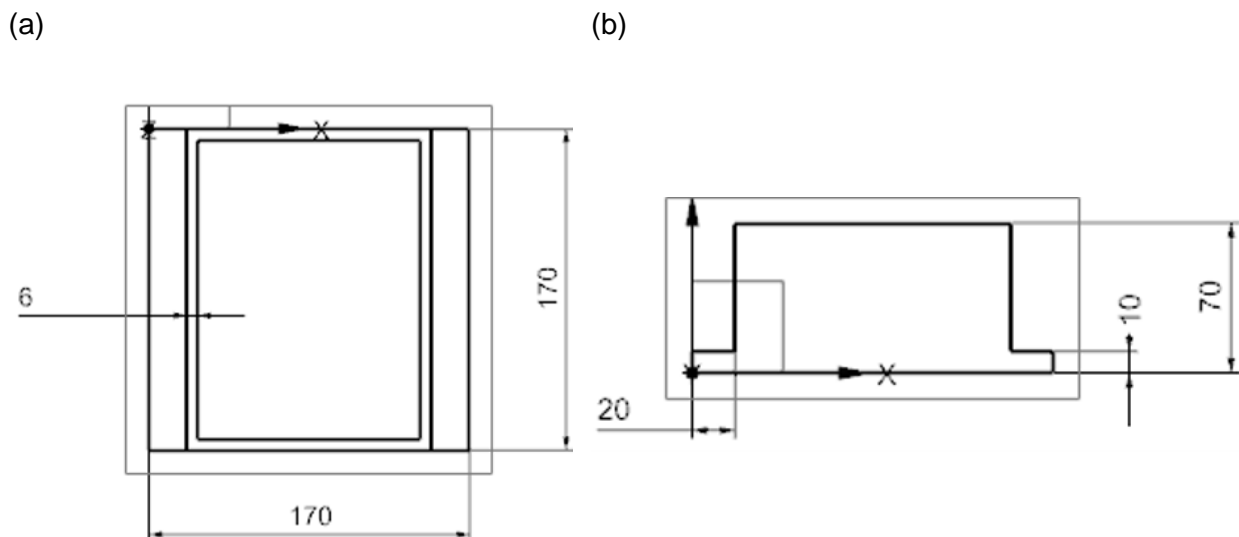


Figure 5-36: (a) Rectangular pocket geometry dimensions top view, (b) Rectangular pocket geometry dimensions top view.

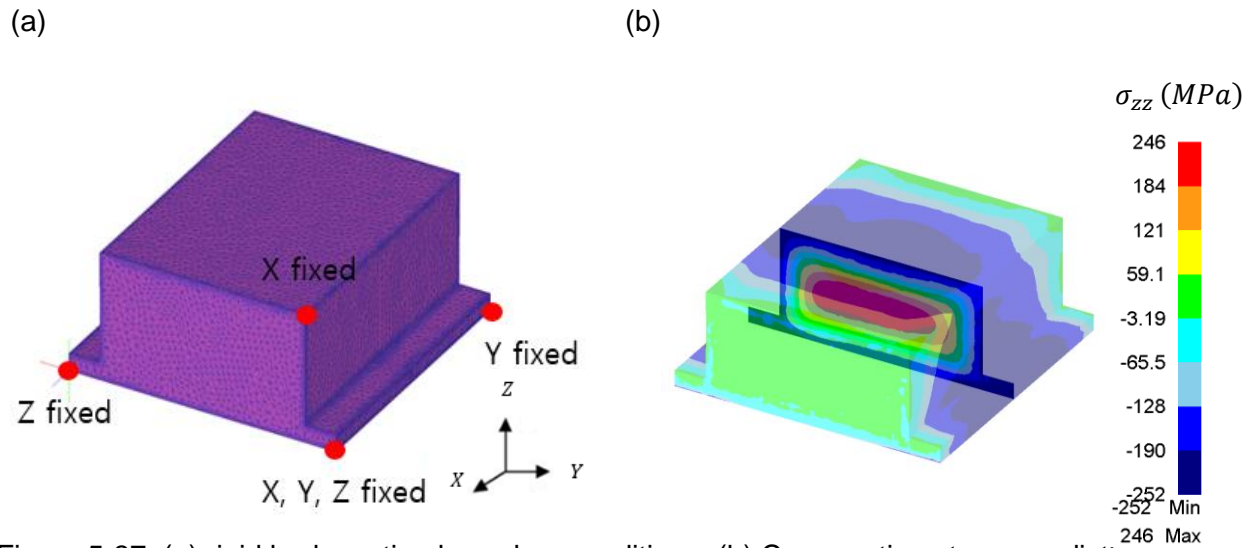


Figure 5-37: (a) rigid body motion boundary conditions, (b) Core section stress prediction.

5.1.3.6 Heat treatment simulation of the representative part

Due to the large length dimension of the representative billet, a 2D FE plane strain model was simulated and was later extrapolated into 3D FE model; this was done to reduce the simulation time. The material data and the HTC used was as the previous simulations. The convection coefficient was applied on all surfaces for the generation of regular residual stress.

The heat treatment model constraint (single points) is shown in Figure 5-38. These constraints were chosen to help with the convergence of the simulation. The input parameters are shown in Table 5-2. The heating up of the coupon was simulated following the T74 process defined in

Table 5-3 and Figure 5-39.

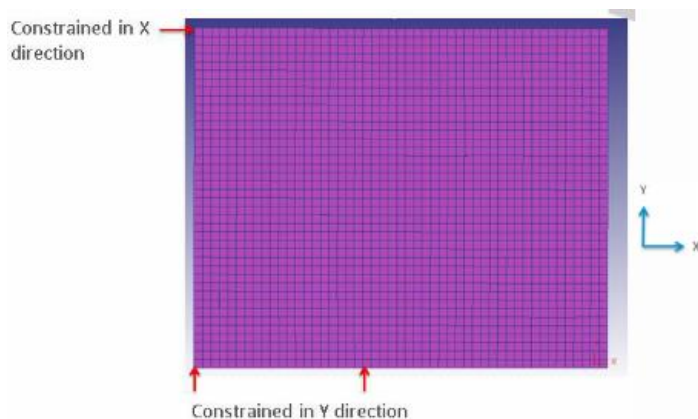


Figure 5-38: Boundary condition used for the model.

Chapter 5: Finite element modelling methodology

Table 5-2: 2D Heat treatment FE model input parameters.

Parameter	Value
Object	Elastic-Plastic
Mesh	Tetrahedral mesh – 8000 elements
Temperature change per step	25 °C/ Step
Environment temperature	20 °C
Heat treatment profile	T74 (Figure 5-39)
Heat transfer coefficient	Figure 5-28 (c)

Table 5-3: T74 process information.

Process name	Temperature (°C)	Holding duration (h)	Quenching medium	Quenching temperature (°C)
Solution heat treatment	477	7 ½	Water	63
Ageing (step 1)	121	6	Air	20
Ageing (step 2)	177	10	Air	20

The 2D FE model was extruded to a 3D model. A comparison was done between the stresses in the mid width line of the 2D FE model and the 3D FE model to ensure that the interpolation was comparable (Figure 5-41). The comparison shows a close match between the two models in both σ_{XX} (Figure 5-41 (a)) and the σ_{YY} orientations (Figure 5-41 (b)) giving confidence to commence with the pocket removal sequence modelling. In addition to this, the simulation as also compared with two experimental bulk residual stress measurements techniques to validate the model as described in section 6.4.

Chapter 5: Finite element modelling methodology

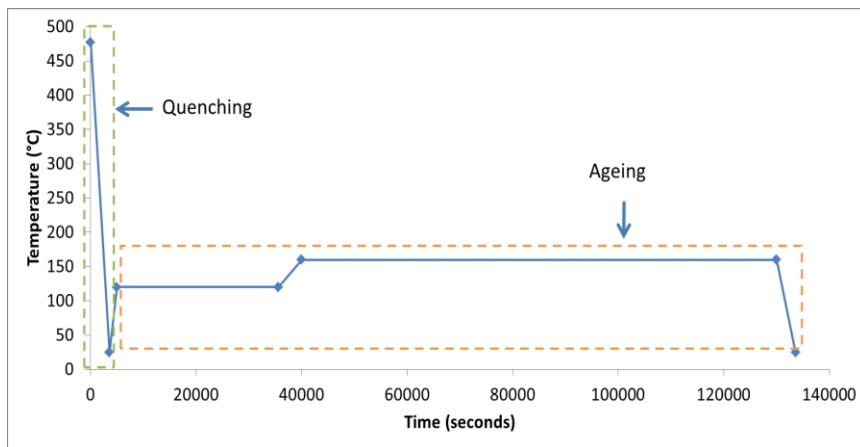


Figure 5-39: Graphic illustration of the T74 heat treatment condition.

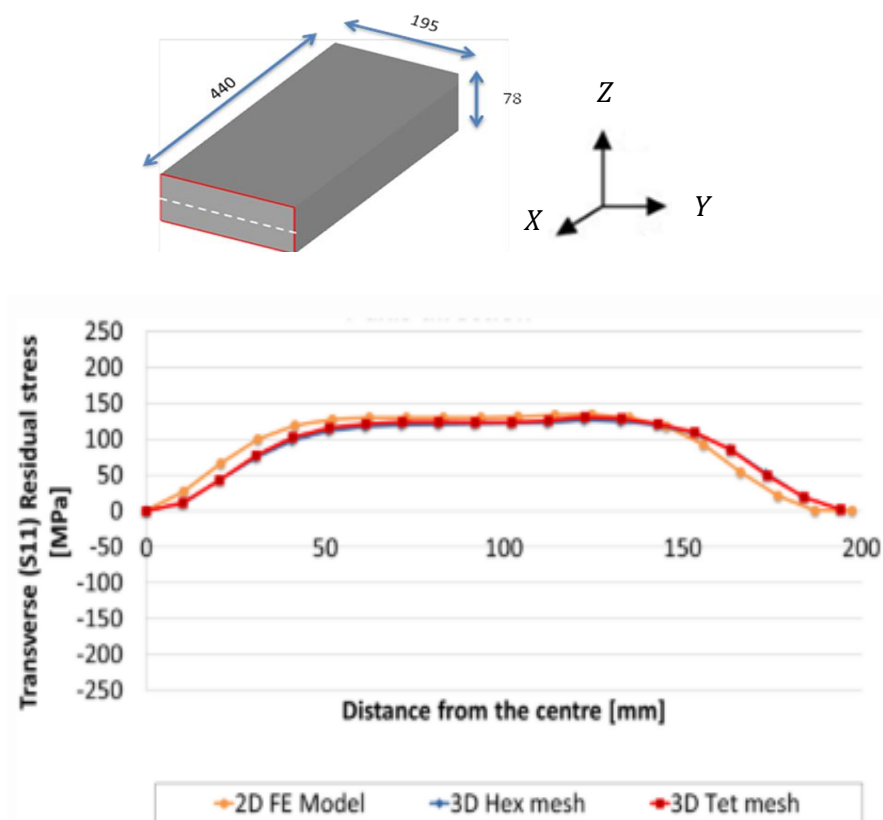


Figure 5-40: 2D to 3D FE model conversion to confirm successful data interpolation and mesh type sensitivity at the mid width line in the σ_{xx} direction.

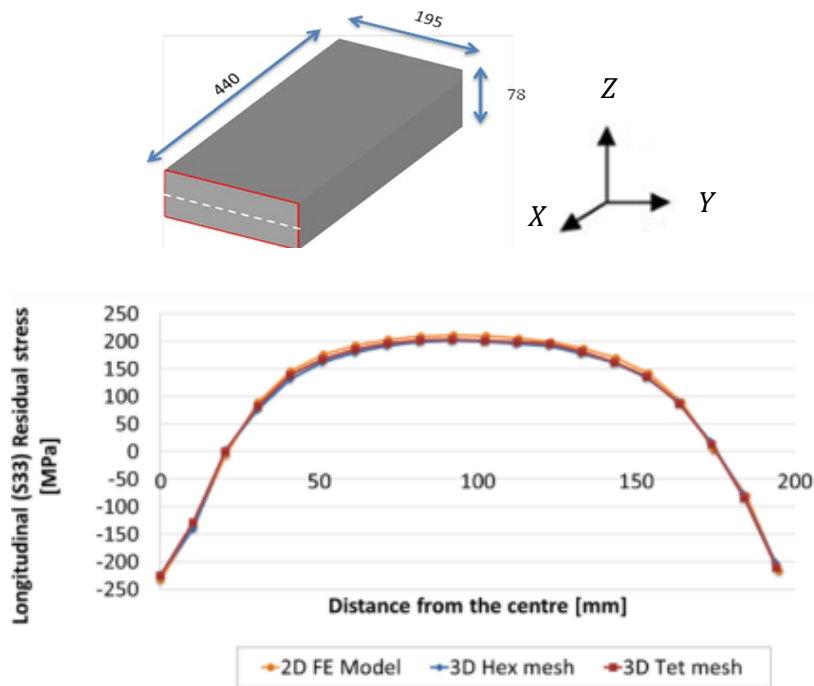


Figure 5-41: 2D to 3D FE model conversion to confirm successful data interpolation and mesh type sensitivity at the mid width line in the σ_{YY} directions.

5.1.4 Numerical simulation of the machining process

In order to verify DEFORM’s capability for machining distortion prediction due to residual stresses, an analytical (Equation 4-1) and numerical model previously validated by Shin [176] was used to validate the distortion prediction in DEFORM. The initial residual stresses, material properties and the boundary conditions were taken from Shin [176]. From the results shown in Figure 5-42, the curvature due to residual stress predicted by DEFORM is found suitable to carry out the machining distortion simulations. The results imply that when a surface layer containing compressive residual stress is removed, the remaining body distorts by developing a positive curvature (curling upward). Upon the removal of the top layer which was in compression, the constraint on the next layer to remain in tension is removed which causes that layer, which is now the top layer of the remaining body, to contract thereby making the block curl upward [176].

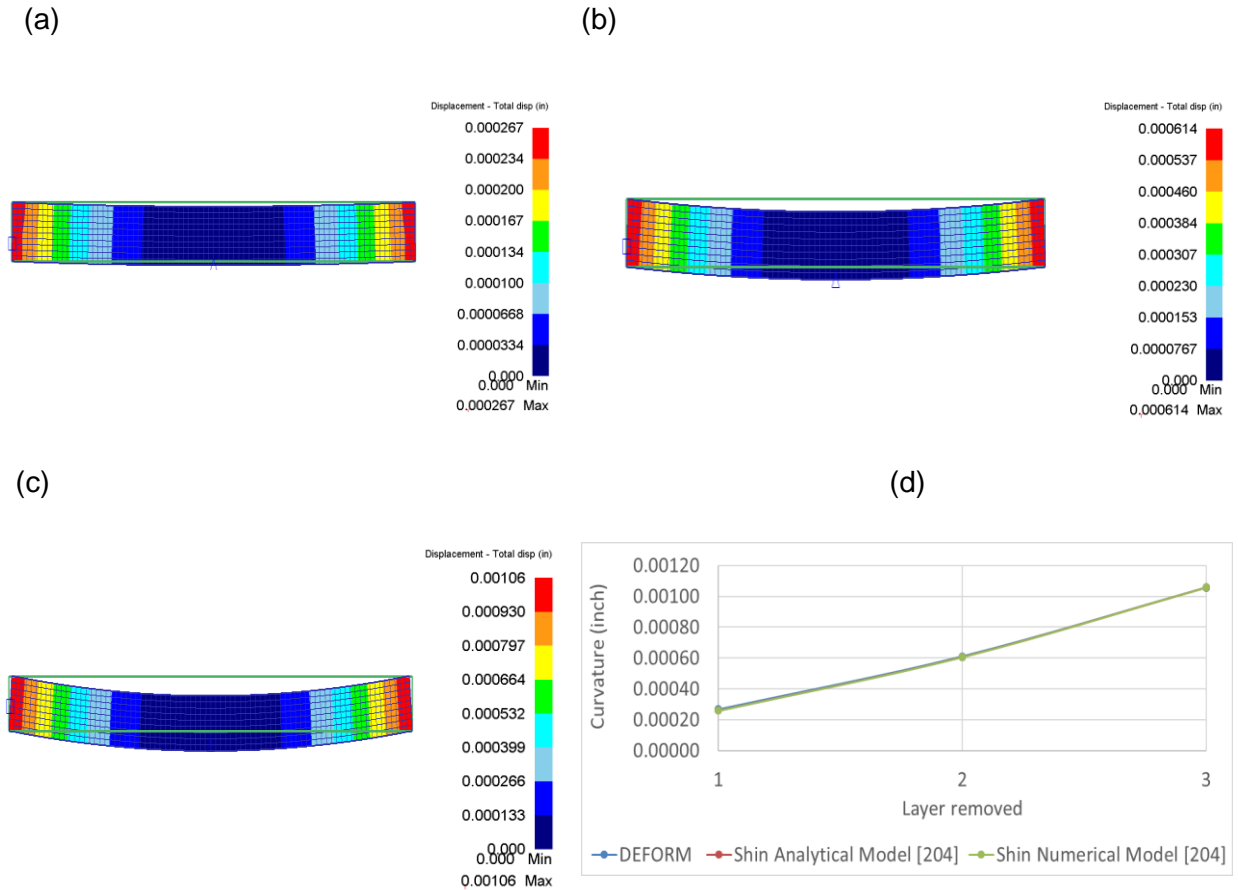


Figure 5-42: Comparison of DEFORM model with analytical, numerical formula from Shin [204].

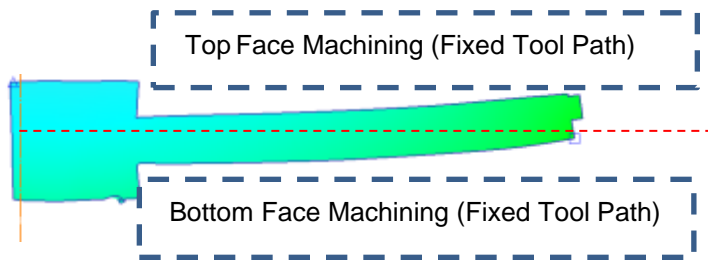
5.1.4.1 Machining distortion simulation for rectangular coupons.

Following the simulation of the quenching process, the next step developed material removal strategies using numerical simulations that would minimise machining distortions in the presence of varying residual stress due to processing or geometric differences. FE analysis was used as the tool to predict accurately the desired machining strategy that will be validated by experimental results. Distortion and stress measurements will be measured to validate the FE model in section 6. Figure 5-43 illustrates the different machining strategies used for this analysis. Figure 5-43 (a) depicts a machining strategy that produces large distortion magnitudes (non-improved tool path). A FE model will be employed to predict a machine strategy that will create high distortions. These high distortion magnitudes will be a benchmark aimed to be reduced by the selection of two different machining strategies illustrated in Figure 5-43 (b) (improved tool path) and Figure 5-43 (c), with the final aim was to establish a robust set of material removal rules that determines the criteria to minimize distortions.

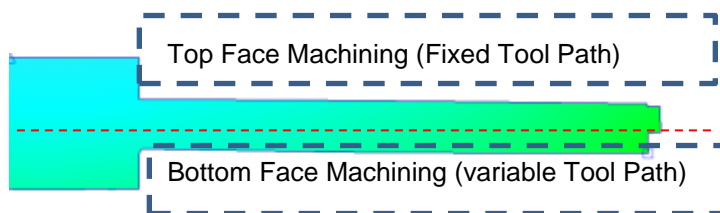
Chapter 5: Finite element modelling methodology

Figure 5-43 (b) illustrates the tool path strategy with the lower distortion (improved tool path). This involves machining a block with a material removal strategy based on stress profile machining (Section 6.1.2) creating low distortion magnitudes. A FE model will be employed to choose the appropriate strategy that will produce the desired distortion magnitude. Figure 5-43 (c) illustrates the robust process validation. The aim of this approach was to show that using the same set of layer material removal rules, a strategy could be generated which allowed for a significantly different quench residual stress map and still generate similar reductions in distortion to the machined strategy B (Figure 5-43 strategy 2). This was to reproduce the machining of an identical shape located in a different position from the same forging as illustrated in Figure 5-43, accommodating any initial stress variation.

(a)



(b)



(c)

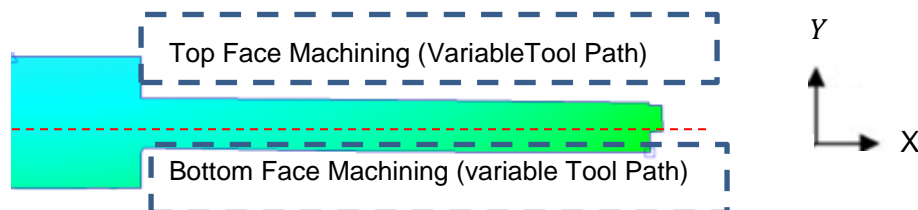


Figure 5-43: Tool path optimization strategies: (a) Strategy one, (b) Strategy two, (c) Strategy three.

Chapter 5: Finite element modelling methodology

In order to propose the different strategies, a modelling analysis was initially carried out to investigate how different axial depths of cut redistribute the residual stress profile into the part, and how this redistribution influences the distortions in the component. The machining FE input information is shown in Table 5-4.

Table 5-4: Machining distortion FE input parameters.

Parameter	Parameter
Mesh	Tetrahedral mesh – 75000 elements
Solution step definition	1 sec/ step
Environment temperature	20 °C
Heat transfer coefficient	0.2 Nsec/mm/C

In general, the methodology used to control the distortion during material removal is based on Figure 5-44 and Figure 5-45. The residual stress prior to material removal is shown in Figure 5-44 (a). Once material is removed on the model workpiece, the residual stress redistributes based on the amount of material removed and the residual stress in the layer of the material removed as shown in Figure 5-45 (the green model is the reference (nominal geometry)).

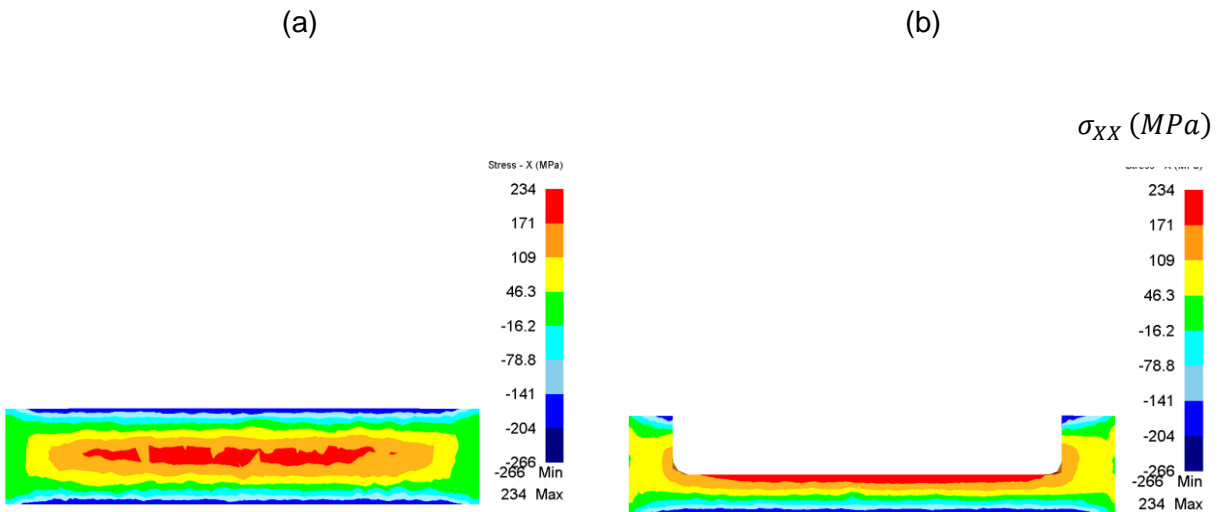


Figure 5-44: Residual stress redistribution due to material removal (fixed condition): (a) Residual stress before material removal, (b) Residual stress after material removal ((fixed condition)).

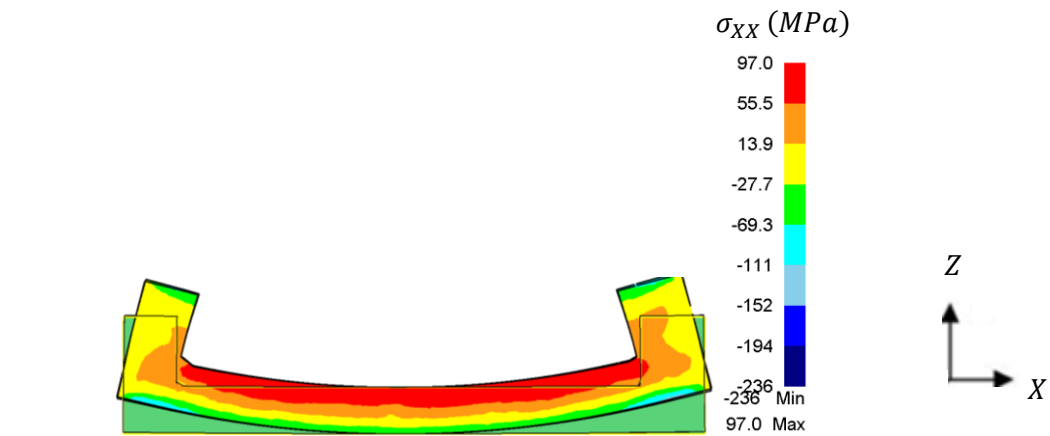


Figure 5-45: Residual stress redistribution due to material removal (unconstrained condition).

Similarly, the common distortion modes were identified during the simulation of the model as shown in Figure 5-46 and Figure 5-47. In this figure, the green model is the reference (nominal geometry) and the purple geometry is the distorted geometry.

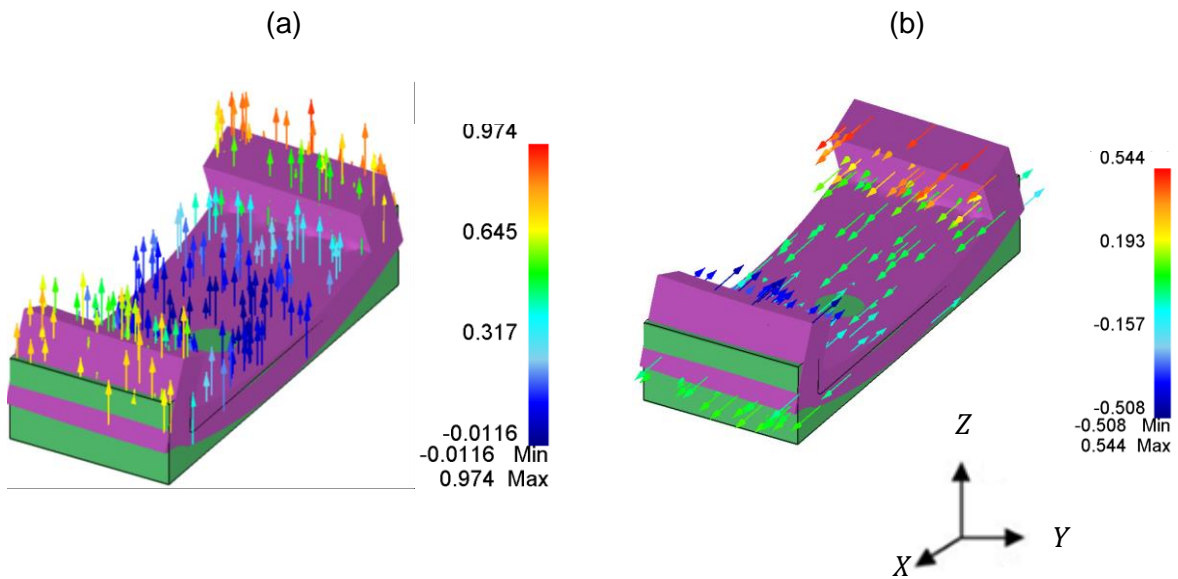


Figure 5-46: Distortion mode in (a) Z direction, (b) X direction.

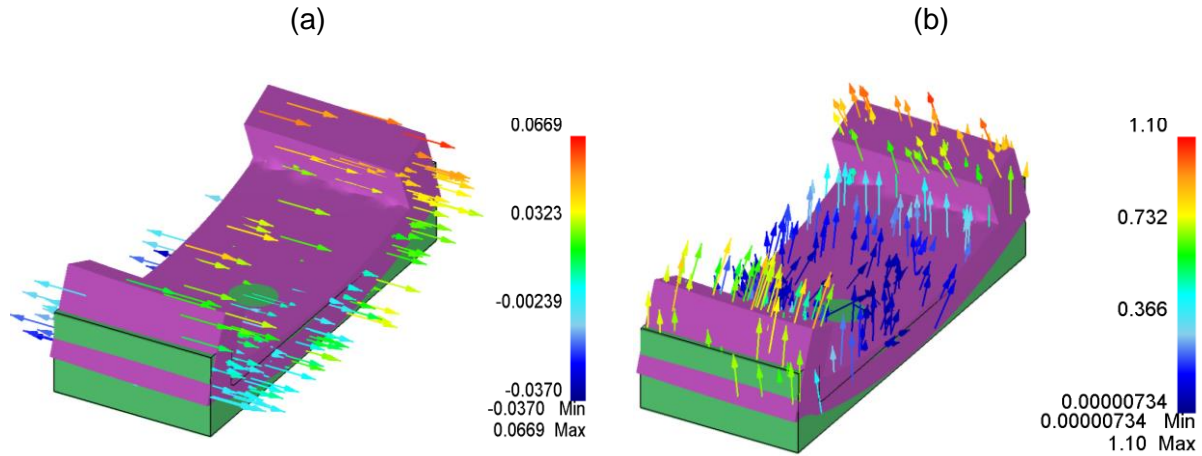


Figure 5-47: Distortion mode in (a) Y direction, (b) Twisting.

A sensitivity study was also performed on the influence of the rigid body motion constrains for predicting the post machining distortion in an unconstrained state. It can be seen in Figure 5-48 and Figure 5-49 that various rigid boundary constraints influences the distortion profile and also the magnitude, therefore it this is a critical step in the simulation of the post machining distortion which is not often mentioned.

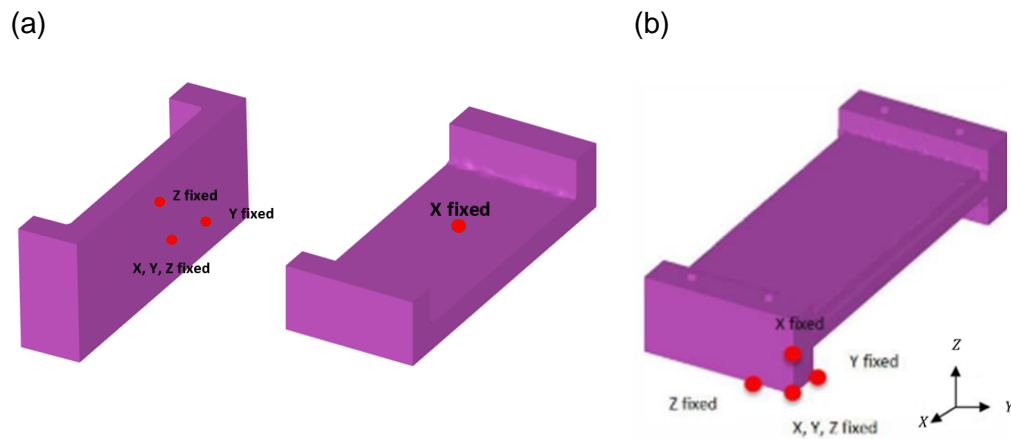


Figure 5-48: Post machining distortion influence of the rigid body motion constraint: (a) Constraint in the centre of the model, (b) Constraint in the end of the model.

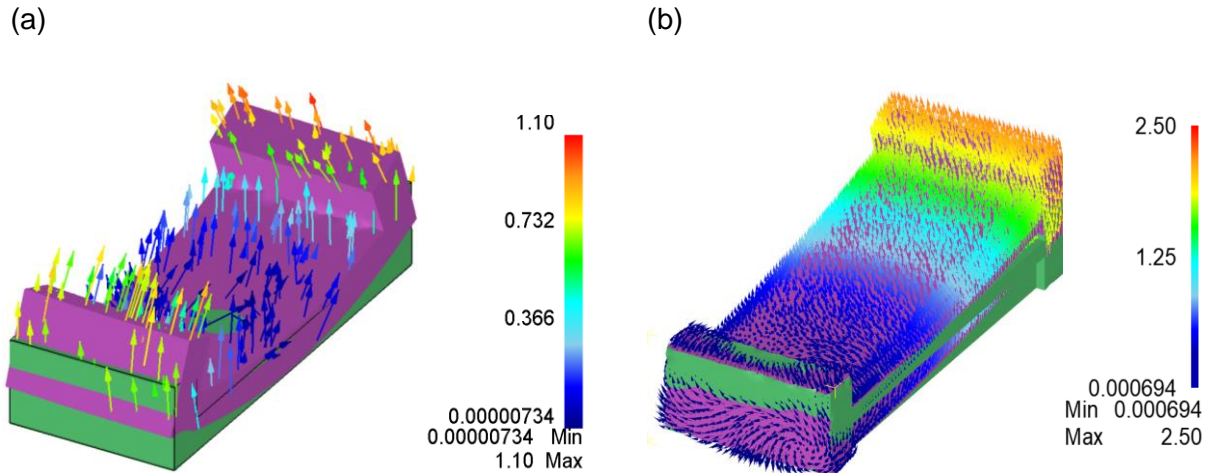
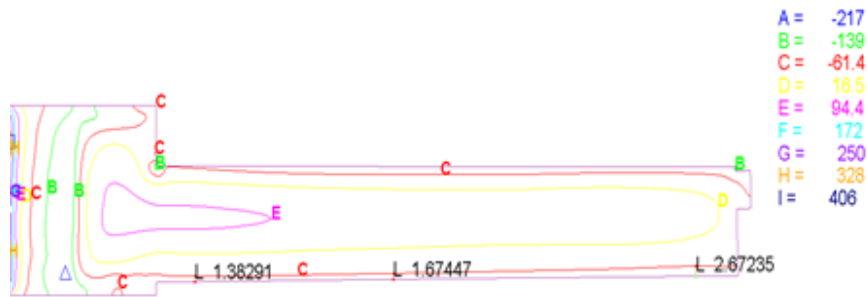


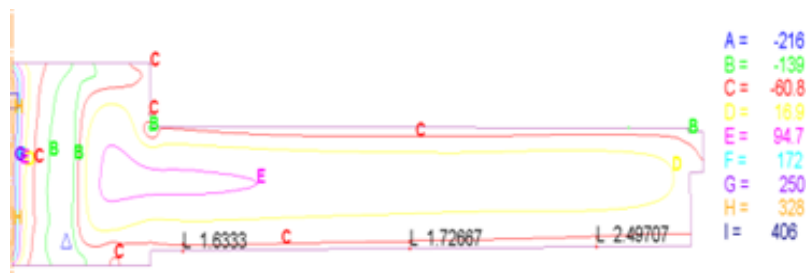
Figure 5-49: Post machining distortion influence of the rigid body motion constraint: (a) Constraint in the center of the model, (b) Constraint in the end of the model.

The Figure 5-50 illustrates an example of the sensitivity FE analysis in which is shown that the machine distortion of the blocks were very sensitive to the magnitude of the stress profile and depth of cut during machining. After simulating the first cut (3 mm depth of cut) on the bottom face of the block, as shown in Figure 5-50 (a), there was a compressive layer between of -139 to -61 MPa in a region of 1.4 – 2.8 mm. When the second cut (3 mm depth of cut) was simulated to remove this compressive region formed from cut one, the residual stress pattern re-equilibrated (stress balance) on the block as shown in Figure 5-50 (b), this re-equilibration (stress balance) of stresses produced extremely low distortion (60 μm). In comparison if a 1 mm material removal is simulated instead of the 3 mm for the second cut as shown in Figure 5-50 (c), a greater unbalanced stress profile is created causing large distortions with magnitudes between 400-500 μm .

(a)



(b)



(c)

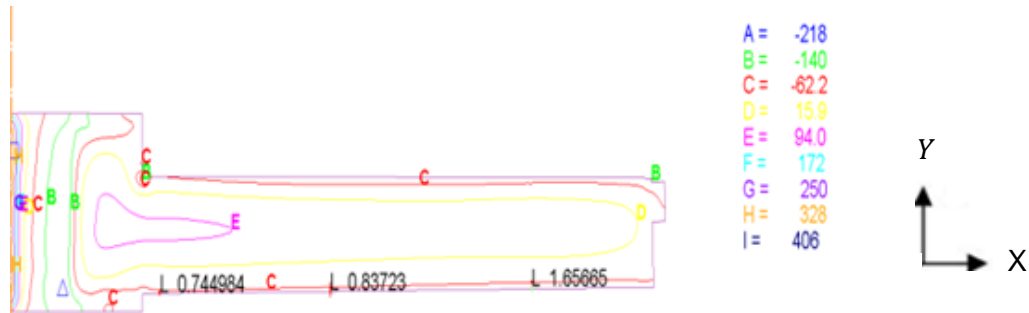


Figure 5-50: Longitudinal stress profile and distortion measurements following material removal at the bottom (a) before taking second cut, (b) 3 mm axial material removal, (c) 1 mm axial material removal.

It was also found that material removal at any depth in low compression/tension gradients does not influence stress profiles by a high magnitude, then consequently the distortions are not influenced by these cuts as shown in Figure 5-51. It should be pointed out here that all these FE analyses require corroboration from residual stress measurements after each cut to validate the findings; this is discussed further in this report.

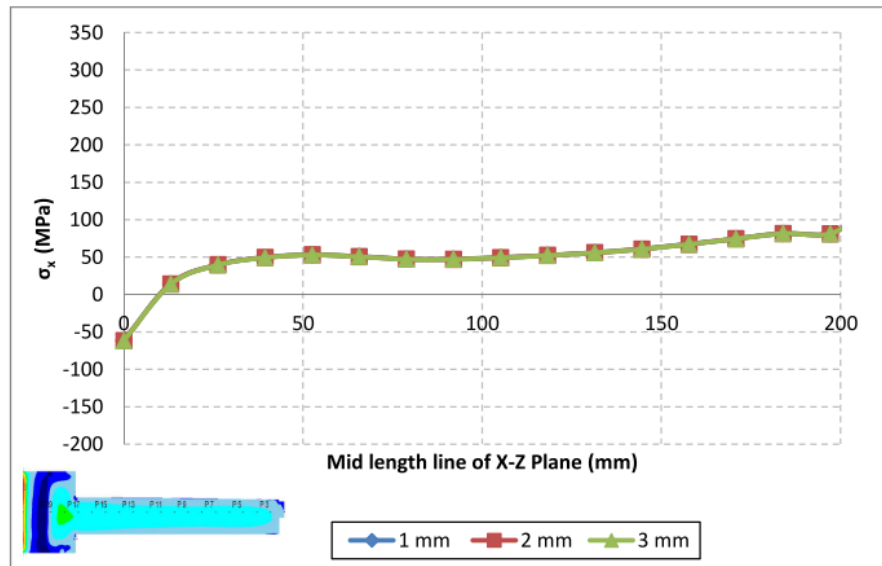


Figure 5-51: Influence of material removal on stress profile variation in the X-Z plane at different depths of cut carried out on a low compression gradient.

Based on the above studies, a set of layer material removal rules were determined for selecting the criteria (Table 5-5) for material removal in the blocks as following:

- Initial material removals of 0.4, 0.4 and 0.2 mm respectively were used to create a level surface prior to the roughing process.
- High depth of cuts (3 mm) were initially used to have high material removal rate during the roughing operation on both the top and bottom faces for the non-improved and improved tool paths.
- For the semi finishing process, a depth of cut of 0.5 mm was used on the top face for both the non-improved tool path and improved strategy blocks. This value was chosen in order to achieve the target depth of cut of 16.5 mm on the top face of the blocks.
- The final cuts (13-15) on the bottom face of the non-improved tool path was performed to machine the block to a semi finishing state.
- Cut 11 on the bottom face varied in the improved tool path by using a 1 mm depth of cut instead of a 3 mm depth of cut. The 1 mm depth of cut showed a higher distortion and stresses in comparison to using a 3 mm depth of cut.
- This decision was taken from the sensitivity analysis performed to see the influence of layer removal on i) Magnitude of the residual stress, ii) Size of the layer of the residual stress and iii) amount of material removed in this layer.

Chapter 5: Finite element modelling methodology

Other layer material removal rules determined for selecting the criteria (Table 5-5) for material removal in the blocks were as follows:

- The final cuts on the bottom face of the improved tool path (14 & 15) were performed to machine the block to a semi finishing state
- A similar strategy was used for the robust process validation with cut 4, by using a 2 mm depth of cut created more distortion than a 3 mm depth of cut.
- A similar cut of 1.5 mm was used for the semi finishing process on the bottom face of the robust selection process blocks. This was found to be sufficient to create the required distortion.

It should be noted that no current best practice strategy was used to machine the blocks because there is none for the non-improved tool path, therefore different modelling analyses were performed to propose the strategy that would cause the highest distortion during machining for the non-improved machining strategy. The non-improved machining strategy (machine Strategy A) was simulated by removal of depths of material to cause large distortions on the blocks as shown in (Table 5-5 (a)). These axial depths of cut was using the maximum depth of cut ($a_p = 3\text{ mm}$) that the tool can manage as suggested by the tooling provider due to the cutting speeds and feedrates used on the experimental trials.

For the improved tool path strategy, a similar strategy as the non-improved tool path was used for machining of the top face of the block; but for the bottom face different depth of cuts were selected depending on the near surface stress profile of the block with the aim to minimize the distortion. This was done by performing a sensitivity analysis on the influence of the combination of the quench residual stress and depth of cut on the redistribution of stresses. This redistribution causes the block to move balance hence moving towards its datum point prior to machining. Therefore using this information, the simulated depth of cuts that caused large stress redistribution on the bottom face of the block was chosen as shown in (Table 5-5 b)).

The robust process validation was performed with the aim of showing that this methodology could be applied to a number of different quench residual stress states. Using the same rules described above a different machine strategy was generated to ultimately give a distortion and stress profile similar to the improved tool path optimization. The top and bottom face of the block was machined based on the selection process mentioned with depths of cut as shown in (Table 5-5 (c)).

Table 5-5: Tool path strategy.

		Axial depth of cut (mm)		
		(a)	(b)	(c)
Top Face	Cut Number			
	1	0.4	0.4	0.4
	2	0.4	0.4	0.4
	3	0.2	0.2	0.2
	4	3	3	2
	5	3	3	3
	6	3	3	3
	7	3	3	3
	8	3	3	3
9	0.6	0.6		
Bottom Face	10	3	3	3
	11	3	1	3
	12	3	2	3
	13	1	2	3
	14	0.5	2.5	0.5
	15	0.5	0.5	0.1

5.1.4.2 Machining distortion simulation for symmetrical and asymmetrical coupons

Following the heat treatment process of the three different HTC models (low, medium and high); three machining distortion models were set up to compare with six symmetric and three asymmetrical residual stress model. During material removal simulation, the coupon was constrained in all directions at the locations shown below (Figure 5-52). The machining FE input information is shown in Table 5-4.

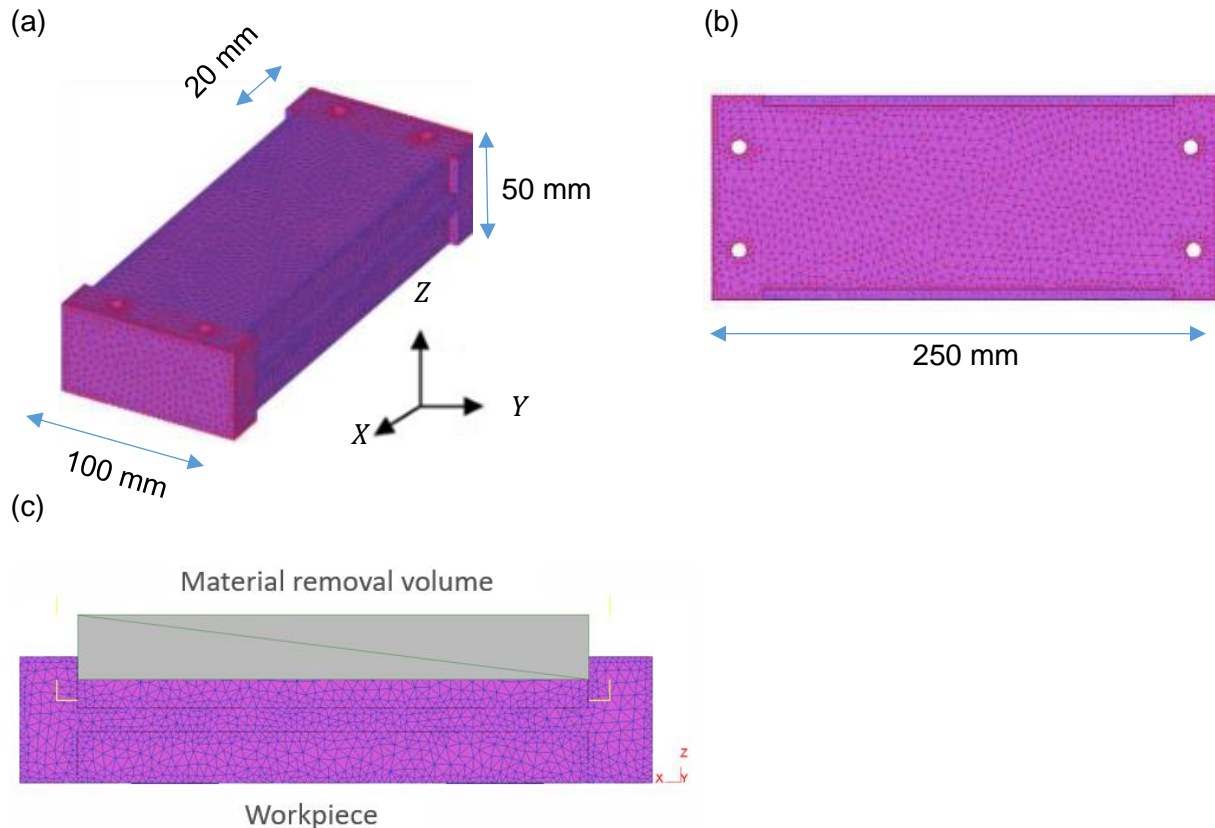


Figure 5-52: Machining distortion model set up: (a) Boundary constraint applied in X, Y and Z direction, (b) Boundary constraint applied in Z direction only, (c) Material removal volume on workpiece.

In order to simulate the appropriate material removal strategy to optimize for machining distortion, the set of rules generated during the simulation of the cantilever beam was used. These set of rules are based on removal of material (axially) in layers with a large stress gradient. This is due to the relationship between the stress redistribution and the stress gradient, which in turn has an influence in the machining distortion.

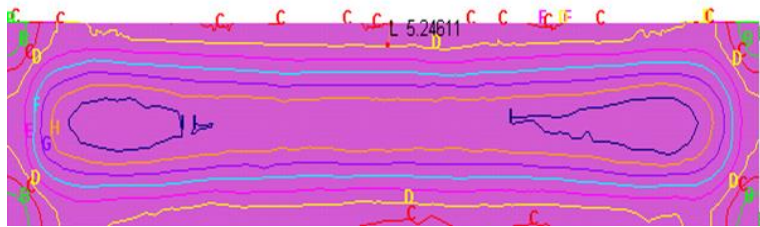
In this study, the three models (Low, Medium, High RS profiles) as shown in Figure 5-53 have different stress magnitudes as shown in the isobars; this would dictate the depth of material removal in order to control how the stress redistributes which would in turn control the distortion magnitude. The maximum depth of cut is the maximum amount of material that can be removed within a specific isobar region without causing large magnitudes of distortion.

For example, in Figure 5-53 (a), 5.24 mm is the maximum depth of cut that can be removed within the top isobar region without causing any large distortions or stress redistribution.

Chapter 5: Finite element modelling methodology

Similarly, in Figure 5-53 (b), 3.65 mm is the maximum depth of cut that can be removed within the top isobar region without causing any large distortions or stress redistribution. Finally in Figure 5-53 (c), 2.3 mm is the maximum depth of cut that can be removed within the top isobar region without causing any large distortions or stress redistribution. This is based on work done for the simple coupons. A newly developed strategy known as a first cut analysis – (FCA) was used to exhibit the level of residual stress magnitude based on a slight material removal. Therefore, an initial material removal of 0.4 mm was simulated. The distortions predicted from this cut was low so a second cut was simulated and this information was used to identify the appropriate material strategy to use for a component distorting with a certain magnitude based on the second cut analysis – (SCA).

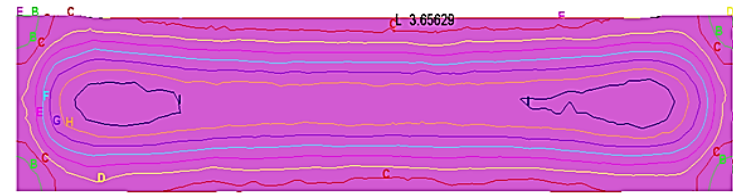
(a)



σ_{YY} (MPa)

A = -219.02
 B = -170.71
 C = -122.40
 D = -74.095
 E = -25.788
 F = 22.518
 G = 70.825
 H = 119.13
 I = 167.44

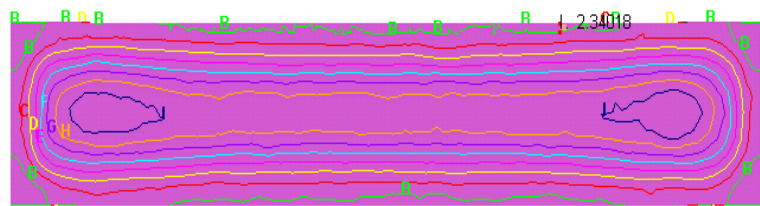
(b)



σ_{YY} (MPa)

A = -223.38
 B = -171.67
 C = -119.96
 D = -68.245
 E = -16.532
 F = 35.180
 G = 86.893
 H = 138.61
 I = 190.32

(c)



σ_{YY} (MPa)

A = -231.02
 B = -171.50
 C = -111.97
 D = -52.446
 E = 7.0796
 F = 66.605
 G = 126.13
 H = 185.65
 I = 245.18

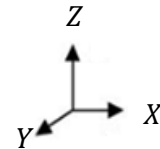


Figure 5-53: Initial material removal based on Stress Profile: a) Low RS profile, b) Medium RS profile, c) High RS profile.

5.1.4.3 Post machining distortion boundary conditions for residual stress coupons

In order to simulate the distortions from the model in an unconstrained condition following the material removal on either faces, the rigid boundary motion conditions used on the FE model is shown in Figure 5-54 (a) and the post machining distortion positions are shown in Figure 5-54 (b). Based on this knowledge, material removal optimization strategies (Table 5-6 and Table 5-7) were developed for this study of machining distortion reduction i.e. maximum material removal at regions of low stress gradients.

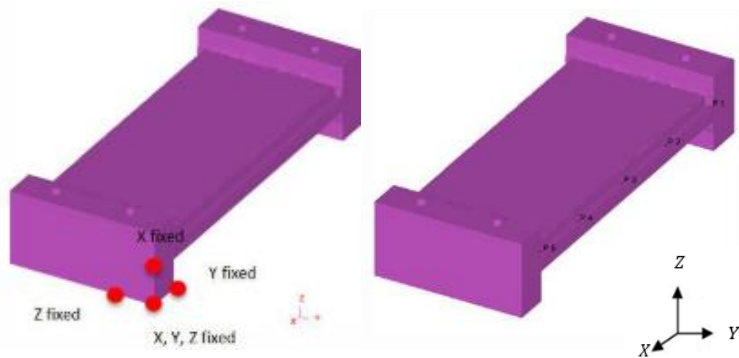


Figure 5-54: Fixture release modelling: (a) Applied rigid boundary motion conditions, (b) Measurement locations.

Table 5-6: Axial depth of cuts of the symmetric stress profile.

RS profile	Axial depth of cut (mm) – Symmetric RS profile														
	Phase one (top)									Phase two (bottom)					
Low	0.4	0.8	1	1.5	4.5	7.5	10.5	13.5	16.5	3	4	7	10	11	12
Medium	0.4	0.8	1	4	7	10	13	15	16.5	3	4	7	10	11	12
High	0.4	0.6	1	4	7	8.5	10.5	13.5	16.5	3	4	7	10	11	12

Table 5-7: Axial depth of cuts of the asymmetric stress profile.

RS profile	Phase one (top)													Phase two (bottom)				
	Low	0.4	3.4	6.4	9.4	12.4	15.4	18.4		3	6	7	8	10	10.1			
Medium	0.04	3.2	6.2	9.2	12.2	15.2	18.2		3	4	5	8	9.7	10.3				
High	0.4	0.8	1	4	7	10	13	16	1	2	5	8	11	12	12.5			

Chapter 5: Finite element modelling methodology

To generate a further understanding, the distortions resulting from the material removal simulation of the “Low Residual Stress” in Table 5-6 was compared with the residual stress redistribution ratio. From Figure 5-55, it can be seen that the residual stress ratio increases so does the distortion for example from 3 to 6 mm, there is a large redistribution therefore a large distortion value. From the simulations, the relationship between the distortions in the z direction with the residual stress redistribution ratio is shown in Equation 5-27. The residual stress redistribution is shown in Equation 5-28, where $\sigma_{XX\ initial}$ is the surface (maximum) residual in the longitudinal direction prior to material removal and $\sigma_{XX\ post}$ post material removal.

$$\sigma_{XX\ redistribution\ ratio} = \frac{1}{z}$$

Equation 5-27: Relationship between the residual stress redistribution ratio and distortion.

$$\sigma_{XX\ redistribution\ ratio} = \frac{\sigma_{XX\ initial}}{\sigma_{XX\ post}}$$

Equation 5-28: Residual stress redistribution ratio.

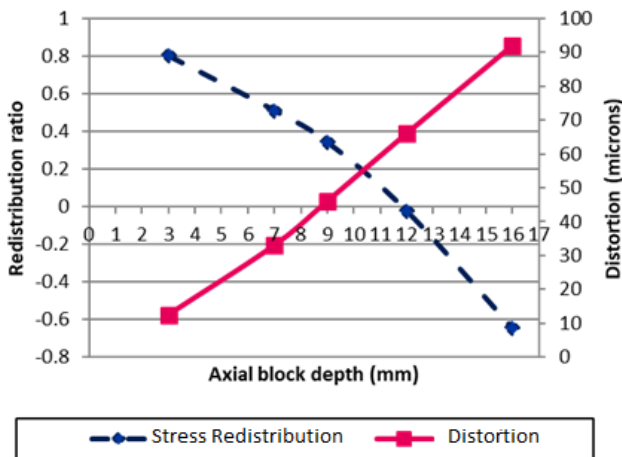


Figure 5-55: Residual stress redistribution and distortion against depth of cut.

5.1.4.4 Machining distortion simulation for the tool path strategy

Similar to the previous studies sections 5.1.3.3 and 5.1.3.4, following the quenching simulation of the pocket geometry, the model was then run the analysis for the effect of tool path layout.

Chapter 5: Finite element modelling methodology

In order to model the material removal process, the work piece was constrained around the bottom face and the flange (Figure 5-56 (a)) to emulate the constraints from machine bed and the clamp locations Figure 5-56 (b). A Boolean operation was performed to create the geometry as shown in (Figure 5-56 (d)). The machining FE input information is shown in Table 5-4.

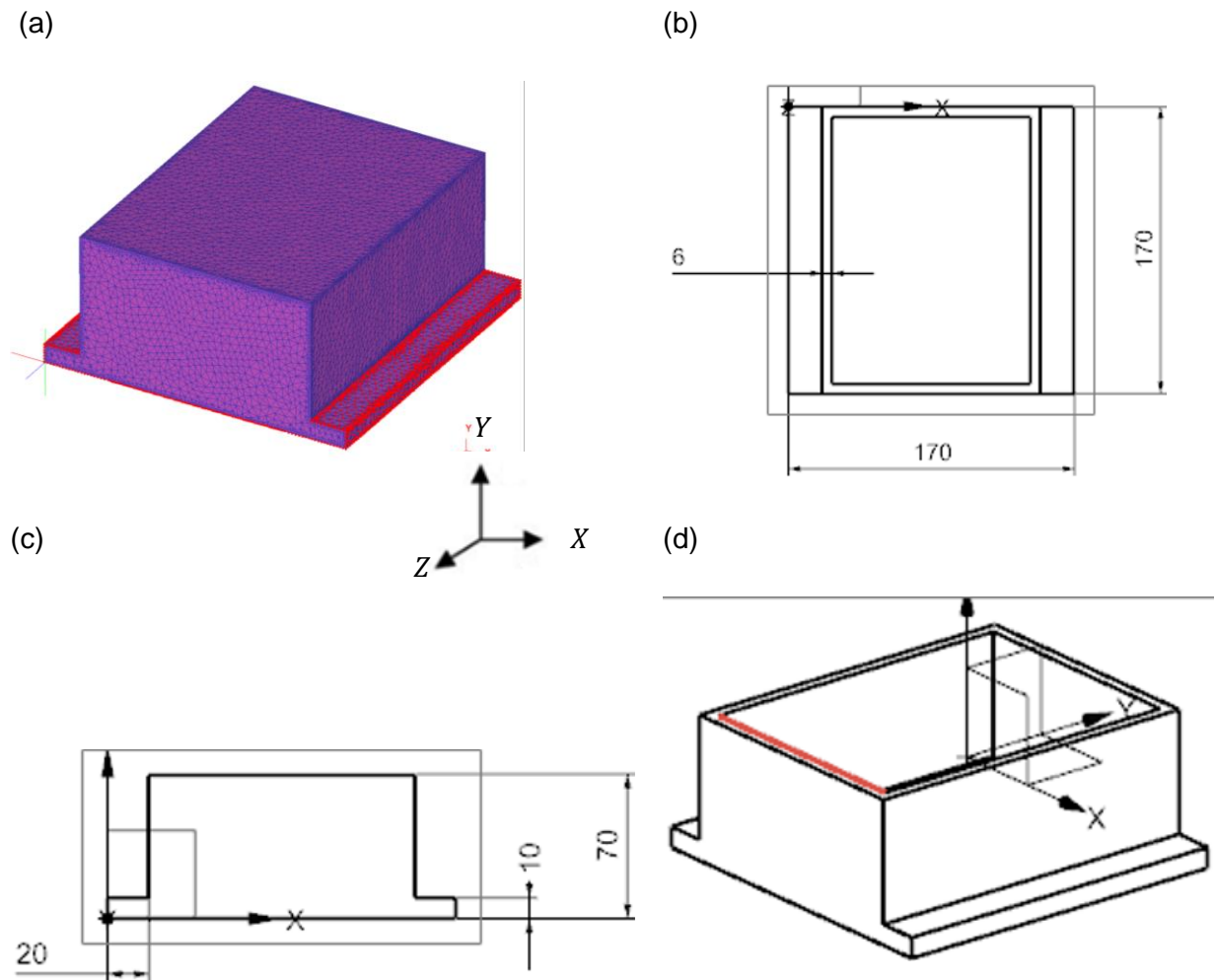


Figure 5-56: Schematic of the machined block; (a) Isometric view, (b) Top view, (c) Front view, (d) Machining FE model with boundary condition (highlighted in red).

5.1.4.5 Effect of tool path layout on machining distortion

There is lack of understanding of the effect of the tool path layout on distortion therefore two widely used tool paths for machining aluminium alloys (zig-zag and helical) for pocketing were simulated to see their effect on the machining distortion as shown in Figure 5-57.

The zig-zag tool path layout had a longer machining duration than the helical tool path as shown in Table 5-8. It should be noted, that the same material volume was removed for both the cases.

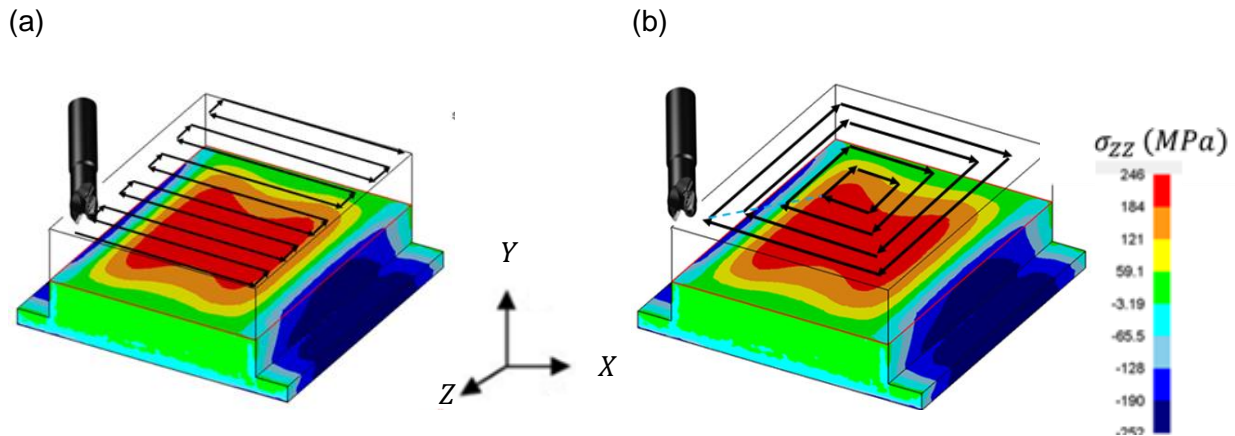


Figure 5-57: Two widely used tool paths for machining aluminium alloys: (a) Zig-Zag layout, (b) Helical layout.

The residual stress evolution during the material removal of the two strategies can be seen in Figure 5-58. From this figure it can be seen that there is not that much residual stresses distinction between the two tool paths for a 2 mm depth of cut (Figure 5-58 (a, b)). The residual stress difference is more evident when material removal towards the centre of the workpiece (Figure 5-58 (c, d)) where the helical tool path has a high tensile residual stress in the bulk in comparison to the zig-zag tool path (Figure 5-58 (c, d)). The post machining residual stresses are higher in the helical tool path, where the stresses are higher in the ridges. This uneven residual stress profile with some regions showing lower stresses and other regions showing a higher residual stress will cause large distortions in the helical tool path. This is not the case with the zig-zag tool path as the residual stresses are within the range of ± 50 MPa.

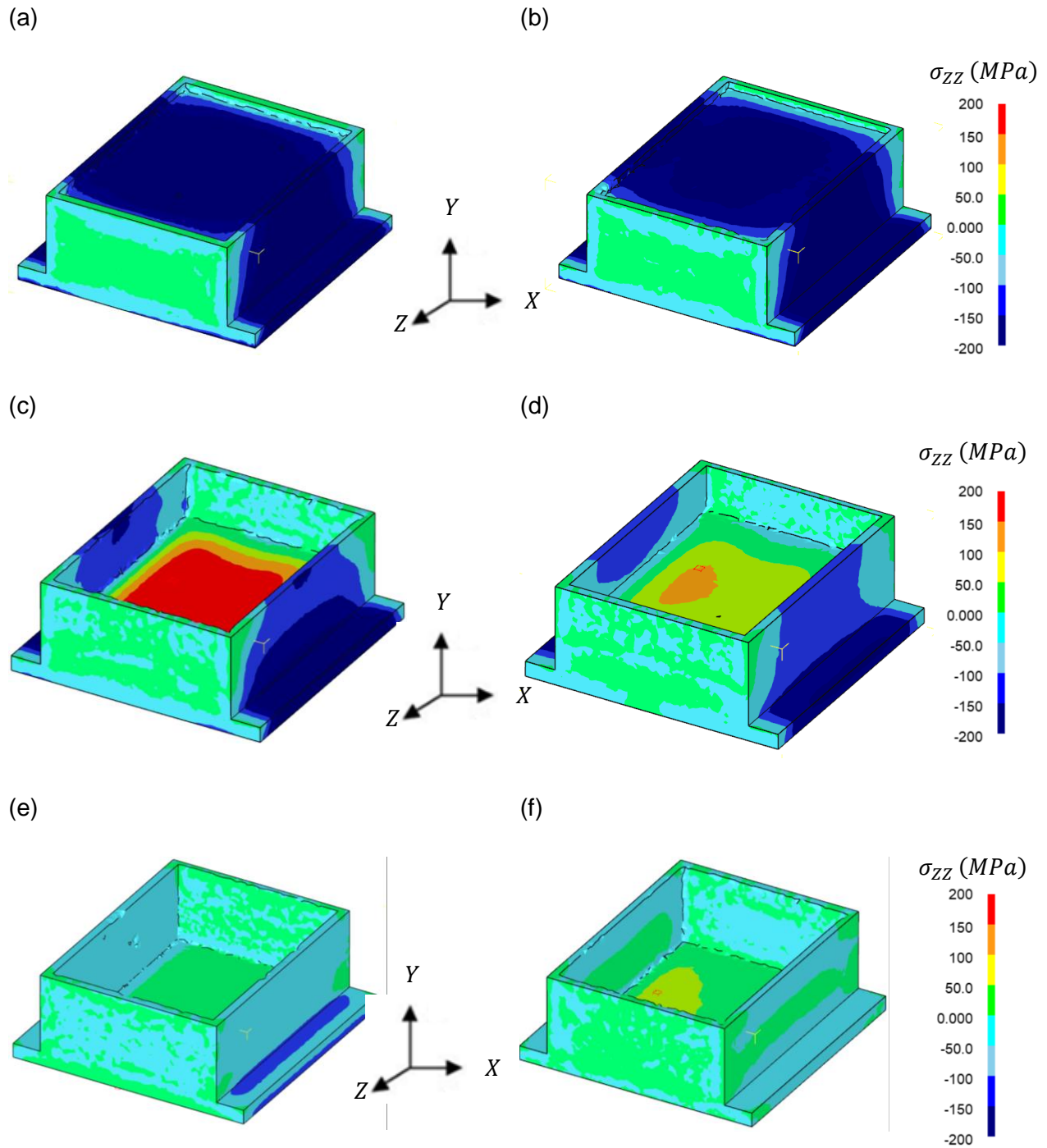


Figure 5-58: Residual stress evolution between helical and zig-zag tool path: (a) 2 mm depth of cut helical, (b) 2 mm depth of cut zig-zag, (c) 35 mm depth of cut helical, (d) 35 mm depth of cut zig-zag, (e) 70 mm depth of cut helical, (f) 70 mm depth of cut zig-zag.

Table 5-8 - Tool path layout durations in Siemens NX 7.

Tool path layout type	Simulated cycle time
Zig-Zag	10 minutes 50 seconds
Spiral Outward	7 minutes 8 seconds

5.1.4.6 Effect of tool entry on machining distortion

In addition to the effect of tool entry strategy (ramping) was simulated. The tool ramping is defined as a rapid radial and axial motion of a cutting tool producing an angular tool path. The tool entry is one of the most critical operations in machining often ignored [264]. Ključanin et al. [265] concluded that apart from the tool diameter, the ramping is the second most important factor to consider in cutting time optimization. Unlike the other machining factors, the effect of ramping on machining distortion has never been studied despite it being an important factor for optimization of the machining time. Therefore the study in this thesis attempts to provide an insight into the effect of the proposed entry angles during aluminium milling using a helical ramping (Figure 5-59 (a –b) and linear ramping as shown in Figure 5-59 (c). The axial depth of cuts (a_p) from the helical ramping for the 3° is 4 mm (Figure 5-59 (a)) and 7° is 9 mm (Figure 5-59 (b)). The quick reference for CNC milling practices and techniques suggests ramping in for non-ferrous alloys using a ramp angle between 3° to 10° [264], although it is always recommended to check with the tool manufacturer for the maximum allowable tool limit. The maximum allowable ramp angle for the tool used for these trials is 19°.

It should be noted, that the similar machining conditions were applied on these cases. Once the study on the tool entry has been performed, the helical tool path was simulated as illustrated in Figure 5-59 (d).

As expected, since the tool entry angle is removing different material volumes at each time, therefore this would influence the residual stress redistribution hence the machining distortion. In addition to this, the tool entry type simulation was varied from the nominal circular to a tool path entry as shown in Figure 5-59 (d). Similarly, by varying the tool entry type, a different material removal volume and direction are used which would influence the residual stress redistribution, therefore the resulting distortion.

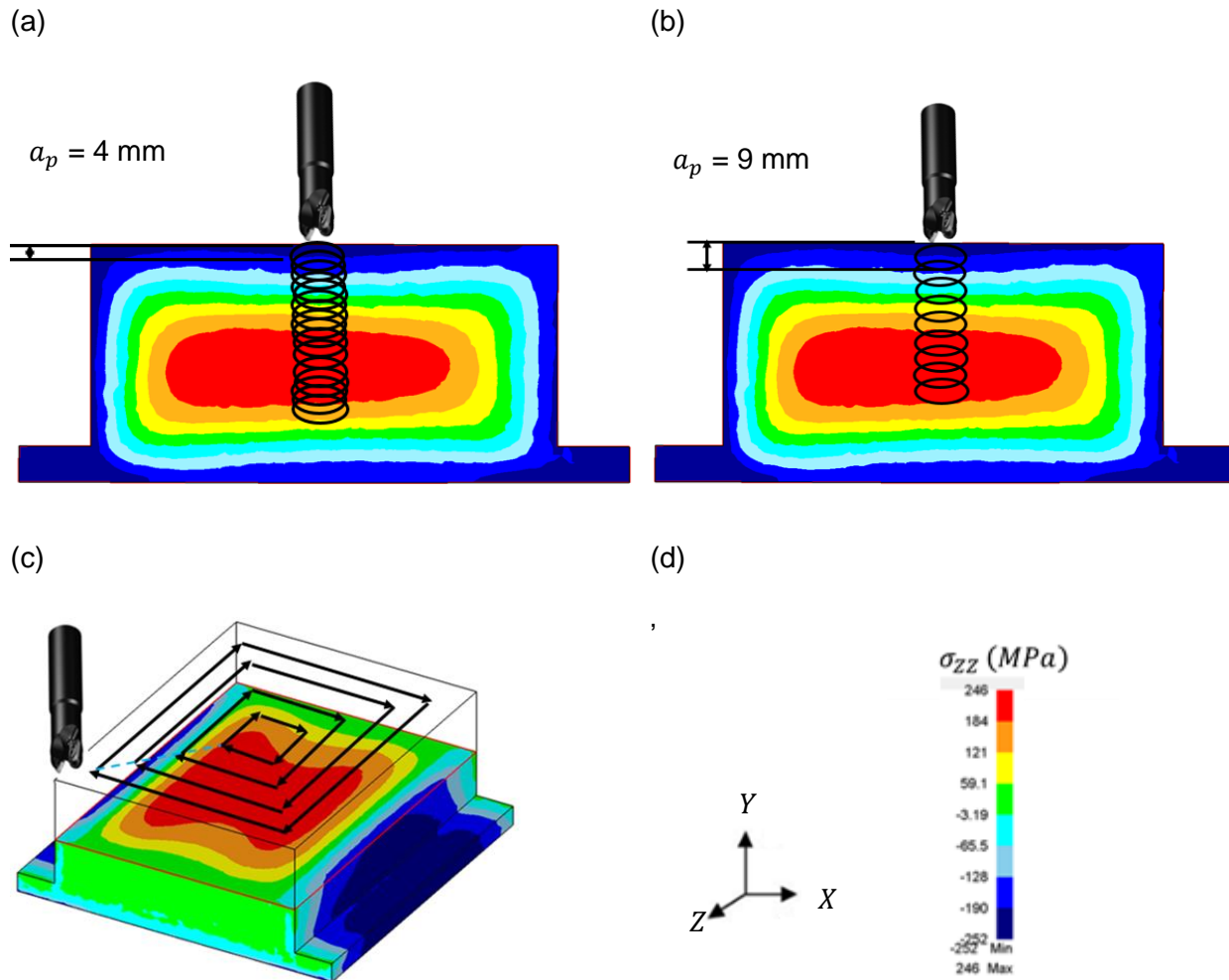


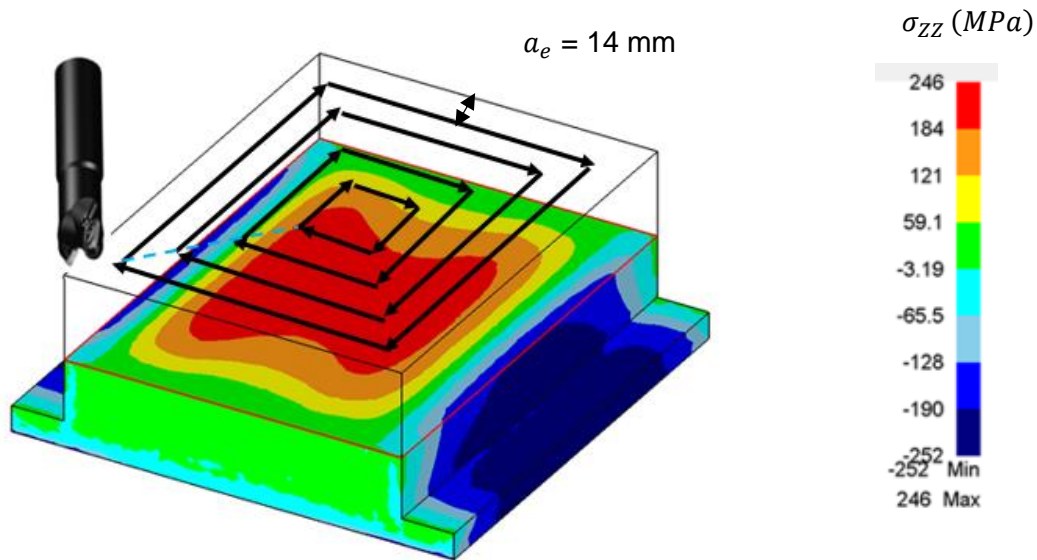
Figure 5-59: Different tool entry angles on machining of aluminium pockets: (a) Helical ramping (3°), (b) Helical ramping (7°), (c) Helical tool path.

The finite element model in DEFORM was set up by converting the ramp angle into a solid geometry and removing material incrementally as per the machining path. Once the tool entry was modelled, the helical tool path was modelled as normal.

5.1.4.7 Effect of radial depth of cut on machining distortion

In addition to this, the effect of radial depth of cut was simulated to understand its effect on machining distortion. The step over chosen were 25% and 70% of the tool diameter as shown in Figure 5-60 (a-b) therefore the radial depth of cut was 5 mm and 14 mm radial increments respectively. The residual stress contour shows that by varying the step over, the distortion would be influenced due to the varying residual stress profile across the machined coupon.

(a)



(b)

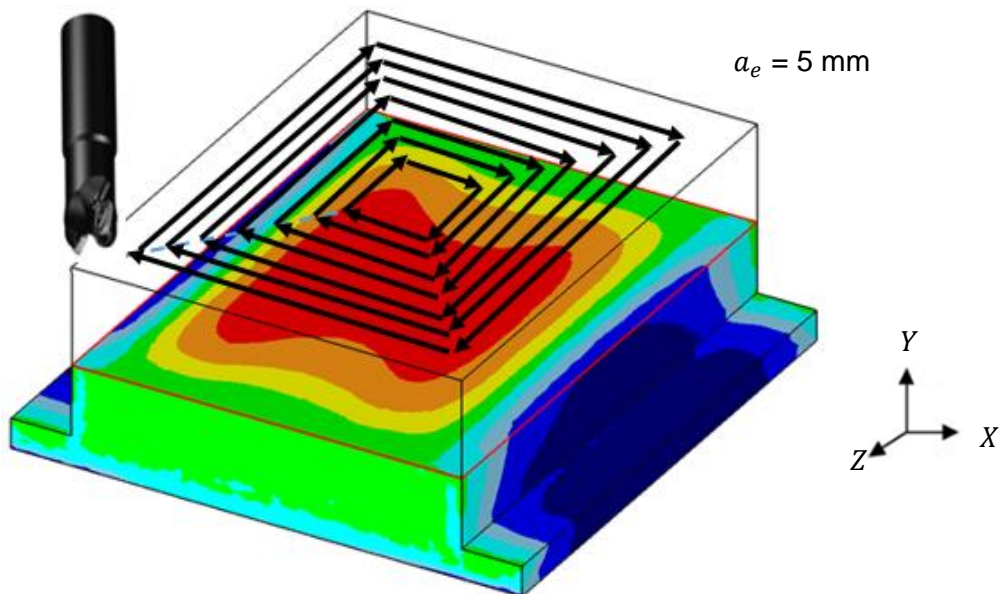


Figure 5-60: Radial depth of cut simulation (a_e): (a) Residual stress contour integration with tool path using $a_e = 14 \text{ mm}$, (b) Residual stress contour integration with tool path using $a_e = 5 \text{ mm}$.

5.1.4.8 Numerical simulation of the machining process for representative part

Following on the knowledge gained from understanding of the effect axial and radial layer material removal, tool path and the tool entry strategies on machining distortion, this research aimed to investigate the effects of:

- Axial part offset on machining distortion.
- Billet orientation
- Sequential pocketing removal strategies.

The process flow chart of the development of the model is shown in Figure 5-61.

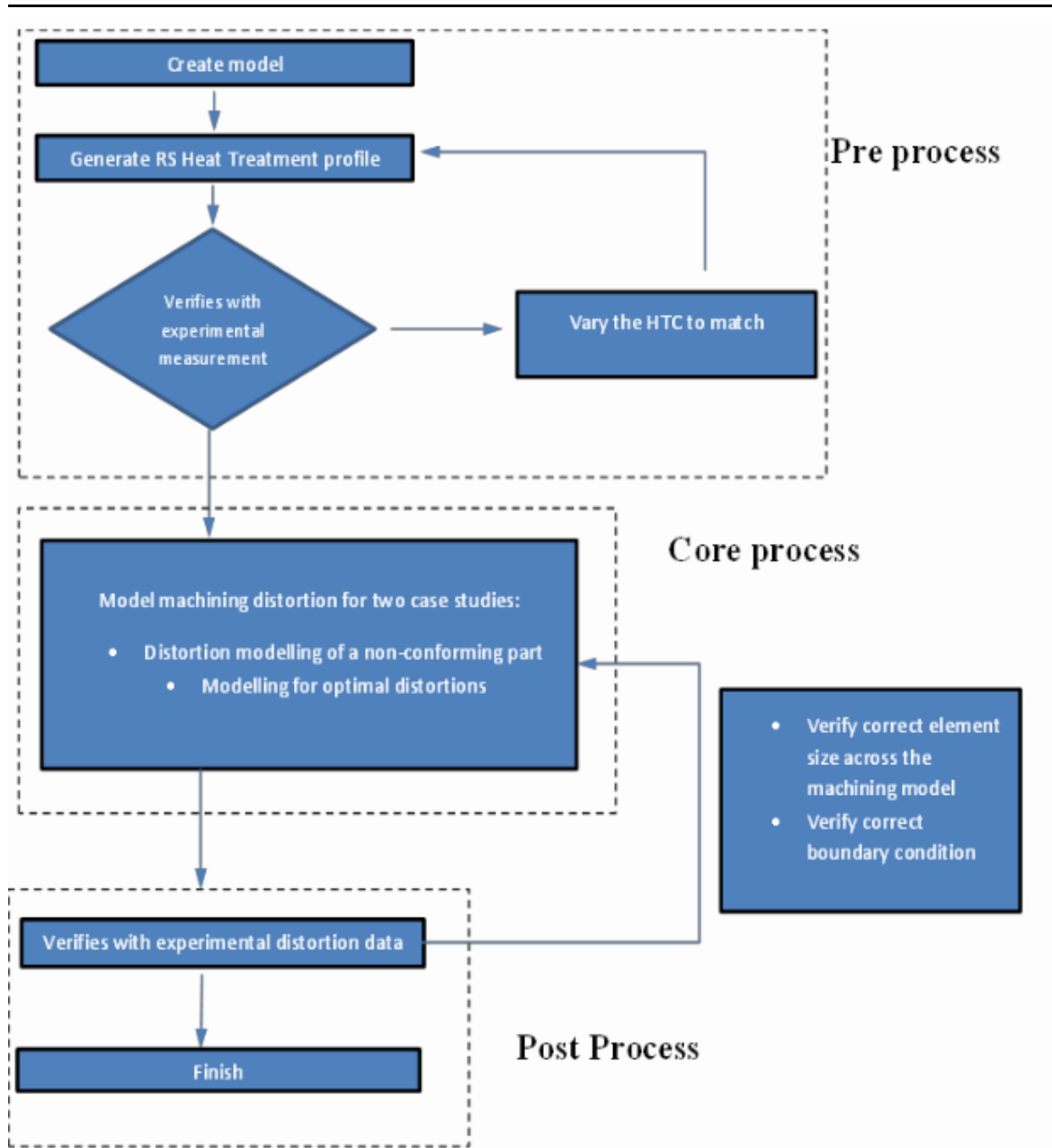


Figure 5-61: Process flow chart of the development of the model for pocketing strategies.

Once the 2D to 3D conversion of the FE model (Section 5.1.3.6), it is required to model the relative sliding motion that can occur between two solid bodies. There are three main friction laws in DEFORM but in this study, the coulomb friction law is used.

Chapter 5: Finite element modelling methodology

The coulomb friction law as defined in DEFORM is shown in Equation 5-29 where τ is the shear stress, μ is the Coulombs friction coefficient, σ_n is the normal stress (interface pressure) between the workpiece and the fixtures and the machine bed. For this simulation, the friction coefficient (μ) between the workpiece and the fixtures and bottom surface is 0.47 which is referenced from a handbook published by Columbia University [266]. A similar value was used by Cerutti [11] in his thesis to represent the contact between steel faces and the workpiece made of aluminium alloy. Ideally, it is recommended to accurately calculate this value using tests defined in Equation 5-29.

$$\tau = \mu\sigma_n$$

Equation 5-29: Coulomb friction law.

The FE model workpiece was constrained on the bottom surface using a rigid body as shown in (Figure 5-62 (a) to prevent any movement in the Z-axis to imitate the machine bed. Similarly, six rigid bodies were applied to constrain the model in the X, Y and Z-axis, replicating the work holding of the part during material removal (Figure 5-62 (b)). The machining FE input information is shown in Table 5-9.

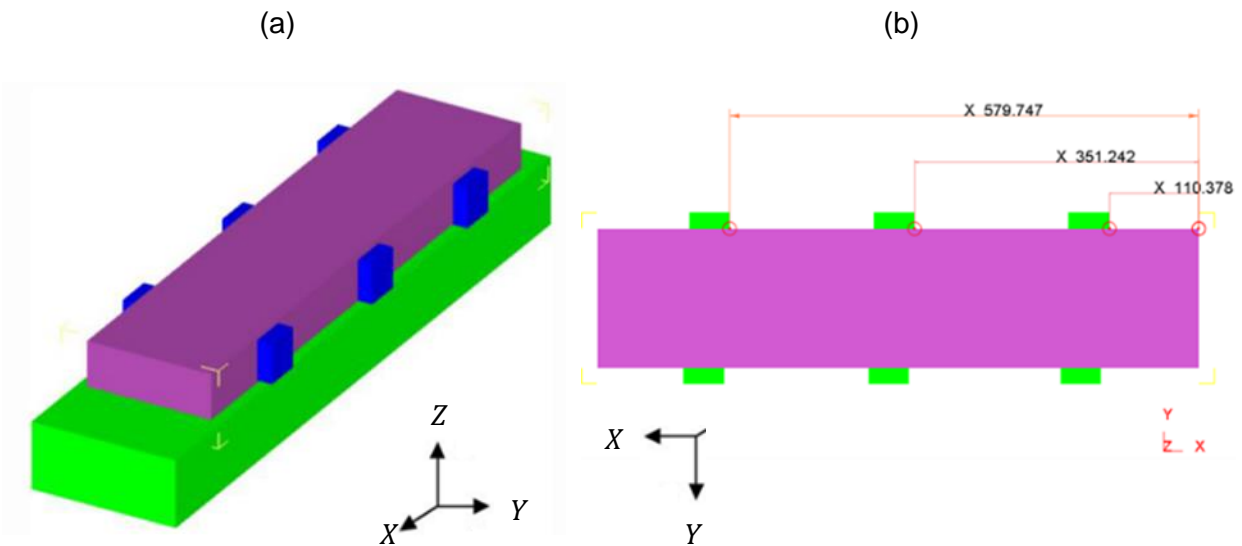


Figure 5-62: Boundary condition model set up for machining distortion simulation (a) Movement constraints in X, Y axis (b) Movement constraints in Z axis.

Table 5-9: Machining distortion FE input parameters.

Simulation settings	Value
Mesh	Tetrahedral mesh – 75000 elements
Solution step definition	1 sec/ step
Environment temperature	20 °C
Heat transfer coefficient	0.2 Neck/mm/C
Workpiece – Machine bed / Fixture	Coulomb friction value – 0.45 [266]

Effect of axial part offset on machining distortion

The axial position of the final machined workpiece in the parent material has an influence in the machining distortion as shown in literature. This is shown in Figure 5-63 where the final machined workpiece is positioned axially by a value (h) from the bottom of the billet along the thickness of the billet (78 mm).

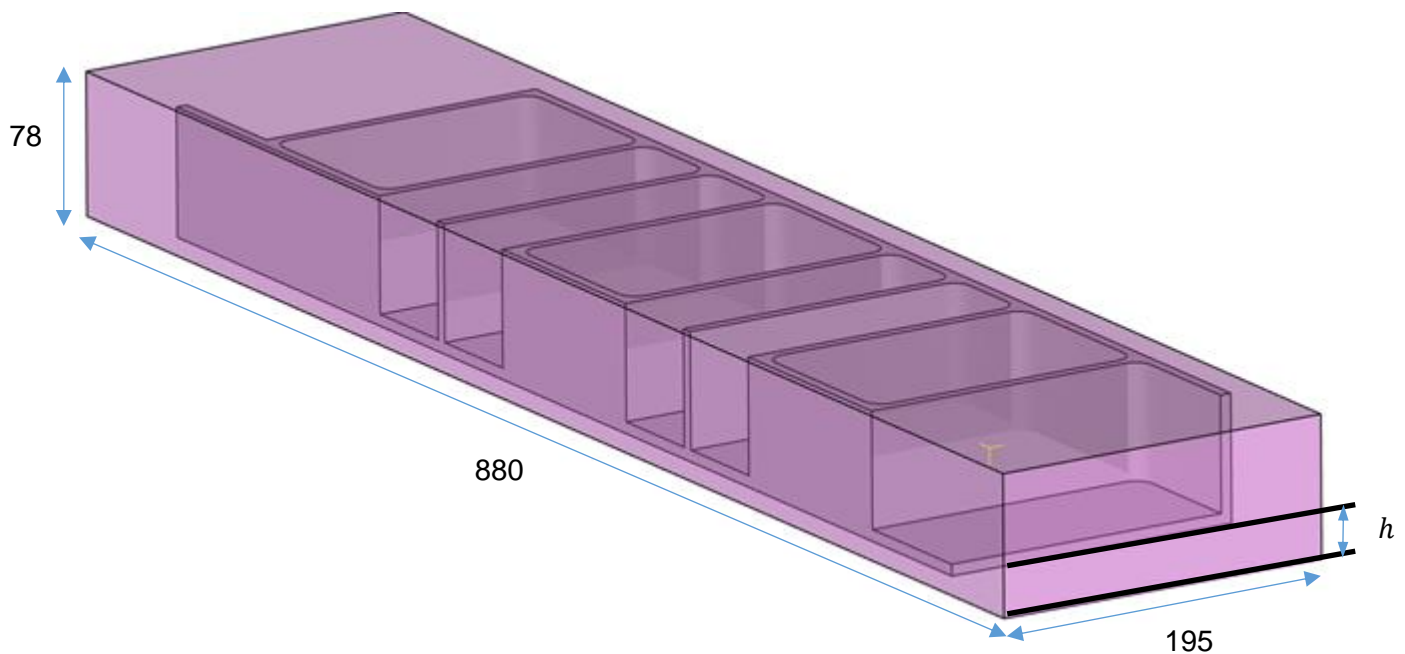
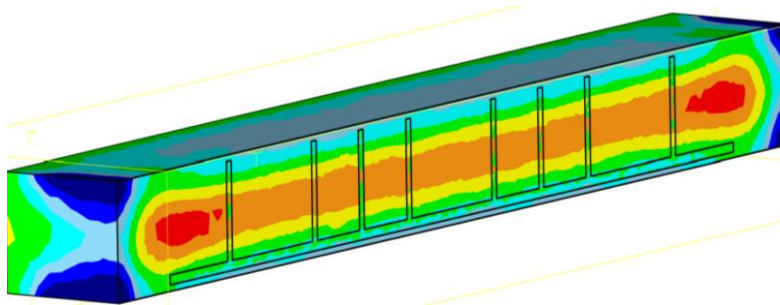


Figure 5-63: Positioning of the machined workpiece in the forged billet (dimensions in mm).

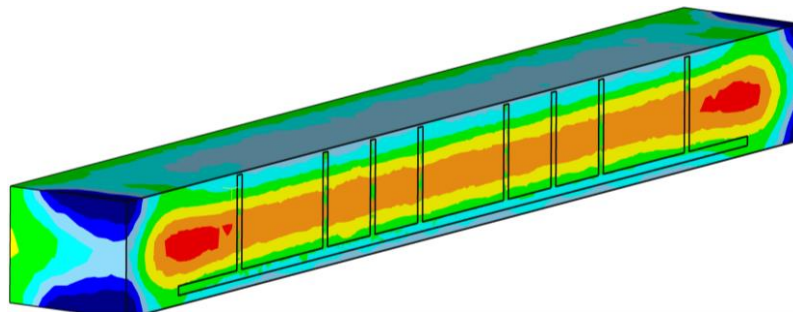
Chapter 5: Finite element modelling methodology

As an initial study on the effect of axial position of the workpiece on the forged billet, three different axial locations of the final machined component was also simulated as shown in Figure 5-64. From the figure, it can be seen that at different axial offsets there is a large residual stress variation. Material removed in this region would cause a large residual stress redistribution rate, which would consequently create a large distortion magnitude.

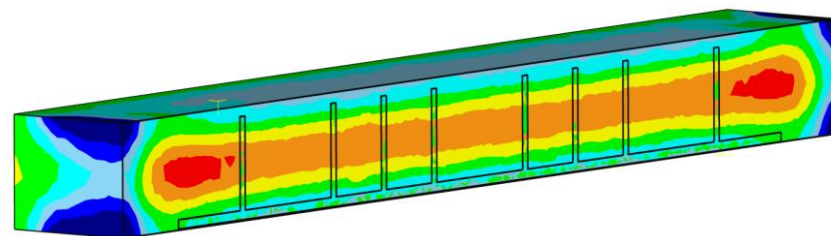
(a)



(b)



(c)



σ_{YY} (MPa)

129

87.0

44.8

2.66

-39.5

-81.6

-124

-166

-208

Min -208

Max 129

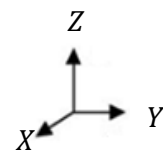


Figure 5-64: Section billet illustrating the axial part offset variation; (a) Billet 1, (b) Billet 2, (c) Billet 3.

Table 5-10: Axial material removal.

Billet identification	Axial material removal
Billet 1	Top: 2 mm
	Bottom: 6 mm
Billet 2	Top: 7.5 mm
	Bottom: 0.5 mm
Billet 3	Top: 4 mm
	Bottom: 4 mm

Effect of part orientation on machining distortion

The effect of part orientation on machining distortion is often a neglected activity in the machine shop. Therefore to overcome this research gap, a machining distortion model was simulated by orientating FE model 1 by 180 degrees in the X direction, this model was named FE model 2 as shown in Figure 5-65 (a-d). Likewise, the residual stress of the billet has also been inverted as shown in Figure 5-65 (e).

Therefore, during the material preparation process, removing material from the top face of FE model 1 would cause the part to have initially higher distortions due to the greater stress redistribution caused due to the material removal of the top face, which had a higher compressive stress. Likewise, removal of the material from the top face of FE model 2 would cause the part to have initially lower distortions due to the lesser stress redistribution caused due to the material removal of the top face which had a lower compressive stress.

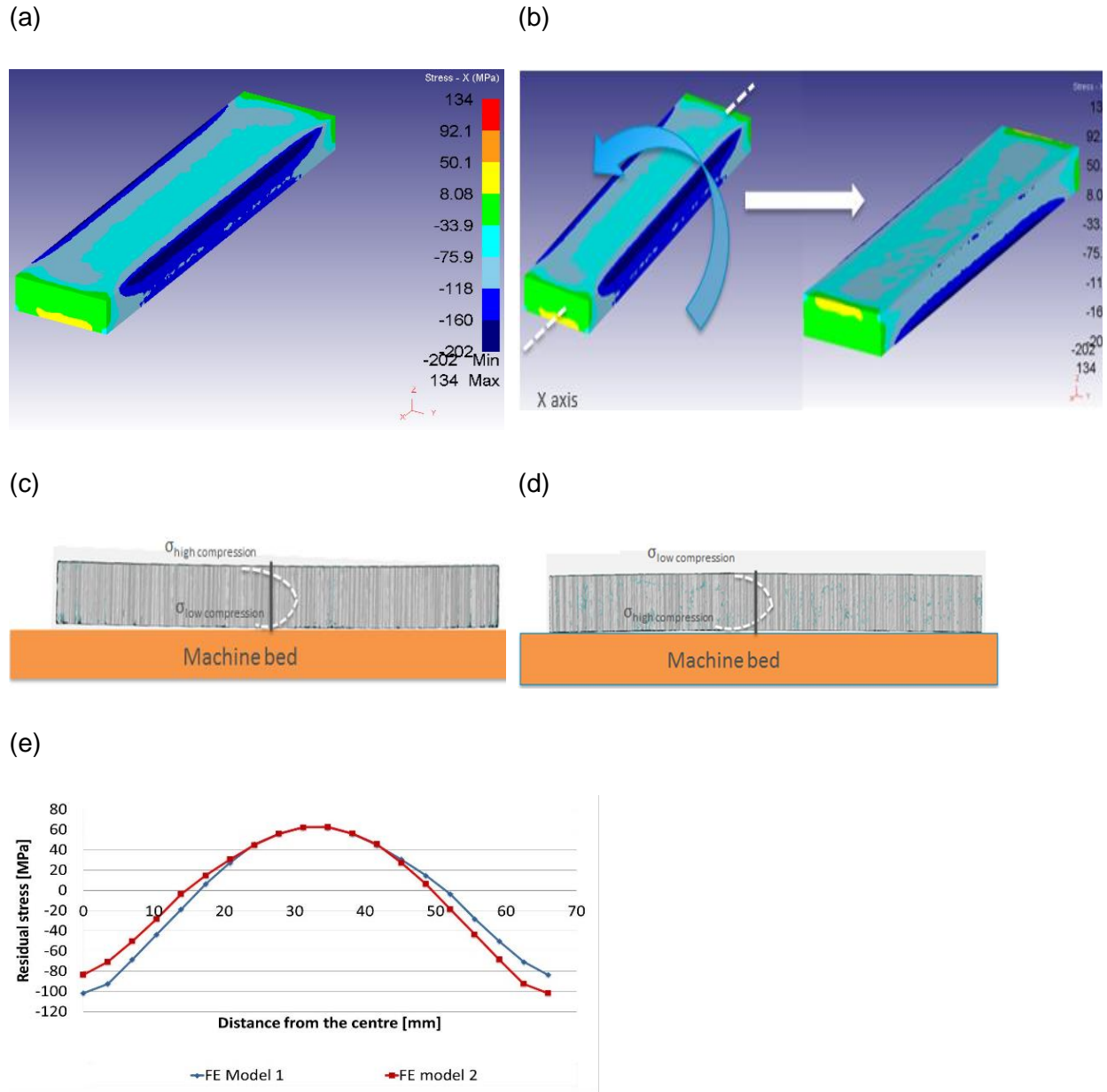


Figure 5-65: FE model comparison: (a) comparison of on machine inspection data, (b) FE model 2 stress profile (FE model 1 rotated 180° in the X axis), (c) Residual stress profile on FE model 1, (d) Residual stress on FE model 2, (e) Residual stress prediction across the thickness.

Effect of pocket sequence on distortion

The selection of the optimal pocketing sequence for distortion reduction is based on analyzing the stress redistribution during the pocketing operation and applying the removal process in a region of low stress redistribution.

Chapter 5: Finite element modelling methodology

Unlike any of the methodologies proposed for distortion control, the reordering of the pocketing sequence is the least tasking since all the manufacturing engineer would do is “drag and drop” the pocket sequence to the desired sequence, reducing the reprogramming time.

The part under investigation contained nine pockets. The rules that were used to decide on the appropriate sequence was based on monitoring the elastic strain (since the effect of plastic strain was found to be negligible) in the mid length section of the part as shown in Figure 5-66 (a). The pocket numbering is shown in Figure 5-66 (b). During the removal of pocket 1, there is a large redistribution of the elastic strain as shown in Figure 5-66 (c).

The following pockets 2-8 show no large redistribution, but during the removal of pocket 9, there is once again a large elastic strain redistribution. Monitoring the elastic strain during the pocketing sequence and the pocketing sequence that produced a lower elastic strain redistribution was selected for the experimental trials.

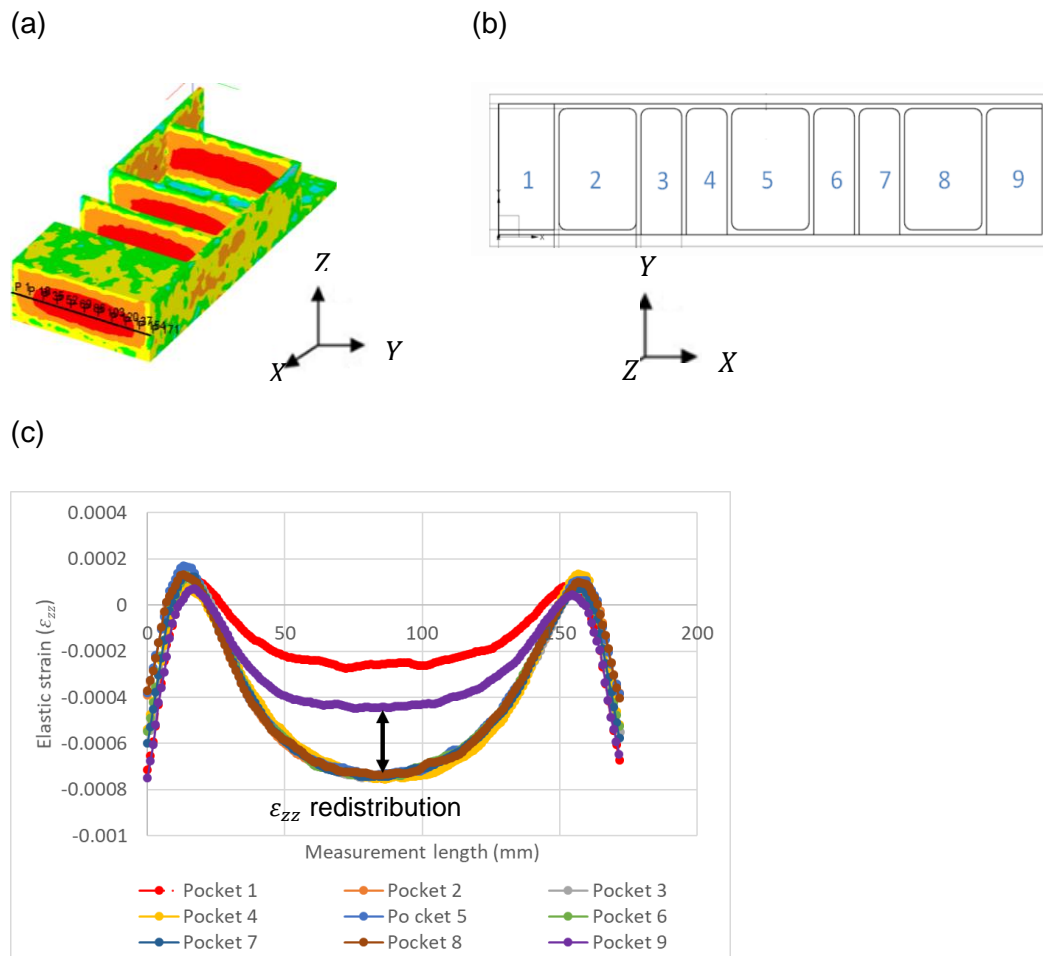


Figure 5-66: Residual stress redistribution rate during volume removal of pockets 1-9.

Chapter 5: Finite element modelling methodology

However only 27 pocket combinations were investigated as shown in Figure 5-67. The simulations were selected to initially predict the distortions of the most common sequence for machining the pockets, for example machining the pockets from a left to right sequence and vice versa (sequence 1 and 2 respectively).

Other variations consisted of machining the pockets starting from the mid-section of the part out towards the edges (sequence 4), or machining from outside of the part towards the mid-section (sequence 8).

Other alternatives of sequences were simulated to investigate the effect on the distortions. The pocket sequence number and distortion predictions are illustrated in Figure 5-67 and the pocket simulation sequence is shown in Table 5-11, from the highest distortion to the lowest. The criteria for choosing the “improved” model was the model that predicted the bending (Z distortions) within ± 0.3 mm at the bottom face while the model that predicted distortions above this tolerance was chosen as the worst-case scenario. More pocket sequence models need to be simulated to be confident that the proposed model is the optimum one.

From the distortion predictions Figure 5-67 (c), sequence 1 showed the highest bending distortion range (maximum – minimum displacement) while sequence 27 showed the lowest distortion range, therefore, sequence number 1 and 27 were used in the experimental analysis to compare with the numerical predictions.

The residual stress redistribution during the pocketing of these two sequences is shown in detail in Appendix A. Note that for the remaining sections in this report, sequence number 1 will remain as sequence 1 while sequence 27 will be referred to as sequence 2.

Chapter 5: Finite element modelling methodology

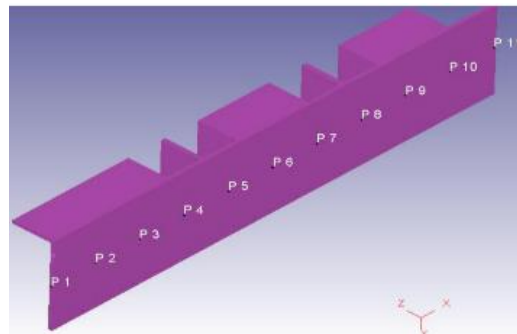
In summary, from Table 5-11 and Figure 5-67, it can be concluded:

- Sequence 1 had the highest bending distortion while sequence 27 had the lowest bending distortion, therefore these will be used for the experimental trials.
- Sequences 1 and 2, 8 and 27 predict different distortions considering that they are inverse sequences.
- Initially generation of closed pockets 2 or 5 (as seen in sequences 3, 4, 6, 10, 16) caused a higher distortion compared to initially generating closed pocket 8 (as seen in sequences 22 - 25).

(a)



(b)



(c)

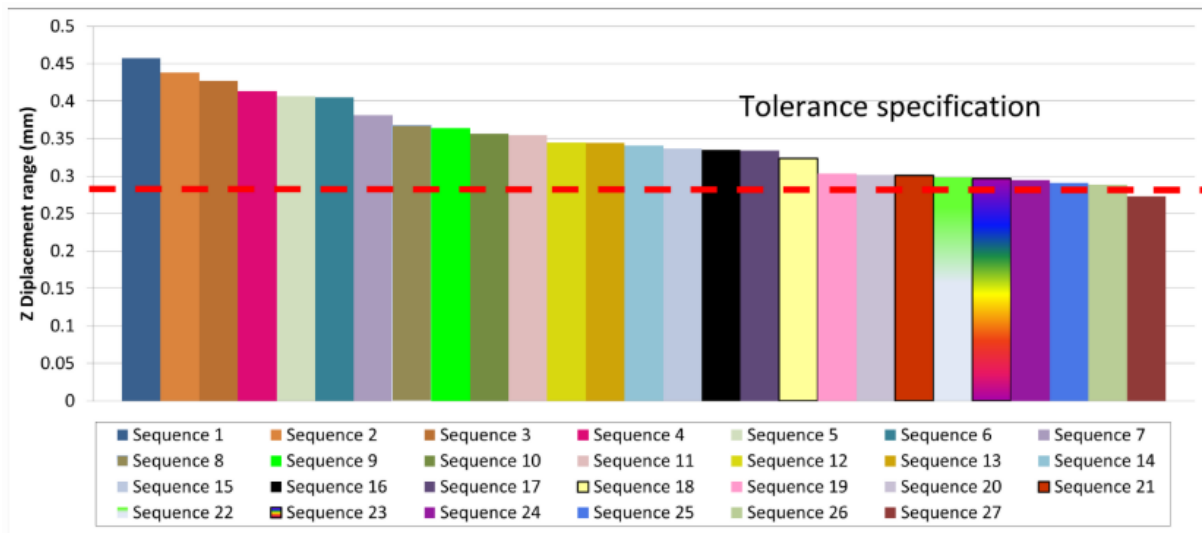


Figure 5-67: Pocket removal analysis; (a) Pocket numbers, (b) Measurement locations, (c) Sequence displacement range comparison.

Chapter 5: Finite element modelling methodology

Table 5-11: Pocket sequence.

Sequence number	Pocket sequence order	Z distortion range (mm)
1	1, 2, 3, 4, 5, 6, 7, 8, 9	0.45752
2	9, 8, 7, 6, 5, 4, 3, 2, 1	0.43839
3	5, 8, 2, 9, 7, 6, 4, 3, 1	0.42713
4	5, 1, 9, 2, 8, 3, 7, 4, 6	0.41320
5	6, 1, 2, 3, 4, 5, 7, 8, 9	0.40649
6	2, 8, 5, 1, 9, 3, 7, 4, 6	0.40524
7	9, 8, 7, 6, 1, 2, 3, 4, 5	0.38118
8	9, 1, 8, 2, 7, 3, 6, 4, 5	0.36778
9	1, 9, 7, 3, 2, 8, 6, 4, 5	0.36396
10	5, 4, 6, 3, 7, 2, 8, 1, 9	0.35638
11	8, 1, 2, 9, 3, 7, 4, 6, 5	0.35493
12	1, 5, 9, 2, 8, 3, 7, 4, 6	0.34521
13	2, 9, 1, 3, 8, 4, 7, 5, 6	0.34468
14	1, 8, 2, 3, 4, 5, 6, 7, 9	0.34107
15	9, 8, 7, 6, 5, 1, 2, 3, 4	0.33689
16	5, 2, 8, 1, 9, 7, 6, 3, 4	0.33506
17	1, 9, 2, 3, 4, 6, 7, 8, 5	0.33412
18	1, 9, 4, 6, 3, 7, 2, 8, 5	0.32363
19	4, 9, 1, 8, 5, 7, 3, 2, 6	0.30372
20	6, 7, 8, 9, 1, 5, 2, 4, 3	0.30144
21	1, 9, 3, 7, 2, 8, 4, 6, 5	0.30088
22	8, 1, 9, 2, 7, 3, 6, 4, 5	0.29797
23	8, 2, 3, 4, 5, 6, 7, 1, 9	0.29634
24	8, 5, 2, 4, 6, 3, 7, 9, 1	0.29486
25	8, 2, 5, 4, 6, 3, 7, 9, 1	0.29094
26	1, 8, 2, 5, 4, 6, 3, 7, 9	0.28828
27	1, 9, 2, 8, 3, 7, 4, 6, 5	0.27293

5.2 Summary and discussion

In this section, the finite element methodology was presented. The heat transfer coefficient was experimentally calculated using an inverse function from the FE software. Following this, a quenching simulation was developed and validated using published data [28] to provide confidence in the finite element methodology in this study.

Once the methodology was validated, a heat treatment model was simulated for different coupon geometries and a representative billet. Following the simulation of the heat treatment simulation, the following machining strategies were simulated to understand their influence in machining distortion:

- Axial depth of cut
- Radial depth of cut
- Tool path strategies
- Tool path entry
- Pocketing sequence
- Part offset
- Billet orientation

From all the different analysis, it was found that the machining distortion could be controlled by controlling residual stress redistribution by managing three main factors (Equation 5-30):

- The residual stress of the billet prior to material removal (σ_{pre})
- The volume of material removal or MRR (cm^3)
- The location of material removal (the x , y and z coordinate).

The material removal rate can be calculated [267] as shown in Equation 5-30:

$$MRR = \frac{\text{Axial depth of cut } (a_p) \times \text{Radial depth of cut } (a_e) \times \text{Table feed } (\text{mm}/\text{min})}{1000}$$

Equation 5-30: Residual stress redistribution relationship during material removal.

From the above bullet points, the most important role is the magnitude of the residual stress in the layer of material to be removed since the distortion magnitude will be highly influenced by this. The second bullet point can increase the distortion magnitude and in some cases can be defined with a linear relationship.

Chapter 5: Finite element modelling methodology

Specifically, to minimize distortion during material removal, stress redistribution per unit volume should be low as shown in Equation 5-31, where σ_{ij} is the residual stress prior to machining and V is location of material removal. Therefore, during material removal simulation, the stress distributions will be monitored.

$$\frac{d\sigma_{ij}}{dV} \cong 0$$

Equation 5-31: Residual stress redistribution relationship during material removal.

In the next section, the experimental methodology used to validate these finite element models will be presented.

6 Experimental methodology

6.1 Flow stress calculation

In this chapter, the development for AA7050 material data at elevated temperatures is generated. While AA7050 has well developed properties in typical operating ranges, to successfully model the quench process it is necessary to know the stress-strain properties of the metal at the elevated transient temperatures of the actual quench process. When combined with the quench thermal loading this allows solution for the correct residual stresses imparted. During water quenching of aluminium blocks, large thermal gradients between the surface and the specimen centre lead to a through-thickness elastic strain gradient. If the cooling rate is sufficiently high, the yield strength of the material will be locally exceeded and small inelastic strains will result. The inelastic (or plastic) strain leads to a residual stress field in the quenched component, which may have implications toward distortion during final machining operations.

In order to predict the residual stresses that may result from quenching, it is necessary to understand the stress-strain behaviour of the aluminium alloy 7050 (AA 7050). As the yield strength of metals and alloys is sensitive to both temperature and strain-rate, it is essential to perform testing at a range of temperature and strain-rates since residual stress forms at these ranges. Most importantly, the accuracy of the residual stress FEA model depends on obtaining this stress-strain data.

On-cooling tensile test experiments are necessary to measure the at temperature stress- strain behavior and enable calculation of the resulting residual stress. Therefore, to acquire there stress-strain data, tensile test experiments were performed at the University of Sheffield Material Department. The testing machine and coupon used for the mechanical tests is shown in Figure 6-1.

The specimen was located inside of heating helicoid in the testing machine and the specimen was mounted on the grips of the Arbitrary Strain Path (ASP) mechanical testing rig.

Chapter 6: Experimental methodology

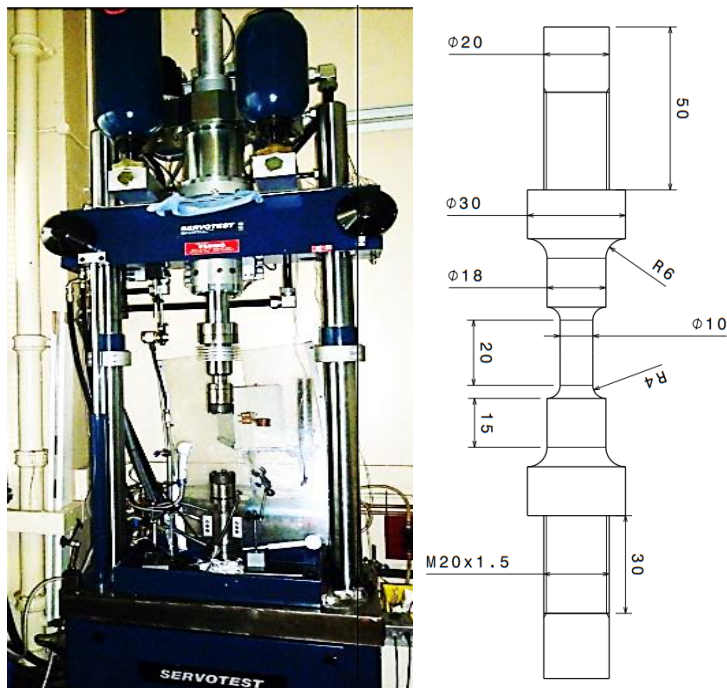


Figure 6-1: (a) Experimental test machine, (b) coupon for material characterization tests.

Three thermocouples were mounted on the test specimen (Figure 6-2), one was placed outside of the gauge section (T_L) and other two inside of the gauge section (T_T , T_M) to survey temperature.

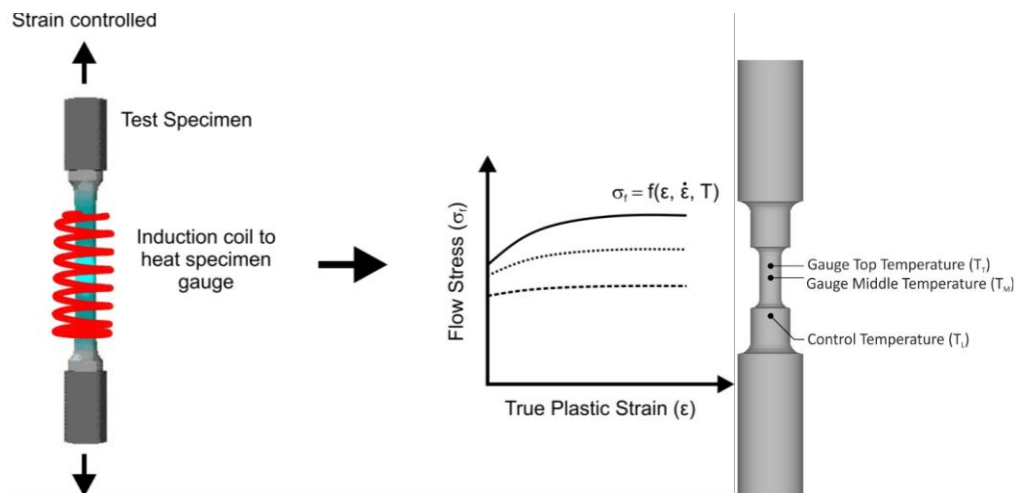


Figure 6-2: Illustration of the test specimen geometry employed for the on-cooling tensile tests.

The heating helicoid was then heated up to solution heat treatment temperature of $477^\circ\text{C} \pm 5^\circ\text{C}$ with a ramp rate of $5^\circ\text{C}.\text{min}^{-1}$. Once the target temperature was reached, the coupon was placed in the heating helicoid and held to stabilize the temperature.

Chapter 6: Experimental methodology

On-heating temperature distributions along the coupon gauge length is shown in Figure 6-3. It can be seen that there was no large thermal variation between the middle and the top of the coupon with a maximum temperature range is 8°C across the coupon. Equivalently, the on-cooling temperature-time plot (Figure 6-3) showing the variation in temperature between the centre of the gauge (T_M) and control thermocouple temperature (T_L). The coupon was rapidly cooled using compressed air to a target temperature of 425°C, held for 15 seconds and further air cooled to a temperature of 360°C. Similarly, the coupon was held at 360°C for 15 seconds and further cooled down to room temperature. No tensile straining was performed during this test.

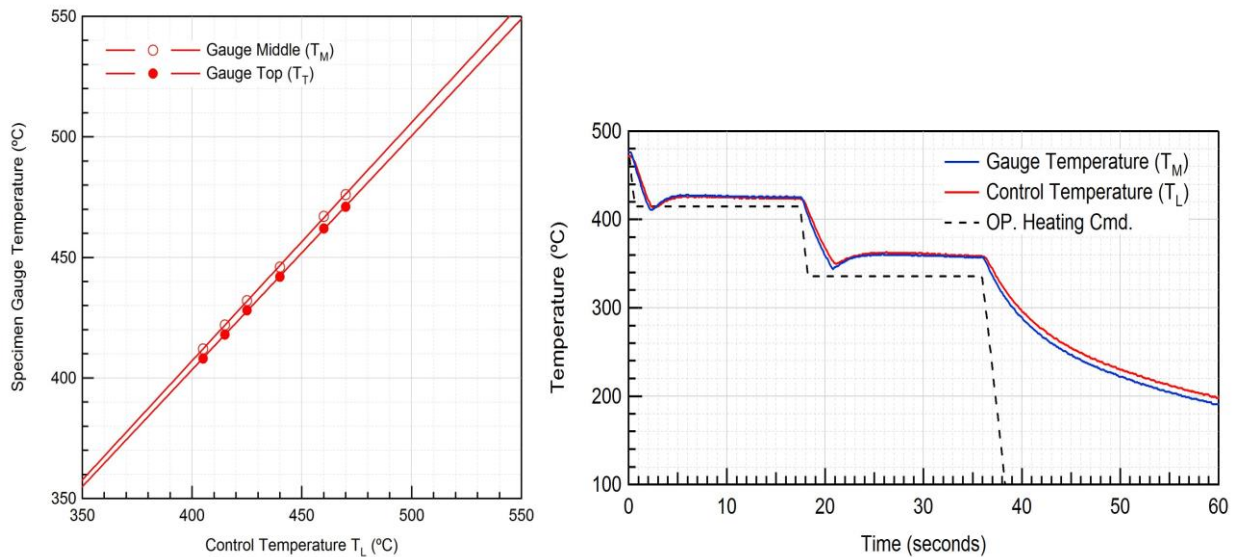


Figure 6-3: Temperature-time plot during testing of the coupon during: (a) On-heating and (b) On-cooling.

Further from the initial tests, isothermal tests was performed for each target temperature and the strain rate selected (Table 6-1). Three temperatures and strain rates were selected and tested for the given temperature. Each test condition was performed twice and 18 specimens was tested. The mechanical data was input into DEFORM as tabulated data.

Chapter 6: Experimental methodology

Table 6-1: Experimental Matrix.

Strain Rate →	0.0001 s ⁻¹	0.001 s ⁻¹	0.01 s ⁻¹
Temperature ↓			
477°C			
450°C			
425°C			
250°C			
25°C			

	No testing
	Tentative testing

The load vs. displacement curves was recorded and stress and strain curves were calculated from the gauge. Typical stress-strain data for the forged condition taken during this experiment are shown in Figure 6-4 and Figure 6-5. The figures illustrate the true stress/true strain at multiple strain rates. The strain rates and temperatures are populated based on the experimental matrix. Strain rate sensitivity is also addressed (Figure 6-5) as it may be needed to interpolate between strain rates.

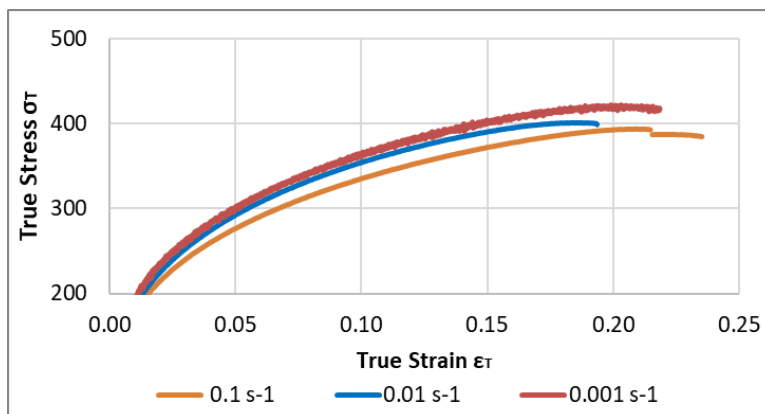


Figure 6-4: Aluminium 7050 True Stress Strain in as Forged Condition.

Chapter 6: Experimental methodology

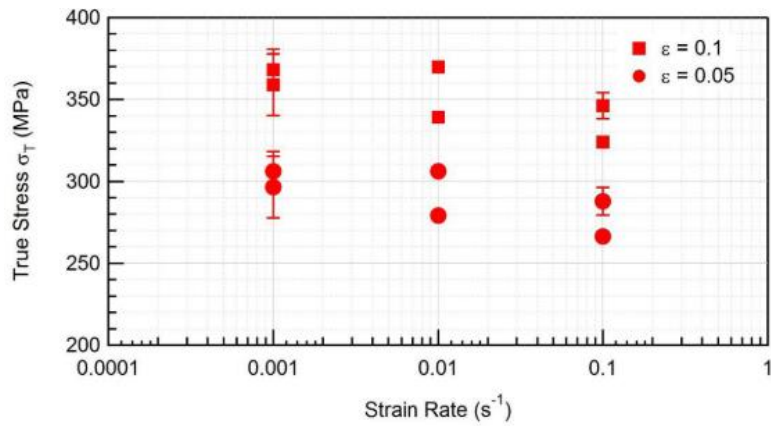


Figure 6-5: Strain rate sensitivity for aluminium 7050 Material data from the forged condition.

Similarly, the constitutive data for the solution heat-treated and water quenched condition is shown in Figure 6-6 for the two strain rates. The strain rate sensitivity is shown in Figure 6-7.

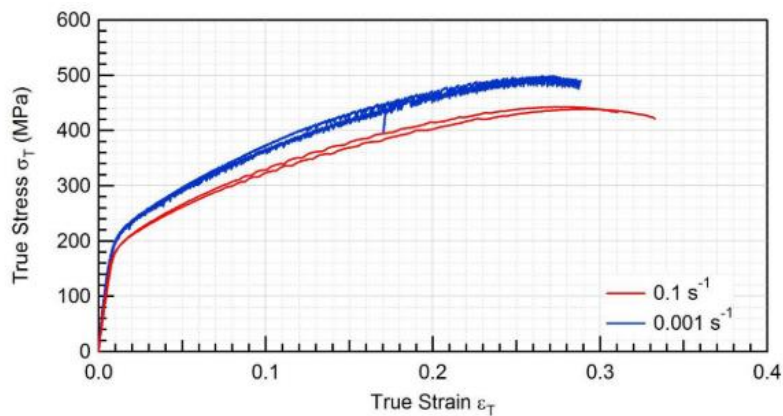


Figure 6-6: Aluminium 7050 Material data from the solution heat-treated and water quench condition.

Chapter 6: Experimental methodology

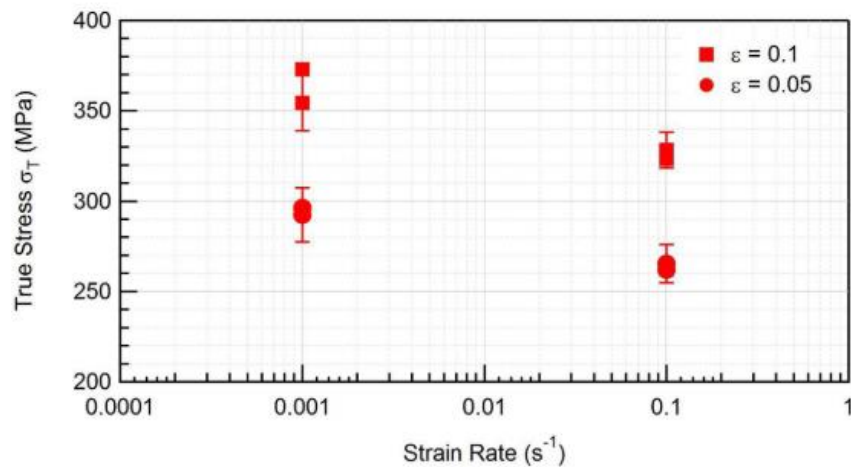


Figure 6-7: Strain Rate Sensitivity in aluminium 7050 Material data from the solution heat-treated and water quench condition.

The results of the tensile tests obtained at higher temperatures were not reasonable due to some problems with the testing machine, and due to the super plastic behaviour of this aluminium alloy. To overcome this, compression testing has been suggested to obtain the flow stress for this alloy. Therefore as a future work, compression tests will be performed to represent the mechanical behaviour of the material for the quenching process.

In this investigation, material data from compression tests were therefore taken from Luo et al (Figure 6-8 and Figure 6-9) and combined with the experimental test data collected at the materials department for the for the modelling predictions.

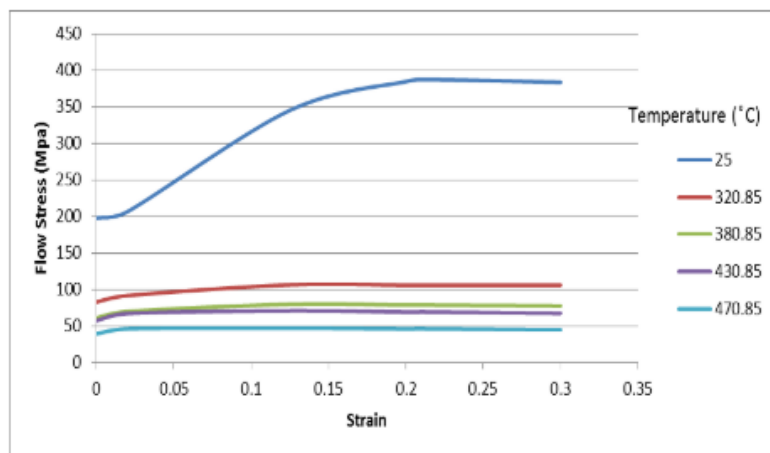


Figure 6-8: Integrated Flow stress calculation from [268] and Experimental results from Sheffield University Materials department with strain rates for 0.1.

Chapter 6: Experimental methodology

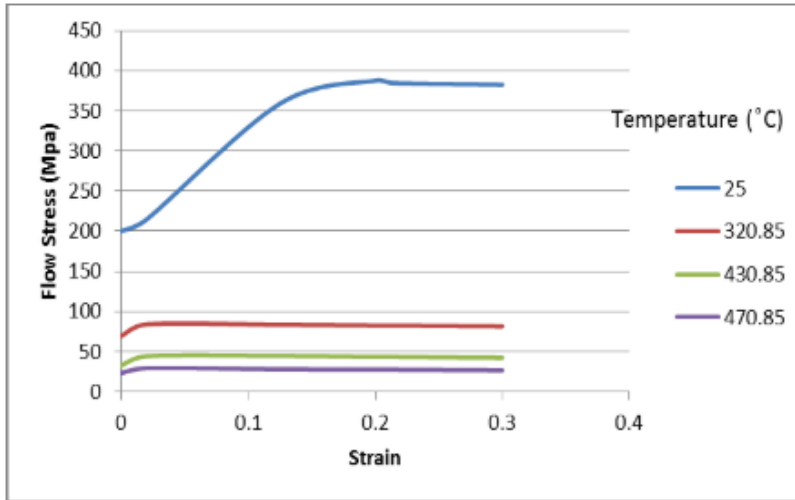
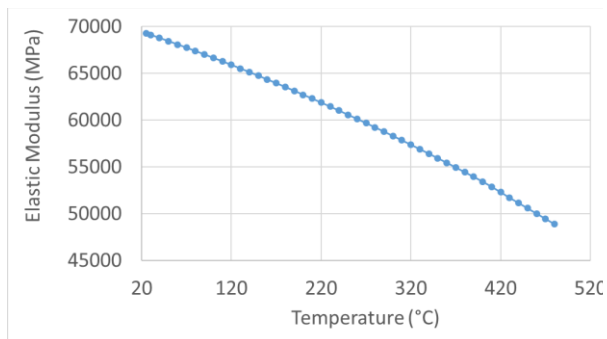


Figure 6-9: Flow stress calculation from [268] and Experimental results from Sheffield University Materials department with strain rates for 0.01.

6.2 Elastic material data

The material used for the simulation of the elastic strains is shown in Figure 6-10 and Figure 6-11.

(a)



(b)

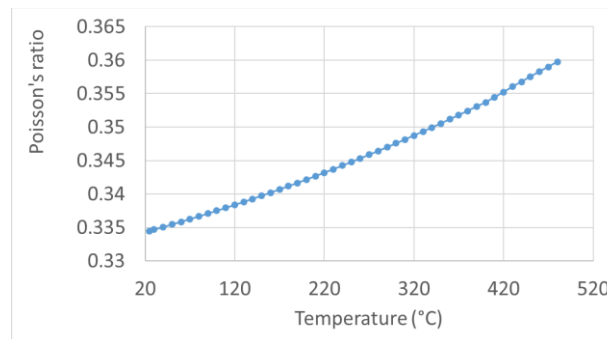


Figure 6-10: Material input data for quenching simulation; (a) Elastic modulus, (b) Poisson's ratio.

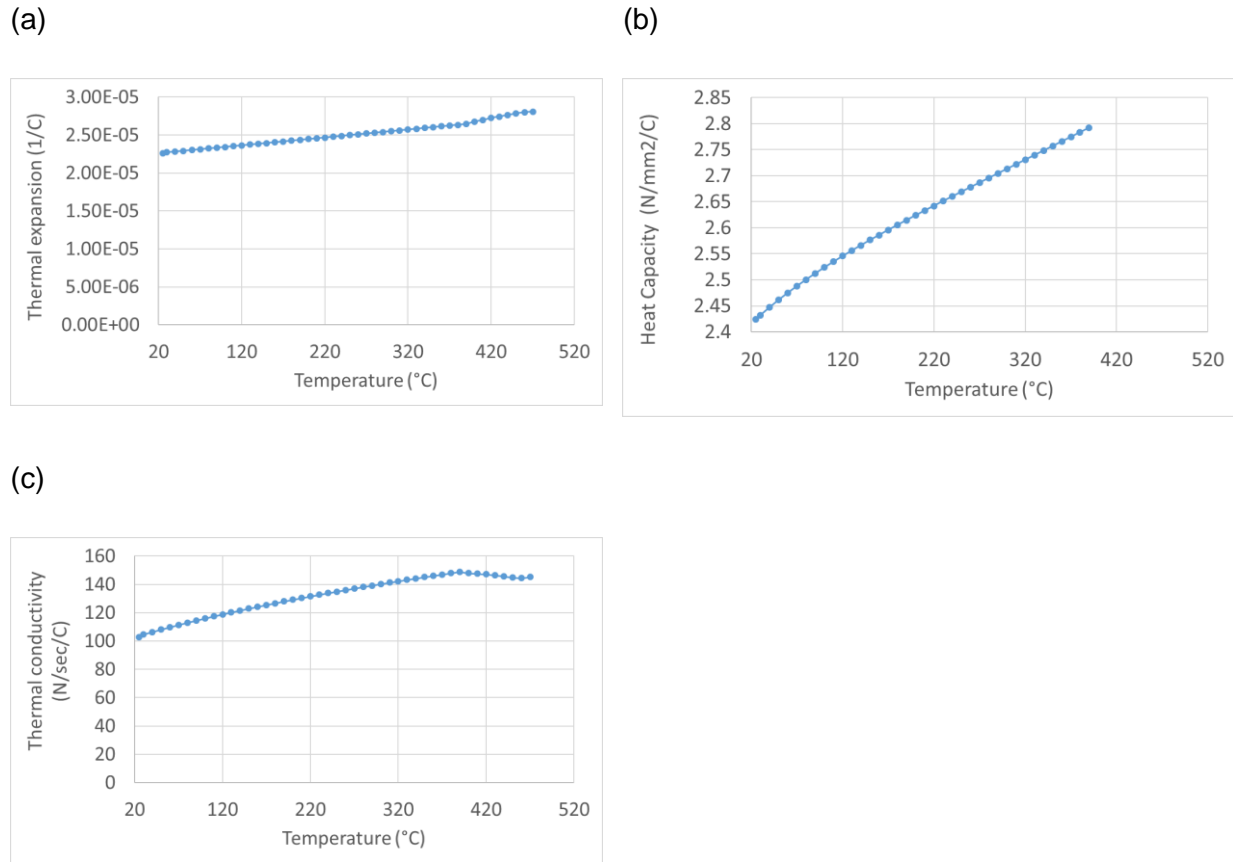


Figure 6-11: Material input data for quenching simulation; (a) Thermal expansion, (b) Heat Capacity, (c) Thermal Conductivity.

6.3 Heat treatment experimental set up

Experimental heat treatment tests were carried out to validate the simulation of the finite element model for each test case. The heat treatment process were done according to the AMS Standard for aluminium Heat Treatment [55] and the residual stresses were measured after each heat treatment for every test case.

6.3.1 Thermocouple set up

Following the advice from the FEA on the appropriate thermocouple locations, thermocouples were inserted into the block as shown in Figure 6-12. To ensure that the thermocouple maintained their pre-set positions, conductive cement was used to bond the thermocouple into the holes. In addition, the wire tails were bent and wired together to ensure that they were not loosened during quenching.

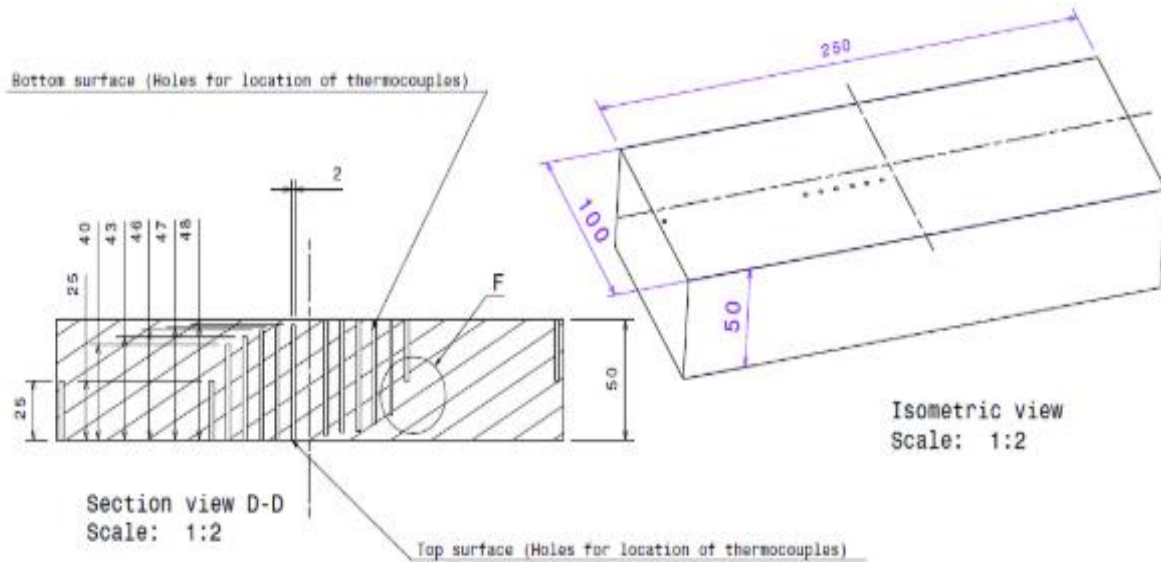


Figure 6-12: Thermocouple location on AA7050 block.

6.3.2 Solution heat treatment and quenching set up

6.3.2.1 Calculation of the heat transfer coefficient trials

Ten aluminium alloy 7050 coupons (labelled A-J) were machined to 250 x 100 x 50 mm from two billets supplied by the Boeing Company. Prior to heat treating, the blocks were degrease to prevent interference of the results during the quenching process as highlighted in [58]. The furnace temperature was set to the solution heat treatment temperature of $477^{\circ}\text{C} \pm 3^{\circ}\text{C}$ with a ramp rate was set to $5^{\circ}\text{C}.\text{min}^{-1}$. The furnace was allowed to stabilize for one hour once the solution temperature was reached. Once the furnace temperature was stabilized, the blocks were placed inside the furnace and heat up of the block to the solution heat treat temperature was monitored using K Type thermocouples (Figure 6-13).

Because to the slow nature of the heating up the blocks to solution temperature, all the thermocouples were similar and produced a heat up curve similar to below. Upon achieving the solution temperature, the block was held for three to four hours in accordance with the AMS aluminium Heat Treatment Standard [55] at that temperature to ensure proper solution treatment prior to quenching (W Condition solution) (Figure 6-13). The air temperature in the furnace and on the AA7050 block was monitored throughout the experimental trials Figure 6-14 (a).

Chapter 6: Experimental methodology

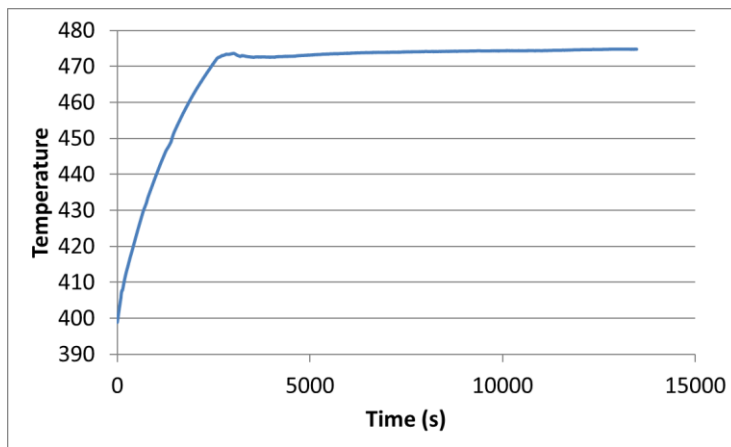


Figure 6-13: Heating up and holding temperature measurements for typical thermocouple.

In parallel, a quench bath of dimensions (length=740 mm, width=300 mm, height=400 mm), was filled with a quenchant (water) (Figure 6-14 (b)) and the water temperature was measured prior to quenching. Furthermore, a steel grate was placed in the quench tank elevated from the bottom of the tank so that the block would be cooled equally from the top and bottom during quenching. Once the holding times were satisfied, the AA7050 block was removed from the furnace and allowed to air cool for 10 seconds as specified in [58].

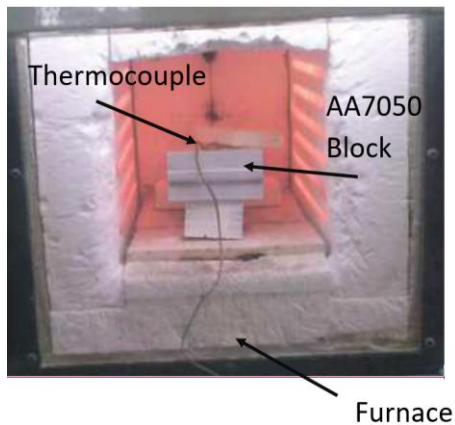


Figure 6-14: Experimental during solution heat treatment.

The AA7050 block(s) was then submerged into water with the thermocouples to record the thermal gradient within different regions of the block. This information was used to calculate the heat transfer coefficients in the case of symmetrical residual stress coupon. In addition to this, it was ensured that there was no agitation of the water prior to quenching, as this would influence the results. The block was then removed from the water after 600 seconds of quenching.

a)



(b)



(c)



Figure 6-15: Experimental set up for: (a) Quench tank (b) Top view of the AA7050 block in quench tank, (c) Post quenched block with thermocouples [13] inserted in coupon.

6.3.2.2 Symmetrical and asymmetrical rectangular coupon

Nine aluminium alloy 7050 coupons were machined to 250 x 100 x 50 mm from two billets supplied by the Boeing Company. Two ridges were then machined on the middle of the side faces of the coupon with dimensions of 5 x 10 mm. This was in order to leave a reference measurement location where machining distortion measurements would be monitored during the machining using different strategies.

Chapter 6: Experimental methodology

In order to generate symmetric and asymmetric residual stress profiles, five coupons were heat-treated independently (Figure 6-16 (a)) while the other four were physically bolted together for heat treatment (Figure 6-16 (b)). Prior to heat treating, the blocks were degreased prior to heat treatment.

All of the coupons were heated to $477\text{ }^{\circ}\text{C} \pm 3^{\circ}\text{C}$ in the same type of furnace and quenched in normal tap water at $20\text{ }^{\circ}\text{C}$ ($\pm 3\text{ }^{\circ}\text{C}$) although the solution holding time for the double bolted blocks were doubled. The quenching was performed at the University of Sheffield's Materials Science and Engineering department according to the Heat Treatment Standard for Aerospace alloys AMS 2770G (W Condition solution). The furnace was left heated overnight prior to the tests at 560°C with a ramp rate of $2000/\text{s}$. The temperature on the surface of the coupons was monitored by a thermocouple. The air transfer of the coupon to the quench tank was kept to a maximum of 7-10 seconds. The operator's coupon handling technique during the quenching procedure was monitored extensively with images and videos taken for each process for data analysis and repeatability.

It should be noted that although nine coupons were heat treated, two of the coupons (6 and 7) generated cracks due to the large amount of stresses during the quenching; and coupon 3 was cut in half for contour RS measurements. This issue has already been introduced in the literature review.

(a)



(b)

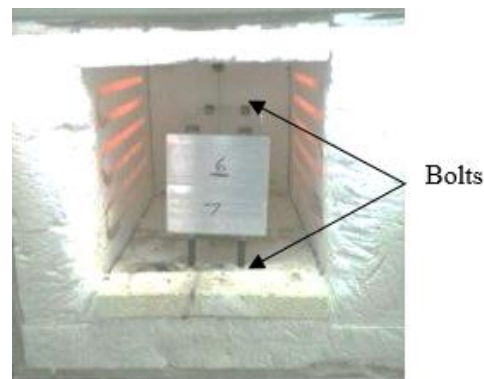


Figure 6-16: Experimental set up for: (a) Symmetrical rectangular coupon, (b) Asymmetrical rectangular coupon.

Chapter 6: Experimental methodology

The quenching of the asymmetrical blocks is shown in Figure 6-17. It can be seen that a similar set up was followed to ensure that the heat transfer coefficient would be similar as the previous trials.



Figure 6-17: Quench of the asymmetrical block.

6.3.2.3 Rectangular pocket blocks

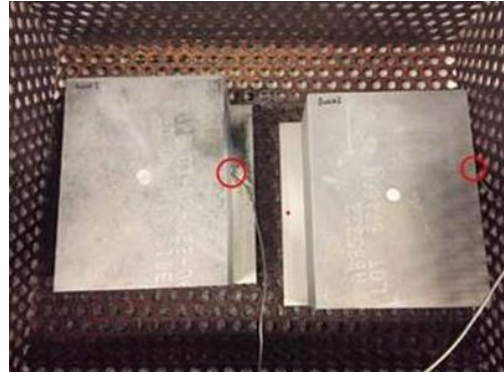
Similarly to the previous coupon, four aluminium 7050 alloy rectangular blocks taken from a large slab of aluminium 7050 (Figure 5-35 (a)). Prior to heat treating, the blocks were degreased prior to heat treatment and the heat treatments of the blocks were performed in an industrial scale furnace. The heat treatment process is shown in Figure 6-18. The blocks were placed in a heat treatment cage (Figure 6-18 (a)). In addition to this, thermocouples were placed on the blocks similar to the previous trials (Figure 6-18 (b)). The blocks were solution heat treated at 477 °C for four and a half hours and quenched in cold water at 20 °C as shown in (Figure 6-18 (c)). From this figure, the block can be seen highlighted in red box, the cage in blue and the thermocouple in white. Finally, the image of the quenching vapour can be seen in Figure 6-18 (d). The air transfer was 10 seconds.

Chapter 6: Experimental methodology

(a)



(b)



(c)



(d)



Figure 6-18: Heat treatment set up for rectangular coupons: (a) Blocks set up (b) Thermocouple on blocks, (c) Air transfer of blocks, (d) Quenching of blocks.

The company that performed these heat treatments were Alloy Heat Solutions who are certified in aluminium alloy heat treatments in the United Kingdom. The furnaces were calibrated according to AMS2750-E, industrial instrument type C, to ensure the furnace delivers temperature uniformity based on air temperature measurements from furnace sensors positioned at points which best represent the hottest and coldest points of the furnace workzone, thus negating the need for load sensors. Further information on the quenching process is shown in Table 6-2 and Figure 6-19.

Chapter 6: Experimental methodology

Table 6-2: Solution heat treatment process.

Process name	Initial temperature (°C)	Duration (h)	Quenching medium	Final temperature (°C)
Heating up	20	1	Air	477
Solution heat treatment	477	4 ½	Air	477
Quenching	477	10	Water	20

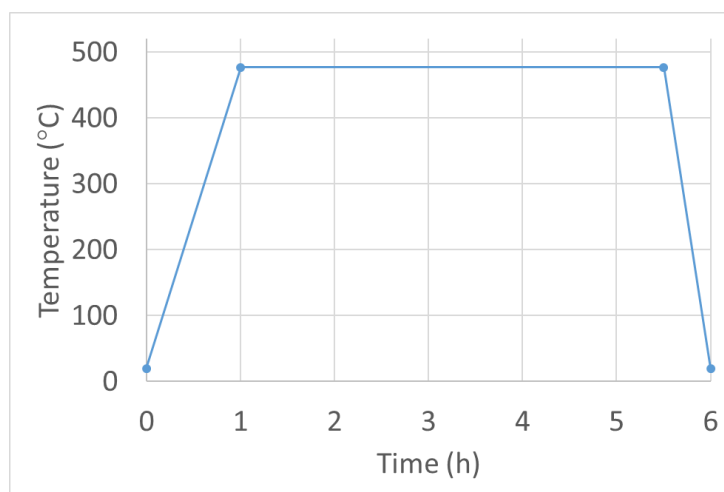


Figure 6-19: Graphic illustration of the solution heat treatment condition.

6.3.2.4 Representative billets

The study initially involved solution heat-treating of twelve Al 7050 billets to generate high residual stresses (RS), which were then machined to the nominal condition followed by two pocketing strategies. Twelve aluminium alloy 7050 billets of dimensions (880 mm x 195 mm x 78 mm) were provided by the Boeing Company.

The as received condition of the billets were tempered at 477 °C for 2 hours 10 minutes (“O” condition). The billets were then degreased and reheat treated to condition T74 according to the AMS standard 2772 [262].

Chapter 6: Experimental methodology

The billets were held in solution temperature and aged with a two-step process (to avoid natural ageing). The process information is shown in Table 6-3 and illustrated in Figure 6-20. Similarly, Alloy Heat Solutions performed the heat treatments of the billets. The heat treatment was performed on a furnace named “Furnace 1A”. The billets were held in a cage during the solution heat treatment. Once they have been held in solution, the cage was lowered down automatically into the quench tank.

Table 6-3: Heat treatment procedure for representative part.

Process name	Temperature (°C)	Holding duration (h)	Quenching medium	Quenching temperature (°C)
Solution heat treatment	477	7 ½	Water	63
Ageing (step 1)	121	6	Air	20
Ageing (step 2)	177	10	Air	20

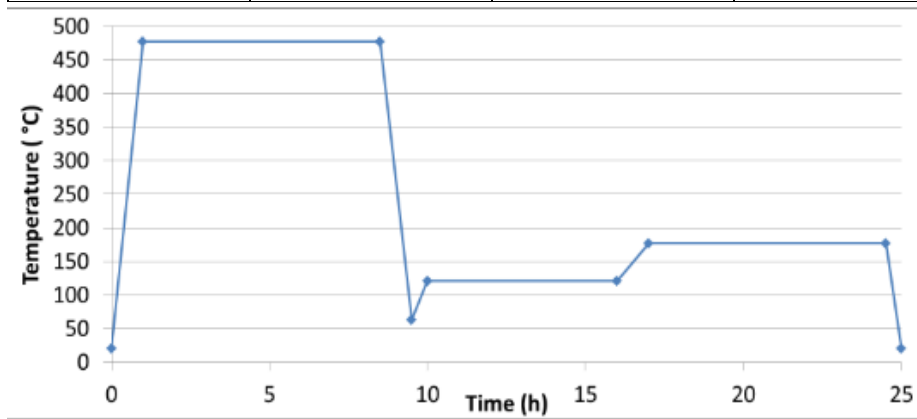


Figure 6-20: Process flow chart of the development of the model for pocketing strategies.

6.4 Residual stress measurements

6.4.1 Contour measurements

The contour measurements was performed by three different centers for each individual test pieces. The different measurements performed by the different centers is shown in Table 6-4. Due to proprietary information from all centers, it was not possible to present the a detailed set up of this technique but a general guideline is presented.

Table 6-4: Contour measurements performed by different centers.

Centre name	Test specimen measured
Hill Engineering	Rectangular coupon
AMRC with Boeing	Rectangular coupon Machined rectangular coupons Machined symmetrical coupons
AMRC with Boeing	Rectangular block
AMRC with Boeing	Billet

The set up used for the contour measurements is shown in Figure 6-21 and Figure 6-22. The test pieces were cut at the AMRC with Boeing using a Mitsubishi wire EDM Fx20 machine Figure 6-21 (a). Following the slitting of the test pieces, a Taylor Hobson Sutronic duo (Figure 6-21 (b)) was used to measure the surface roughness on both test pieces and it was found to be within the 10 - 100 μm) as defined by Prime et al [128].

Once the surface roughness was found to be satisfactory, 3D displacement scan using a GOM ATOS scanner as shown in Figure 6-22 (a) was used to measure the displacements on both test pieces caused during the slitting operation.

Chapter 6: Experimental methodology

To avoid any systematic or user errors, the scanner was calibrated according to the normal standard procedure and the test pieces were sprayed with white chalk spray and applied in accordance to BS EN ISO 571-1 [269].

Once the displacement scanning had completed and produced satisfactory results. The measurements were post processed and data points were extracted from the scan and imported into a MATLAB Graphical User Interface developed by the Process Modelling Group within the Advanced Manufacturing Research Centre with Boeing, was used to remove any errors and create an average profile from the two slit test pieces (Figure 6-22 (b)). Furthermore, using the displacement data was aligned to the coordinates of a 3D FE model created for the test piece. Once the data was aligned appropriately, the data was extracted and imported into the FE Model, the simulation was ran and the resulting residual stress is shown in Figure 6-22 (c).

To provide confidence in the GOM scan measurements, CMM was also performed alongside the GOM scan results and the resulting residual stresses were compared. It was found for the level of these stresses, the different between the two systems were minimal, and therefore the GOM scanner was utilized where necessary for further tests.

(a)



(b)

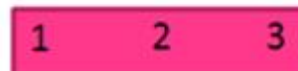


Figure 6-21: Contour measurement set up: (a) Wire EDM machine, (b) Surface roughness measurements.

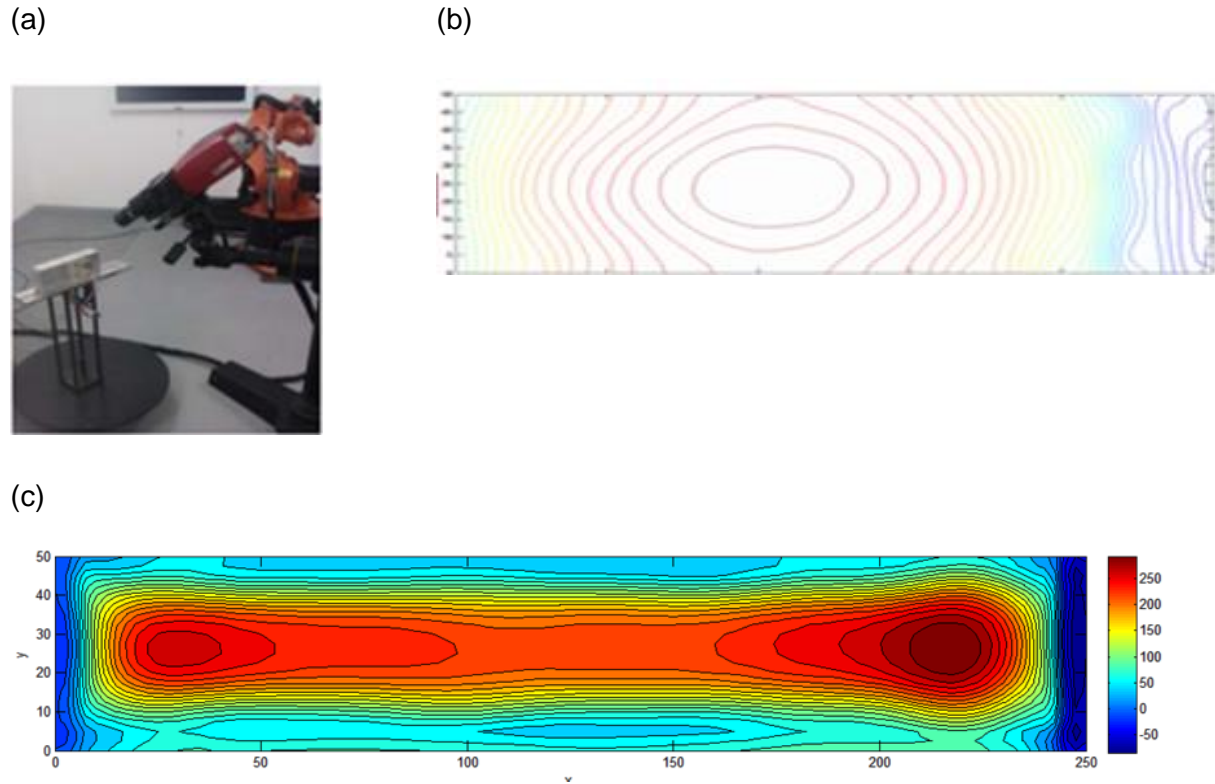


Figure 6-22: Contour measurement set up: (a) 3D displacement measurements, (b) Data handling in MATLAB, (c) Residual Stress Contour.

The contour method performed on the representative billet is shown in Figure 6-23.

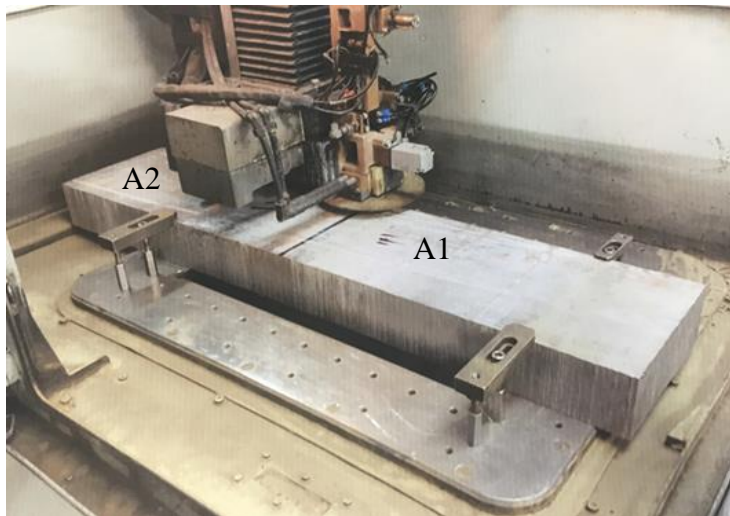


Figure 6-23: Slitting the billet into sections A1 and A2 using wire EDM.

6.4.2 Neutron diffraction

In order to measure the bulk residual stress/strain on the blocks, Neutron diffraction measurement technique was used. Similar to the contour method, the measurements were performed by different centers Table 6-5.

Table 6-5: Neutron diffraction measurements performed by different centers.

Centre name	Test specimen measured
Engin-X beamline, Rutherford Appleton Laboratory	Rectangular coupon
	Symmetrical coupons
Australia's Nuclear Science and Technology Organization (ANSTO)	Rectangular block
	Machined symmetrical coupon
	Machined asymmetrical coupon
	Billet
	Part offset

The measurements were taken at the Science and Technology Facilities Council's (ISIS) Rutherford Appleton Laboratory in Didcot, Oxford. The blocks were mounted at two orientations to measure the desired stress components (Figure 4-8 (b)) and they were positioned on top of each other in order to perform fast measurements and to maintain the same conditions during the analysis (Figure 4-8 (c)). Since information in the bulk of the block was required, reference coordinates were taken in the midpoint of the blocks calculated from the coordinates on the edge of each blocks in the x, y and z directions. These reference coordinates were then used to program the movement of the rotor directing it to measure the strain in each block.

Neutrons were then shot from the beam through the block and received by the collimators. The neutron scattering is then used to calculate the lattice spacing, and hence the strain on the block.

Chapter 6: Experimental methodology

Calculations by the beamline scientists have shown that 5 minutes per point will be needed to give an acceptable accuracy (under 50 $\mu\epsilon$) for the longest path lengths (75 mm) with a gauge volume of $3 \times 3 \times 3 \text{ mm}^3$. Measurements for the orthogonal stress components along three orthogonal line scans in each block (i.e. in X, Y and Z directions) with 20 points in each line.

Accuracy of the measurements depends on the measurement time; generally, doubling the counting time, reduces the error by a square root of two. In order to get the three strain components needed to find the corresponding stresses, each location would need to be measured with two coupon orientations, so the total number of runs per block would be $2 \times 3 \times 20 = 120$, or 10 hours per block with two hours for setting up the coupons on the beam line.

The calculation used for the calculation of the normal stresses in the X, Y and Z direction respectively are shown in Equation 6-1 where E_{hkl} is the Elastic Modulus, ν_{hkl} is the poisons ratio along the crystal grain structure. The strains $\epsilon_{xx}, \epsilon_{yy}, \epsilon_{zz}$ (Equation 6-2) are the strain in the X, Y and Z direction respectively which are calculated by the d and d_0 in the respective directions.

$$\lambda = \frac{E_{hkl}}{(1 + \nu_{hkl})(1 - 2\nu_{hkl})}$$

$$\begin{aligned}\sigma_{XX} &= \lambda (1 - \nu_{hkl})\epsilon_{XX} + \nu_{hkl}(\epsilon_{ZZ} + \epsilon_{YY}); \\ \sigma_{YY} &= \lambda (1 - \nu_{hkl})\epsilon_{YY} + \nu_{hkl}(\epsilon_{ZZ} + \epsilon_{XX}); \\ \sigma_{ZZ} &= \lambda (1 - \nu_{hkl})\epsilon_{ZZ} + \nu_{hkl}(\epsilon_{XX} + \epsilon_{YY});\end{aligned}$$

Equation 6-1: Stress calculation in X, Y and Z directions.

$$\begin{aligned}\epsilon_{XX} &= \left(\frac{d - d_0}{d_0}\right) 10^{-6}; \\ \epsilon_{YY} &= \left(\frac{d - d_0}{d_0}\right) 10^{-6}; \\ \epsilon_{ZZ} &= \left(\frac{d - d_0}{d_0}\right) 10^{-6};\end{aligned}$$

Equation 6-2: Strain calculation in X, Y and Z directions.

(a)



Rotating Fixture

(b)

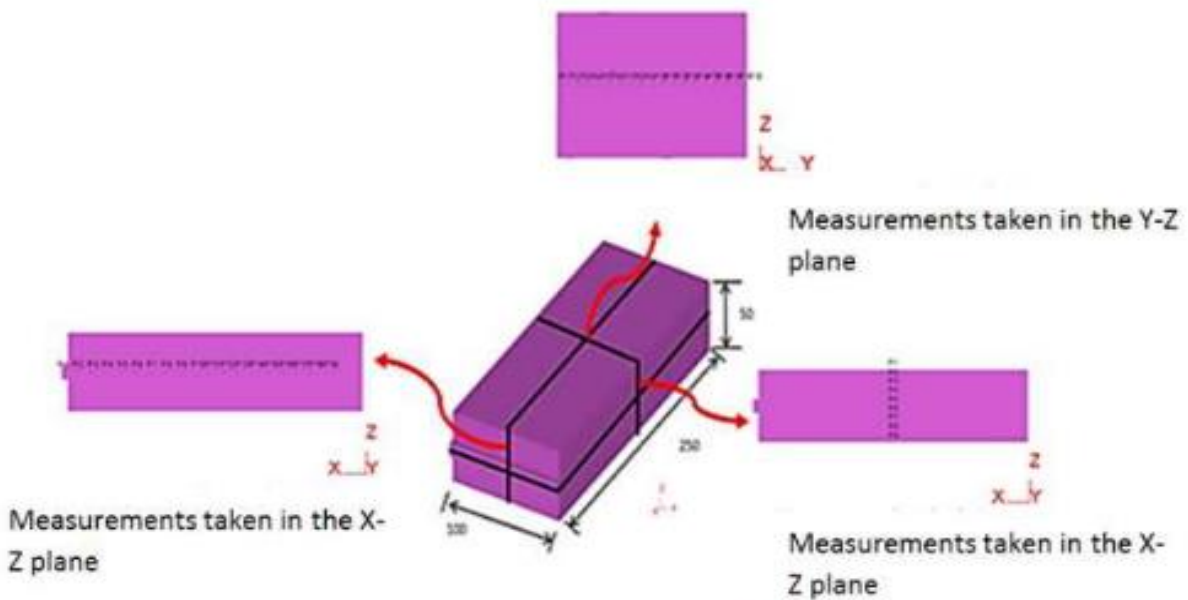


Figure 6-24: Residual stress measurement carried out using Neutron diffraction showing (a) Block fixturing (b) Measurement strategy.

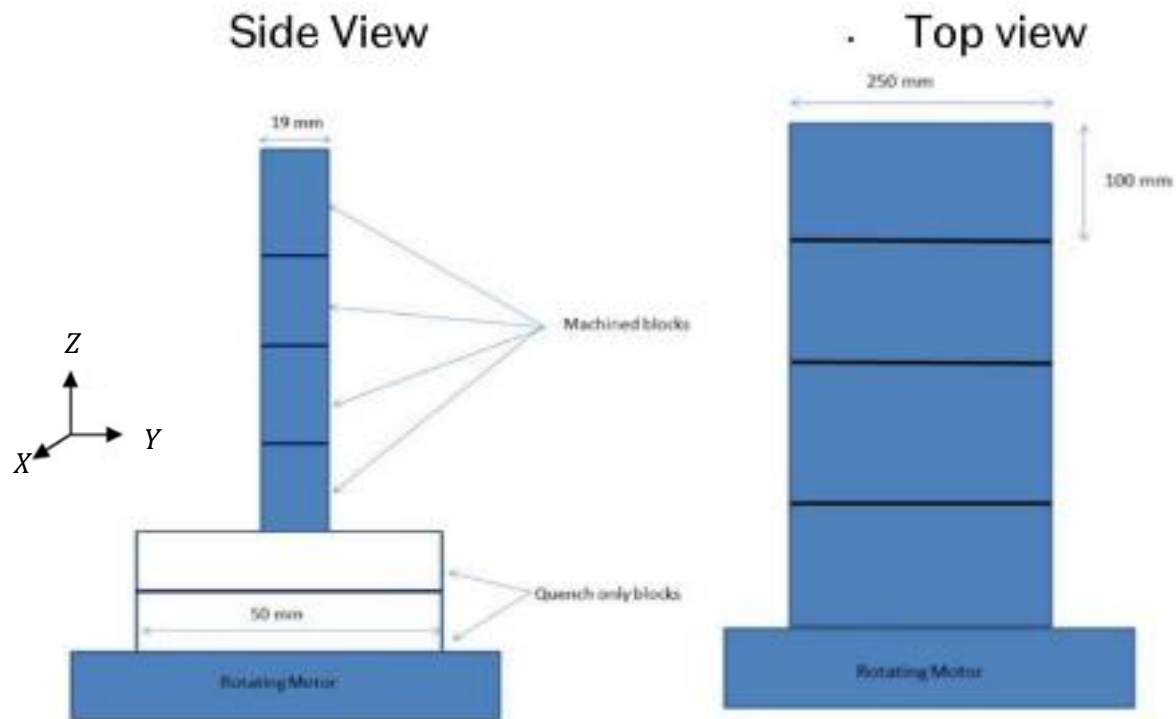


Figure 6-25: Block orientations for residual stress measurements.

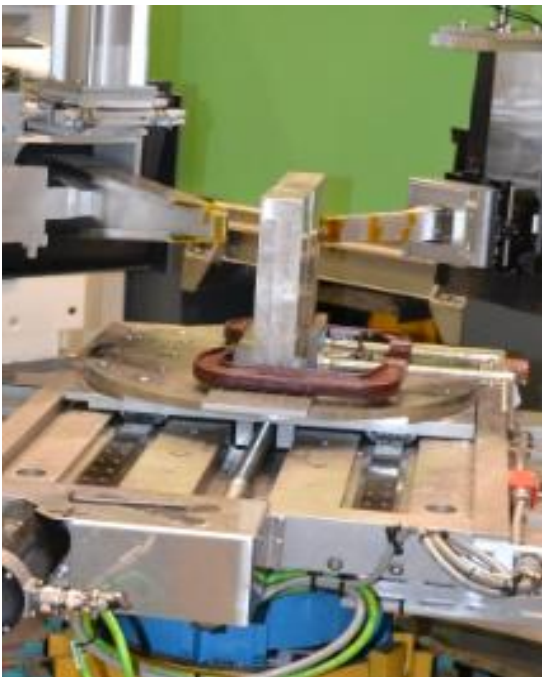
Diffraction conducted using KOWARI instrument at ANSTO considering Al (3 1 1) atomic plane. The summary of the measurement parameters used by both Engin-X and ANSTO is shown in Table 6-6. The measurements of the coupons and billets in ANSTO is shown in Figure 6-27 and the billet (Figure 6-28, Figure 6-29). Markers were used to distinguish the top and bottom face of the billet in order to relate it to the measurement positions. The neutrons were approached from the Y direction (measuring the σ_{XX} and σ_{ZZ}) and the Z direction (measuring the σ_{XX} and σ_{YY}). The orientation and the coordinates used for the measurements of the rectangular coupons and the billets as shown in Figure 6-27 and Figure 6-29. The measurements were performed in three orientations along the main coordinate systems (σ_{XX} , σ_{YY} and σ_{ZZ}) and in the dash line locations as detailed in Figure 6-29.

Chapter 6: Experimental methodology

Table 6-6: Diffraction parameters performed by different centers.

	Engin-X (Quench blocks)	ANSTO (Quench blocks)	ANSTO (Phase 1 machined blocks)	ANSTO (Phase 2 machined blocks)	ANSTO (Billet measurement)
Elastic Modulus (E_{311})	70 GPa	71.3 GPa	71.3 GPa	71.3 GPa	71.3 GPa
Poisson's ratio (ν_{311})	0.33	0.354	0.354	0.354	0.354

(a)



(b)

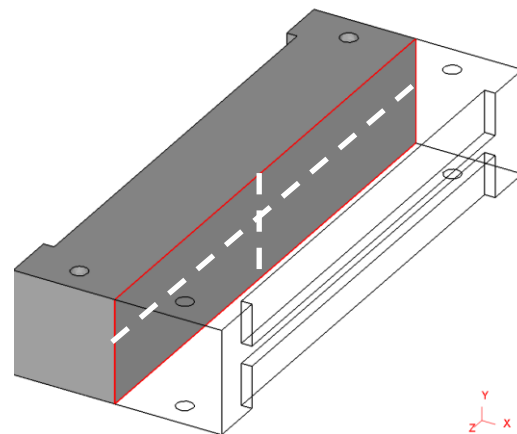


Figure 6-26: Measurement locations using neutron diffraction for the coupons: a) Mid width line direction, (b) Mid length line direction. Note that dimensions in the figures are in mm.

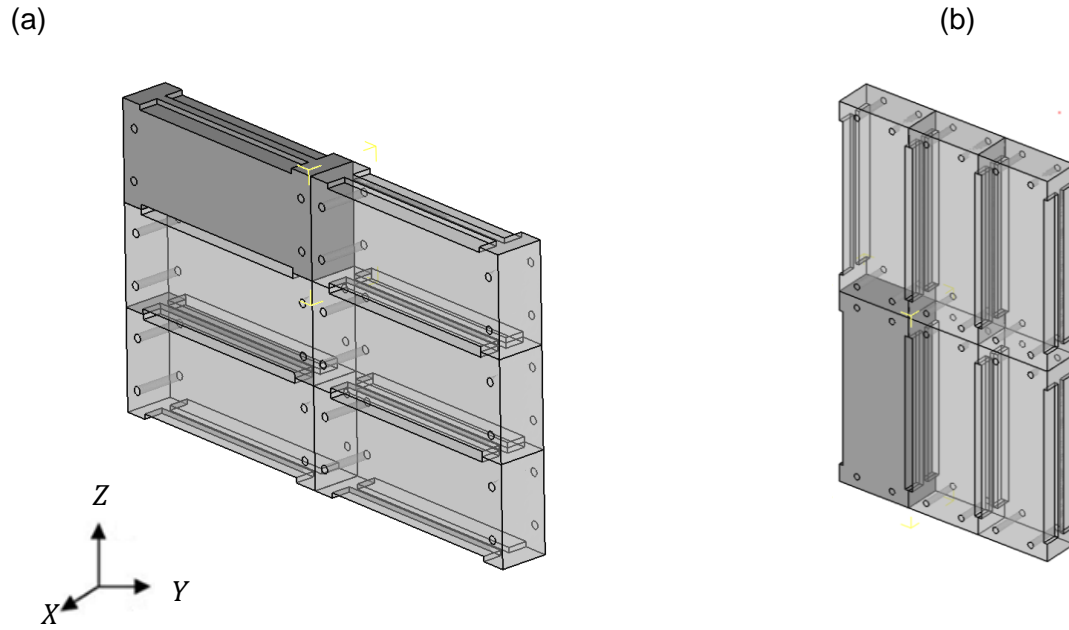


Figure 6-27: Measurement locations using neutron diffraction for the coupons: a) Mid width line direction, (b) Mid length line direction. Note that dimensions in the figures are in mm.

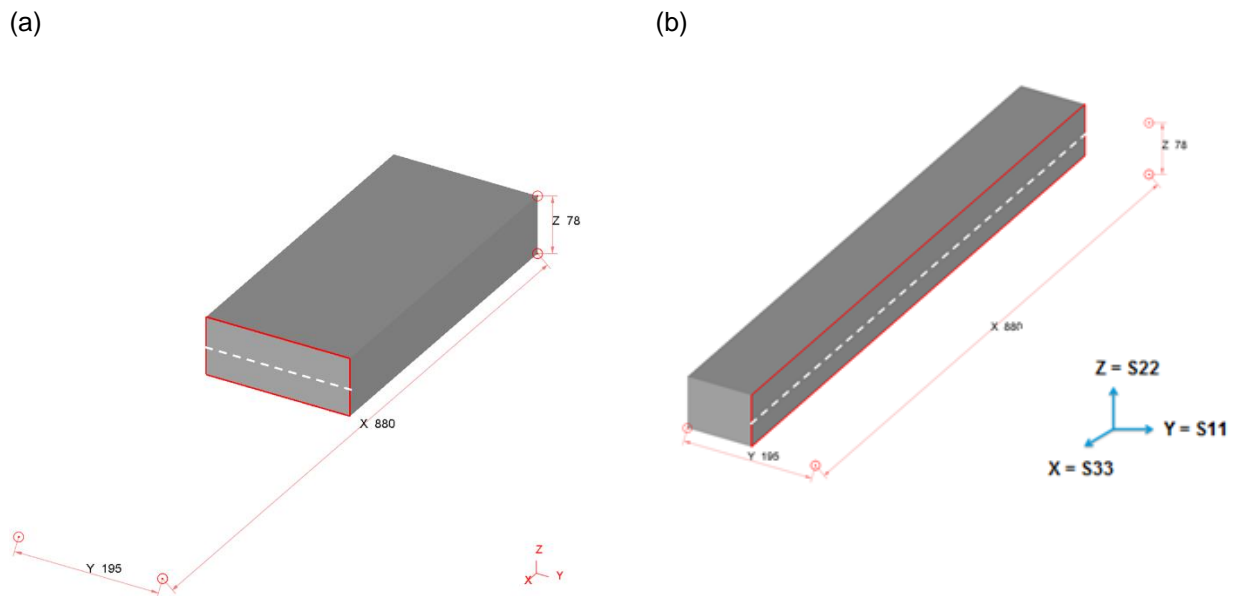


Figure 6-28: Measurement locations using neutron diffraction; (a) Mid width line direction, (b) Mid length line direction.

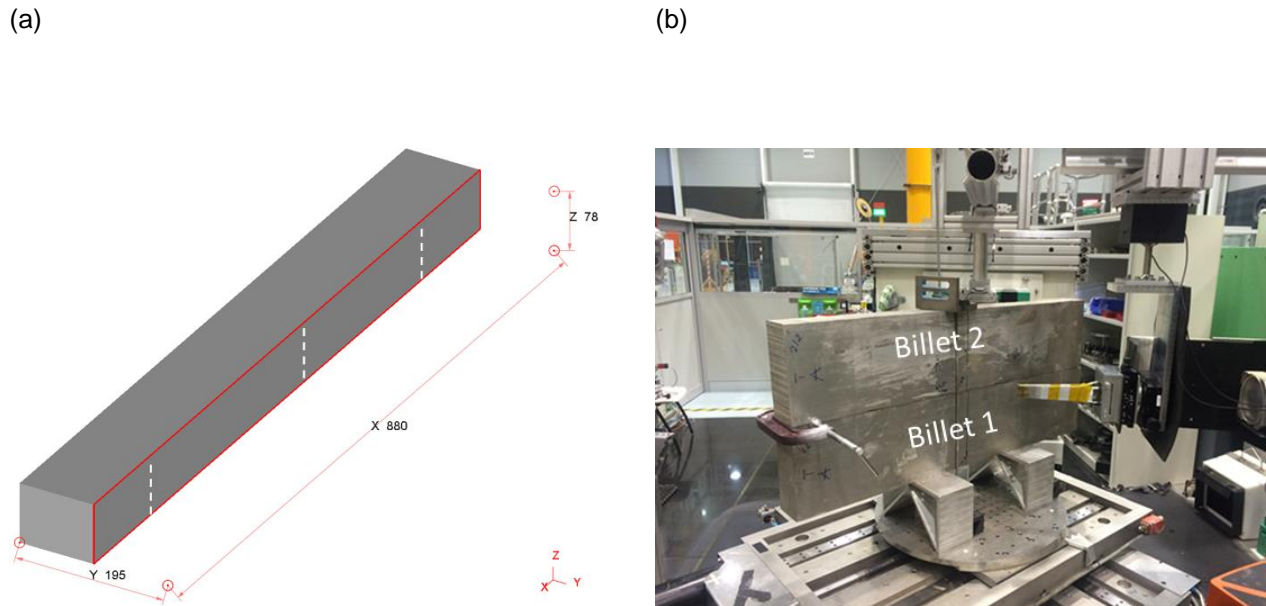


Figure 6-29: Measurement locations using neutron diffraction: (a) Thickness direction, (b) Set up. Note that dimensions in the figures are in mm.

6.5 Strain measurements using strain gauges

Strain measurements during the machining process were also recorded using strain gauges. Four strain gauges were used on the block with three strain gauges mounted on the top face (Figure 6-30, Figure 6-31) at 25 mm apart from each other, while one strain gauge was mounted on the side of the block 25 mm from top edge. The strain gauges were mounted following the British Society of Strain Measurement Strain Measurement Certificate level 1. The strain gauges at the locations were placed following FE predictions.

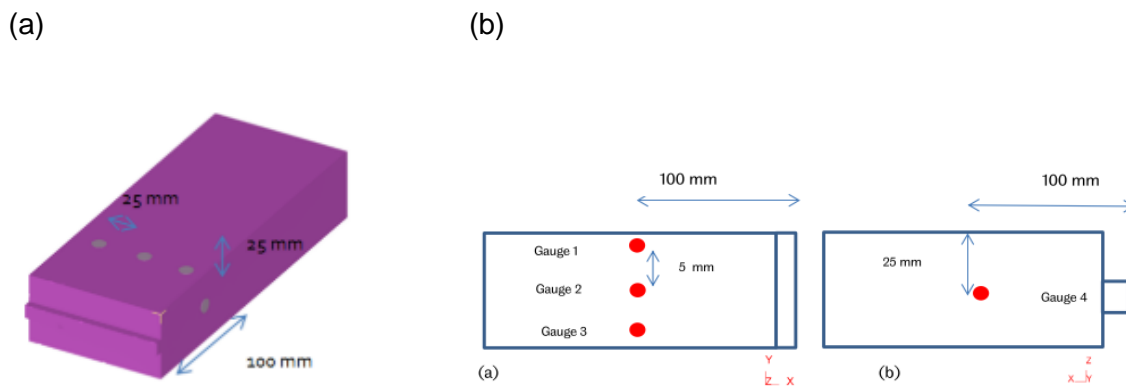


Figure 6-30: Strain measurements using strain gauges with (a) Strain gauge mounting on blocks, (b) Strain gauge locations.



Figure 6-31: Strain measurements using strain gauges.

Quarter bridge strain gauges with thermal compensation were mounted respectively with their principle measurement directions as shown in Figure 6-31. Gauges 1-3 were positioned at the bottom face during the machining of the top phase, and new gauges (1-3) were mounted on the top face when machining the bottom face. Gauge 4 was mounted on the side face of the block in order to record the strain data during the whole process. Strain gauges were only used for the machining strategies 1 and 2, but they were not used in the strategy 3 since the initial results from preceding machining strategies indicated that the large magnitudes of distortions experienced on the block were detaching the gauges and it was not possible to track the whole strain data using this technique.

6.6 Machining trials

6.6.1 Machining trial set up for symmetric and asymmetric coupons

The Cincinnati FTV 5 machine was used for the experimental trials. All coupons were constrained using four finger clamps holding the coupon at 25 mm each end leaving an overhang of 200 mm for machining (Figure 4-1).

Chapter 6: Experimental methodology



Figure 6-32: Experimental set up.

The aim of this machining trial is to finish off with a thickness of 20 mm regardless of the position of the machined section, and a distortion tolerance of 30 μm . The machining parameters are provided in Table 6-7.

Table 6-7: Machining parameters.

Machining parameters	
Tool body	25 mm diameter Sandvik R790
Insert	R790-160431H-NM.
Insert Grade	Grade H13A
Cutting speed (v_c)	730 m/min
Feed/tooth (f_z)	0.2 mm
Axial depth of cut (a_p)	0.4 - 3 mm
Radial depth of cut (a_e)	25 mm
Spindle speed (rpm)	18000

6.6.2 Experiment: tool path layout trials

The Cincinnati FTV 5 machine was used for the experimental trials. Prior to machining, the four heat-treated blocks were wire EDM to the dimensions as shown in (Figure 5-56 (b) (c) (d)). This was in order to create locations for clamping the workpiece during machining.

Chapter 6: Experimental methodology

Due to the low stress magnitude on the block, there was a negligible distortion after wire EDM the block to create the clamping locations. The blocks were machine using a Sandvik CoroMill ® 790. The selected machining parameters are shown in Table 6-8. A high spindle speed of 18000 rpm was selected to replicate a production environment and is desirable due to its reduced effect on distortion.

Table 6-8 - Machining parameters.

Machining parameters		
1	Spindle Speed (<i>rpm</i>)	18000
2	Feed rate (<i>mm/min</i>)	8000
3	Axial depth of cut (<i>a_p</i>)	2 mm
4	Radial depth of cut (<i>a_e</i>)	10 mm

6.6.3 Machining trial set up for representative part

The Cincinnati FTV 5 machine was used for the experimental trials of the sequences 1 and 2. Four heat-treated billets were initially “blocked” up for the pocketing trials of the two selected sequences and their repeats trials. The billets were blocked up as described below (Figure 6-33):

- Faces A and B (short ends of the part) were band sawed by 40 mm on each end leaving 20 mm prior to blocking up.
- Face C and D (top and bottom surface of the part) were machined by 4 mm.
- Faces E and F (long sides of the part) was machined by 11.6 mm.

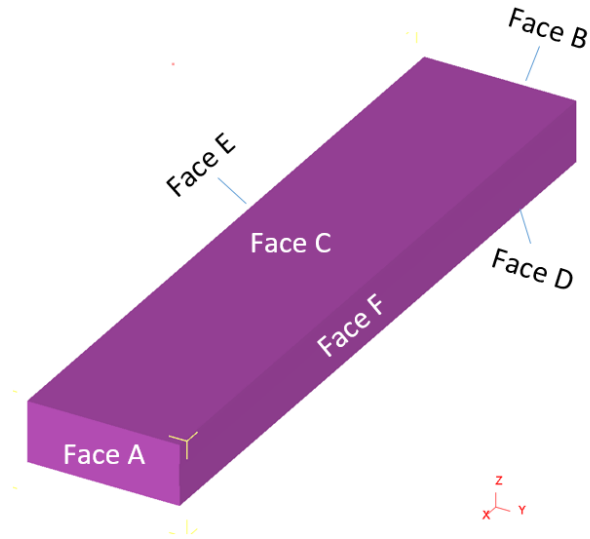


Figure 6-33: Set up for blocking up the billet. Faces 2, 4 and 6 are in the opposite face.

After the blocking up, the part was constrained using six side clamps as shown in Figure 6-34.



Figure 6-34: Experimental set up for pocketing trials.

The pockets of the part were initially machined with a roughing operation leaving an envelope of 5 mm on the wall of the pockets this was done with a roughing tool- CoroMill ® 790. The part was then finished to the final dimension using a Coromill 316 solid carbide tool with a cylindrical shank.

Chapter 6: Experimental methodology

Due to initial vibrations observed during the first machining trial, tap testing was performed (Table 5 1) on the tools to predict the dynamic behavior during high speed machining. This assisted in selecting proper cutting parameters to avoid problems of vibrations and in reducing machine induce stresses on the part. Due to initial vibrations observed during the first machining trial, tap testing was performed (Table 6-9) on the tools to predict the dynamic behavior during high speed machining. This assisted in selecting proper cutting parameter to avoid problems of vibrations, and in reducing induce stresses on the part.

Table 6-9: Tap test information.

	Cutting tool	Tap test hammer information	Tap test accelerometer information
1	CoroMill 790	Kistler hammer 9722A500, Serial number 2151145 – 11.63 mV/N	Dytran 3224A1, serial number 2608, 9.2 mV/g
2	Coromill 316	Dytran 5800SL, serial number 7708, 23.16 mV/N	

Table 6-10: Machining parameters.

	Machining parameters		
1	Spindle Speed (<i>rpm</i>)		18000
2	Feed rate (<i>mm/min</i>)	Roughing	8000
		Finishing	16000
3	Axial depth of cut (a_p)	Roughing	2 <i>mm</i>
		Finishing	1 <i>mm</i>
4	Radial depth of cut (a_e) (mm)	Roughing	10 <i>mm</i>
		Finishing	1 <i>mm</i>

6.7 Summary

From the experimental tests, the cooling rates at different thermocouple locations were obtained to determine the heat transfer coefficients on each surface as a function of temperature; and the material data was taken from J. Luo et al. [268] , and tensile tests conducted at the Sheffield materials department for the for the modeling predictions. This data was used in the models as inputs to accurate predict the residual stress profile after quenching.

Nine coupons were quenched to generate both symmetrical and asymmetrical RS profiles. Neutron diffraction RS measurements were performed on the coupons after the heat treatment process to capture the RS generated.

Residual stress measurements were also taken throughout the different machining stages to capture the stress redistribution caused by the material removal process.

7 Residual stress and distortion analysis

7.1 Residual stress analysis

7.1.1 Residual stress analysis on rectangular coupons

The residual stress results measured using neutron diffraction (details of the measurements is defined in section 6.4.2) in the mid length line and mid width line of the blocks labelled block 1, block 2 and block 3 is shown in Figure 7-1 and Figure 7-2. From this figure, it can be seen that there was good repeatability between blocks 1 and 2 but not in 3. It is also showed a decreased in stress magnitude could be affected by the total time held in the solution temperature i.e. the longer the time the block is held at solution temperature (above 4 hrs.) the higher the stresses. The blocks 1 and 2 were held for a longer period at SOHT than block 3 (Figure 7-3). The increase of stresses had an impact on the distortions on the blocks prior to machining.

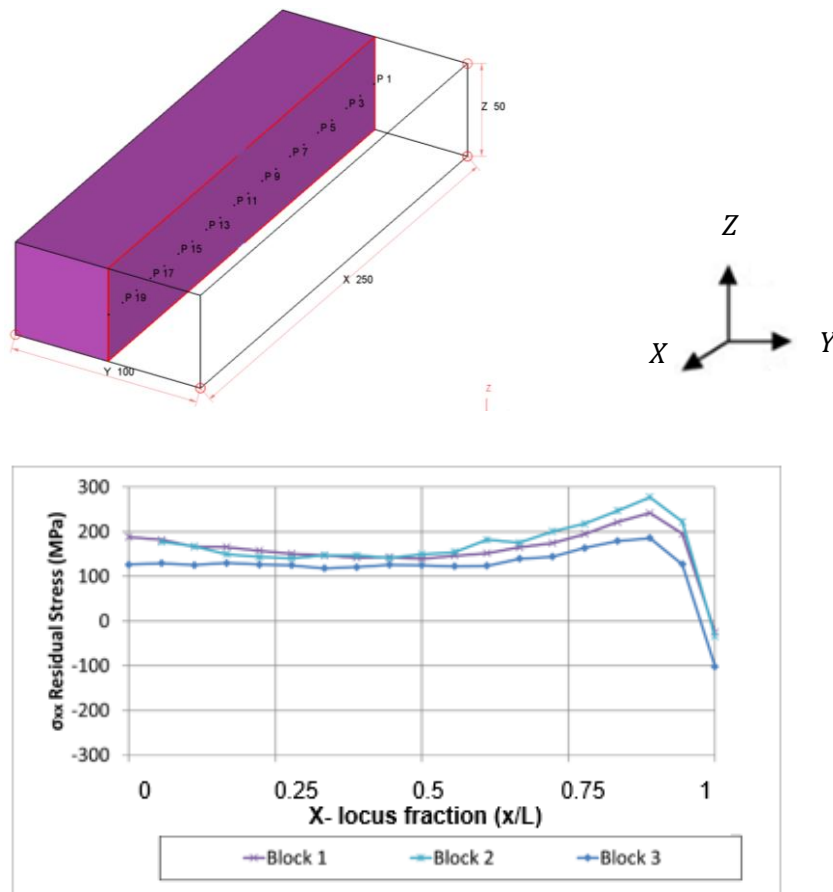


Figure 7-1: σ_{XX} stress measurements in the X-Z plane for blocks 1, 2 and 3 after quenching.

Chapter 7: Residual stress and distortion analysis

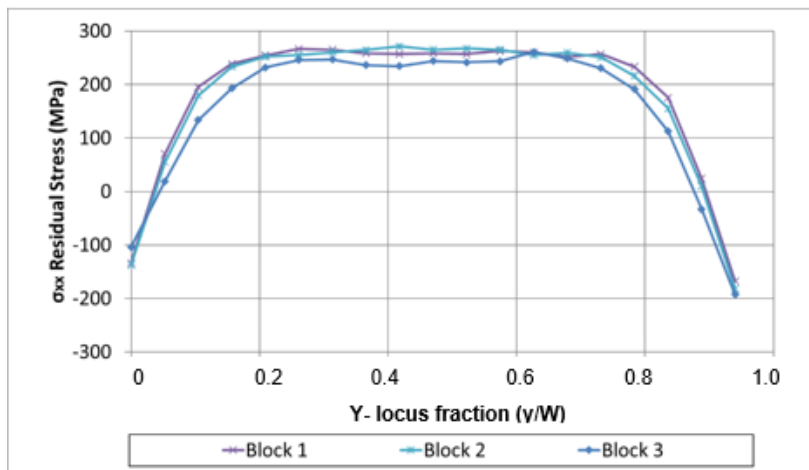
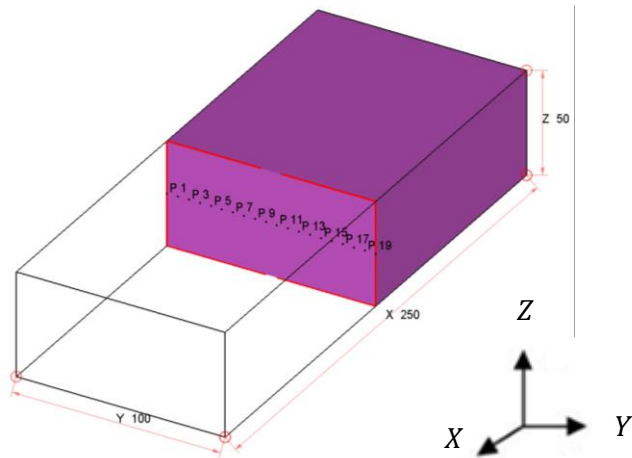


Figure 7-2: σ_{XX} stress measurements in the Y-Z plane for blocks 1, 2 and 3 after quenching.

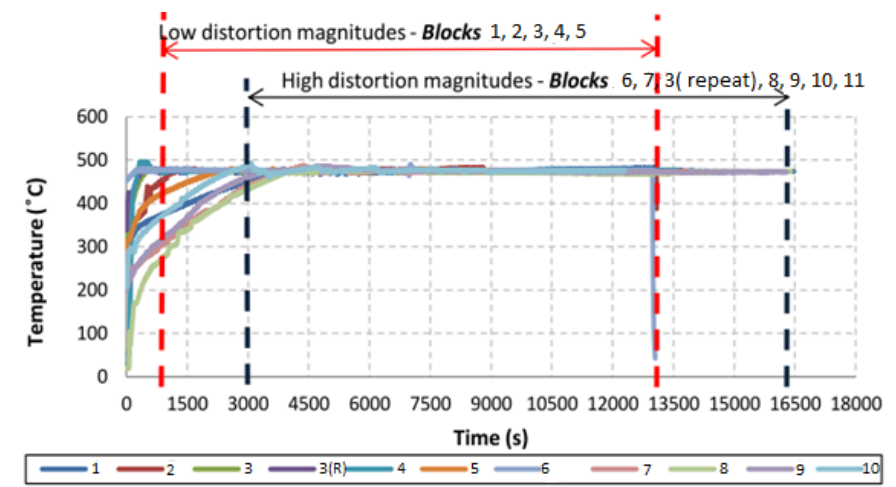
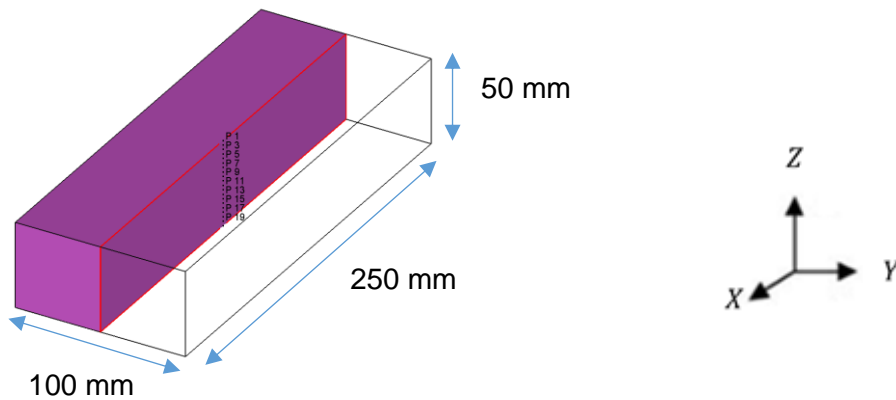


Figure 7-3: Data from the thermocouple mounted on the surface of all the quenched blocks.

Chapter 7: Residual stress and distortion analysis

Following the FE simulation of the quenching process as defined in section 5.1.3.3, the residual stress prediction was compared with experimental measurements using contour measurement technique (section 6.4.1) and neutron diffraction measurements (section 6.4.2) at the thickness in the length direction as shown in Figure 7-4. The blocks were quenched following the process as defined in section 6.3.2.2. The locations on the FE model were equidistant locations across the thickness of the block. The FE prediction captured the trend accurately and a good magnitude prediction of less than 10% between the thickness of 5 to 55 mm. However, the model over predicts the residual stress magnitude near the ends for the contour measurements. This could be due to large errors usually associated during the entry and exit of the Wire EDM wire.

(a)



(b)

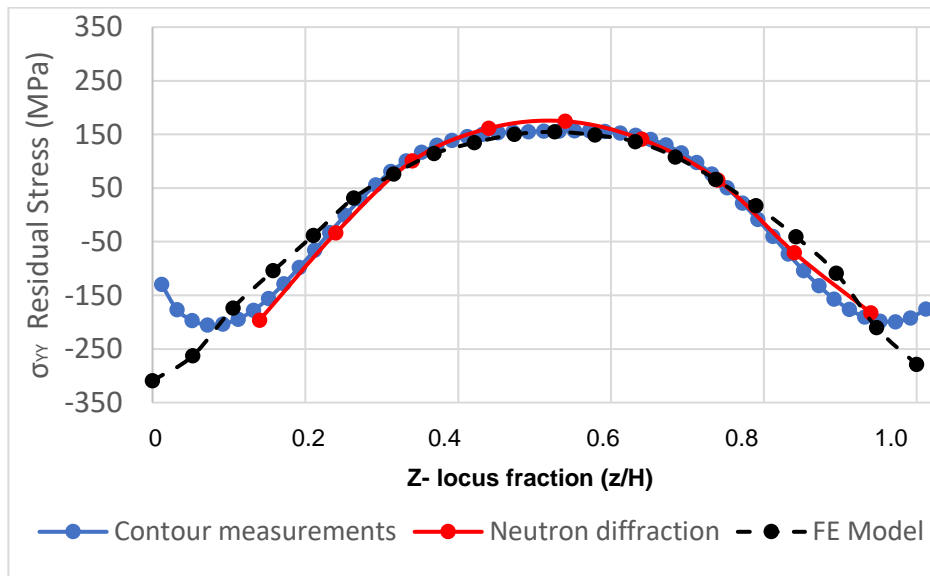


Figure 7-4: FE model comparison with experimental RS measurements in σ_{YY} .

Chapter 7: Residual stress and distortion analysis

A comparison analysis was carried out between experimental data for block 3 and the FE models at the mid length (Figure 7-5) of the blocks. The FE model showed an average stress magnitude difference of 30 MPa when compared with the neutron diffraction technique in the mid length line. When compared to the contour measurement, the FE model showed an average stress magnitude difference of 18 MPa.

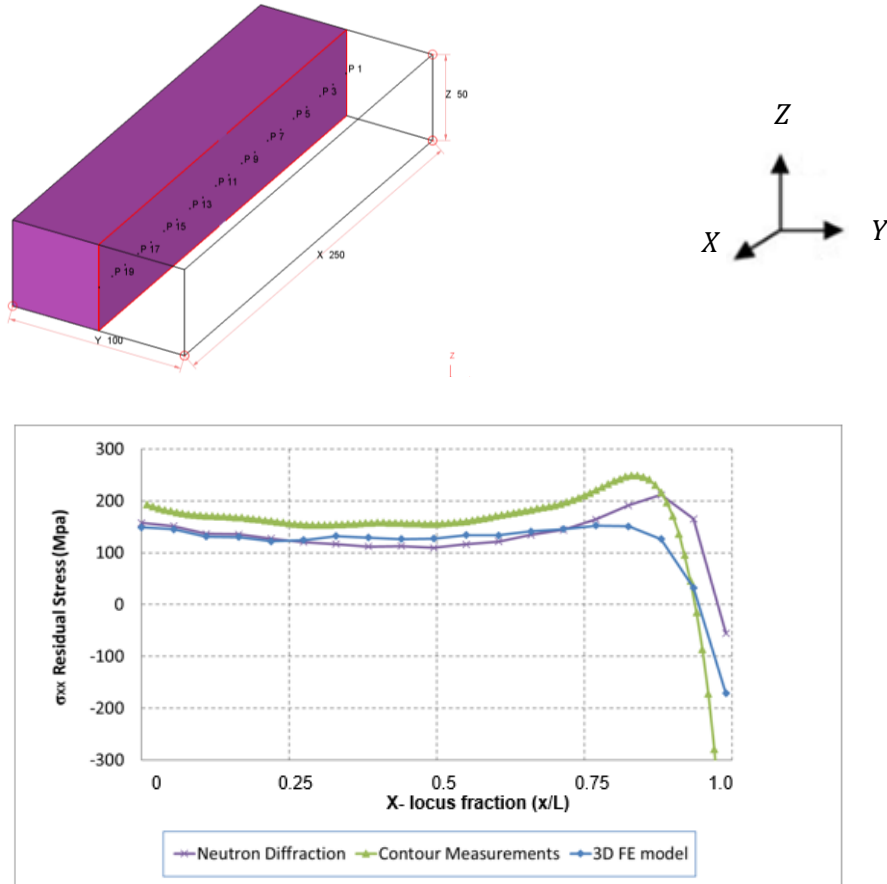


Figure 7-5: σ_{XX} comparison of residual stress measurements on the mid thickness of the X-Z plane length.

Following the validation of the heat treatment FE model, the model was validated with experimental stress data following the non-improved tool path (Figure 7-6). From the comparison, it can be seen that the model predicted the trend of the residual stress with an average difference between the FE model and the experimental data of 20 MPa.

Chapter 7: Residual stress and distortion analysis

Although the model predicts the trend of the stress profile following machining, the difference in the FE model's prediction with experimental measurements would be due to its lack of predicting the residual stress more accurately in conjunction with the assumptions made in the FE model assumptions defined in section 5.1.2.

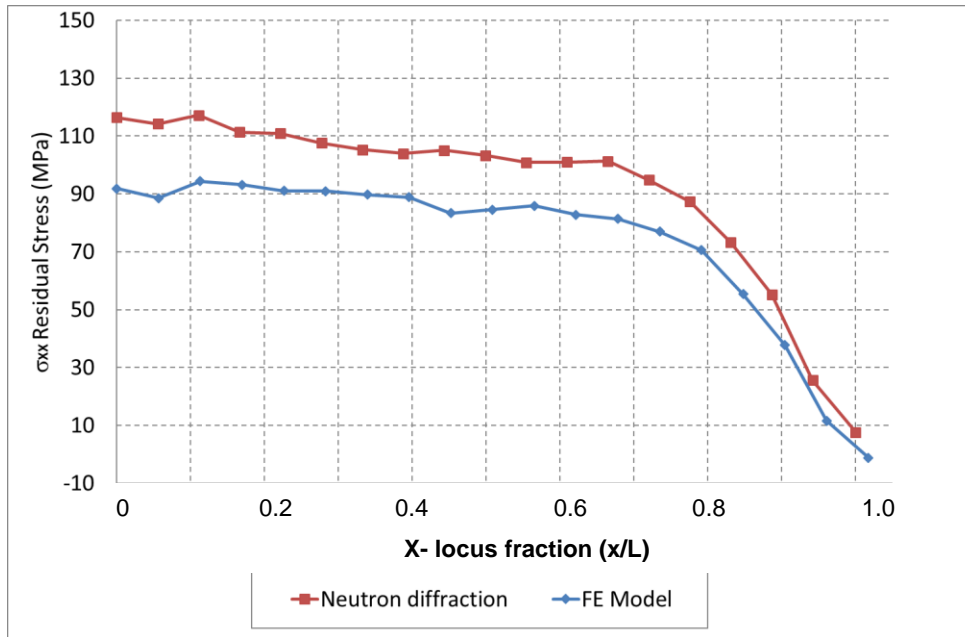


Figure 7-6: σ_{xx} comparison between experimental stress data and numerical analysis for non-improved tool path in the X-Z plane.

Similarly, the experimental residual stress of improved tool path was compared with the finite element model. It can be observed that the FE models predicted the same tendency with the experimental data, with a difference of 30 MPa average (Figure 7-7) which occurs at the workpiece length between 30-70 mm. This difference could be due to either the microstructural issues or porosity in the material caused during the heat treatment process as the difference occurs between this position and matches the FE model at the other measurement positions. Further tests would need to be performed to confirm this is the case.

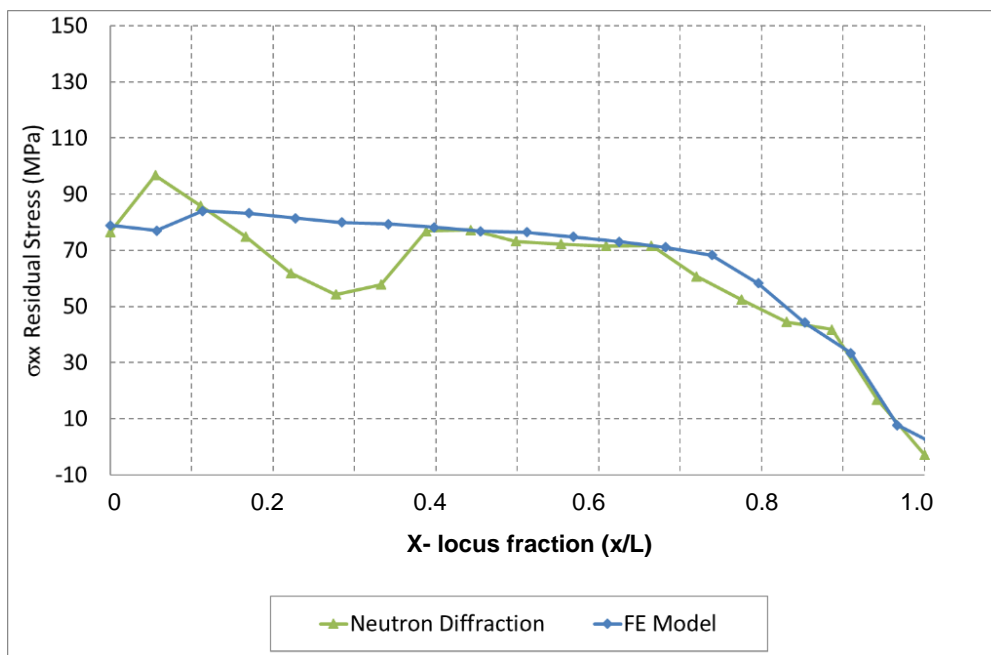


Figure 7-7: σ_{xx} comparison between experimental stress data and numerical analysis for improved tool path in the X-Z plane.

Finally, the stress profile for the robust selection process was compared with the FE model as shown in Figure 7-8. The results show the FE model has a good correlation with the experimental data with an average magnitude difference of 5 MPa between 0 – 170 mm. The percentage difference increases towards the end of the block by 50 MPa. Similarly to the difference illustrated in non-improved tool path (Figure 7-6), although a decent attempt has been made to model the stress profile following machining operation, the difference in the FE model’s prediction would be due to its lack of predicting the residual stress more accurately in conjunction with the assumptions defined in section 5.1.2.

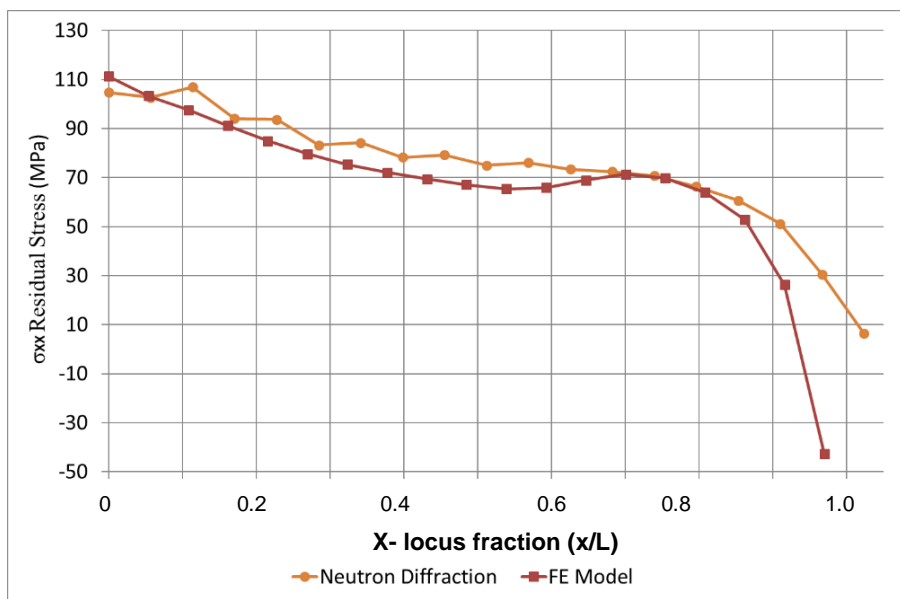


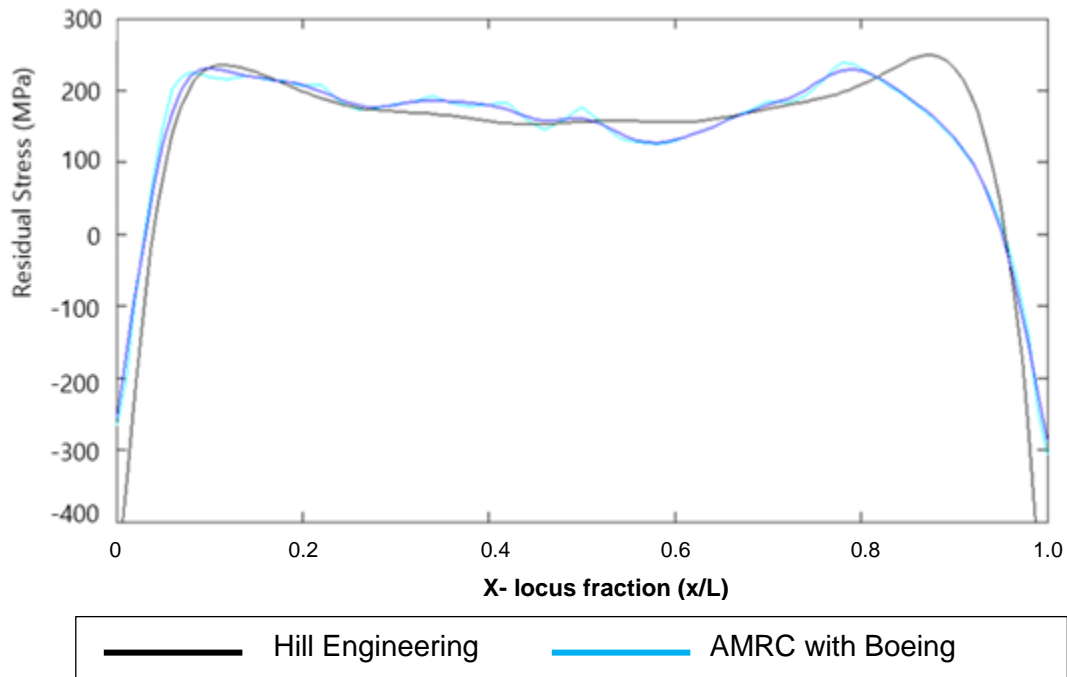
Figure 7-8: σ_{xx} comparison between the robust process validation in mid thickness section of the block.

Regardless of the differences displayed by the FE models in Figure 7-7 to Figure 7-8, it is observed from the experimental measurements that the improved tool path and robust selection process achieved similar final stress profiles regardless of different tool path strategies applied. It is also observed that the residual stress profiles of the non-improved tool path is slightly higher in magnitude than the other two strategies.

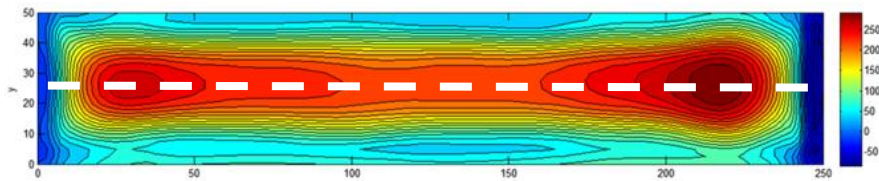
Following this study, the heat-treated block measured by Engin-X was sent to ANSTO for residual stress measurements. The measurement parameters used for the calculation of the residual stresses were attempted to be kept as close as possible to provide an acceptable comparison.

Similarly, residual stress measurements using the contour method were compared in the longitudinal direction between Hill Engineering and at the AMRC with Boeing as shown in Figure 7-9. The displacement measurements were performed using the GOM ATOS scanner while the measurements performed by Hill Engineering used a CMM. This could explain the reason of the difference between the two measurements due to the measurement errors normally induced by 3D displacement scanners.

Chapter 7: Residual stress and distortion analysis



(a)



(b)

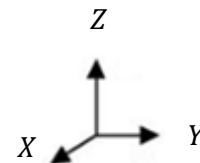
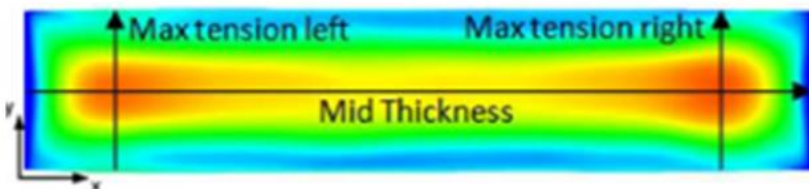


Figure 7-9: σ_{XX} contour measurement comparison along the block length (white line) between the (a) AMRC with Boeing and (b) Hill Engineering.

Chapter 7: Residual stress and distortion analysis

The following conclusions can be made from this study:

- The total SOHT furnace time affected the distortion and residual stress profile of the blocks; lower stress and distortion profiles of the blocks corresponded to the SOHT furnace time for less than 4 hours.
- Successful comparisons were made between the FE models, neutron and contour measurements
- In addition to this, two centres for residual stress using neutron diffraction; Engin-X and ANSTO, were compared and found to be in good agreement.
- Similarly, contour residual stress measurements were compared between Hill Engineering and the AMRC and found to be in good agreement. Although there was a difference at around 200 – 250 mm which could be due to the displacement measurements using the 3D displacement scanner.
- Although the FE model predicted the trend well, it did not capture the magnitude especially towards the edges. This discrepancy could be due to not incorporating the correct material data, which includes the appropriate hardening model, therefore requiring the need to perform extra experimental trials to determine the correct hardening model.
- The quench simulation did not incorporate the microstructural effects, which might have an influence on the stress prediction at the edges.
- Finally, there could have been errors in the calculation of the heat transfer coefficient from DEFORM.

7.1.2 Residual stress analysis for symmetric and asymmetric RS on coupons

7.1.2.1 Heat treatment

The symmetric residual stress measurements of the quenched coupons are shown in Figure 7-10. Similar to Figure 7-1 and Figure 7-2, it can be seen that there is a variation in the residual stress experimental measurements. These differences would be associated with the heat treatment regardless of the amount of effort to minimize any quenching variation of each of the blocks. These variations could be due to the furnace, air transfer or the quenching as highlighted in Figure 7-3.

When comparing this measurement with the FE model prediction across equidistant locations across the thickness of the block, the models predicted the correct trends but the magnitudes were lower by an average of around 20 % when compared to the right side of the curves for coupons 1, 2 and 5; while the difference was 33 MPa for coupon 4. The differences increase at the left side of the curves to around 32 MPa (coupon 1, 2, 5) and 43 MPa (coupon 4). The comparisons between the FE model and the residual stress in the bulk was around 40 MPa, however there is a distinct difference at both the top and bottom edge of the block thickness.

These large differences were associated to the varying heat treatment coefficients on each surface used for the quenching simulations as highlighted in section 2.4. In order to accurately simulate the residual stresses, further investigation would be required in order to obtain the correct heat transfer coefficient as defined in section 2.4 and section 5.1.3.2.

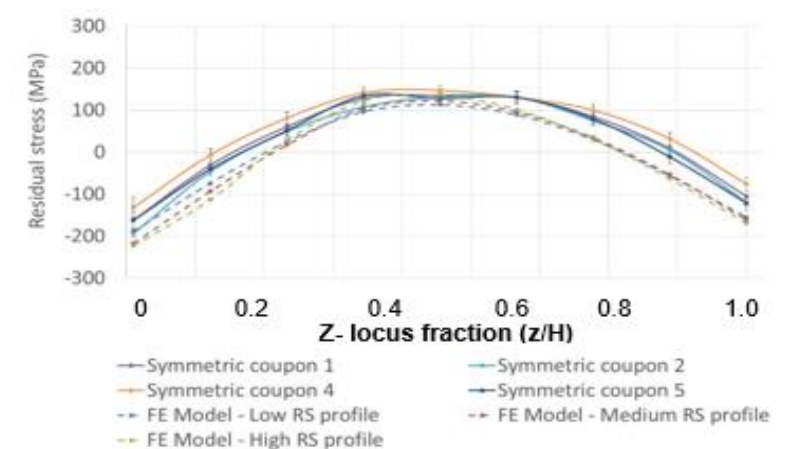


Figure 7-10: σ_{XX} symmetric residual stress measurements compared with FE models.

Chapter 7: Residual stress and distortion analysis

Similarly, residual stress measurements were performed on the coupons quenched bolted together (asymmetrically). The comparison between the FE models and measurements are shown in Figure 7-11.

The FE model for the low RS profile predicts the stresses well for experimental coupon 2 and 3 with around 10 MPa difference respectively. The locations on the FE model were equidistant locations across the thickness of the block. For coupon 4, the medium RS profile predicted with a difference between 5 – 10 MPa within the 20 to 33 mm although it did not predict well at the edges of the thickness. Similarly, the High RS profile FE model predicts closely for the residual stresses measured in coupon 1 although it does not predict the stresses at the edges of the thickness. This dissimilarity between the model and the experimental measurement would be due to the application of an incompatible heat transfer coefficient on these models. Therefore, to predict accurately the residual stresses, additional experimental trials are needed to acquire the appropriate heat transfer coefficient for each of these coupons as defined in section 2.4 and section 5.1.3.2. In addition to this, the experimental measurements do not show any repeatability therefore to avoid variations, the furnace, air transfer and quenching need to be kept as low as possible.

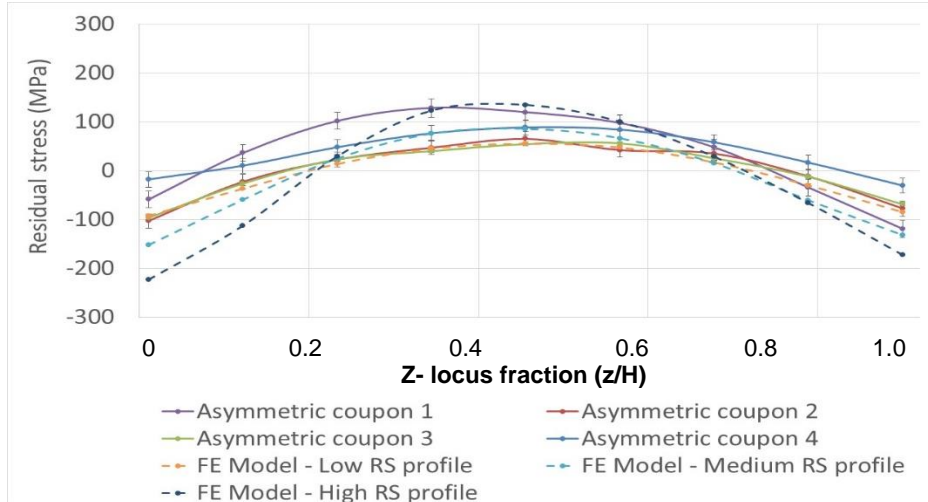


Figure 7-11: σ_{XX} residual stress measurements compared with FE models.

Following the residual stress measurements using neutron diffraction, an attempt was made to measure the residual stress of the asymmetrical stress profile but the block cracked due to the high magnitude of residual stresses as shown in Figure 7-12. A similar behaviour has been documented as shown in Figure 2-4 (a).



Figure 7-12: Crack across coupon caused due to excessive residual stresses generated during the quenching process.

7.1.2.2 Post machining residual stress comparison of Phase 1

Experimental residual stress measurements were also performed after machining the top face of the coupons and compared with the FE model (Figure 7-13). From Figure 7-13 it can be observed that the FE model reasonably predicted both magnitude and direction with an average difference of 17 MPa for coupons 1-3 respectively.

The FE model was incapable accurately predicting the residual stress following stage 1 due to the error carried forward from the heat treatment residual stresses prediction. Secondly, the mesh resolution during material removal deteriorates which affects the accuracy of the FE model.

Regardless of the FE model's prediction difference with experimental data, Figure 7-13 captures the residual stress redistribution caused during material removal, a phenomenon not captured previously. The experimental measurements show that the stresses have redistributed and reduced by 50 % following the machining of the top face.

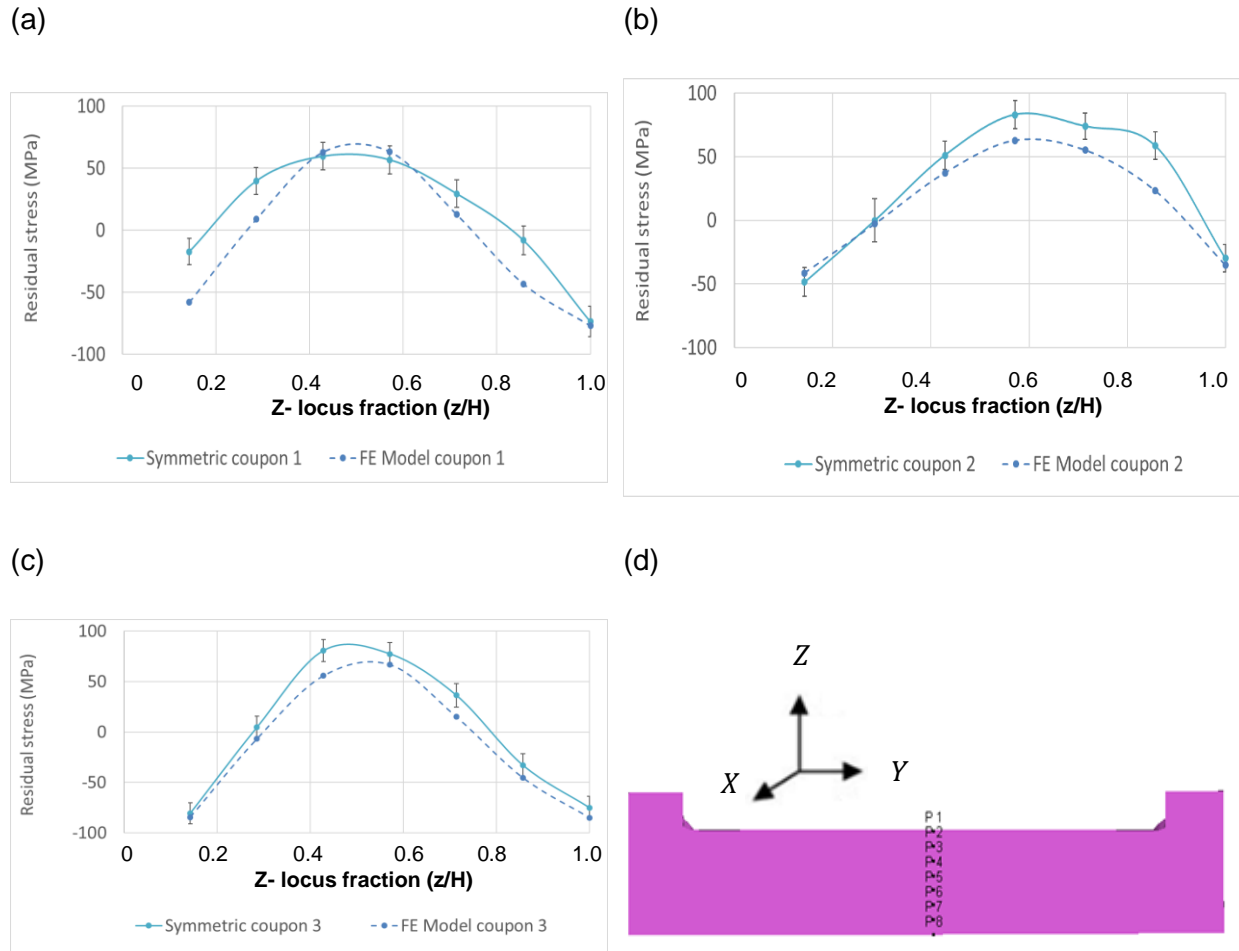


Figure 7-13: σ_{XX} residual stress profile after machining the top face: (a) Coupon 1, (b) Coupon 2; (c) Coupon 3 (Coupon 4), (d) Measurement locations across coupon thickness.

Similarly, FE model results were compared with experimental residual stress measurements following the machining of the top face of the asymmetrical residual stress coupons. Figure 7-14 illustrates that the FE model predicts the trends of coupon 1 and 2, but not the magnitude accurately especially between 12 to 23 mm for coupon 1 and 2.

The neutron diffraction measurements between 14 -18 mm for coupon 1 is 5 MPa, which would be an error, associated with the measurements. Regardless of this variations, the insight provided by these measurements are valuable and show that the stresses have redistributed during the machining of the top face and reduced by 70 %.

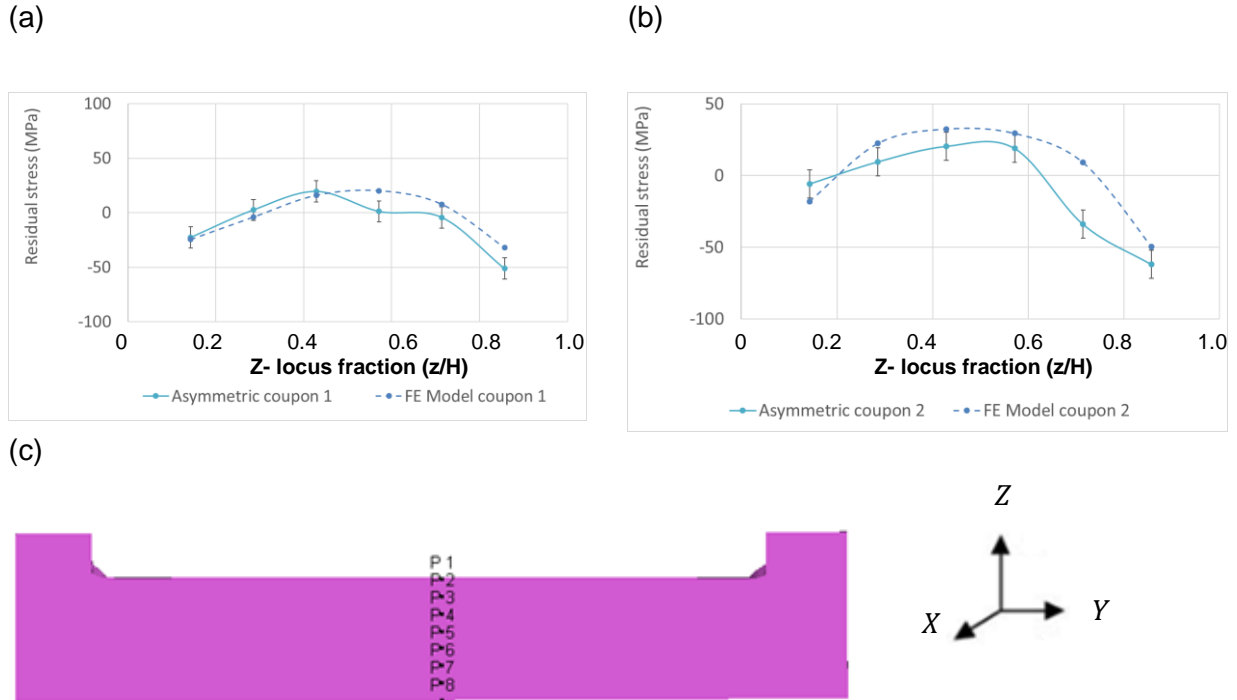


Figure 7-14: σ_{XX} residual stress profile after machining the top face: (a) Coupon 1, (b) Coupon 2, (c) Measurement locations across coupon thickness.

7.1.2.3 Post machining residual stress comparison of Phase 2

Residual stress measurements were also taken after machining the bottom face of the coupons to compare with the FE model (Figure 7-15). It can be seen that the FE model predicts the trends but not the magnitudes. From Figure 7-15 (a) it can be seen that the FE model predicts the stresses near the edges but not in the bulk with a difference of around 40 MPa. Similarly, the FE model in Figure 7-15 (b) under predicts the residual stresses through thickness of the coupon. From Figure 7-15 (c), it can be observed that the FE model could simulate the magnitudes of the stress by 25 MPa in most cases. This difference is accumulative, and is carried forward from the previous machining phase. This is summarised simply in Equation 7-1.

$$\sigma_{error} = \sigma_{Heat\ treatment} + \sigma_{Stage\ 1} + \sigma_{Stage\ 2}$$

Equation 7-1: Cumulative error in FE modelling of residual stresses.

Moreover it can be seen from Figure 7-15 that the residual stresses redistribute further following machining of phase 1, with Figure 7-15 (a) and (c) redistributing symmetrically and Figure 7-15 (b) redistributing asymmetrically. In addition to this, it can be seen that the maximum residual stress has reduced by a third of the heat treatment residual stress.

Chapter 7: Residual stress and distortion analysis

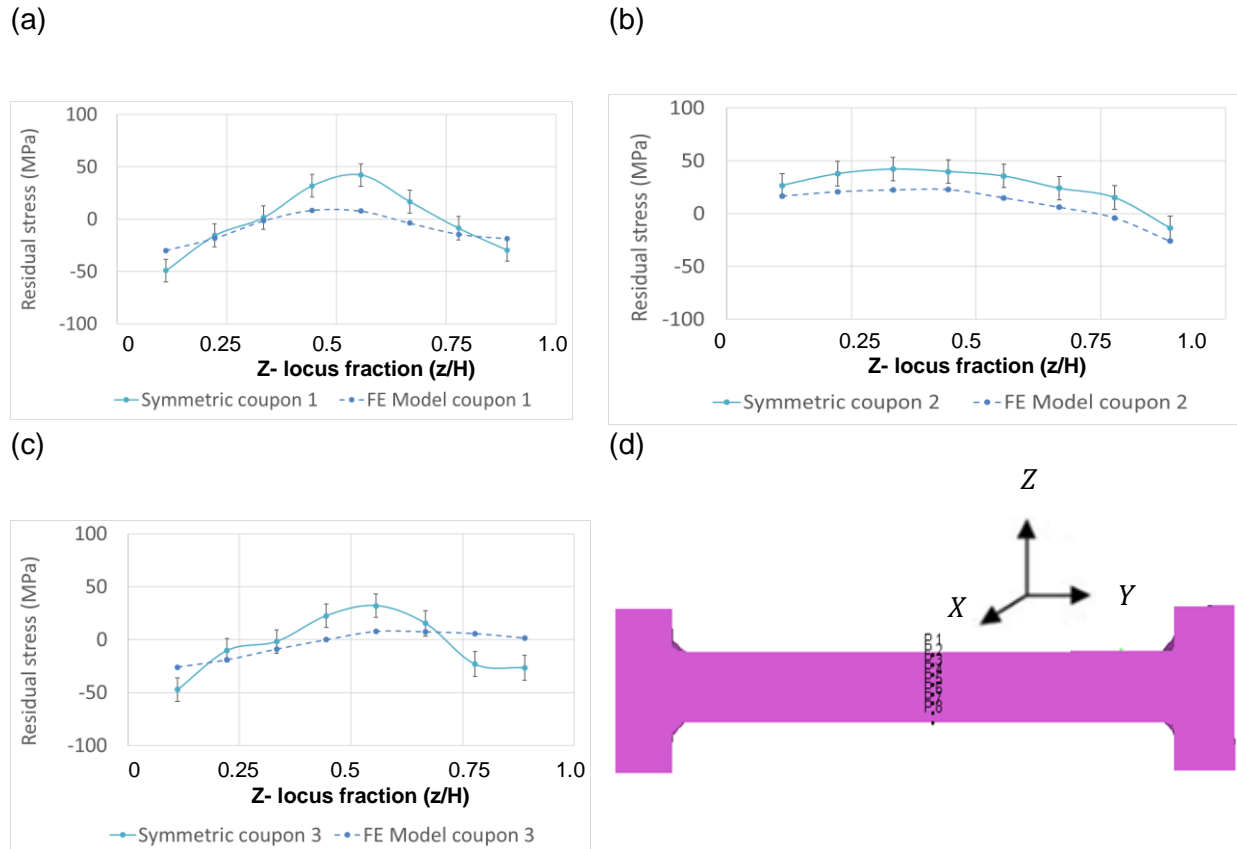


Figure 7-15: σ_{XX} residual stress profile after machining the bottom face:(a) Coupon 1, (b) Coupon 2, (c) coupon 4, (d) Measurement locations across coupon thickness.

Following the machining of the top face, the bottom face was machined and residual stress measurements of the coupons were taken to allow comparisons with the FE model (Figure 7-16).

From the plots, it can be observed that the FE models were not able to fully predict the profile trends and the magnitudes of coupon 1 and 2, with 50 MPa and decreasing between 5 to 15 mm. Similarly, a difference of 25 MPa increases between positions 12 to 15 mm can be seen in Figure 7-16 (b).

The difference between the FE model and the experimental measurements is carried forward from the previous phase as defined in Equation 7-1. It can also be seen that the residual stresses have redistributed asymmetrically and have reduced by a further 88 % in coupon 1 and 50 % in coupon 2 from their original quenched residual stress state. In addition to this, the experimental variation in the measurements are large, further work would involve repeat measurements to provide more confidence in the measurements.

Chapter 7: Residual stress and distortion analysis

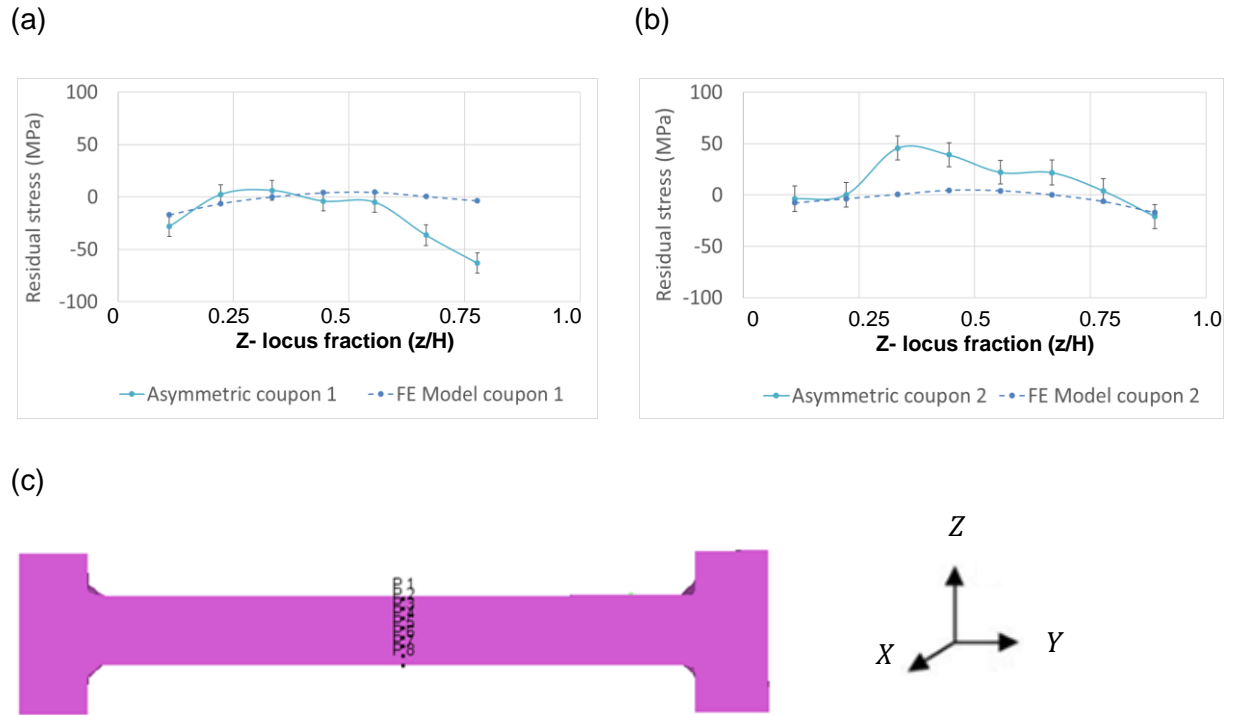


Figure 7-16: Residual stress profile after machining the bottom face: (a) Coupon 1, (b) Coupon 2, (c) Measurement locations across coupon thickness.

From this work, the following conclusions can be made:

- FE models were generated to predict the stresses after the heat treatment. The model showed a difference of 38 % against the experimental data for the symmetrical RS profile (coupon 1, 2, 5) and 43% for coupon 4. The asymmetric RS profile showed differences of 10 % (coupons 7 and 8) and 50 - 70 % for coupons 6 and 9.
- Residual stress measurements were also taken throughout the different machining stages to capture the stress redistribution caused by the material removal process. When the FE model for phase one was compared with the experimental data, the model had a stress difference of 35 % (coupon 2), 30 % (coupon 5) and 53 % (coupon 4). For the asymmetric stress profile, there was a difference of 22 % (coupon 8) and 25 % (coupon 9).
- Following the material removal of the second phase, the FE residual stress model showed a difference of 25 % (coupon 4), 28 % (coupon 5) and 89 % for coupon 2. This was due to the difference carried forward from the previous phase.
- For the asymmetric residual stress profile coupons, at depth locations from 0 to 8 mm there was a difference of 21 % and for depth locations 0 mm and 15 mm there was a difference of 15 % for the asymmetric residual stress profile.

7.1.3 Residual stress measurement on rectangular blocks

Residual stress measurements were compared with the FE model for the quenched block (Figure 7-18). When comparing these measurement with the FE model in the transverse direction (Figure 7-18), the models predicted the correct trends but not the magnitudes as seen between 5 to 30 mm, where the model over predicted by over 100 MPa when compared in the transverse direction. When the model was compared with the measured data in the longitudinal direction, the model, under predicted the residual stress magnitude between 5 to 40 mm as shown in Figure 7-18.

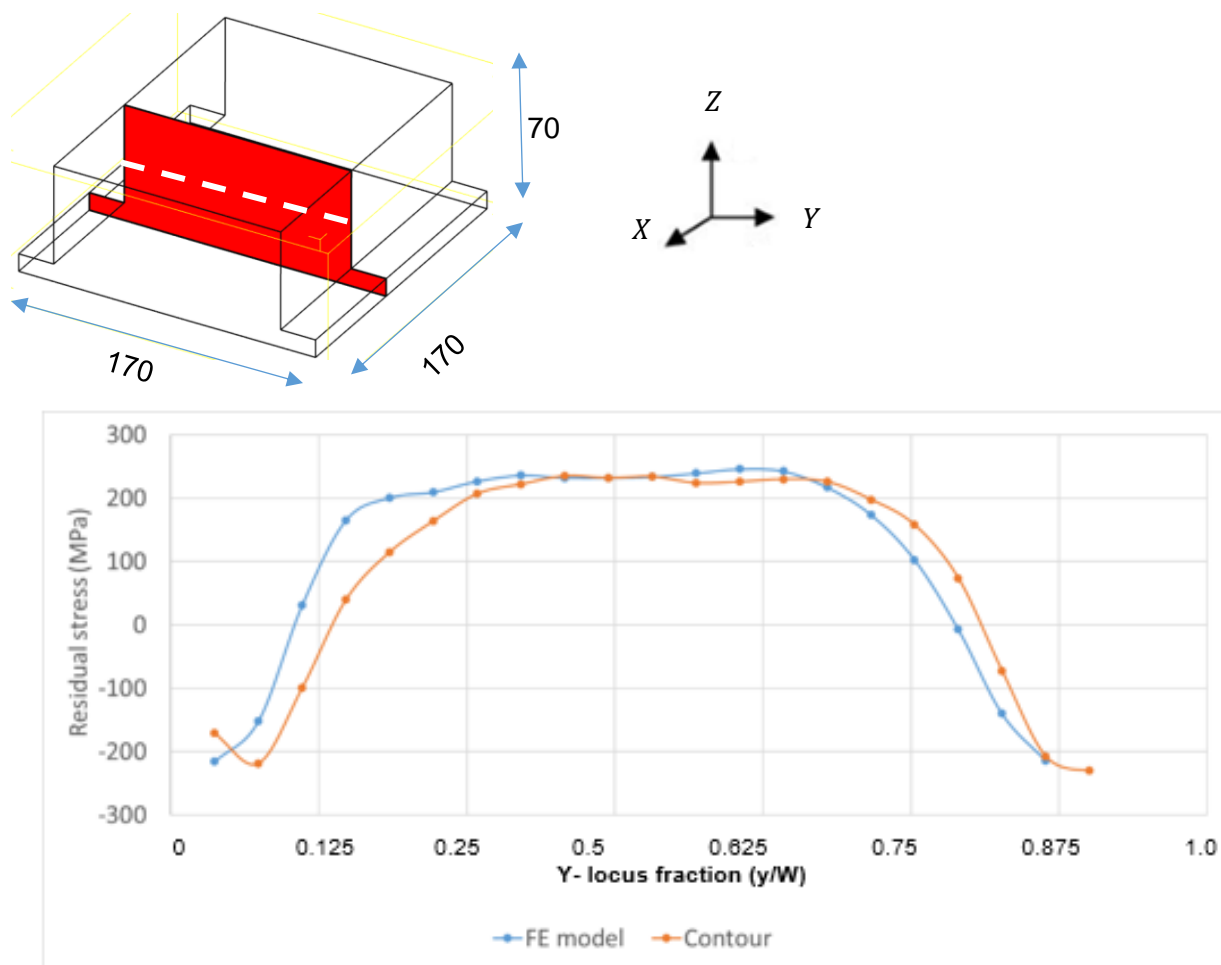


Figure 7-17: σ_{XX} residual stress comparison with FE Model across the transverse direction.

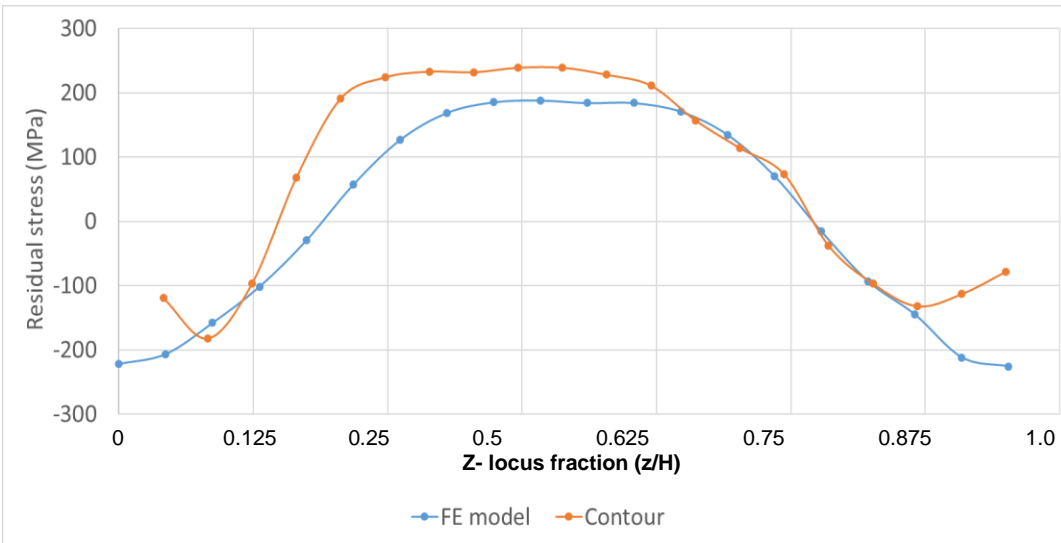


Figure 7-18: σ_{XX} residual stress comparison with FE Model across the thickness.

7.1.4 Residual stress measurement on representative part

Comparison of the residual stress between the model and the experimental techniques in mid width line, is shown in Figure 7-20, Figure 7-21 with the following observations. In general, the neutron diffraction measurements show that the stresses are compressive in the edges of the billet tending towards a tensile regime in the bulk of the material as a bell trend. It is observed in Figure 7-20 that there is a large dissimilarity between the contour method and both the neutron diffraction and the FE model, where the contour method measures a larger stress magnitude in the ranges of 70 to 180 mm. This difference could be due to errors induced during the slitting operation as highlighted by Mike Prime and Adrian DeWald [128] or during the displacement measurements done by the 3D displacement scanner at this location. Figure shows a better comparison between the neutron diffraction, the contour and the FE model with the trends and magnitudes matching closely. The measured and predicted stress show that in the longitudinal direction there is the normal residual stress “bell” curve distribution. Similar errors highlighted in the contour method in Figure 7-20 can be noticed between the ranges of 70 to 180 mm.

Chapter 7: Residual stress and distortion analysis

Comparing the two magnitudes for the different directions, σ_{YY} has a higher stress magnitude than σ_{XX} . The average magnitudes of RS in σ_{XX} are -50 MPa maximum compressive, and 150 MPa maximum tensile; and for σ_{YY} the magnitudes are -250 MPa maximum compressive, and 200 MPa maximum tensile.

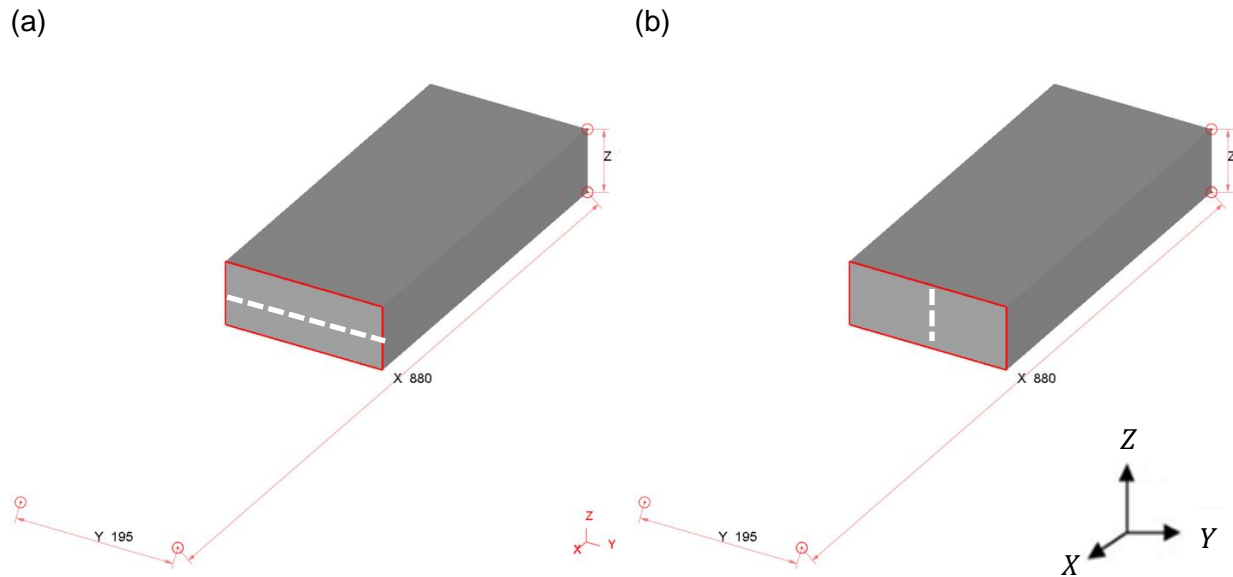


Figure 7-19: Measurement locations: (a) Across the width, (b) Across the thickness.

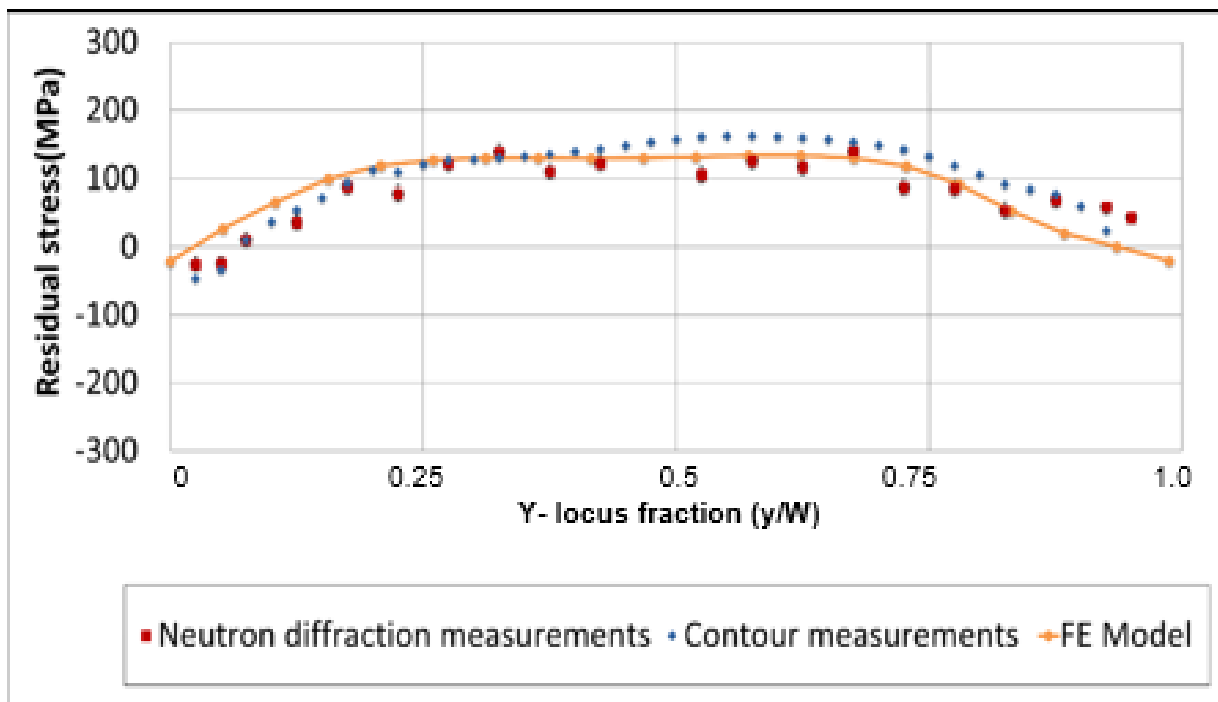


Figure 7-20: Residual stresses in the mid width line of the billet in σ_{XX} .

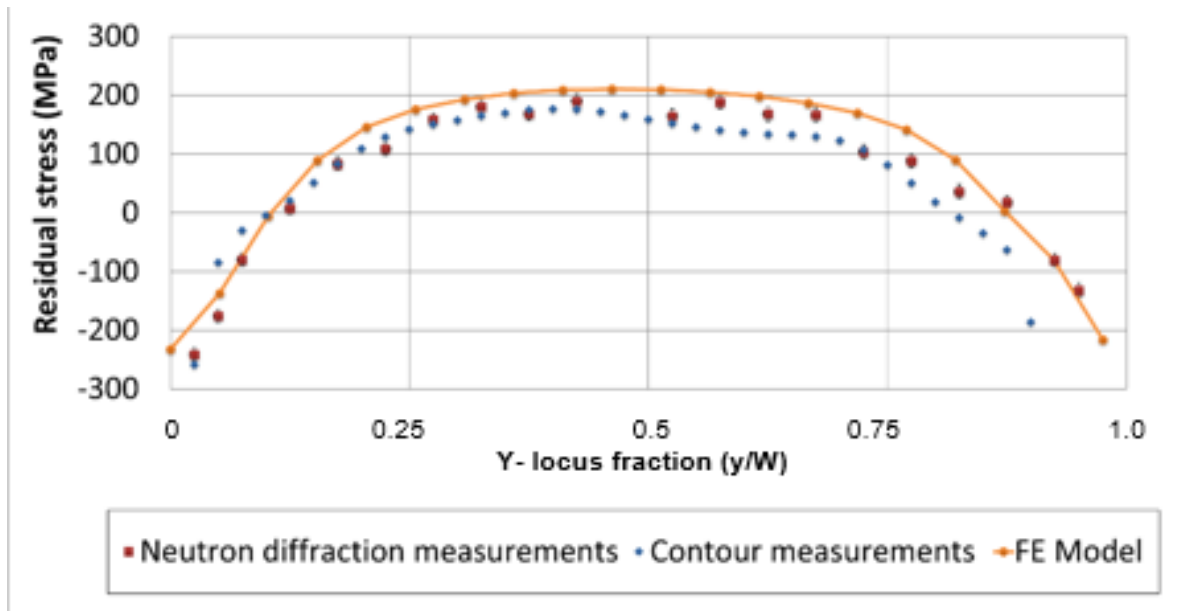


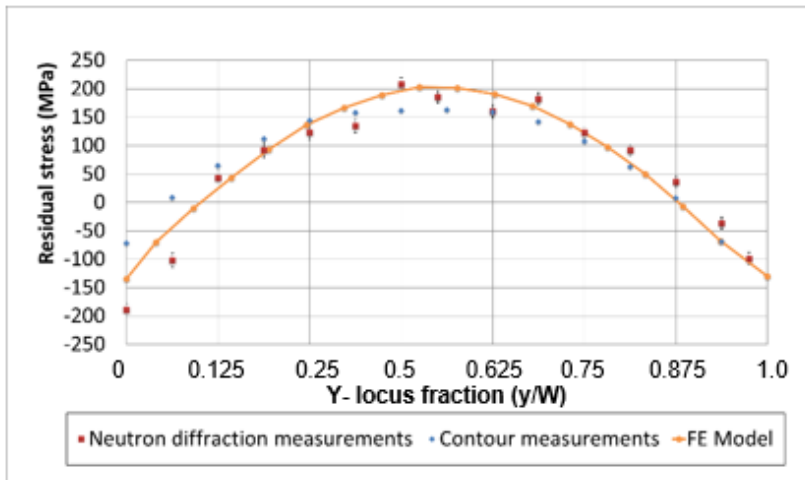
Figure 7-21: Residual stresses in the mid width line of the billet in σ_{YY} .

Similarly a comparison was done in the middle mid thickness line of the billet in the σ_{XX} and σ_{YY} direction as shown in Figure 7-22 . Both the measurement techniques and the FE model prediction capture the “bell” curve stress profile with the bottom surface of the billet having a higher stress magnitude than the top surface.

In the σ_{XX} direction Figure 7-22 (a), the contour method and the FE model have a good magnitude correlation (less than 10%) but not with the neutron diffraction with a difference of over 100% from a distance of 5 mm decreasing to 10% at 45 mm, then increasing from a distance of 50 mm to 65 mm. The neutron diffraction measures a higher compressive stress magnitude at 15 – 25 mm from the bottom surface and higher tensile stresses from 45 -60 mm from the bottom surface.

In the σ_{YY} direction (Figure 7-22 (b)) both measurement techniques have a good correlation apart from the first two measurement points at the bottom surface of the billet with the neutron diffraction measuring large compressive stresses (difference of over 100%) unlike the contour and the FE model prediction.

(a)



(b)

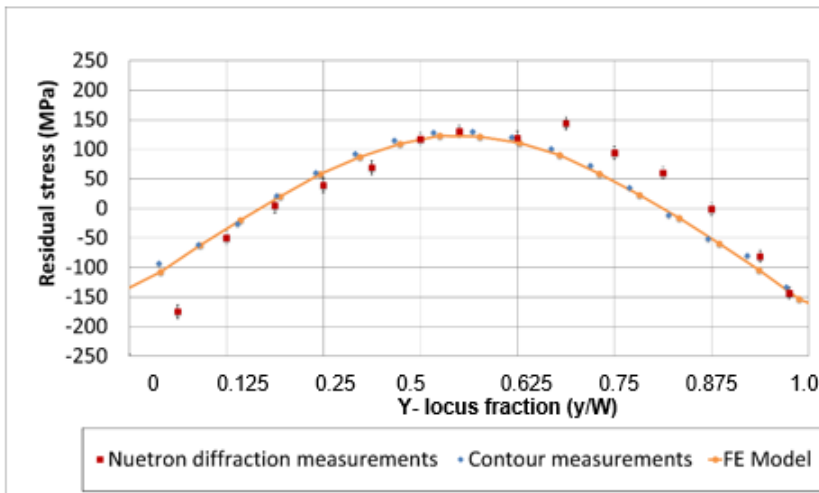
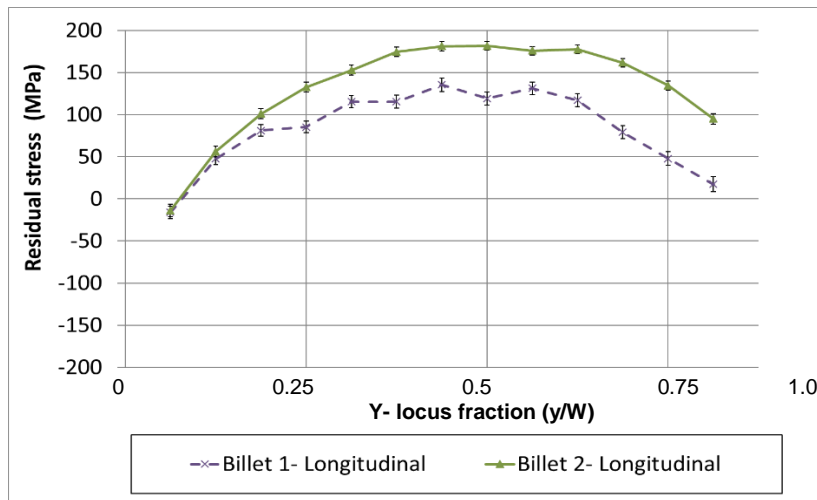


Figure 7-22: Residual stresses in the mid width line of the billet; (a) in σ_{xx} , (b) in σ_{yy} .

7.1.5 Effect of part offset on representative part

The billets for these trials were machined using three different strategies as defined previously. The billets were residual stress measured as shown in Figure 7-23. There is a clear difference in the residual stress created simply by preparing the billet using different part offsets prior to machining the final part.

(a)



(b)

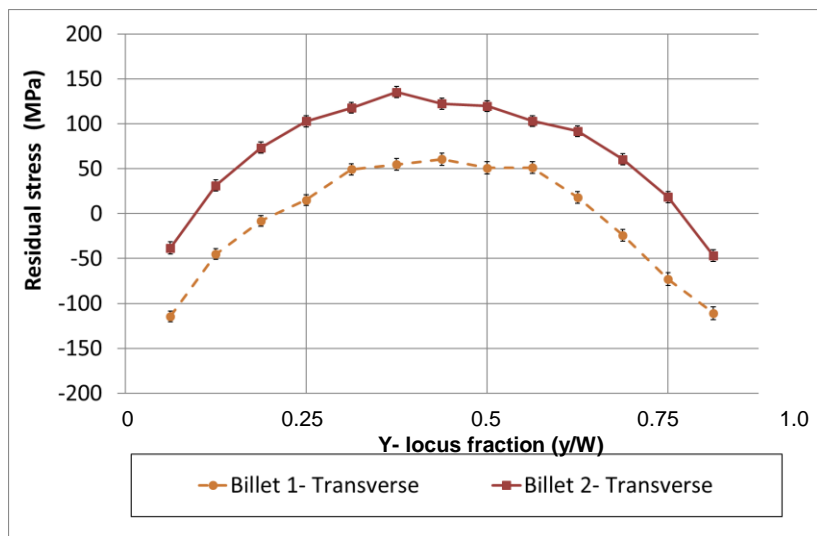
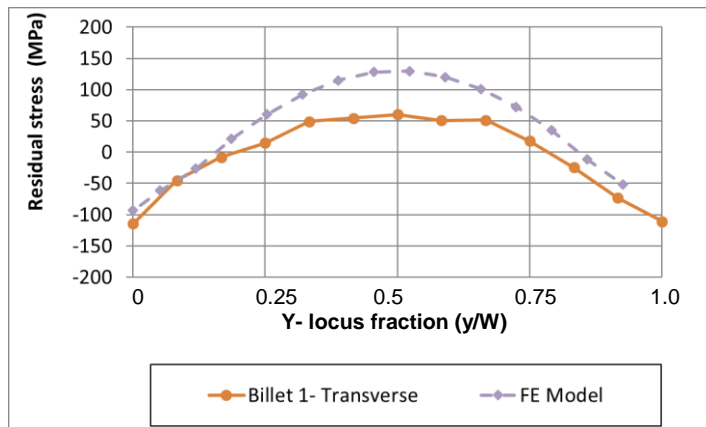


Figure 7-23: Residual stresses measurements in the mid width line of the billet; (a) σ_{XX} , (b) σ_{YY} .

Following this, the finite element model was created to compare with the FE model as shown in Figure 7-24. The FE model predicts the trend and magnitude well between 20 to 50 mm but not at the edges as shown in Figure 7-24 (a).

This difference between the FE model and neutron measurements can be accounted due not modelling accurately the billet preparation process i.e. not modelling the work holding correctly. Another factor that could influence the results is the mesh resolution deteriorates during the material removal process.

(a)



(b)

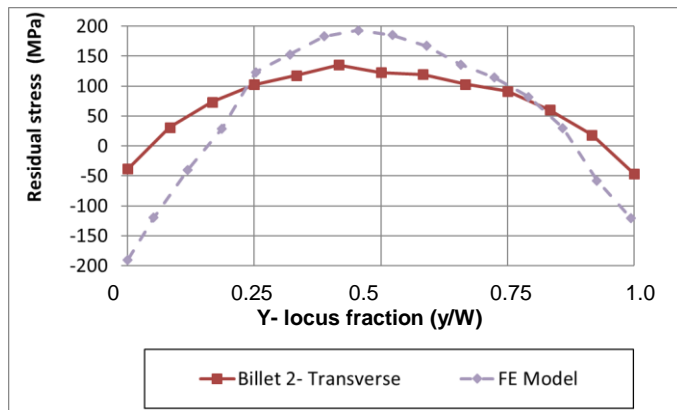


Figure 7-24: σ_{xx} residual stresses comparison in the mid width line for: (a) Billet 1, (b) Billet 2.

7.2 Strain measurements during machining of coupons

A further comparison of the experimental data was performed to see the influence of machining strategy between the non-improved, improved using the strain gauge data. The main conclusion from these measurements can be found in Figure 7-25 which is showing the maximum strain of for a 3 mm and 1 mm cut.

As illustrated in this figure, by modifying the non-improved depth of cut of (3 mm) to improved depth of cut (1 mm) the strain level increases around three times the magnitude. This finding is significant in this research, as the strain energy, a function of strain, is found to be related to the machine distortion and this result confirms the FE predictions as shown in Figure 5-50 (b) and Figure 5-50 (c) respectively.

Machining the block at 1 mm depth of cut around the high compression region generates high strains, which in turn produces high strain energy release magnitudes, causing large distortion magnitudes, forcing the block from its initial state towards its original position hence optimizing the machining process.

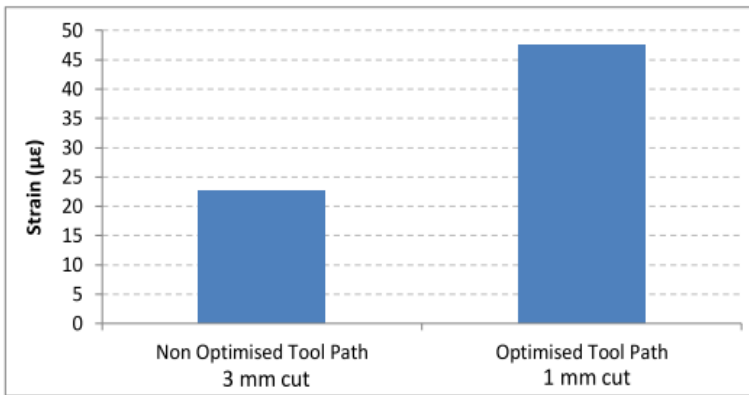


Figure 7-25: Influence of improved cut 11 on strain.

7.3 Distortion analysis

7.3.1 Distortion analysis on rectangular coupons

Non-improved tool path was based on a normal machining operation with the aim of a high material removal rate; the proposed sequence caused a high distortion. Figure 7-27 shows the comparison results between the on machine inspection (OMI) probing data and the FE modelling. The machine distortion was measured using a calibrated 3 mm Renishaw OMP 60 probe.

The simulation results showed that the FE model predicts the trend but not the magnitude. The predictions exhibited an under prediction of 350 μm in the final cut for the top face machining. For the bottom face machining, the 3D FE model predicts the distortion well for cuts 9 and 10. Following these cuts, the 3D FE model no longer follows the experimental distortion profile and begins to over predict the distortion values by 400 μm for the final cut.

The FE model, although still over predicting, manages to follow the same distortion profile as the experimental data.

Chapter 7: Residual stress and distortion analysis

This increase in the difference could be due to:

- Over constraining the FE model but constraining the nodes fully instead of modelling the actual fixturing.
- Not taking into account the accurate volumetric change of the block due to unclamping release effect after machining the top face of the block. This correlates well with Figure 7-13.
- Inaccuracy of simulating the correct amount of material removal i.e. overcutting or undercutting.
- Inaccuracies of residual stress predictions (Figure 7-4, Figure 7-5, Figure 7-7)

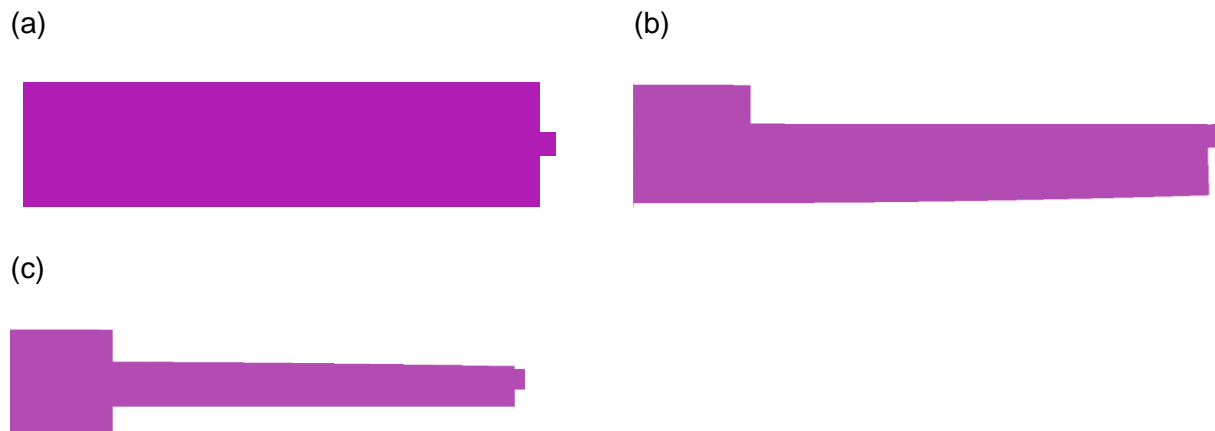


Figure 7-26: Different stages of material removal; (a) Initial stage, (b) Machined top face, (c) Machined bottom face.

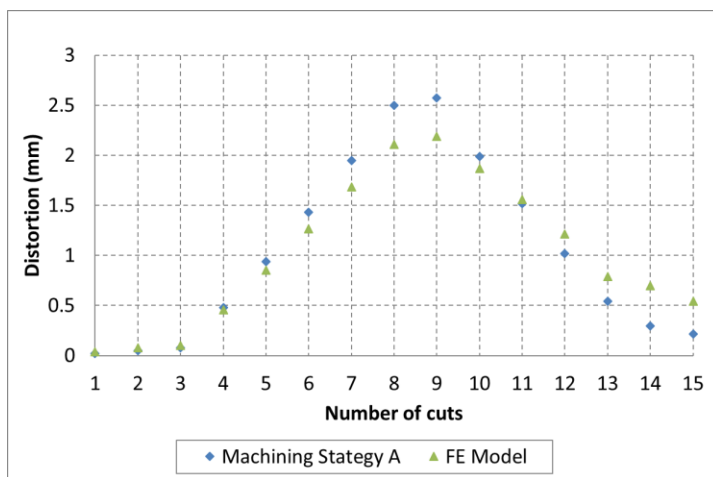


Figure 7-27: Comparison of experimental distortion data with numerical simulation for machining strategy A (non-improved tool path).

Chapter 7: Residual stress and distortion analysis

Similarly, the FE model was compared to OMI data for improved tool path (Figure 7-28). The models predicts the trend but not the magnitude during the top face machining although under predicting the final distortion by 350 μm . For the bottom face machining, the model predicts well for cut 10 but from cut 11, the FE model was not capable of predicting the magnitude showing a large a difference of around 400 μm . The reason the FE model was incapable of predicting the distortions correctly would be due to the reasons mentioned previously including the incapability of the model simulating accurately the residual stresses (Figure 7-7).

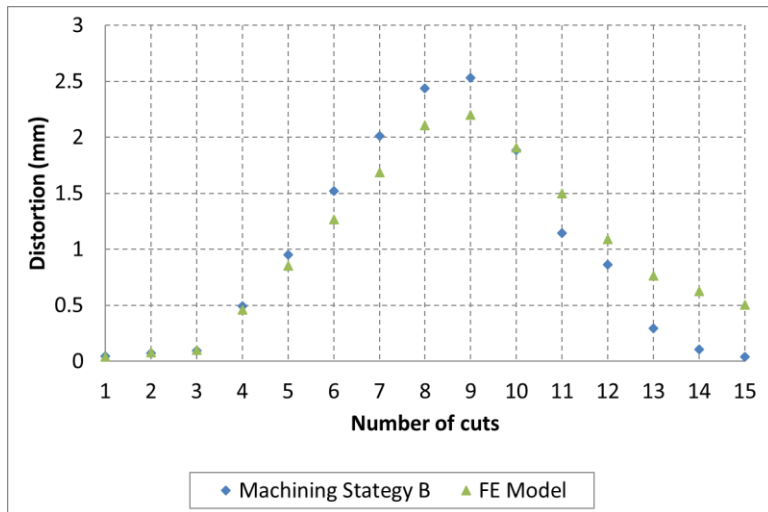


Figure 7-28: Comparison between experimental distortion data and numerical analysis for machining strategy B (Improved tool path).

Finally, the FE model was compared with the OMI data from machining using robust selection process (Figure 7-29). The distortion prediction from the FE model showed a good trend but with a magnitude difference of 600 μm for the top face distortions and 300 μm for the bottom face distortions. The reason the FE model was incapable of predicting the distortions correctly would be due to the reasons mentioned previously including the incapability of the model simulating accurately the residual stresses (Figure 7-8).

Chapter 7: Residual stress and distortion analysis

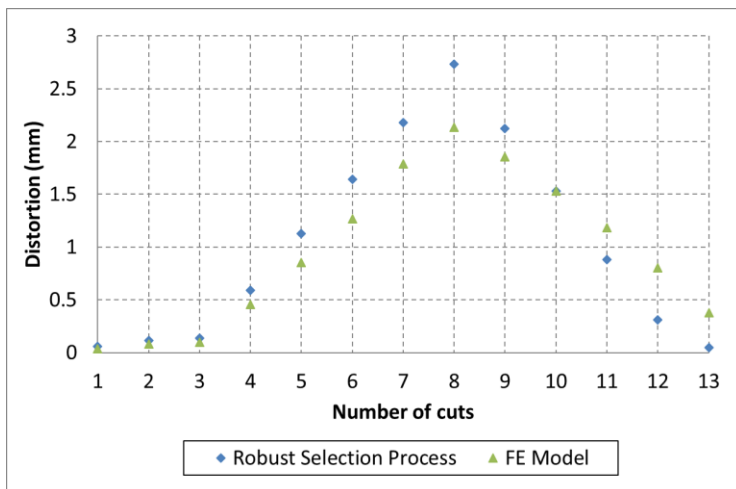


Figure 7-29: Comparison between experimental distortion data and numerical analysis for robust selection process.

Regardless of the inaccuracies of the model, it accomplished its mission on creating machining strategies that would reduce the distortions as shown in Figure 7-30.

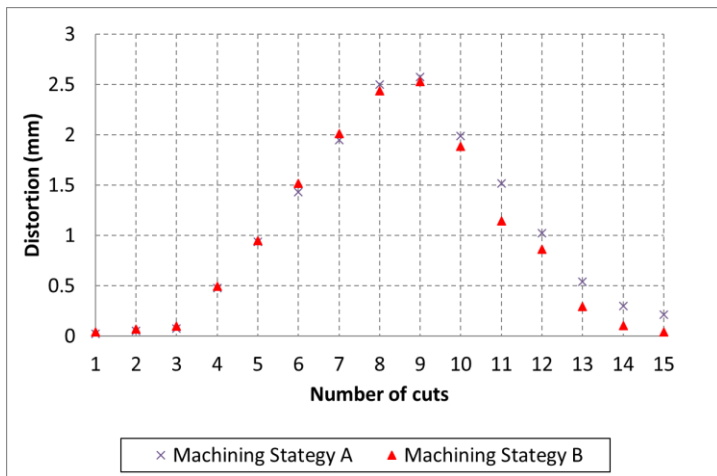


Figure 7-30: Distortion comparison between non-improved tool path (A) and improved tool path (B).

From this study, the following conclusion can be made:

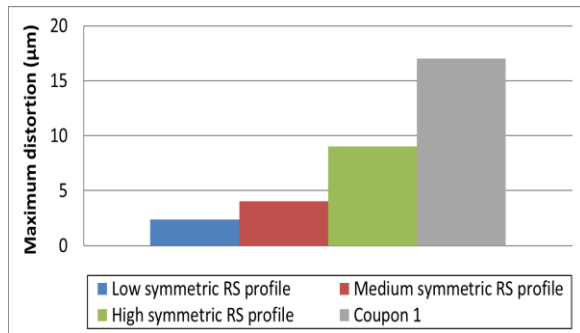
- The models were effectively used to determine the theoretical machining strategies to minimize distortions from a non-improved tool path to an improved/robust selection process. They were then used to provide an analysis to investigate the machining strategies.
- The FE model predicted the distortion trend for all the three strategies and final distortion magnitudes, although over predicting during the machining process. The FE model was used to establish a set of rules used to optimize the machining process and the robust validation process. Modelling of machining improvement was achieved by reducing the distortion by 1.038 mm prior to unclamping using a machine induced stress balance strategy while the experimental process .
- The distortion reduction strategy reduced the distortion from non- improved tool path (214 μm) to improved tool path strategy (35 μm) prior to unclamping. This optimization was similarly modeled was due to the stress profile material removal strategy (Figure 6-17).
- the final reduction distortion optimization above 50 % was achieved for the improved tool path strategy, while a distortion reduction of 83% was achieved for the robust selection process

7.3.2 Distortion analysis during machining of symmetric and asymmetric RS on coupons

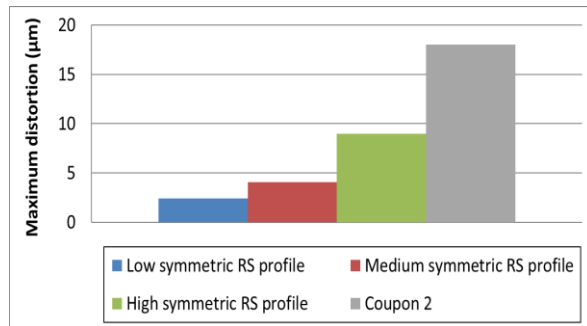
Initial machining cuts of 0.4 mm and second cuts of 0.4 mm (0.8 mm in total) were experimentally performed in all coupons. The distortions were measured (in the region which was unconstrained) and compared with the three initial FE models generated (Figure 7-31). The FE model that best matches the experimental measurements of this second cut would be used later on for proposing the layer removal optimization in the trials. It can be seen from this figure that the FE model that matches well with the experimental results is the high symmetrical residual stress FE model (Figure 7-10). This model would be used for predicting the machining distortion for the consequent cuts.

Chapter 7: Residual stress and distortion analysis

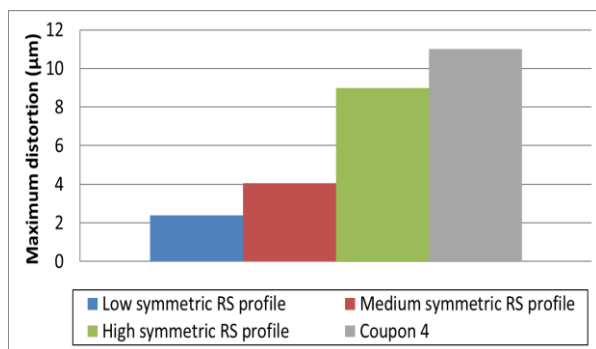
(a)



(b)



(c)



(d)

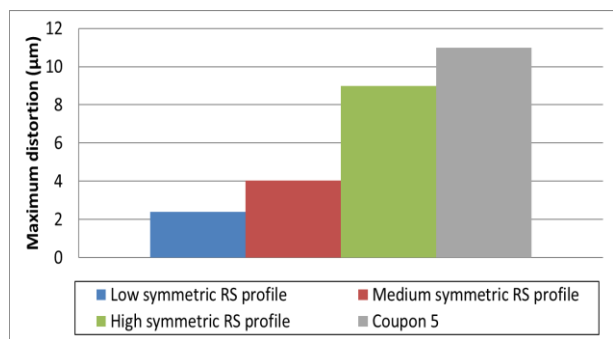
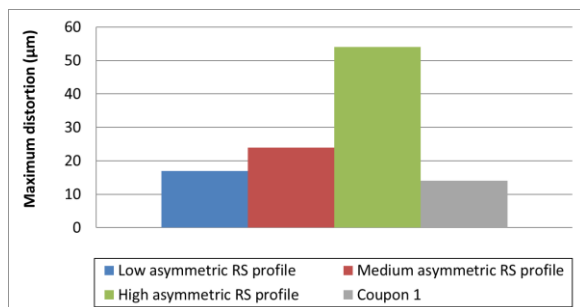


Figure 7-31: Second cut analysis for symmetric residual stress coupons: (a) Coupon 1, (b) Coupon 2, (c) Coupon 3, (d) Coupon 4.

For coupon 1 the low asymmetric residual stress profile was used (Figure 7-32 (a)), while for coupon 2 the medium asymmetric residual stress profile was used (Figure 7-32 (b))

(a)



(b)

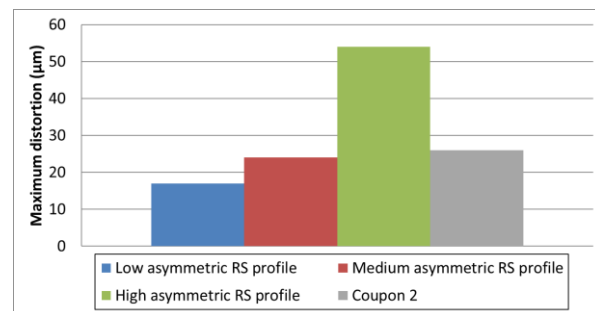


Figure 7-32: Second cut analysis for asymmetric residual stress coupons: (a) Coupon 1, (b) Coupon 2.

Chapter 7: Residual stress and distortion analysis

Results of the FE simulations and comparisons against the measurement data for the symmetric RS simulations are shown in Figure 7-33. For coupon 2 (Figure 7-33 (a)), distortion predictions for the top face machining (cuts 1 to 9) presented a difference of 38 % compared to the experimental data, while the bottom face distortion prediction had an average difference of 46 %. For coupon 4 (Figure 7-34 (a)), distortion predictions for the top face (cuts 1 to 9) had a difference of 26 % while the bottom face similarly showed a difference of 46 % overall. For coupon 5 (Figure 7-34 (b)) distortion predictions for the top face (cuts 1 to 9) had a difference of 18 %.

During the phase one machining, the predictions were closer to the measurement data. The variance between the FE model and the experimental data was due to the difference in the quench residual stress profile comparison (Figure 7-10) which is critical for distortion predictions, especially for aluminium alloys. The greater differences were found during machining distortion predictions of the bottom face. This could have been due to the model not being able to predict accurately the fixture release of phase one as any errors associated in this would be carried forward to the next phase. The influence on the rigid body motion is shown in Figure 5-49 and is a critical step on predicting accurately the post machining distortion.

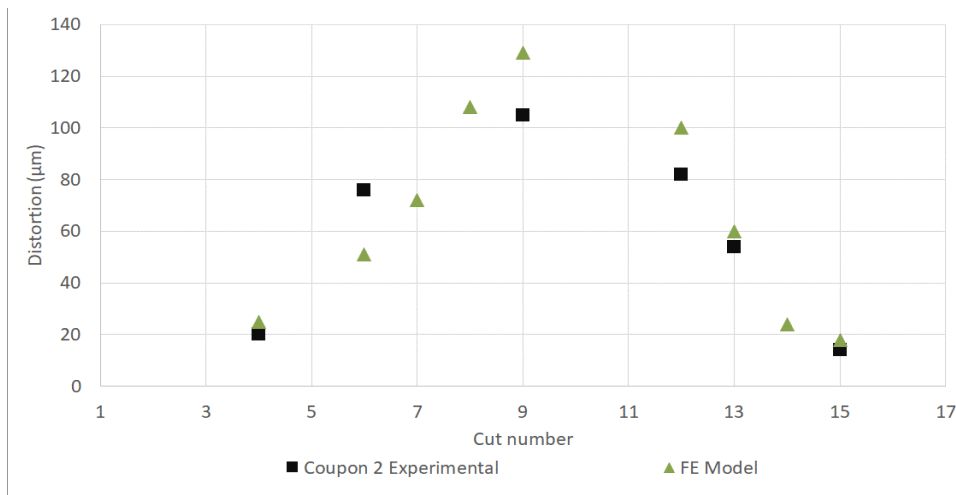


Figure 7-33: Effect of Tool Path Strategy on machining Distortion Machining distortion comparison with experimental data for the symmetric RS coupon 1.

Chapter 7: Residual stress and distortion analysis

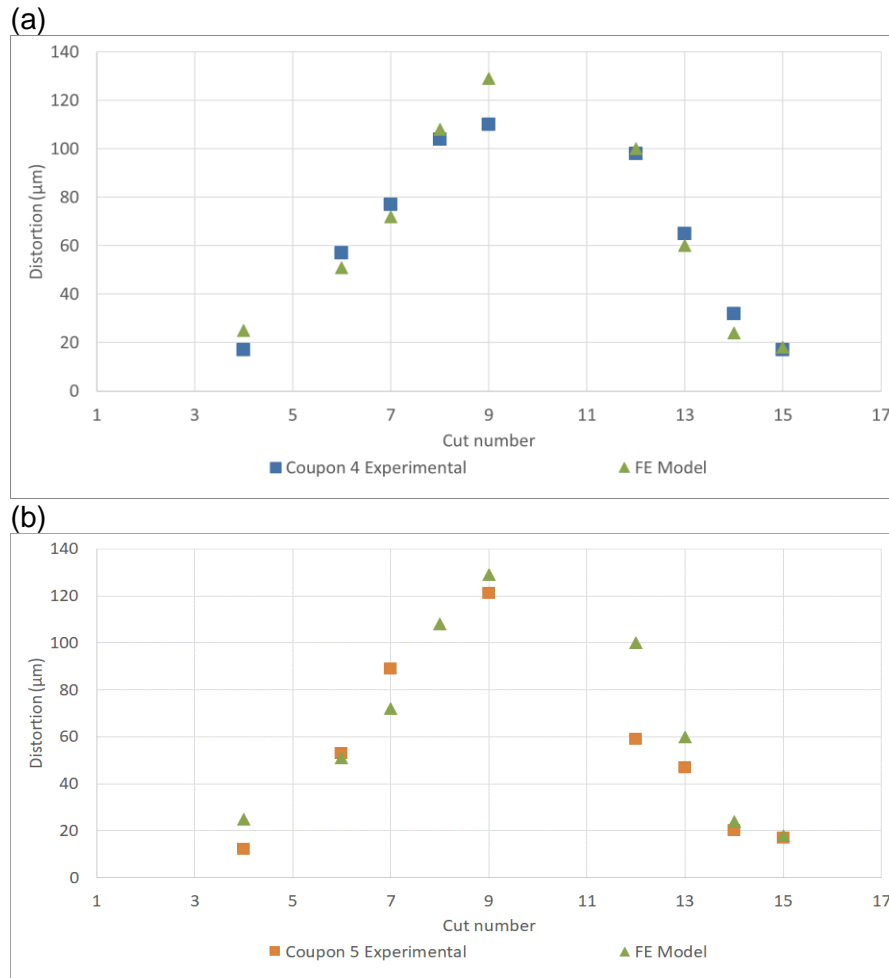


Figure 7-34: Effect of Tool Path Strategy on machining Distortion Machining distortion comparison with experimental data for the symmetric RS coupons: (a) Coupon 4, (b) Coupon 5.

Similar to the asymmetric residual stress predictions, the FE model accurately predicted the trend in the top face machining distortion for coupon 8 with a difference of 18 %. In the case of the phase two machining of coupon 8 (Figure 7-35 (a)), the FE model predicted the tendency of the distortion profile but the magnitude was largely over predicted with a maximum of 42 %. This was not the case for coupon 9 with an under predicted difference of 27 % for the top face and 38 % for the bottom face machining (Figure 7-35 (b)).

Similar to the results obtained from the symmetric RS profile coupons, the FE model and measurement data were in acceptable agreement for the top face machining. The major differences between the models and distortion data were observed from phase two machining (bottom face machining), which could be due to the model not predicting the stress distribution correctly as previously discussed.

Chapter 7: Residual stress and distortion analysis

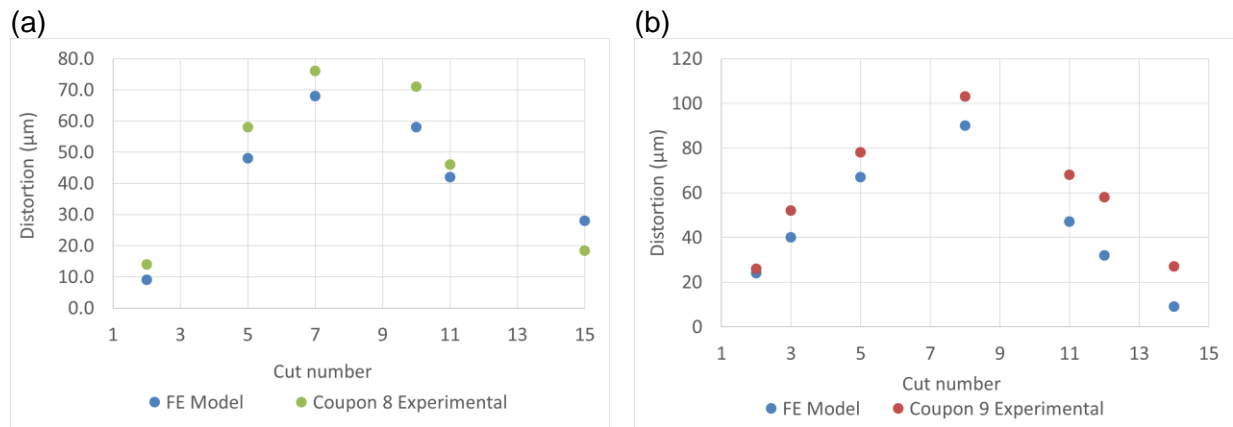


Figure 7-35: Effect of Tool Path Strategy on machining Distortion Machining distortion comparison with experimental data for the asymmetric RS coupons: (a) Coupon 1, (b) Coupon 2.

Finally, the FE model was compared to CMM post machining for the symmetrical RS coupon as shown in Figure 7-36 and Figure 7-37. It can be observed that all coupons distorted in a similar way, with the right end of the coupon having a higher distortion (p5) than the left end (p1). When the CMM data was compared against the FE models, it was found that the FE simulations were able to represent the distortion trends; but the models were mostly under predicting the distortion magnitudes with around 20 μm difference between the FE model and CMM. The difference of the prediction would be accounted to not accurately capturing the residual stress redistribution or not applying the correct fixture conditions.

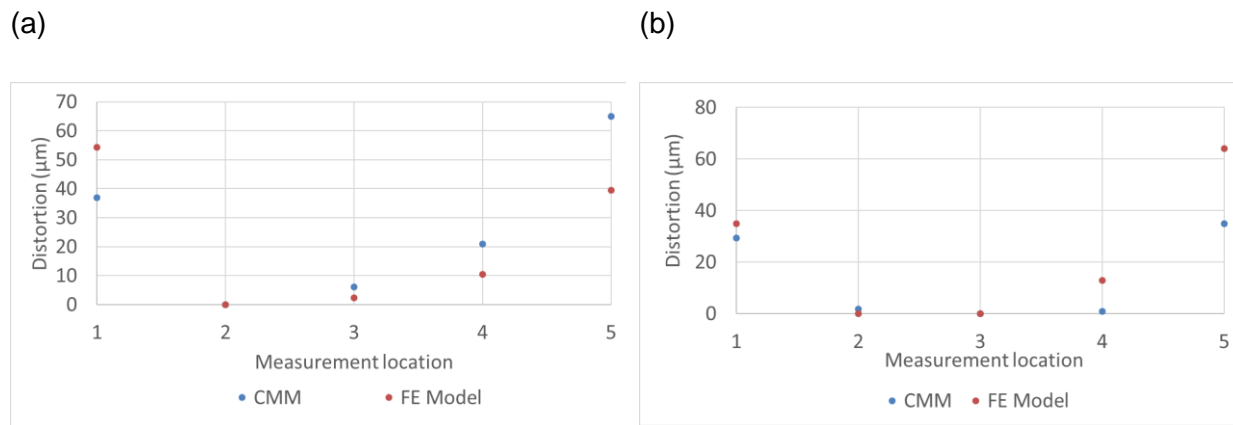


Figure 7-36: FE model comparison with post machining distortion for the symmetric RS coupons: (a) Coupon 1, (b) Coupon 2.

Chapter 7: Residual stress and distortion analysis

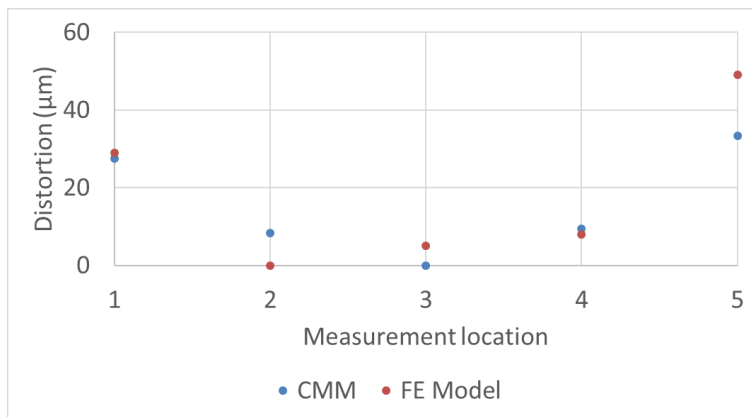
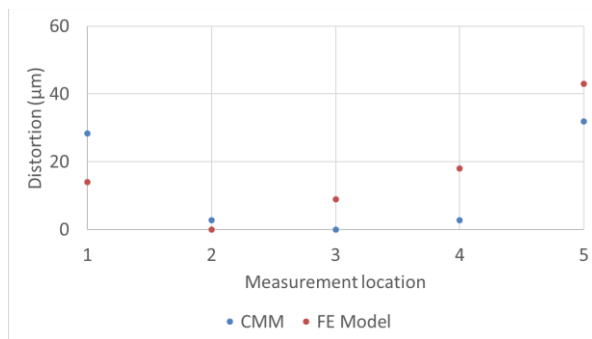


Figure 7-37: FE model comparison with post machining distortion for the symmetric RS coupon 4.

Similar to the symmetrical RS profile coupon, FE distortion simulations were compared with post machining distortion for the asymmetrical RS coupons Figure 7-38. From the figures, it can be seen that the FE model over predicted the distortion for coupons 1 and 2 at the ends would be accounted to not accurately capturing the residual stress redistribution or not applying the correct fixture conditions.

(a)



(b)

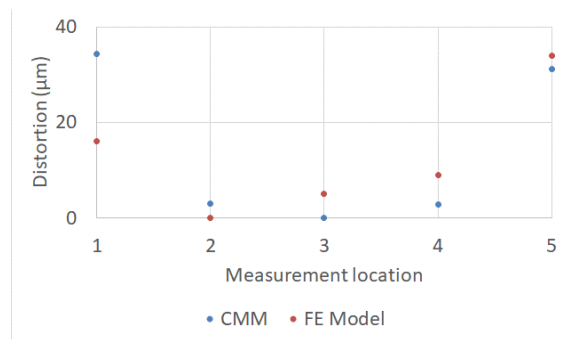


Figure 7-38: FE model comparison with post machining distortion for the asymmetric RS coupons: (a) Coupon 1, (b) Coupon 2.

The following conclusion can be made from this study:

- For the on machine distortion measurements, the FE model predicted the trends but not the magnitude. This was due to the errors carried forward from residual stress predictions. For the top face comparisons: symmetric RS profiles, there was a difference of 38 % (coupon 1), 26 % (coupon 2), 13 % (coupon 4), and 18 % (coupon 5). For the asymmetrical residual stress profile there were differences of 18 % (coupon 1) and 27 % (coupon 2). While for the bottom face, there were differences of 38-60 % for the symmetric residual stress profile and 35 – 42 % for the asymmetric residual stress profile.
- The FE model predicted the trend but not the distortion magnitude for the post machining distortions, with the FE model having an average difference of 20 μm when compared for all analysis.

7.3.3 Distortion analysis on tool path strategy

To capture the distortions that result from different tool path strategies, 3D displacement scanning was performed by the GOM ATOS III structured light. Block 1 represents the zig-zag tool path while Block 4 represents the helical tool path. It can be seen in Figure 7-39 that the helical tool path although is attractive in reducing the machining time, has a higher distortion by around 100 μm at 5 mm and around 50 μm at 243 mm. The difference between the two methodologies seem to be higher between 135 mm to 216 mm.

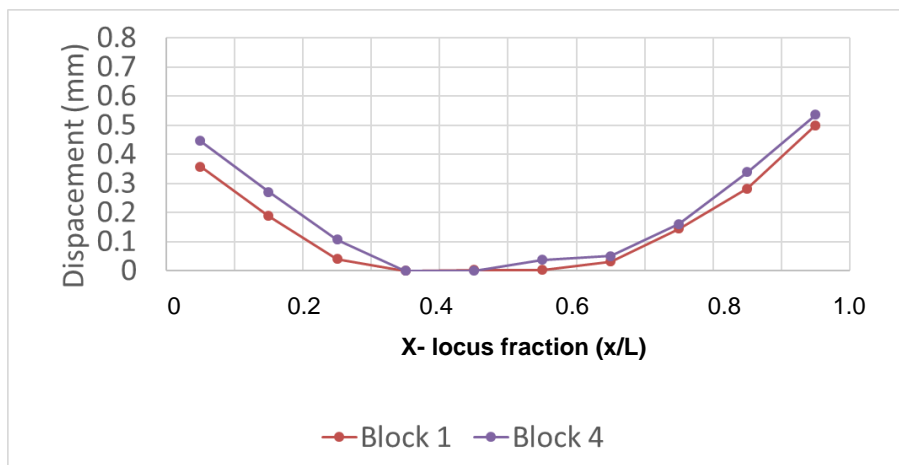
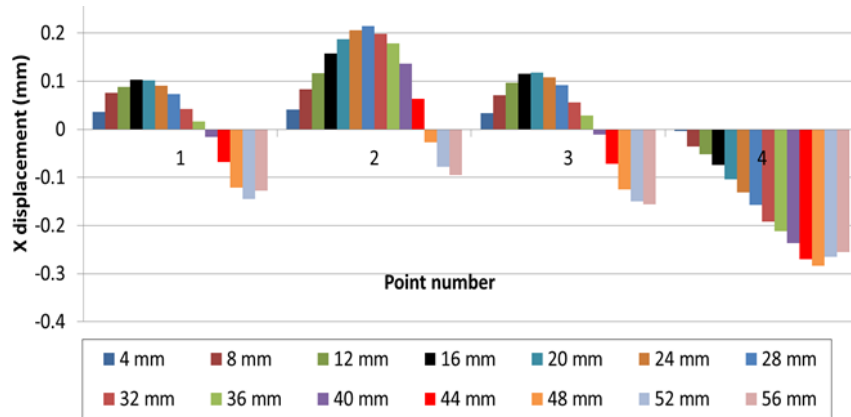


Figure 7-39: Post machining distortion comparison between tool path strategies used for pocketing operation.

Chapter 7: Residual stress and distortion analysis

The tool paths and the FE model were compared as shown in Figure 7-40. From the results it can be seen that the distortion increases but at a certain axial depth of cut, the distortion begins to decrease and tend towards zero. This is summarized in Figure 7-41. During machining in the regions highlighted in the dark hatched above the (NA), the distortion is positive, in contrast during machining in the light hatched region below the NA, the distortion is decreasing. This knowledge is paramount for controlling distortion during pocket milling.

(a)



(b)

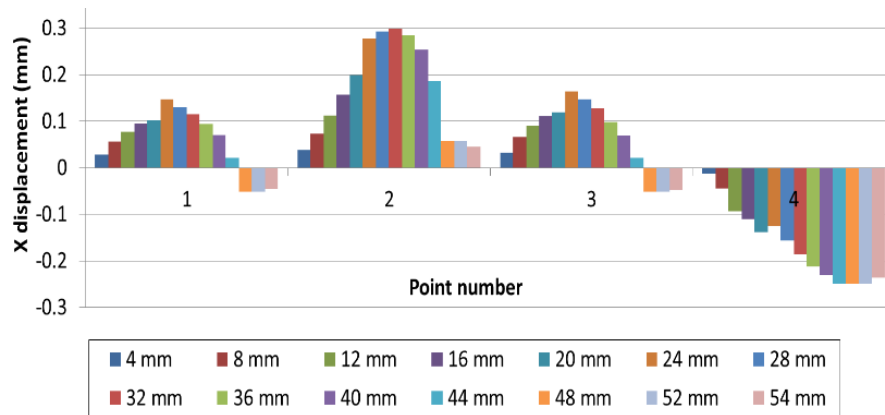


Figure 7-40: FE Model comparison with On Machine Inspection for: (a) Zig-Zag tool path, (b) Helical tool path.

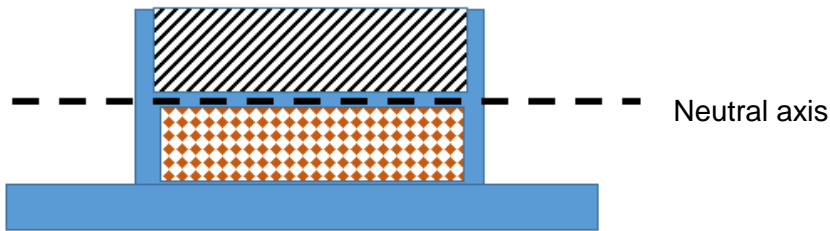


Figure 7-41: Effect of Neutral Axis on machining distortion.

The comparison between the zig-zag tool path and the FE model is shown in Figure 7-42. It can be seen that the FE model predicts the trend but not the distortion magnitude. This could be due the difference with the residual stress predictions from the heat treatment, not incorporating the actual work holding strategy.

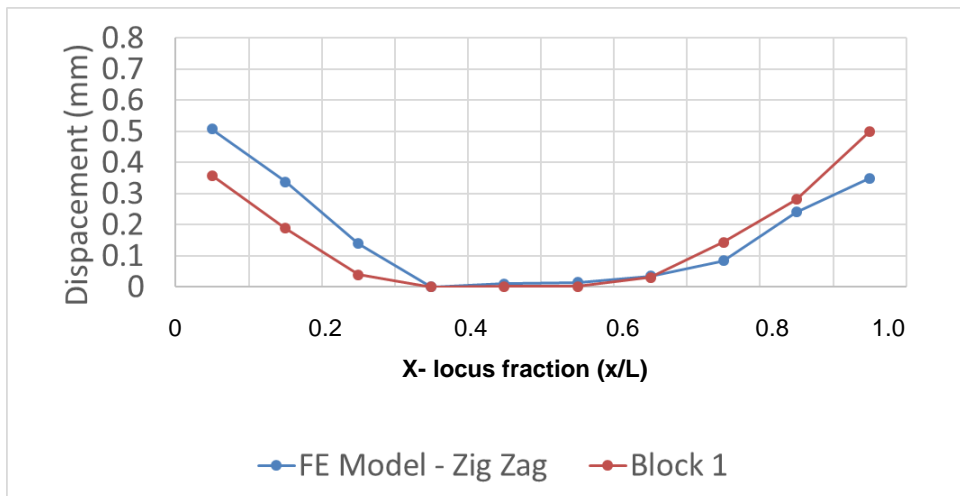


Figure 7-42: FE comparison with post machining distortion data for zig-zag tool path.

The comparison between the helical tool path and the FE model is shown in Figure 7-43. It can be seen that the FE model predicts the trend but not the distortion magnitude. This could be due the difference with the residual stress predictions from the heat treatment, not incorporating the actual work holding strategy.

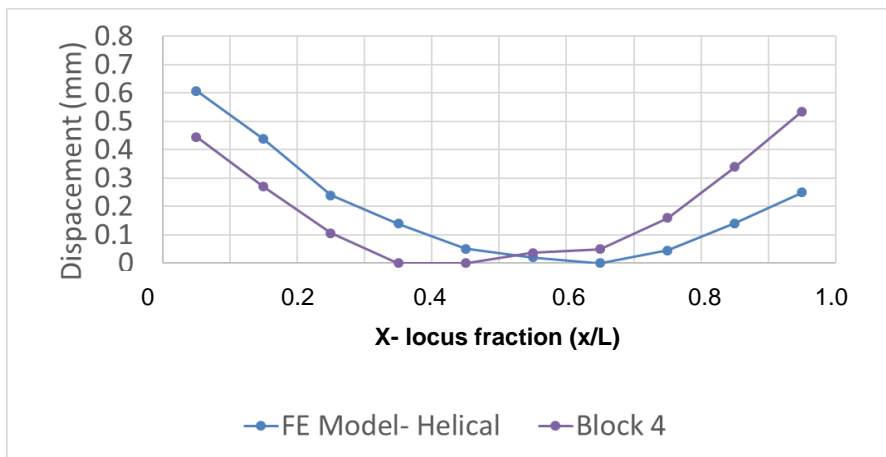


Figure 7-43: FE comparison with post machining distortion data for helical tool path.

7.3.3.1 Effect of Ramp Angle on machining distortion

The influence on the ramp angle on machining distortion was captured using CMM as illustrated in Figure 7-44. The difference between the two techniques is around 20 μm from both ends. Although the difference between the two methodologies might not seem to be large, there is still a noticeable variation between the two and this might play an influencing role during the machining of structures with multiple pockets.

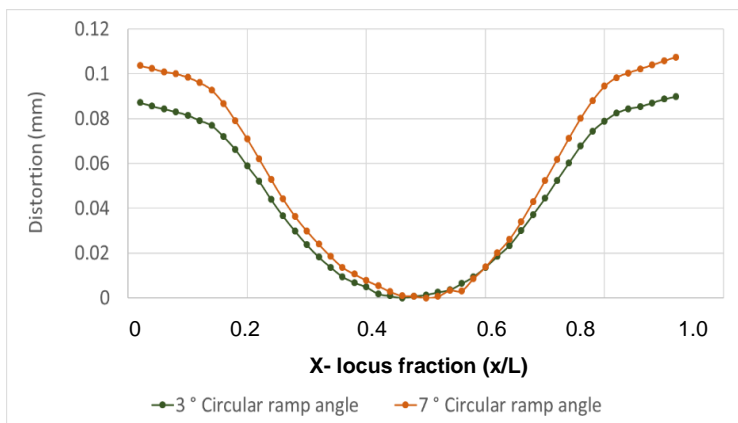


Figure 7-44: Post machining distortion comparison for helical ramp angles.

The FE model was compared with the post machining distortion for the 3 ° ramp angle machining as shown in Figure 7-45. The FE model predicted the trend but not the magnitude especially at the edges. The possible error would due to the boundary conditions used during the material removal and post material removal. The model did not include either the friction coefficient or the fixture loadings used during the process, which would assist in the accuracy of the model.

Chapter 7: Residual stress and distortion analysis

The importance of incorporating the fixtures loading for the prediction of machining distortions has been highlighted in their thesis by Cerutti [11], Jitender [243]. In addition to this, a case study done by Siebenaler et al [270] showed that the accuracy of the FE model can be increased by 98% by incorporating the accurately workpiece and fixture contact modelling. From these studies, it was illustrated on the influence of fixtures on the machining distortion magnitude and the profile, which can explain why there is a difference between the FE model prediction and the experimental measurements. An additional source of error was issues with mesh distortions, although every attempt was made to increase the mesh resolution for each material removal simulation, there were mesh distortions, which consisted of remeshing and interpolation, hence increasing errors.

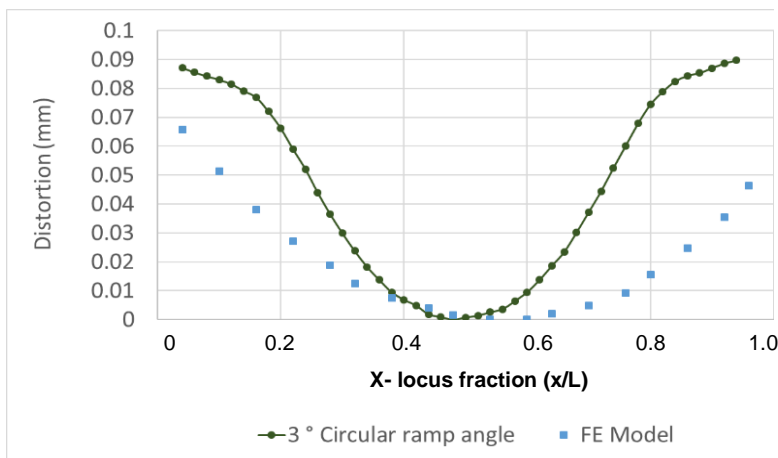


Figure 7-45: FE model comparison with CMM for 3 ° ramp angle.

Similarly, the FE model was compared with the distortion measurements as shown in Figure 7-46. The FE model captures the trend but not the magnitude. The FE model predicted the trend but not the magnitude especially at the edges. This could be due to the over constrained boundary conditions applied on the model during the material removal. An additional source of error was issues with mesh distortions, although every attempt was made to increase the mesh resolution for each material removal simulation, there were mesh distortions, which consisted of remeshing and interpolation, hence increasing errors.

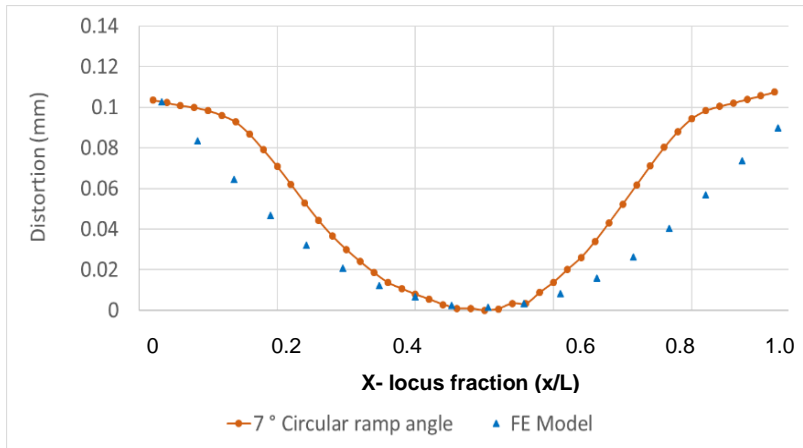


Figure 7-46: FE model comparison with CMM for 7 ° ramp angle.

7.3.3.2 Effect of radial depth of cut on machining distortion.

Machining trials using the 3 ° circular ramp were performed to understand the influence of the radial depth of cut on machining distortion (Figure 7-51). The comparison by varying the radial depth of cut was minimal in comparison to the axial depth of cut. The increase in the distortion would be accounted to the increase in the material removal layer by around 50%.

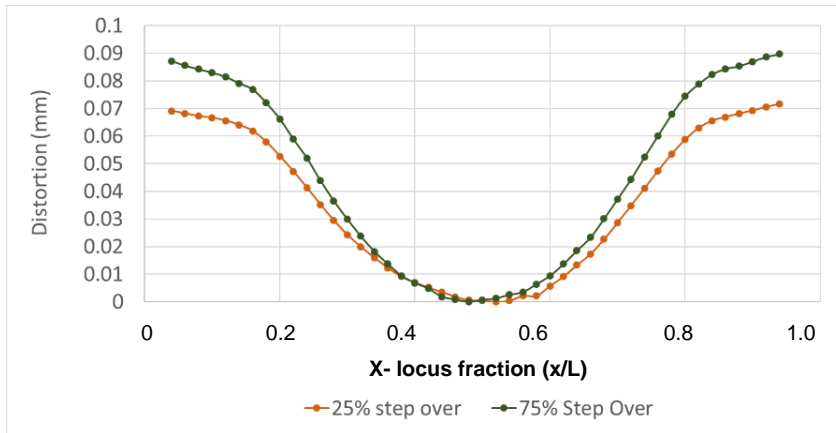


Figure 7-47: FE model comparison with CMM for 3 ° ramp angle.

The following summary and conclusions can be made from this study:

- There is an influence of varying the ramp angle on the machining distortion with a 3 ° circular ramp exhibiting a lower distortion than the 7 ° circular ramp angle. This is due to the amount of material removed in an instance between the two strategies (in Figure 7-44).
- The FE model was successful in capturing the trend but not the magnitude especially at the ends of the block. This would be accounted to the differences associated with the residual stress from the heat treatment condition (Figure 7-44, Figure 7-45)
- Similarly, by increasing the radial depth of cut (step over) by 50%, there is an increased distortion due to the increased volume amount of material removed in an instance.
- This study highlights the importance of considering aspects during machining that influence distortion.

7.3.4 Distortion analysis due to the varying billet orientation

The displacement scanning prior to machining was done by the GOM ATOS III structured light. This technique was chosen in order to initially capture the geometric profile of the billet prior to machining. The advantage of this system to the CMM is these scanning systems are portable, and allow much faster rates of data capture than CMM.

It can be seen from Figure 7-48; the two billets scanned show a concave shape (Billet 5 and 8). It was assumed that the billet 5, which had a convex shape, had the same profile since the machining procedure was the same. Therefore, for the effect of pocketing sequence, Billet 8 (Sequence A) and Billet 5 (Sequence B) will be compared and for the effect of billet orientation, Billet 5 (Orientation A) and Billet 3 (Orientation B) will be compared.

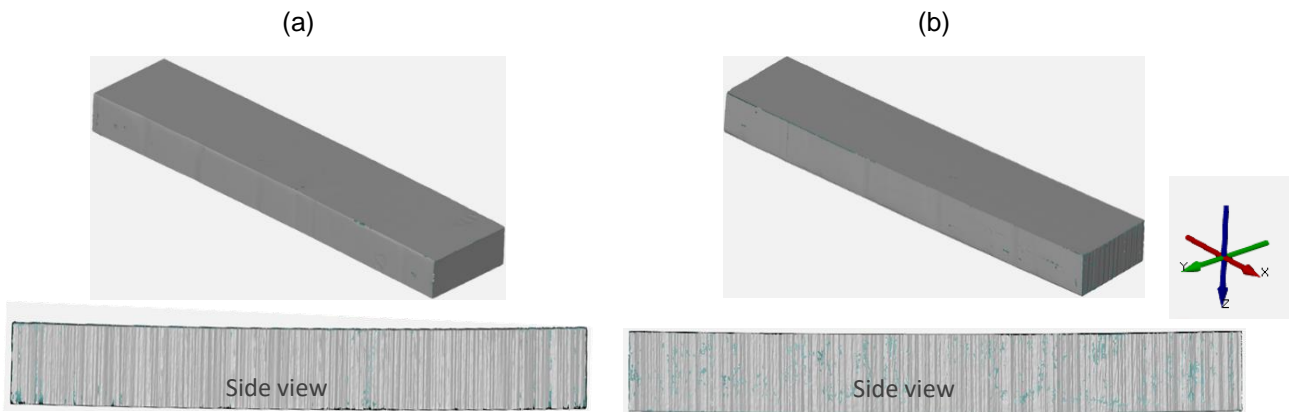


Figure 7-48: 3D displacement scanning for billets: (a) Convex, (b) Concave.

Chapter 7: Residual stress and distortion analysis

In addition to this, On Machine Inspection data was performed on the billet as shown in Figure 7-49 which confirmed the shape of the measurements.

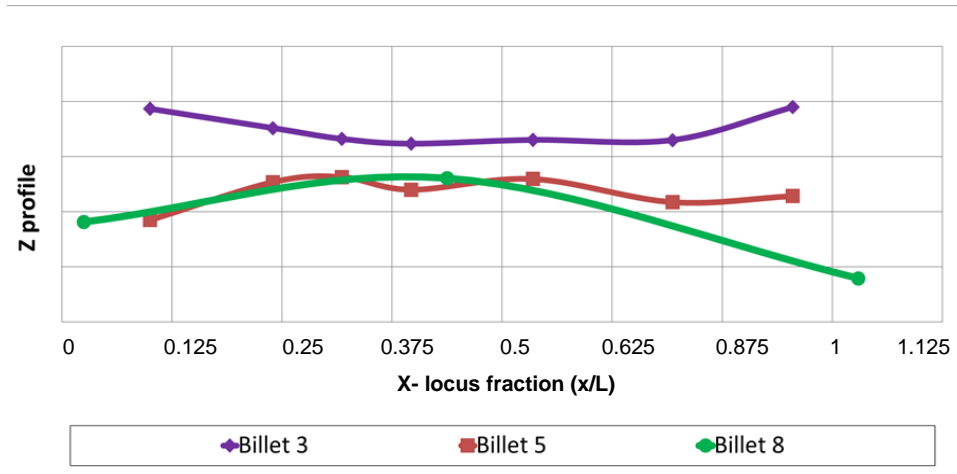


Figure 7-49: 3D displacement scanning for billets: (a) Convex, (b) Concave.

To provide confidence in the 3D scanning post machining distortion, a repeatability study was performed as shown in Figure 7-50. The repeatability of these measurements was an average of $23 \mu\text{m}$.

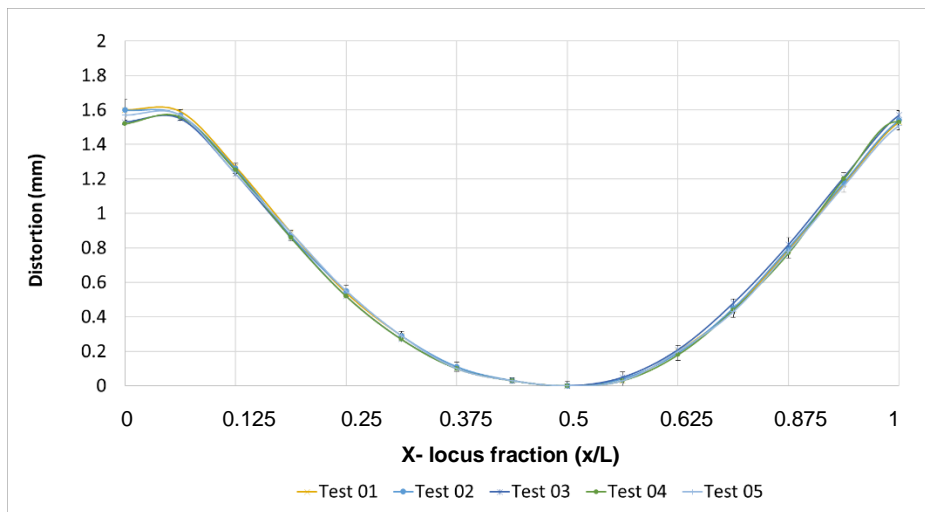


Figure 7-50: 3D scanning repeatability assessment.

For the effect of billet orientation, the FE model prediction was compared with post machining distortion for Billet orientation A using pocketing strategy B (Figure 7-51). The FE model under predicted the distortion magnitudes, especially the edges of the billet, with a difference of over 100%.

Chapter 7: Residual stress and distortion analysis

From the region of 50 – 300 mm along the measurement length, the model under predicts distortions with a difference of 100%. At a length of 390 and 450, the difference is reduced to 50% but then increases from 500 – 650 mm.

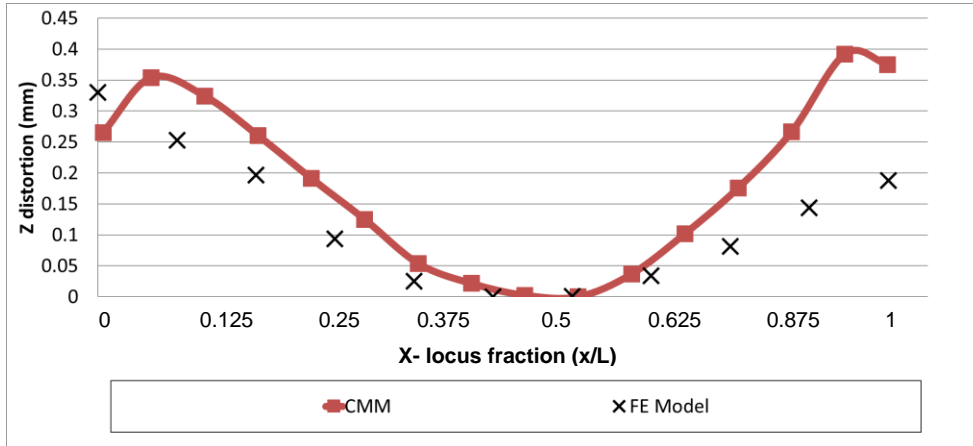


Figure 7-51: FE model comparison with CMM for effect of pocketing sequence on machining distortion.

For the Billet orientation B (Figure 7-52), the model over predicts the distortion, with a difference of around 400 μm at 0 mm decreasing towards 650 mm. The difference then increases from 700 – 743 mm to 400 μm .

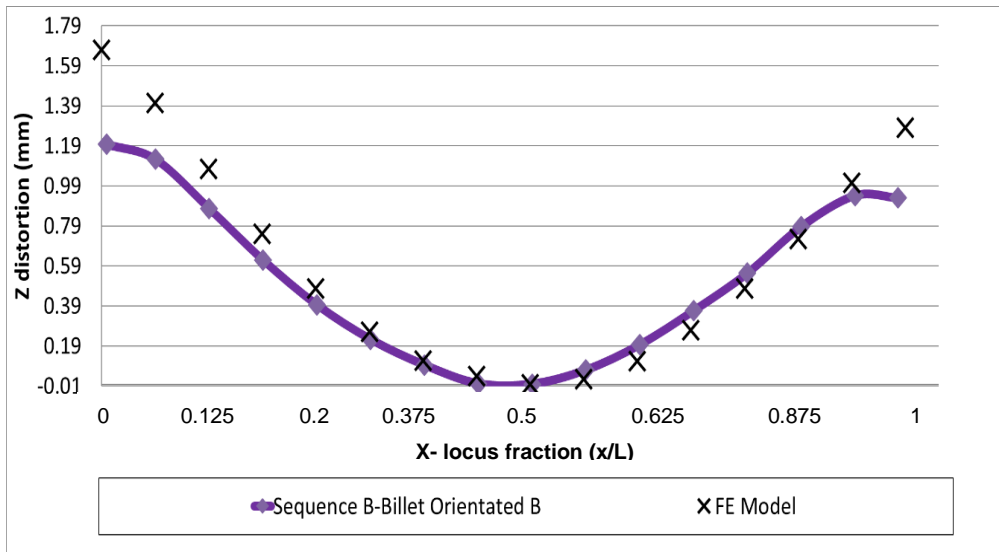


Figure 7-52: FE model comparison with CMM for effect of billet orientation on machining distortion.

Chapter 7: Residual stress and distortion analysis

For the effect of pocketing sequence, the FE model was compared to CMM data as shown in Figure 7-53. The FE model predicted well the “valley” distortion profile capturing the non-symmetrical distortion at the edges of the part, but under predicts the distortion in most cases. This under prediction may be due to under predicting compressive stresses in the FE model prior to the pocketing sequence. As previously stated, another factor that needs to be considered is instead of generating the pockets incrementally by a series of passes, the pockets were generated by removing the full volume of the pocket in one pass. The distortion magnitude using sequence A is shown to be a close prediction between 0-150 mm and 600 – 743 mm along the measurement length but not between regions of 250 -550 mm where a difference between actual and predicted distortions of over 50% can be observed.

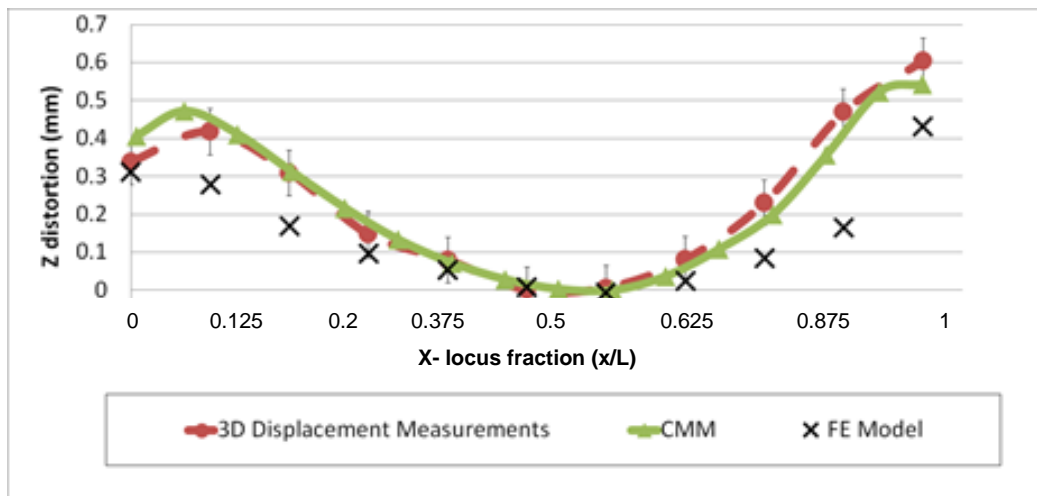


Figure 7-53: FE model comparison with CMM and 3D displacement scanner for pocketing using sequence A.

Regardless of the FE model’s difference with the experimental measurements, the FE model was able to create pocketing sequences that would reduce the machining distortion. In addition to this, the effect of billet orientation was captured. The summary of the machining trials is shown in Figure 7-54.

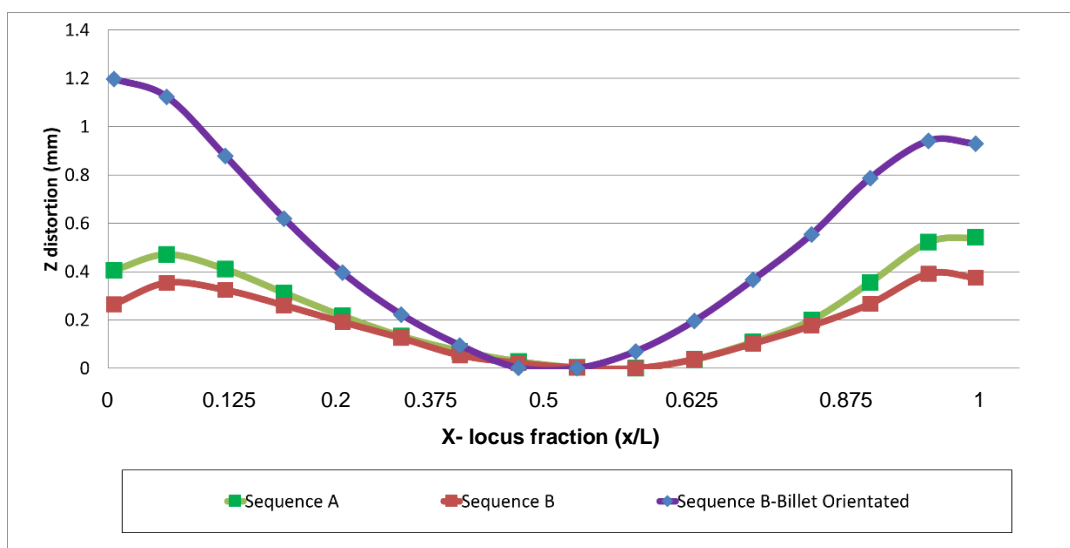


Figure 7-54: FE model comparison with CMM for effect of billet orientation and pocketing sequence.

7.3.5 Distortion analysis on varying part location

The comparison between the FE model and CMM data after machining the representative part is shown in Figure 7-55. It can be seen that the FE model predicts the trend but not the magnitude especially at the ends where the FE model under predicts the distortion from regions 0 to 300 and over predicts from 300 to 700 mm.

A possible source of error would be due to the boundary constraints used. Although a fixture coefficient was used to model the interaction between the FE model and the fixture model, the friction coefficient used for these simulations was taken from literature and might not accurately model the interaction. To overcome this, it can be recommended in further work, an experimental trail would need to be performed. Another source of error would be due to not including the fixture loading in the simulation.

As highlighted previously, incorporating this would accurately predict the distortions since the simulation is now incorporating actual constraints in the experimental trials. A final source of error could be due to using an inappropriate rigid body motion constraint for the post machining distortion, as it can be seen that on one section distorts more than the other does while the CMM results are more balanced.

Chapter 7: Residual stress and distortion analysis

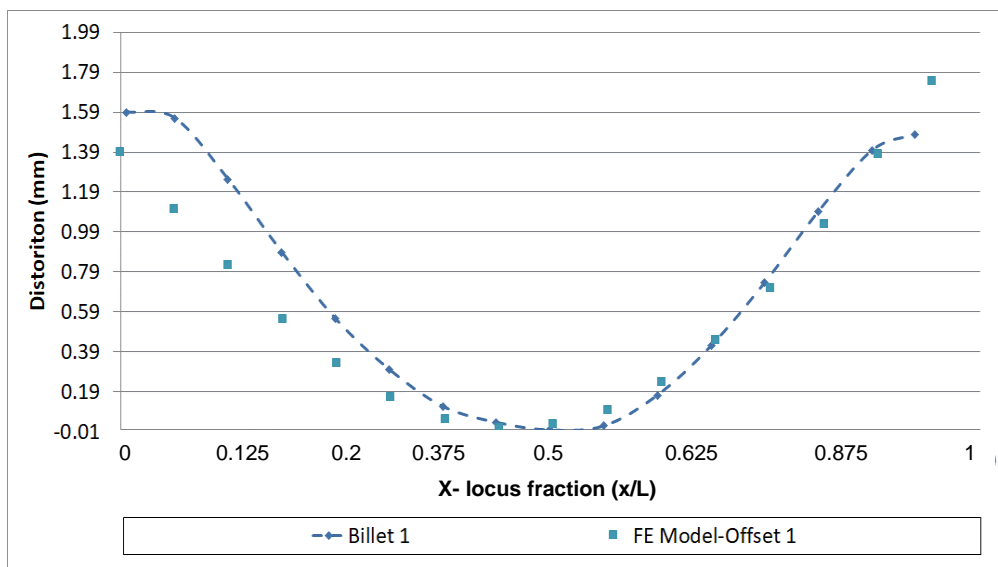


Figure 7-55: FE model comparison with CMM for effect of billet orientation.

Similarly, the comparison between the FE model and CMM data after machining the representative part is shown in Figure 7-56. It can be seen that the FE model predicts majority of the trend but not the magnitude especially at the ends where the FE model initially over predicts until 400 mm and over predicts the distortion to 500 mm and finally under predicts the distortion by around 300 μm . This prediction difference from the FE model could be factors highlighted previously due to the boundary conditions used.

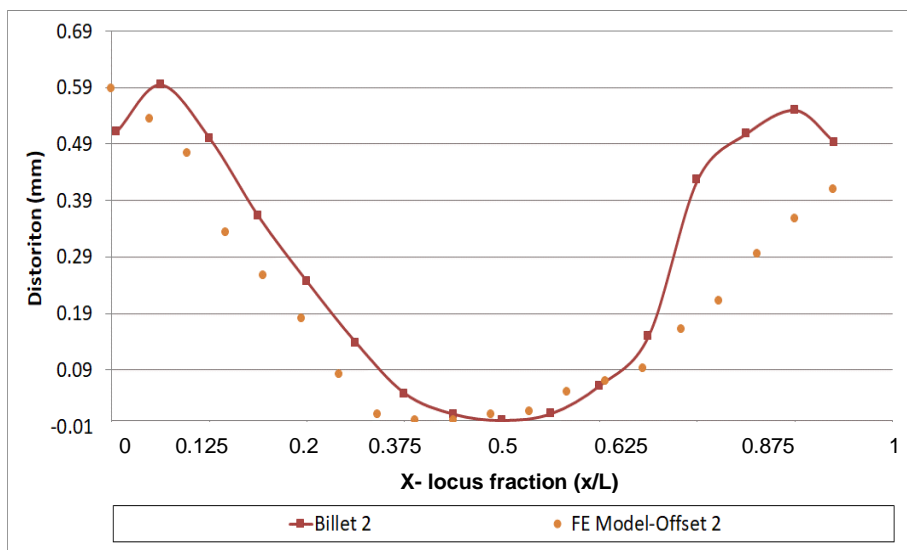


Figure 7-56: FE model comparison with CMM for effect of billet orientation.

Chapter 7: Residual stress and distortion analysis

From this study, the following conclusions can be made:

- In regards to the effect of resequencing of the pockets, were compared for investigating the effect of resequencing of pockets. The model and experimental work proved that sequence 1 resulted in higher distortion after the machining process compared to sequence 2. This demonstrated that the effect of resequencing of the pockets has an influence on distortions.
- The CMM measurements of the bending of the part showed that for sequence 1, 15 points are higher than 300 μm . For sequence 2, none of the measured points are higher than 300 μm .
- In regards to the part orientation, initial 3D scanning measurement prior to machining confirmed that the billets had different orientations when placed on the machine bed. It was concluded that the different orientations significantly influenced the final distortions due to the stress profile. This can be seen in the CMM measurements after the machining the billets with the concave and convex orientation, which were machined using the same sequences. The billet, which had a convex shape with respect to the machine bed, which has a higher compressive stress magnitude at the top face than the bottom face (this was corroborated with the stress measurements). It was contrary for the concave, which had a lower residual stress on the top face prior to machining.
- It should be highlighted that the FE prediction was demonstrated to be a powerful tool to initially investigate the effect of resequencing the machining of pockets to minimize distortions. This assisted in selecting the studies of worst case and the enhanced best case machining sequence without expensive machining trials

8 Machining Process Strategy for Distortion Mitigation from Bulk Residual Stress

Following the study on the impact of different machining methodologies for controlling distortion, a final part was machined combining knowledge attained from this study. Similar to the previous work, the representative part was used for this analysis and the process flow illustrated in Figure 8-1 was followed.

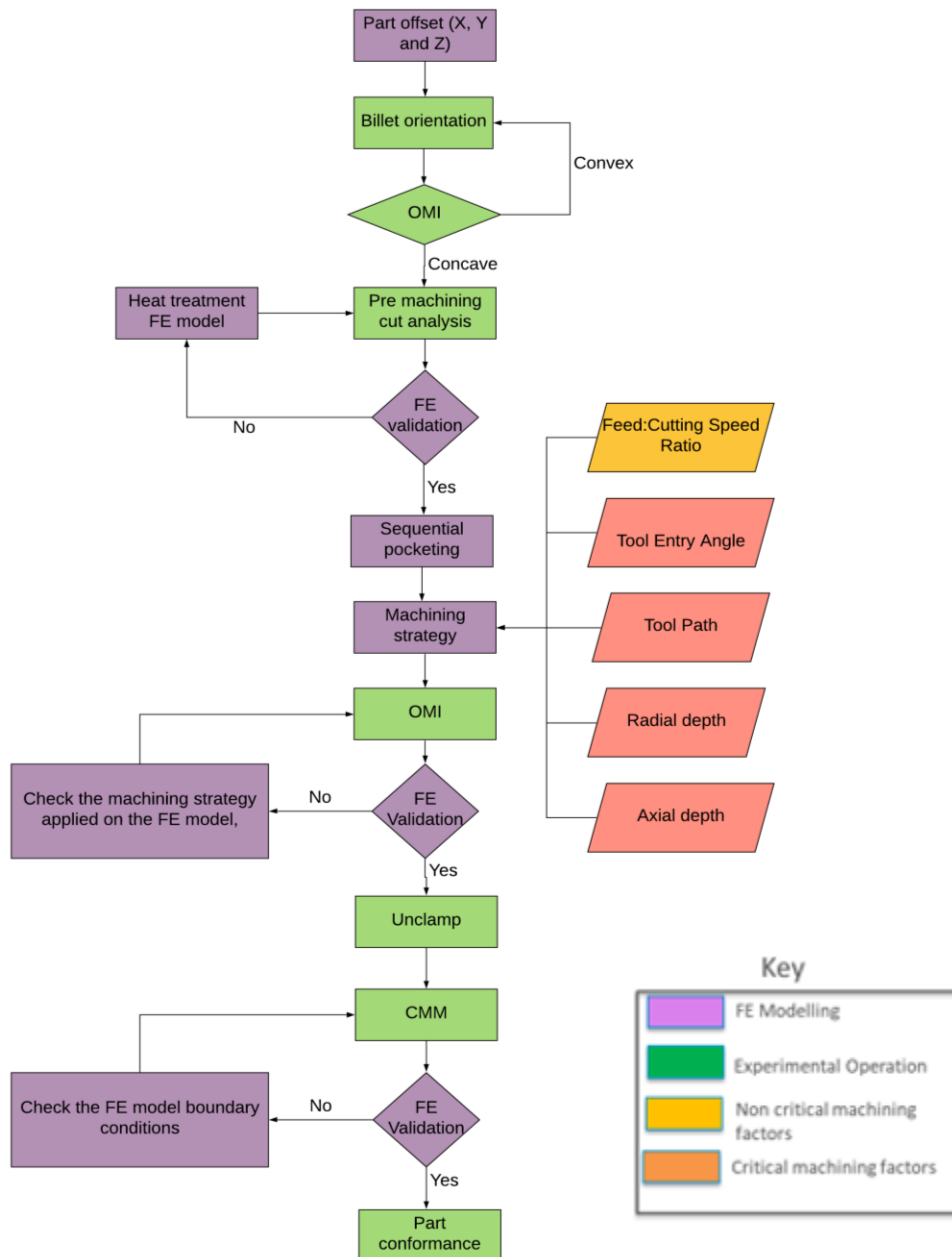


Figure 8-1: Production manufacturing strategy flow chart.

Chapter 8: Machining Process Strategy for Distortion Mitigation from Bulk Residual Stress

The billet was 3D scanned prior to machining to capture its volumetric profile. The billet was then placed in the preferred orientation on the machine bed; this was then validated using On Machine Inspection. The next step would be to perform the first cut analysis on the billet and the distortion measured using On Machine Inspection (OMI) to define the appropriate FE model to use. In this analysis, this would not be necessary, since the FE model had already been validated.

Part location analysis in the parent work piece would need to be performed in width and longitudinal direction to find the appropriate part location (part offset in the thickness has already been performed).

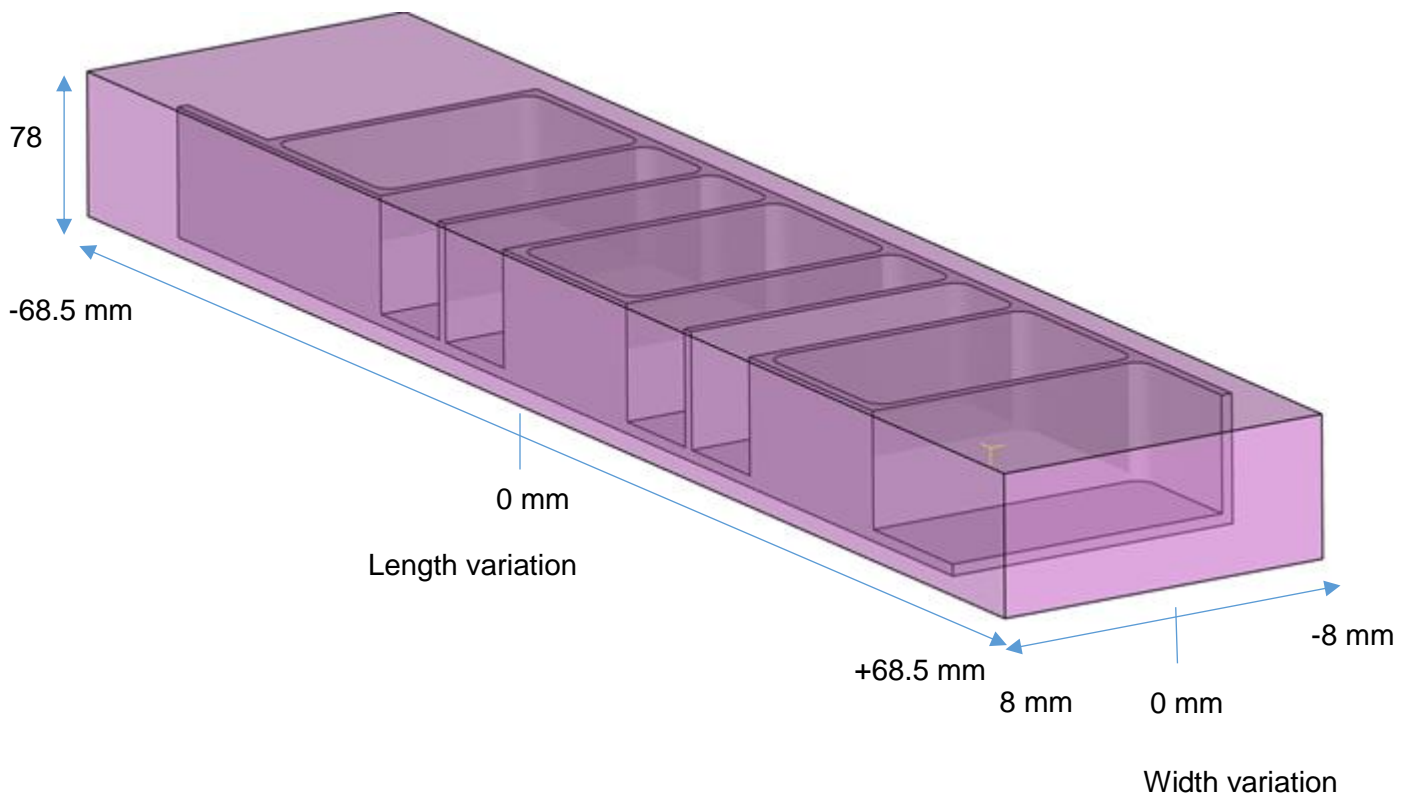


Figure 8-2: Positioning of the machined workpiece in the forged billet (dimensions in mm).

This is shown in Figure 8-3. It can be seen that varying the part in the width direction has an influence in the final machining distortion, which has not been previously presented. This information is useful especially for billets thicknesses that have been produced to a near to final part tolerance reducing the effect of performing a part offset analysis in the thickness direction. This simulation result also emphasizes the need to perform a tri-axial part offset analysis to improve the chances of controlling machining distortion.

Chapter 8: Machining Process Strategy for Distortion Mitigation from Bulk Residual Stress

In addition to this, the residual stress contour has regions of extreme high and low gradients which when machined off or removed, will cause large or low distortions, hence, it is critical to find this region.

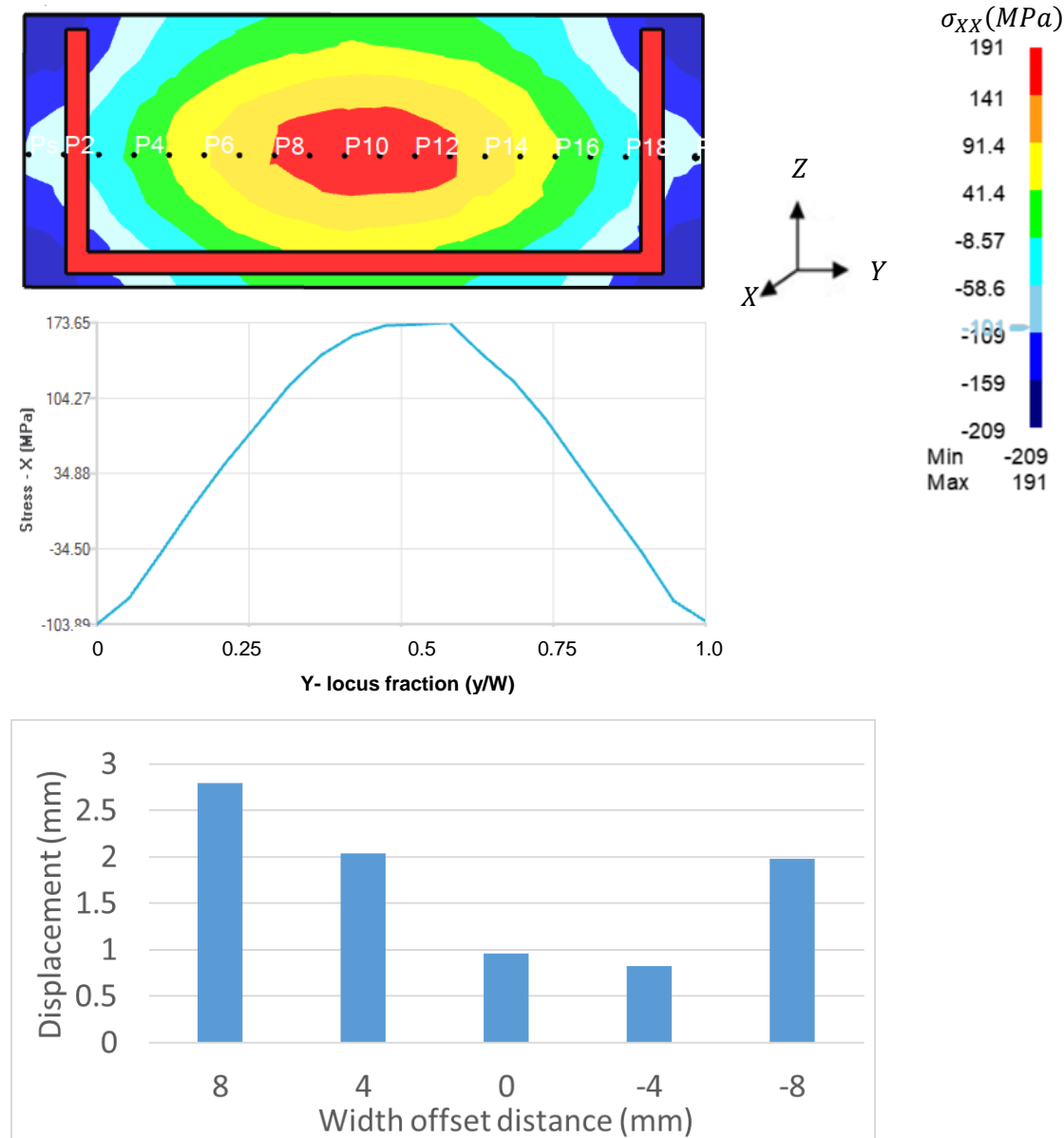


Figure 8-3: Part offset in the width direction.

Interestingly enough, it can be seen that the gradient across the length doesn't vary as much as shown in Figure 8-4. Therefore the variation in distortion could be in conjunction to the influence of the residual stresses within width and thickness direction of billet as shown in the Equation 8-1.

Chapter 8: Machining Process Strategy for Distortion Mitigation from Bulk Residual Stress

Therefore to provide the suitable part offset, it is critical to utilise the advantages of finite element simulation due to the complexity involved.

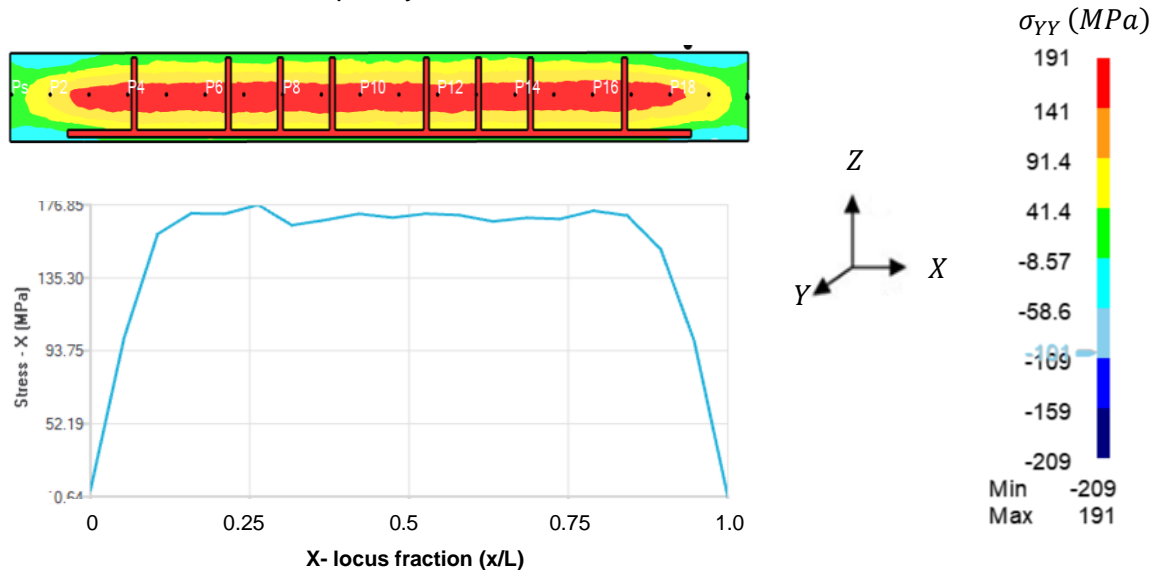


Figure 8-4: Residual stress variation across the longitudinal direction.

$$Part\ offset\ location\ (X, Y, Z) = f(\sigma_{Longitudinal}, \sigma_{Transverse}, \sigma_{Thickness})$$

Equation 8-1: Part offset relationship with tri-axial stresses.

Additionally, part offset in the longitudinal direction was performed as shown in Figure 8-5. Unlike the width direction, the longitudinal direction varies with length with the location that predicts the lowest distortion lies around 22.5 mm in the right of the billet.

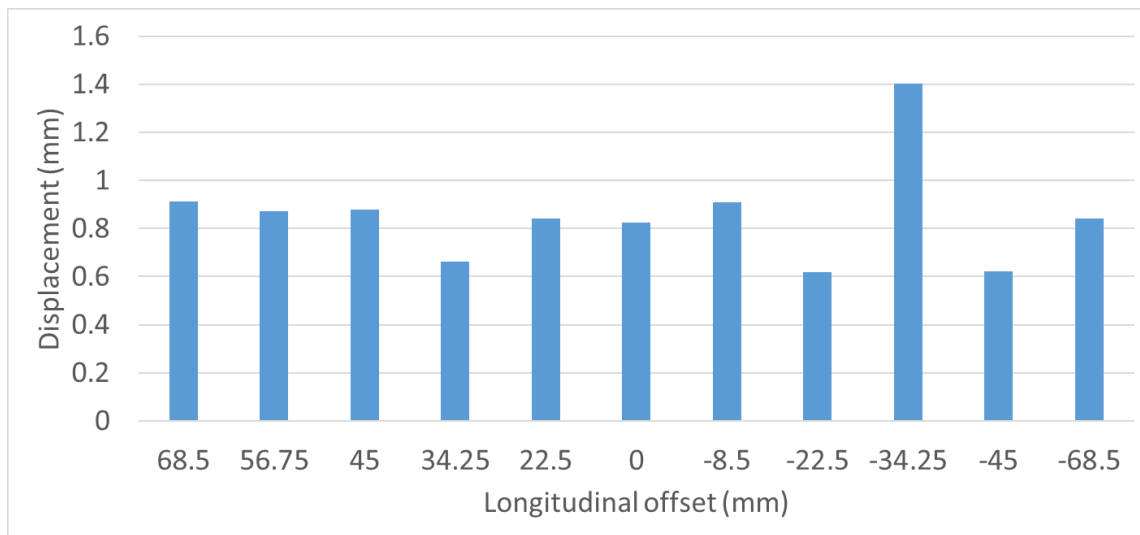


Figure 8-5: Part offset in the longitudinal direction.

Chapter 8: Machining Process Strategy for Distortion Mitigation from Bulk Residual Stress

Once the appropriate part offset, step overs, tool entry, tool path strategy and axial depth of cuts have been simulated, the similar pocketing sequence and machining strategy was used as introduced in section 5.1.4. Using this proposed Method of Manufacture (MoM) the representative part was machined and reduce the distortion magnitude.

Figure 8-6 shows the difference between the Proposed MoM simulation in comparison to the current experimental MoM (Figure 7-51). From this figure, it can be seen that the distortion has reduced considerably by simply controlling the MoM. This knowledge although time consuming, can in the end, benefit the production company. Although to validate this model, experimental trials would need to be performed in future.

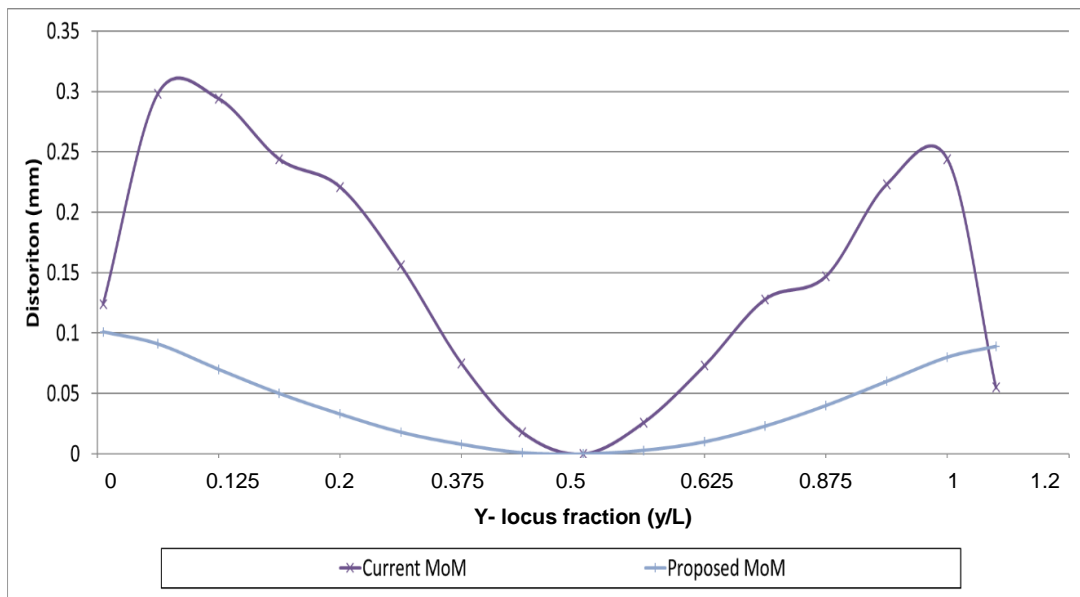


Figure 8-6: Post machining distortion comparison between current MoM and Proposed MoM.

9 Final conclusion

The thesis worked towards developing an in-depth understanding of the effect of residual stresses redistribution on machining distortion for aluminium coupons and components currently lacking. This study utilized extensive experimental measurements from both contour and neutron diffraction. In addition to the novelty of this study, residual stress measurements were performed of a specimen at different stages to understand the residual stress evolution from the quenching process to the final machining operation. Access to residual stress data enabled extensive research to be performed on the key inputs normally considered in the machining process plan and their consequence on post machining distortion.

To bridge this gap of understanding, the aim of this research was to utilize the advantages of Finite Element Analysis (FEA) to provide an understanding on the mechanics of machining distortion due to residual stress redistribution. To reach this objective, a systematic approach was performed in order to develop the required input data for accurately predicting the residual stresses from the quenching process and the consequent machining distortions. This study also enabled to break down each machining operation and study individually their influence on machining distortion.

In the interim stage, material and heat transfer coefficient data was experimentally acquired to provide as an input in the quench Finite Element Model. The quench model was verified and validated using residual stress measurements from the contour method and seemed to match well therefore was deemed suitable to carry out a machining distortion study. The conclusion from this study was to highlight the importance of accurate material properties and the heat transfer coefficients, which comes from testing. This information is the most critical input to accurately predicting the residual stresses during quenching.

Following this validation, the simulation of the machining distortion was carried out based on the assumptions summarized from previous literature on the modeling of the machining distortion for aluminium alloys:

- The stresses from the quenching operation are the key cause of machining distortion
- The machining strategy influences the distortion

Chapter 9: Final conclusion

Based on previous literature, three steps were then performed:

- Generation of quench residual stresses on individual case studies.
- Machining strategies were studied and their influence on the residual stress redistribution was analysed.
- Integration of all these strategies to control post machining distortions

From the studies, it was found that utilizing each strategy correctly could have positive influence in the control of the machining distortion. By varying the part location in X, Y and Z of the final workpiece within the billet was found to have reduced the distortions by a significant amount. The part orientation on the machine bed also showed to have an influence in the post machining distortions. Additionally, the axial (a_p)/ radial (a_e) depths of cut, the tool path strategies can have an influence on the machining distortions. All these factors play important roles in controlling post-machining distortions.

A process strategy was generated defining the procedure and factors to consider when planning machining an aluminium structural component. This strategy has two advantages:

- Enables the user to be more aware of the factors that influence post-machining distortion such as the billet orientation, part location and the machining strategy prior to creating a numerical control program.
- Develop optimized strategies that would reduce the costs associated with trial and error or experimental trials.

As a conclusion, numerical analysis using Finite Element Analysis (FEA) was utilized for the prediction of residual stresses from the quenching process of coupons to large billets. These FEA models were validated using experimental measurements. Machining distortion simulations were performed for different machining strategies and validated using experimental trials.

10 Future work

This study has initiated the understanding the relationship between the post machining distortion behavior due to residual stresses from the quenching process in Aluminium 7050. This research utilized Finite Element Analysis (FEA) to predict the post machining distortion depending on the machining strategy. Using FEA, an understanding was developed and an improved process was proposed. However, there was some limitations on the methodology and the FEA was performed using assumptions highlighted in this study. The following further work was identified that would assist in creating an accurate and robust model for both the quenching and machining process:

- A study should be performed on factors that cause variation of the residual stresses caused due to quenching. This would enable accurately predicting the post machining distortions using a single FE model rather than remodeling the quenching process to accurately model the residual stresses in the component.
- A residual stress variability study could be performed using the contour method or neutron diffraction to understand the variability due to measurement, operator and also specimen
- Improvement would be on acquiring the material models most especially the hardening laws. This is important to determine the bulk residual stress generated from the quenching process.
- The heat transfer coefficient is critical to accurately predict accurately the residual stresses during the quenching process. Therefore, experimental trials would need to be performed for each specimen to accurately predict the quench residual stresses.
- A repeatability study could be performed on the machining process to capture the sources and effects of any variability in the machining process. Once captures, an effort should be made to minimize them. This will provide confidence in the data coming from the machining process and later comparing it with the FE model.
- As highlighted in the study, the importance of modelling the fixture loadings should be included in the simulations. This can be done by experimentally measuring the forces exerted onto the workpiece by the fixtures.
- The friction coefficient should be experimentally calculated for the appropriate fixture geometry and materials with the workpiece.

11 References

- [1] Boeing, "Commercial Market Outlook," *Boeing*, 2018.
- [2] Airbus, "Global Networks, Global Citizen," 2018.
- [3] Klemen Ferjan, "IATA Airline Operational Cost Task Force," *Airl. Cost Conf. Geneva*, 2013.
- [4] I. F. Edem and V. A. Balogun, "Energy Efficiency Analyses of Toolpaths in a Pocket Milling Process," *Int. J. Eng.*, vol. 31, no. 5, 2018.
- [5] P. Rambabu, N. E. Prasad, and V. V. Kutumbarao, "Aluminium Alloys for Aerospace applications," in *Aerospace Materials and Material Technologies*, 2017.
- [6] A. M. Market, S. Annual, and A. Materials, "Spacious Skies Ahead for Alcoa Aerospace," 2012.
- [7] Airbus, "Airbus technical magazine." [Online]. Available: <http://www.airbus.com/support/publications/>. [Accessed: 11-Jun-2013].
- [8] M. D. Platzer, "U.S. Aerospace Manufacturing: Industry Overview and Prospects," *Aerospace*, 2009.
- [9] K. Michaels, "Aerospace Supply Chain & Raw Material Outlook," pp. 1–27, 2014.
- [10] S. International, "Advanced Aluminum Solutions for Next-Gen Aerospace Structures," no. February, 2013.
- [11] X. Cerutti, "Numerical modelling and mechanical analysis of the machining of large aeronautical parts : Machining quality improvement," MINES ParisTech, 2015.
- [12] D. Acker/, "More 737 fuselage problems cloud Boeing's plan to ramp up production," *Bloomberg*), Wichita, Kansas, pp. 1–7, 28-Mar-2018.
- [13] R. Bilkhu and C. Pinna, "Layer Material Removal Selection for Residual Stress Relief," *High Speed Mach. Conf.*, no. 1, pp. 1–4, 2018.
- [14] Y. Yang, M. Li, and K. R. Li, "Comparison and analysis of main effect elements of machining distortion for aluminum alloy and titanium alloy aircraft monolithic component," *Int. J. Adv. Manuf. Technol.*, vol. 70, no. 9–12, pp. 1803–1811, 2014.
- [15] G. S. Schajer, *Practical Residual Stress Measurement Methods*, First edit., vol. 42, no. 6. John Wiley & Sons, Ltd, 2013.
- [16] J. Rolph, "RESIDUAL STRESS CHARACTERISATION IN FORGINGS FOR AERO-ENGINE APPLICATION," 2012.
- [17] D. Ulutan, B. Erdem Alaca, and I. Lazoglu, "Analytical modelling of residual stresses in machining," *J. Mater. Process. Technol.*, vol. 183, no. 1, pp. 77–87, 2007.
- [18] B. Denkena, D. Boehnke, and L. León, "Machining induced residual stress in structural aluminum parts," *Prod. Eng.*, vol. 2, no. 3, pp. 247–253, 2008.

Chapter 11: References

-
- [19] D. M. Bowden, B. J. Sova, A. L. Beisiegel, and J. E. Halley, "Machined Component Quality Improvements Through Manufacturing Process Simulation," no. 724, 2001.
- [20] D. Chantzis, S. Van-Der-Veen, J. Zettler, and W. M. Sim, "An industrial workflow to minimise part distortion for machining of large monolithic components in aerospace industry," *Procedia CIRP*, vol. 8, pp. 281–286, 2013.
- [21] K. A. Young, "MACHINING-INDUCED RESIDUAL STRESS AND DISTORTION OF THIN PARTS," Sever Institute of Washington University, 2005.
- [22] F. T.-D. A. Andrade-Campos, F. Neto da Silva, "Modelling and numerical analysis of heat treatments on aluminium parts," *Int. J. Numer. Methods Eng.*, vol. 70, no. 148, pp. 582–609, 2007.
- [23] S. Rasouli Yazdi, D. Reiraint, and J. Lu, "Study of through-thickness residual stress by numerical and experimental techniques," *J. Strain Anal. Eng. Des.*, vol. 33, no. 6, pp. 449–458, 1998.
- [24] M. B. Prime, M. a. Newborn, and J. a. Balog, "Quenching and Cold-Work Residual Stresses in Aluminum Hand Forgings: Contour Method Measurement and FEM Prediction," *Mater. Sci. Forum*, vol. 426–432, no. January 2003, pp. 435–440, 2003.
- [25] A. M. Osman and J. V. Beck, "Investigation of Transient Heat Transfer Coefficients in Quenching Experiments," *J. Heat Transfer*, vol. 112, no. 4, p. 843, 1990.
- [26] D. S. M. George E. Totten, *Handbook of Aluminum*. 2003.
- [27] M. Boivin, "Numerical calculation of residual stress relaxation in quenched plates," *Mater. Sci. Technol.*, vol. 1, no. October, pp. 786–792, 1985.
- [28] M. Koç, J. Culp, and T. Altan, "Prediction of residual stresses in quenched aluminum blocks and their reduction through cold working processes," *J. Mater. Process. Technol.*, vol. 174, no. 1–3, pp. 342–354, 2006.
- [29] S. Jafari Mehrabadi, M. Azizmoradi, and M. M. Emami, "Stress relief and material properties improvement through vibration vs. common thermal method," *J. Solid Mech.*, vol. 4, no. 2, pp. 170–176, 2012.
- [30] L. Mordfin, *Mechanical Relaxation of Residual Stresses*. 1988.
- [31] X. Cerutti, S. Arsene, and K. Mocellin, "Prediction of machining quality due to the initial residual stress redistribution of aerospace structural parts made of low-density aluminium alloy rolled plates," *Int. J. Mater. Form.*, vol. 9, no. 5, pp. 677–690, 2016.
- [32] B. Denkena, M. Krüger, and S. Dreier, "Simulation of Process Induced Part Distortion for Milling of Aircraft Components," in *New Production Technologies in Aerospace Industry*, 2013, pp. 1–8.
- [33] L. D'Alvise, D. Chantzis, B. Schoinochoritis, and K. Salonitis, "Modelling of part distortion due to residual stresses relaxation: An aeronautical case study," *Procedia CIRP*, vol. 31, pp. 447–452, 2015.
- [34] H. C. Möhring and P. Wiederkehr, "Intelligent Fixtures for High Performance Machining," *Procedia CIRP*, vol. 46, pp. 383–390, 2016.

Chapter 11: References

-
- [35] M. Knezevic *et al.*, “Modeling machining distortion using the finite element method: Application to engine disk,” *Trans. North Am. Manuf. Res. Inst. SME*, vol. 40, 2012.
- [36] G. Sridhar and R. B. P, “Understanding the challenges in machining thin walled thin floored Avionics components,” *Int. J. Appl. Sci. Eng. Res.*, vol. 2, no. 1, pp. 93–100, 2013.
- [37] J. Denkena, B and de Leon Garcia, L and Kohler, “FEM-Simulation of High-Performance-Milling,” *10th CIRP Int. Work. Model. Mach. Oper.*, pp. 149–156, 2007.
- [38] D. Niederwestberg and B. Denkena, “Simulation of thermal and mechanical workpiece load,” *CIRP J. Manuf. Sci. Technol.*, vol. 7, no. 4, pp. 315–323, 2014.
- [39] P. Rambabu, N. E. Prasad, and V. V. Kutumbarao, “Aerospace Materials and Material Technologies,” in *Aerospace Materials and Material Technologies*, 2017, pp. 29–52.
- [40] D. L. Ball, “An Update on the Impact of Forging Residual Stress in Airframe Component Design,” *Mater. Perform. Charact.*, vol. 7, no. 4, p. 20170099, 2018.
- [41] J. Waldman, “Aluminum Alloy Forgings Property/Performance Attributes.”
- [42] J. Williams and A. Fatemi, “Fatigue Performance of Forged Steel and Ductile Cast Iron Crankshafts,” *SAE Tech. Pap. Ser.*, vol. 1, pp. 1–32, 2010.
- [43] C. Blog, “Special forged parts for aircraft 16.,” 2019. .
- [44] H. K. D. H. Bhadeshia, *Handbook of Residual Stress and Deformation of Steel*. ASM International, 2002.
- [45] K. Ma *et al.*, “Modeling of Residual Stress and Machining Distortion in Aerospace Components,” *Am. Soc. Met. Handb.*, vol. 88ABW-2010, pp. 1–41, 2010.
- [46] D. S. Mackenzie and D. Lambert, “Effect of Quenching Variables on Distortion and Residual Stresses,” no. November, pp. 24–27, 2003.
- [47] H. M. M. A. Rashed, “Control of Distortion in Aluminium Heat Treatment,” in *Fundamentals of Aluminium Metallurgy: Recent Advances*, R. Lumley, Ed. Australia: Elsevier Ltd., 2018, pp. 495–524.
- [48] J. R. Davis, “Aluminum and Aluminum Alloys,” *Light Met. Alloy.*, p. 66, 2001.
- [49] S. D. W. D.A. Tanner, J.S. Robinson, “Heat Transfer and Distortion in 7010 forgings,” 1999.
- [50] J. S. Robinson, D. A. Tanner, C. E. Truman, A. M. Paradowska, and R. C. Wimpory, “The influence of quench sensitivity on residual stresses in the aluminium alloys 7010 and 7075,” *Mater. Charact.*, vol. 65, pp. 73–85, 2012.
- [51] J. S. Robinson, D. A. Tanner, C. E. Truman, and R. C. Wimpory, “Measurement and Prediction of Machining Induced Redistribution of Residual Stress in the Aluminium Alloy 7449,” *Exp. Mech.*, vol. 51, no. 6, pp. 981–993, 2011.
- [52] The Aluminum Association Inc., *Aluminium Standards and data*. 1997.
- [53] R. M. Jones, “Prediction of Residual Stress and Distortion from Residual Stress in Heat Treated and Machined Aluminum Parts,” 2014.

Chapter 11: References

-
- [54] R. M. A. Lombardi, D. Sediako, A. Machin, C. Ravindran, "Effect of solution heat treatment on residual stress in Al alloy engine blocks using neutron diffraction.pdf," *Mater. Sci. Eng.*, pp. 238–247, 2017.
- [55] S. International, "SAE AMS 2770-Heat Treatment of Wrought Aluminum Alloy Parts."
- [56] M. Rogante, P. Battistella, and F. Rustichelli, "Residual stress measurement by neutron diffraction in AA6082 extruded samples submitted to different quenching rates," *J. Alloys Compd.*, vol. 378, no. 1–2, pp. 335–338, 2004.
- [57] D. S. M. George E. Totten, *Handbook-of-aluminum-Volume 1-physical-metallurgy-and-processes*. 2003.
- [58] W. S. Mattos, G. E. Totten, and L. C. F. Canale, "Quenching of Aluminum Alloys," in *ASM Handbook Heat Treating of Nonferrous Alloys*, vol. 4, no. 5, ASM International, 2016, p. 20160125.
- [59] J. S. Robinson and D. A. Tanner, "Reducing Residual Stress in 7050 Aluminum Alloy Die Forgings by Heat Treatment," *J. Eng. Mater. Technol.*, vol. 130, no. 3, p. 031003, 2008.
- [60] D. A. Tanner and J. S. Robinson, "Reducing residual stress in 2014 aluminium alloy die forgings," *Mater. Des.*, 2008.
- [61] M. Fontecchio, M. Maniruzzaman, and R. D. Sisson, "Quench Factor Analysis and Heat Transfer Coefficient Calculations for 6061 Aluminum Alloy Probes Quenched in Distilled Water," *Cent. Heat Treat. Excell. Mater. Sci. Eng. Program, Mech. Eng. Dep. Worcester Polytech. Inst. (WPI), Worcester, MA 01609*, pp. 53–75, 2002.
- [62] X. W. Yang, J. C. Zhu, Z. H. Lai, Y. Liu, D. He, and Z. S. Nong, "Finite element analysis of quenching temperature field, residual stress and distortion in A357 aluminum alloy large complicated thin-wall workpieces," *Trans. Nonferrous Met. Soc. China (English Ed.)*, vol. 23, no. 6, pp. 1751–1760, 2013.
- [63] A. Buczek and T. Telejko, "Investigation of heat transfer coefficient during quenching in various cooling agents," *Int. J. Heat Fluid Flow*, vol. 44, pp. 358–364, 2013.
- [64] L. Zhang, X. Feng, Z. Li, and C. Liu, "FEM simulation and experimental study on the quenching residual stress of aluminum alloy 2024," *Proc. Inst. Mech. Eng. Part B J. Eng. Manuf.*, vol. 227, no. 7, pp. 954–964, 2013.
- [65] S. Masoudi, G. Amirian, E. Saeedi, and M. Ahmadi, "The Effect of Quench-Induced Residual Stresses on the Distortion of Machined Thin-Walled Parts," *J. Mater. Eng. Perform.*, vol. 24, no. 10, pp. 3933–3941, 2015.
- [66] V. Paschkis and G. Stolz, "Quenching as a Heat Transfer Problem," *JOM*, vol. 8, no. 8, pp. 1074–1075, 1956.
- [67] B. L. H. M. Tensi and Lauralice C. F. Canale George E. Totten, *Quenching Theory and Technology, Second Edition*. Taylor and Francis Group, 2010.
- [68] R. Becker, M. E. Karabin, J. C. Liu, and R. E. Smelser, "Distortion and Residual Stress in Quenched Aluminum Bars," *J. Appl. Mech.*, vol. 63, no. 3, p. 699, 2008.

Chapter 11: References

-
- [69] Y. N. Li *et al.*, "Effects of Heat Transfer Coefficients on Quenching Residual Stresses in 7055 Aluminum Alloy," *Mater. Sci. Forum*, vol. 877, pp. 647–654, 2016.
- [70] N. Chobaut, D. Carron, S. Arsène, P. Schloth, and J. M. Drezet, "Quench induced residual stress prediction in heat treatable 7xxx aluminium alloy thick plates using Gleeble interrupted quench tests," *J. Mater. Process. Technol.*, vol. 222, pp. 373–380, 2015.
- [71] Y. B. Dong, W. Z. Shao, L. X. Lu, J. T. Jiang, and L. Zhen, "Numerical Simulation of Residual Stress in an Al-Cu Alloy Block During Quenching and Aging," *J. Mater. Eng. Perform.*, vol. 24, no. 12, pp. 4928–4940, 2015.
- [72] D. D. Hall and I. Mudawar, "Experimental and numerical study of quenching complex-shaped metallic alloys with multiple, overlapping sprays," *Int. J. Heat Mass Transf.*, vol. 38, no. 7, pp. 1201–1216, 1995.
- [73] I. Urresti, S. Nikov, P. Brown, and P. J. Arrazola, "Aerospace Gas Turbine Disc Distortion Modelling: Machining Sequence Optimization," *12th CIRP Conf. Model. Mach. Oper. San Sebastian*, 2009.
- [74] R. Kopun, L. Škerget, M. Hriberšek, D. Zhang, B. Stauder, and D. Greif, "Numerical simulation of immersion quenching process for cast aluminium part at different pool temperatures," *Appl. Therm. Eng.*, vol. 65, no. 1–2, pp. 74–84, 2014.
- [75] ASM International, "Heat Treating of Aluminum Alloys," in *ASM Handbook*, vol. 4, 1991, pp. 841–879.
- [76] C. M. D. Pan, Ran, Thilo Pirling, Jinghua Zheng, Jianguo Lin, "Quantification of thermal residual stresses relaxation in AA7xxx aluminium alloy through cold rolling.pdf." 2019.
- [77] J. Zhang, Y. Deng, W. Yang, S. Hu, and X. Zhang, "Design of the multi-stage quenching process for 7050 aluminum alloy," *Mater. Des.*, vol. 56, pp. 334–344, 2014.
- [78] M. B. Prime and M. R. Hill, "Residual stress, stress relief, and inhomogeneity in aluminum plate," *Scr. Mater.*, vol. 46, no. 1, pp. 77–82, 2002.
- [79] A. S. Ahmad, W. Yunxin, G. Hai, and L. Lei, "Determination of the Effect of Cold Working Compression on Residual Stress Reduction in Quenched Aluminium Alloy 2219 Block," *Strojniški Vestn. – J. Mech. Eng.*, vol. 65, pp. 311–318, 2019.
- [80] Z. Zhang, Y. Yang, L. Li, and J. Yin, "Distribution of residual stress in an asymmetric T-section beam by stretch-bending," *Int. J. Mech. Sci.*, vol. 164, no. March, p. 105184, 2019.
- [81] Z. Zhang, Y. Yang, L. Li, B. Chen, and H. Tian, "Assessment of residual stress of 7050-T7452 aluminum alloy forging using the contour method," *Mater. Sci. Eng. A*, vol. 644, pp. 61–68, 2015.
- [82] W. Shaohui, "Study on quenching residual stress of 7085 aluminum alloy monolithic structural parts and its reduction process," 2011.
- [83] Z. Jiang, Y. Liu, L. Li, and W. Shao, "A novel prediction model for thin plate deflections considering milling residual stresses," *Int. J. Adv. Manuf. Technol.*, vol. 74, no. 1–4, pp. 37–45, 2014.

Chapter 11: References

- [84] F. Heymes, B. Commet, B. DuBost, P. Lassince, P. Lequeu, and G. M. Raynaud, "Development of new Al alloys for distortion free machined aluminium aircraft components." pp. 249–255, 1997.
- [85] and A. D. V. Songmene, R. Khettabi, I. Zaghbani, J. Kouam, *Machining and Machinability of Aluminum Alloys, Aluminium Alloys, Theory and Applications*. École de technologie supérieure (ETS), Department of Mechanical Engineering, 1100 Notre-Dame Street West, Montreal Quebec H3C 1K3 Canada, 2011.
- [86] J. Drezet, A. Evans, T. Pirling, and B. Pitié, "Stored elastic energy in aluminium alloy AA 6063 billets: residual stress measurements and thermomechanical modelling," *Int. J. Cast Met. Res.*, vol. 25, no. 2, pp. 110–116, 2012.
- [87] M. Thoben, K.-D., Lubben, Th., Clauen, B., Schulz A., Rentsch, R., Kusmierz, R., Nowag, L., Surm, H., Freichs, F., Hunkel, M., Klein, D., "A system-oriented view of component warpage," in *Distortion engineering: HTM -Hardening Technical Announcements*, 2002, no. April 2002.
- [88] J. Borradaile, "Future Aluminium Technologies and Their Application to Aircraft Structures," 2000.
- [89] D. Hornbach and P. Prev y, "Development of Machining Procedures to Minimize Distortion During Manufacture," *ASM Proc. 17th Heat Treat. Soc. Conf. Expo. Heat Treat.*, pp. 13–18, 1998.
- [90] X. Z. Wang, "Research and Optimization on NC Milling Technology for Two Typical Aeronautical Materials," Dalian University of Technology (People's Republic of China), 2005.
- [91] J. guang Li and S. qi Wang, "Distortion caused by residual stresses in machining aeronautical aluminum alloy parts: recent advances," *Int. J. Adv. Manuf. Technol.*, pp. 1–16, 2016.
- [92] J. CHATELAIN, J. LALONDE, and A. TAHAN, "A Comparison of the Distortion of Machined Parts Resulting From Residual Stresses Within Workpieces," *Wseas.Us*, no. 1, pp. 2–7, 2010.
- [93] H. Gao, Y. Zhang, Q. Wu, and C. Liu, "Influence of initial residual stress distribution on machining deformation of plate blank," *AIP Conf. Proc.*, vol. 1829, 2017.
- [94] P. Rambaud and K. Mocellin, "New numerical approach for the modelling of machining applied to aeronautical structural parts," *AIP Conf. Proc.*, vol. 1960, 2018.
- [95] V. Schulze, P. Arrazola, F. Zanger, and J. Osterried, "Simulation of distortion due to machining of thin-walled components," *Procedia CIRP*, vol. 8, pp. 45–50, 2013.
- [96] M. Guo, X. Jiang, Y. Ye, Z. Ding, and Z. Zhang, "Investigation of redistribution mechanism of residual stress during multi-process milling of thin-walled parts," 2019.
- [97] X. Jiang, Y. Wang, Z. Ding, and H. Li, "An approach to predict the distortion of thin-walled parts affected by residual stress during the milling process," *Int. J. Adv. Manuf. Technol.*, 2017.

Chapter 11: References

- [98] H. Gao, Y. Zhang, Q. Wu, and B. Li, "Investigation on Influences of Initial Residual Stress on Thin-walled Part Machining Deformation Based on a Semi-Analytical Model," *J. Mater. Process. Technol.*, 2018.
- [99] Q. Wu, D.-P. Li, and Y.-D. Zhang, "Detecting Milling Deformation in 7075 Aluminum Alloy Aeronautical Monolithic Components Using the Quasi-Symmetric Machining Method," *Metals (Basel)*, vol. 6, no. 4, p. 80, 2016.
- [100] H. Gao, Y. Zhang, Q. Wu, and J. Song, "An analytical model for predicting the machining deformation of a plate blank considers biaxial initial residual stresses," *Int. J. Adv. Manuf. Technol.*, no. 37, 2017.
- [101] Z. T. Tang, T. Yu, L. Q. Xu, and Z. Q. Liu, "Machining deformation prediction for frame components considering multifactor coupling effects," *Int. J. Adv. Manuf. Technol.*, vol. 68, no. 1–4, pp. 187–196, 2013.
- [102] Y. Ma, J. Zhang, D. Yu, P. Feng, and C. Xu, "Modeling of machining distortion for thin-walled components based on the internal stress field evolution," *Int. J. Adv. Manuf. Technol.*, 2019.
- [103] W. E. Fu, P. H. Cohen, and C. O. Ruud, "Experimental investigation of the machining induced residual stress tensor under mechanical loading," *J. Manuf. Process.*, vol. 11, no. 2, pp. 88–96, 2009.
- [104] X. Cerutti and K. Mocellin, "Influence of the machining sequence on the residual stress redistribution and machining quality: Analysis and improvement using numerical simulations," *Int. J. Adv. Manuf. Technol.*, vol. 83, no. 1–4, pp. 489–503, 2016.
- [105] Z. T. Tang, Z. Q. Liu, Y. Z. Pan, Y. Wan, and X. Ai, "The influence of tool flank wear on residual stresses induced by milling aluminum alloy," *J. Mater. Process. Technol.*, vol. 209, pp. 4502–4508, 2009.
- [106] J.-F. Chatelain, J.-F. Lalonde, and A. S. Tahan, "Effect of Residual Stresses on the Distortion of Components after Machining," *International J. Mech.*, vol. 6, no. 1, pp. 43–51, 2012.
- [107] E. Brinksmeier, J. T. Cammett, W. König, P. Leskovar, J. Peters, and H. K. Tönshoff, "Residual Stresses - Measurement and Causes in Machining Processes," *CIRP Ann. - Manuf. Technol.*, vol. 31, no. 2, pp. 491–510, 1982.
- [108] A. Hussain and I. Lazoglu, "Distortion in milling of structural parts," *CIRP Ann. - Manuf. Technol.*, 2019.
- [109] B. Li, H. Gao, H. Deng, H. Pan, and B. Wang, "Investigation on the influence of the equivalent bending stiffness of the thin-walled parts on the machining deformation," 2018.
- [110] X. Huang, J. Sun, and J. Li, "Finite element simulation and experimental investigation on the residual stress-related monolithic component deformation," *Int. J. Adv. Manuf. Technol.*, vol. 77, no. 5–8, pp. 1035–1041, 2015.
- [111] H. Guo, D. W. Zuo, H. B. Wu, F. Xu, and G. Q. Tong, "Prediction on milling distortion for aero-multi-frame parts," *Mater. Sci. Eng. A*, vol. 499, no. 1–2, pp. 230–233, 2009.

Chapter 11: References

- [112] Z. Zhang, L. Li, Y. Yang, N. He, and W. Zhao, "Machining distortion minimization for the manufacturing of aeronautical structure," *Int. J. Adv. Manuf. Technol.*, vol. 73, no. 9–12, pp. 1765–1773, 2014.
- [113] H. Yuan, Y. Wu, and C. Lei, "Simulation and Experimental Study on Asymmetrical Quenching Deformation of 7075 Al Alloy Thick Plate," no. Icmra, pp. 581–584, 2015.
- [114] J.-H. Zheng, R. Pan, R. C. Wimpory, J. Lin, C. Li, and C. M. Davies, "A novel manufacturing process and validated predictive model for high-strength and low-residual stresses in extra-large 7xxx panels," *Mater. Des.*, p. 107767, 2019.
- [115] Y. Yang *et al.*, "Investigation on deformation of single-sided stringer parts based on fluctuant initial residual stress," *J. Mater. Process. Tech.*, vol. 271, no. April, pp. 623–633, 2019.
- [116] J. Chen, "Study on Machining Distortion of Residual Stress Release," *Adv. Mater. Res.*, vol. 426, pp. 143–146, 2012.
- [117] B. Denkena, L. De León-Garcia, and J. Kohler, "Influence of High Performance Cutting Operations on the Residual Stresses of aluminium structural workpieces," *Proceeding 25TH Int. Congr. Aeronaut. Sci.*, pp. 1–7, 2006.
- [118] W. Sim, "Residual Stress Engineering in Manufacture of Aerospace Structural Parts," *Int. Conf. distortions Eng.*, no. i, pp. 187–194, 2011.
- [119] L. Liu, J. Sun, W. Chen, and P. Sun, "Study on the machining distortion of aluminum alloy parts induced by forging residual stresses," *Proc. Inst. Mech. Eng. Part B J. Eng. Manuf.*, 2015.
- [120] B. Li, X. Jiang, J. Yang, and S. Y. Liang, "Effects of depth of cut on the redistribution of residual stress and distortion during the milling of thin-walled part," *J. Mater. Process. Technol.*, vol. 216, pp. 223–233, 2015.
- [121] J. K. Rai and P. Xirouchakis, "Finite element method based machining simulation environment for analyzing part errors induced during milling of thin-walled components," *Int. J. Mach. Tools Manuf.*, vol. 48, no. 6, pp. 629–643, 2008.
- [122] D. H. HUANG Zhi-gang , KE Ying-lin, "Finite element model of milling process sequence for frame monolithic components," *J. Zhejiang Univ.*, 2005.
- [123] S. Dreier, J. Brüning, and B. Denkena, "Simulation based reduction of residual stress related part distortion," *Materwiss. Werksttech.*, vol. 47, no. 8, pp. 710–717, 2016.
- [124] S. Nervi, "A mathematical model for the estimation of the effects of residual stresses in aluminum plates," Sever Institute of Washington University, 2005.
- [125] M. B. Prime, "Residual Stress Measurement Methods : Making an Informed Choice LA-UR-13-27700," no. October, 2013.
- [126] M. B. Prime, "CROSS-SECTIONAL MAPPING OF RESIDUAL STRESSES BY MEASURING THE SURFACE CONTOUR AFTER A CUT," *J. Eng. Mater. Technol.*, vol. 836, no. October, pp. 162–168, 2001.

Chapter 11: References

-
- [127] H. F. Bueckner. ASME, "The Propagation of Cracks and the Energy of Elastic Deformation," *ASME, Transactions*, vol. 80, pp. 1225–1230, 1958.
- [128] M. B. Prime, A. T. Dewald, and G. S. Schajer, "The Contour Method," in *Practical Residual Stress Measurement Methods*, 2013.
- [129] M. R. Hill and M. D. Olson, "The Contour Method for Residual Stress Measurement," 2015.
- [130] M. R. Hill and M. D. Olson, "Repeatability of the Contour Method for Residual Stress Measurement," *Exp. Mech.*, vol. 54, no. 7, pp. 1269–1277, 2014.
- [131] F. Hosseinzadeh, J. Kowal, and P. J. Bouchard, "Towards good practice guidelines for the contour method of residual stress measurement," *J. Eng.*, vol. 2014, no. 8, pp. 453–468, 2014.
- [132] G. Johnson, "Residual stress measurements using the contour method," *Sch. Mater.*, vol. Ph.D, p. 244, 2008.
- [133] N. S. Rossini, M. Dassisti, K. Y. Benyounis, and A. G. Olabi, "Methods of measuring residual stresses in components," *Mater. Des.*, vol. 35, pp. 572–588, 2012.
- [134] P. J. Withers, H. K. D. H. Bhadeshia, P. J. Withers, and H. K. D. H. Bhadeshia, "Residual stress . Part 1 – Measurement techniques," vol. 0836, no. 2001, 2013.
- [135] J. Drezet, N. Chobaut, and T. Pirling, *Measurement and Modelling of Residual Stresses : As Cast Stresses in AA7050 Rolling Plate Ingots*, vol. 2, no. 10. Elsevier Ltd., 2015.
- [136] H. Drezet, J.-M.; Chobaut, N.; Schloth, P. & van Swygenhoven, "Internal Stress Generation during Quenching of Thick Heat Treatable Aluminium Alloys," *EPD Congr. 2013*, no. L, pp. 63–72, 2013.
- [137] N. Chobaut *et al.*, "Stress generation during the quenching of large AA2618 forgings: Finite element computations and validation against neutron diffraction measurements," *Finite Elem. Anal. Des.*, vol. 131, no. August 2016, pp. 17–24, 2017.
- [138] J.-F. Lalonde, "Contribution to residual stress measurement techniques of raw and machined parts by neutron diffraction," 2009.
- [139] M. N. Islam, "An analysis of machining accuracies in CNC machining operations," THE UNIVERSITY OF WOLLONGONG, 1990.
- [140] W. Conference, N. Testing, Y. Kudryavtsev, J. Kleiman, and S. Integrity, "Ultrasonic Measurement of Residual Stresses in Welded Elements and Structures," no. 420x80x10 mm, pp. 1–10, 2016.
- [141] D. Flack, "CMM Measurement Strategies - Good Practice Guide No. 41," 2014.
- [142] W. Saleem, H. Ijaz, M. Zain-ul-Abdein, A. A. Taimoor, and Y. Wang, "Studying control strategies for dimensional precision in aerospace parts machining," *Int. J. Precis. Eng. Manuf.*, vol. 18, no. 1, pp. 39–47, 2017.
- [143] W. S. Awan and T. Mabrouki, "Numerical and experimental investigations of post-machining distortions in thin machined structures considering material-induced residual stress," *J. Brazilian Soc. Mech. Sci. Eng.*, vol. 39, no. 2, pp. 509–521, 2017.

Chapter 11: References

- [144] J. Bryan, "International Status of Thermal Error Research," *CIRP Ann. - Manuf. Technol.*, vol. 39, no. 2, pp. 645–656, 1990.
- [145] YIHUI, "The difference between Coordinate Measuring Machine and Image Measuring Instrument," 2016. [Online]. Available: <https://medium.com/@chinayihui/the-difference-between-coordinate-measuring-machine-and-image-measuring-instrument-2f23193063b0>. [Accessed: 15-Jul-2019].
- [146] S. Afazov *et al.*, "A methodology for precision additive manufacturing through compensation," *Precis. Eng.*, 2017.
- [147] V. Kupriyanov, "Comparison of optical and tactile Coordinate Measuring Machines in a production environment," 2018.
- [148] T. Tóth and J. Živčák, "A comparison of the outputs of 3D scanners," *Procedia Eng.*, vol. 69, pp. 393–401, 2014.
- [149] U. Manual, "ATOS v5.4.1," vol. 49, no. 0.
- [150] R. Mendricky, "DETERMINATION OF MEASUREMENT ACCURACY OF OPTICAL 3D SCANNERS," pp. 1565–1572, 2016.
- [151] M. M. Quazi, M. A. Fazal, A. S. M. A. Haseeb, F. Yusof, H. H. Masjuki, and A. Arslan, "Laser-based Surface Modifications of Aluminum and its Alloys," *Crit. Rev. Solid State Mater. Sci.*, vol. 41, no. 2, pp. 106–131, 2016.
- [152] J. Tiscareño, J. Santolaria, and J. A. Albajez, "Measurement procedure for application of white light scanner in the automotive sector," *Procedia Manufacturing*, 2017. [Online]. Available: <https://doi.org/10.1016/j.promfg.2017.09.094>.
- [153] T. Luhmann and K. Wendt, "Recommendations for an acceptance and verification test of optical 3-D measurement systems," *Int. Arch. Photogramm. ...*, vol. XXXIII, pp. 493–500, 2000.
- [154] B. R. Barbero and E. S. Ureta, "Comparative study of different digitization techniques and their accuracy," *CAD Comput. Aided Des.*, vol. 43, no. 2, pp. 188–206, 2011.
- [155] I. Wright, "Why Choose 3D Laser Scanning over Touch Probes in Manufacturing Quality Control." [Online]. Available: <https://www.engineering.com/AdvancedManufacturing/ArticleID/12301/Why-Choose-3D-Laser-Scanning-over-Touch-Probes-in-Manufacturing-Quality-Control.aspx>. [Accessed: 01-Aug-2019].
- [156] "White Light vs. Blue Light 3D Scanning." [Online]. Available: <https://3space.com/blog/white-light-vs-blue-light-3d-scanning/>. [Accessed: 01-Aug-2019].
- [157] R. Smusz, "High speed machining of the thin-walled aircraft constructions," vol. 7075, no. 8, pp. 726–729, 2017.
- [158] P. Conradie, T. Oosthuizen, D. Dimitrov, and M. Saxer, "Effect of Milling Strategy and Tool Geometry on Machining Cost When Cutting Titanium Alloys," *South African J. Ind. Eng.*, vol. 26, no. 3, pp. 137–151, 2015.

Chapter 11: References

- [159] S. Ratchev, S. Liu, W. Huang, and A. A. Becker, "Milling error prediction and compensation in machining of low-rigidity parts," *Int. J. Mach. Tools Manuf.*, vol. 44, no. 15, pp. 1629–1641, 2004.
- [160] David A. Stephenson & John S. Agapiou, *Metal Cutting Theory and Practice*, Third. Taylor & Francis Group, LLC, 2016.
- [161] A. Achouri, "Advances in the Contour Method for Residual Stress Measurement," Open University, 2018.
- [162] M. Zawada-Michałowska, J. Kuczmaszewski, and P. Pieśko, "Influence of pre-machining on post-machining deformation of thin-walled elements made of aluminium alloy EN AW-2024," *IOP Conf. Ser. Mater. Sci. Eng.*, vol. 393, p. 012100, 2018.
- [163] S. Hinduja, *Proceedings of the 34th International MATADOR Conference*. 2000.
- [164] D. Umbrello, M. Davies, I. S. Jawahir, and P. J. Arrazola, "Recent advances in modelling of metal machining processes," vol. 62, pp. 695–718, 2013.
- [165] A. P. Markopoulos, "Cutting Mechanics and Analytical Modeling," in *Finite element method in machining processes*, Springer, 2012.
- [166] W. Volk *et al.*, "Models and modelling for process limits in metal forming," *CIRP Ann. - Manuf. Technol.*, 2019.
- [167] Z. Wang, J. Sun, L. Liu, R. Wang, and W. Chen, "An analytical model to predict the machining deformation of frame parts caused by residual stress," *J. Mater. Process. Tech.*, vol. 274, no. 37, p. 116282, 2019.
- [168] W. Shi *et al.*, "Distortion Engineering," in *1st international conference on Distortion Engineering*, 2005.
- [169] D. D. Kong, C.A. van Luttervelt; T. H.C. Childs, I.S. Jawahir F. Klocke, P. K. Venunod, Y. Altintas, E Armarego and S.-H. S. I. Grabec , J. Leopold , B. Lindstrom, D. Lucca, T. Obikawa, "Present Situation and Future Trends in Modelling of Machining Operations," 1998.
- [170] W. M. Sim, "Challenges of residual stress and part distortion in the civil airframe industry," *Int. J. Microstruct. Mater. Prop.*, vol. 5, no. 4/5, p. 446, 2010.
- [171] M. Gulpak and J. Sölter, "Development and validation of a hybrid model for the prediction of shape deviations in dry machining processes," *Procedia CIRP*, vol. 31, pp. 346–351, 2015.
- [172] B. Aksel and W. R. Arthur, "A Study of Quenching : Experiment and Modelling," *J. Eng. Ind.*, vol. 114, no. August 1992, 1992.
- [173] C. H. Gur, "Simulation of Quenching : A Review," vol. 1, no. 1, pp. 1–37, 2012.
- [174] L. na Zhang, H. Wang, and S. hui Li, "Compliant assembly modeling and deformation analysis considering macro residual stress in engineering component," *J. Shanghai Jiaotong Univ.*, vol. 20, no. 6, pp. 641–648, 2015.

Chapter 11: References

- [175] K. Lin, W. Wang, R. Jiang, Y. Xiong, and D. Zhao, "Evaluation of Residual Stress Distribution and Relaxation on In Situ TiB₂/7050 Al Composites.," *Mater. (Basel, Switzerland)*, vol. 11, no. 5, p. 706, 2018.
- [176] S. H. S. Shin, "Prediction of the dimensional instability resulting from machining of residually stressed components," pp. 13–14, 1995.
- [177] A. Madariaga, P. J. Arrazola, I. Perez, R. Sanchez, J. J. Ruiz, and F. J. Rubio, "REDUCTION OF DISTORTION OF LARGE ALUMINIUM PARTS BY CONTROLLING MACHINING-INDUCED RESIDUAL STRESSES," pp. 1–15, 2017.
- [178] Q. Wu, D.-P. Li, L. Ren, and S. Mo, "Detecting milling deformation in 7075 aluminum alloy thin-walled plates using finite difference method," *Int. J. Adv. Manuf. Technol.*, pp. 1291–1302, 2015.
- [179] O. Fergani, I. Lazoglu, A. Mkaddem, M. El Mansori, and S. Y. Liang, "Analytical modeling of residual stress and the induced deflection of a milled thin plate," *Int. J. Adv. Manuf. Technol.*, vol. 75, no. 1–4, pp. 455–463, 2014.
- [180] I. Llanos, J. L. Lanzagorta, and A. Beristain, "Part Distortion Modeling on Aluminum Slender Structural Components for Aeronautical Industry," *Procedia CIRP*, vol. 58, pp. 158–162, 2017.
- [181] J. R. Rice, "Solid Mechanics," 2010.
- [182] R. M. Pidaparti, *Engineering Finite Element Analysis*, vol. 1, no. 1. 2017.
- [183] L. E. Holden, Thomas M, Ondrej Muransky, *International Conference on Residual Stresses 2016 ICRS-10*. Materials Research Forum LLC, 2016.
- [184] Z. Wang, J. Sun, W. Chen, L. Liu, and R. Wang, "Machining Distortion of Titanium Alloys Aero Engine Case Based on the Energy Principles," *Metals (Basel)*, vol. 8, no. 6, p. 464, 2018.
- [185] Q. C. Wang, X. D. Hu, W. Li, and J. L. Yuan, "Numerical Simulation of Machining Distortion of Residually Stressed Aircraft Aluminum Components," *Key Eng. Mater.*, vol. 315–316, pp. 235–238, 2006.
- [186] R. W. Schultz and M. E. Karabin, "Characterization of Machining Distortion by Strain Energy Density and Stress Range," *Materials Science Forum*, vol. 404–407. pp. 61–68, 2009.
- [187] N. Mohamad and M. K. a. Ariffin, "Development of genetic algorithm toolbox using MATLAB in cutting tool path optimization," *Sci. Res.*, vol. 8, no. 38, pp. 1848–1857, 2013.
- [188] S. Nervi, B. A. Szabo, and K. A. Young, "Prediction of Distortion of Airframe Components Made from Aluminum Plates," *Aiaa J.*, vol. 47, no. 7, pp. 1635–1641, 2009.
- [189] B. M. F. de Veubeke, "The Equations of Linear Elasticity," Manchester University, 2011, pp. 81–134.
- [190] J. L. Yeow, "PREDICTION OF MACHINED PARTS DISTORTION," 2001.
- [191] J. P. Davim, *Machining Fundamentals and Recent Advances*. 2008.

Chapter 11: References

-
- [192] A. P. Markopoulos, "Finite Element Modeling: Questions and Answers on Finite Element Modelling," in *Finite Element Method in Machining Processes*, 1st ed., Springer, 2012, pp. 29–59.
- [193] N. S. Zhanli Guo *, "Modelling phase transformations and material properties critical to the prediction of distortion during the heat treatment of steels," *Microstruct. Mater. Prop.*, vol. 4, no. 2, pp. 187–195, 2009.
- [194] L. Crocker, "Good Practice Guide to the Application of Finite Element Analysis to Erosion Modelling," no. 146.
- [195] M. Tiryakioglu and G. Totten, "Quenching Aluminum Components in Water: Problems and Alternatives," no. June, 2016.
- [196] SFTC DEFORM, "v11 . 2 _ System _ Documentation."
- [197] M. Reich and O. Kessler, "Quenching Simulation of Aluminum Alloys Including Mechanical Properties of the Undercooled States," *Mater. Perform. Charact.*, vol. 1, no. 1, p. 104632, 2012.
- [198] W. J. J. Vorster and A. M. Korsunsky, "Analysis of residual strain and stress states due to heat treatment and thermal processing," *J. Strain Anal. Eng. Des.*, vol. 44, no. 1, pp. 71–91, 2009.
- [199] A. del Prete, A. A. de Vitis, and R. Franchi, "Numerical-Experimental Correlation of Distortions Induced by Machining Process on Thin-Walled Nickel Super Alloy Forged Components," *Key Eng. Mater.*, vol. 504–506, pp. 1299–1304, 2012.
- [200] S. Afazov, "Simulation of manufacturing processes and manufacturing chains using finite element techniques.," University of Nottingham, 2009.
- [201] A. Kumar, Y. Kaymak, E. Specht, and A. Bertram, "Sensitivity of material properties on distortion and residual stresses during metal quenching processes," *J. Mater. Process. Technol.*, no. January, 2010.
- [202] J. S. Robinson and W. Redington, "The influence of alloy composition on residual stresses in heat treated aluminium alloys," *Mater. Charact.*, vol. 105, pp. 47–55, 2015.
- [203] W. JOMAA, "CONTRIBUTIONS TO UNDERSTANDING THE HIGH SPEED MACHINING EFFECTS ON AERONAUTIC PART SURFACE INTEGRITY," Montreal, 2015.
- [204] K. Zhang, Z. Liu, Y. Wang, and Y. Liu, "Method of strain-rate difference calculation in high-speed metal cutting," *Meas. J. Int. Meas. Confed.*, vol. 91, pp. 474–478, 2016.
- [205] K. M. Vernaza, "Thermal measurements during high speed machining," no. February, 2017.
- [206] M. Gutachter and M. Prof, "Simulation of Metal Quenching Processes for the Minimization of Distortion and Stresses," 1978.
- [207] F. Hosseinzadeh, A. Mahmoudi, C. E. Truman, and D. J. Smith, "Prediction and measurement of through thickness residual stresses in large quenched components," *World Congr. Eng.*, vol. 2, pp. 1–6, 2009.

Chapter 11: References

-
- [208] T. Al. Semiatin, S L, "MEASUREMENT AND INTERPRETATION OF FLOW STRESS DATA FOR THE SIMULATION OF METAL- FORMING PROCESSES," 2010.
- [209] L. T. Li, Y. C. Lin, H. M. Zhou, and Y. Q. Jiang, "Modeling the high-temperature creep behaviors of 7075 and 2124 aluminum alloys by continuum damage mechanics model," *Comput. Mater. Sci.*, vol. 73, pp. 72–78, 2013.
- [210] R. C. Wimpory *et al.*, "Residual stress in 7449 aluminium alloy forgings," *Mater. Sci. Eng. A*, vol. 527, no. 10–11, pp. 2603–2612, 2009.
- [211] G. Guo, "Aluminum microstructure evolution and effects on mechanical properties in quenching and aging process," 2017.
- [212] B. Xiao, K. Li, Q. Wang, and Y. Rong, "Numerical simulation and experimental validation of residual stresses in water-quenched aluminum alloy castings," *J. Mater. Eng. Perform.*, vol. 20, no. 9, pp. 1648–1657, 2011.
- [213] M. L. Newman, B. J. Robinson, H. Sehitoglu, and J. A. Dantzig, "Deformation, residual stress, and constitutive relations for quenched W319 aluminum," *Metall. Mater. Trans. A Phys. Metall. Mater. Sci.*, vol. 34 A, no. 7, pp. 1483–1491, 2003.
- [214] A. Standard, "ASTM E8/E8M - Standard Test Methods for Tension Testing of Metallic Materials," 2019.
- [215] G. D. Lahoti and C. Laboratories, "Determination of Flow Stress Data for Practical Metal Forming Analysis," vol. 30, no. 1, pp. 129–134, 1981.
- [216] V. M. Sample and L. A. Lalli, "Effects of thermomechanical history on hardness of aluminium," *Mater. Sci. Technol.*, vol. 3, no. 1, pp. 28–35, 1987.
- [217] J. K. Holmen, B. H. Frodal, O. S. Hopperstad, and T. Børvik, "Strength differential effect in age hardened aluminum alloys," no. October, 2017.
- [218] A. Standard, "ASTM E9-19: Standard Test Methods of Compression Testing of Metallic Materials at Room Temperature," 2019.
- [219] Jackson, "Homogenisation effects on the hot working of Al-Zn-Mg-Cu alloys," 1992.
- [220] S. Denis, P. Archambault, E. Gautier, A. Simon, and G. Beck, "Prediction of Residual Stress and Distortion of Ferrous and Non-Ferrous Metals: Current Status and Future Developments," *J. Mater. Eng. Perform.*, vol. 11, no. 1, pp. 92–102, 2002.
- [221] N. Jarvstrat, S. Tjøtta, and C. Model, "A Process Model for On-Line Quenching of Aluminium Extrusions , Temperature," vol. 27, no. June, pp. 501–508, 1996.
- [222] M. N. Mats Werke, Mikael Hedlind, "GEOMETRIC DISTORTION ANALYSIS USING CAD/CAM BASED MANUFACTURING SIMULATION," pp. 1–13, 2014.
- [223] D. A. Tanner, J. S. Robinson, and J. S. Robinson, "Time transient validation of residual stress prediction models for aluminium alloy quenching," vol. 0836, 2016.
- [224] R. A. Hardin and C. Beckermann, "Simulation of Heat Treatment Distortion," *Proc. 59th SFSA Tech. Oper. Conf.*, no. 3, pp. 1–32, 2005.

Chapter 11: References

- [225] J. C. R. Albino and L. A. Gonc, "On the convergence of solid meshes for the prediction of part distortions due to residual stresses," vol. 0, no. 0, pp. 1–9, 2019.
- [226] T. D. T. Marusich, S. Usui, and K. J. K. Marusich, "Finite Element Modeling of Part Distortion," *Intell. Robot. Appl.*, pp. 329–338, 2008.
- [227] R. A. Izamshah, "Hybrid Deflection Prediction for Machining Thin-Wall Titanium Alloy Aerospace Component," no. August, p. 183, 2011.
- [228] S. E. Benzley, E. Perry, K. Merkley, B. Clark, and G. Sjaardama, "A Comparison of All Hexagonal and All Tetrahedral Finite Element Meshes for Elastic and Elasto-plastic Analysis."
- [229] C. Q. Shen, L. Jiao, Z. H. Dong, L. Zhang, and S. Peng, "Experimental Investigation and Simulation of Machining Thin-Walled Aluminum Alloy Workpiece Center," *Appl. Mech. Mater.*, vol. 543–547, pp. 370–373, 2014.
- [230] M. Nasr, "On the Role of Interaction between Different Stress Components and Material Plasticity when Predicting Machining-induced Residual Stresses Using FEM," *J. Manuf. Sci. Eng.*, vol. 139, no. July, pp. 1–8, 2017.
- [231] M. Grevstad and S. L. T. D. Marusich, D. A. Stephenson, S. Usui, "Modeling Capabilities to Part Distortion Management for Machined Components," in *Asm. Confex.Com*, 2006.
- [232] K. Ma, R. Goetz, and S. K. Svrivatsa, "Modeling of Residual Stress and Machining Distortion in Aerospace Components," *Am. Soc. Met. Handb.*, vol. 88ABW-2010, pp. 1–41, 2010.
- [233] P. Rambaud, I. Perez, K. Mocellin, and A. Madariaga, "Modeling of post machining distortions in thin walls applied to aluminum parts compared to experimental results 1 st Esaform Mobility Grant : Modeling of Post Machining Distortions in Thin Walls Applied to Aluminum Parts compared to experimental results," vol. 080015, no. July, pp. 2–8, 2019.
- [234] A. Rakshit, S. Usui, T. Marusich, K. Marusich, L. Zamorano, and H. Elanvogan, "Predictive Modeling for Distortion in Large, Thin-Walled Machined Components," *Model. Mach. Oper.*, vol. 223, pp. 56–65, 2011.
- [235] B. H. Wu, "Study on numerical simulation and experiment of milling process for aerospace monolithic," Zhejiang University (People's Republic of China), 2008.
- [236] T. Ozel, I. Llanos, J. Soriano, and P. J. Arrazola, "3d finite element modelling of chip formation process for machining inconel 718: Comparison of FE software predictions," *Mach. Sci. Technol.*, vol. 15, no. 1, pp. 21–46, 2011.
- [237] H. Bil, S. E. Kiliç, and A. E. Tekkaya, "A comparison of orthogonal cutting data from experiments with three different finite element models," *Int. J. Mach. Tools Manuf.*, vol. 44, no. 9, pp. 933–944, 2004.
- [238] D. Joel, A. David, and J. D. Gardner, "Comparative study of finite element simulation software," 2005.
- [239] L. Mamundiazaath, U. Natarajan, and E. Mohan, "Comparative analysis of tool tip temperature using DEFORM2D and AdvantEdge," pp. 8–12, 2017.

Chapter 11: References

-
- [240] MATLAB, "Boolean subtraction- Matlab minus," 2019. [Online]. Available: <https://uk.mathworks.com/help/matlab/ref/minus.html>. [Accessed: 27-Jul-2019].
- [241] R. Bilkhu, S. Ayvar-Soberanis, C. Pinna, and T. McLeay, "Machining distortion in asymmetrical residual stress profiles," in *Procedia CIRP*, 2019, vol. 82.
- [242] I. G. Erdogan Madencii, *The Finite Element Method and Applications in Engineering Using ANSYS*, Second Edi. Springer International Publishing, 2015.
- [243] J. K. RAI, "A Finite Element Based 3D Transient Milling Simulation Environment for Process Plan Verification and Optimization," *Techniques*, vol. 4190, 2008.
- [244] A. Del Prete *et al.*, "Numerical Simulation of Machining Distortions on a Forged Aerospace Component following a One and a Multi-Step Approaches," vol. 070009, 2018.
- [245] J. P. C. Kleijnen, "VALIDATION OF MODELS: STATISTICAL TECHNIQUES AND DATA AVAILABILITY," 1999.
- [246] J. Li, T. Freiheit, S. Jack Hu, and Y. Koren, "A Quality Prediction Framework for Multistage Machining Processes Driven by an Engineering Model and Variation Propagation Model," *J. Manuf. Sci. Eng.*, vol. 129, no. 6, p. 1088, 2007.
- [247] J. P. Davim, *Machining*. 2008.
- [248] O. J. Carlisle, "Modelling the effects of residual stress and material removal in sheet metal forming University of Ulster," 2012.
- [249] C. Maccormack and J. Monaghan, "2D and 3D finite element analysis of a three stage forging sequence," vol. 127, pp. 48–56, 2002.
- [250] M.D. Prakash, *Modeling of metal forming and machining processes*, 1st ed. London: Springer, 2008.
- [251] O. Muránsky, C. J. Hamelin, M. C. Smith, P. J. Bendeich, and L. Edwards, "The effect of plasticity theory on predicted residual stress fields in numerical weld analyses," *Comput. Mater. Sci.*, vol. 54, no. 1, pp. 125–134, 2012.
- [252] N. P. H. CHOBOUT, "Measurements and modelling of residual stresses during quenching of thick heat treatable aluminium components in relation to their microstructure Resistivity measurements," ÉCOLE POLYTECHNIQUE FÉDÉRALE DE LAUSANNE POUR, 2015.
- [253] N. Chobaut, D. Carron, S. Arsène, P. Schloth, and J. M. Drezet, "Quench induced residual stress prediction in heat treatable 7xxx aluminium alloy thick plates using Gleeble interrupted quench tests," *J. Mater. Process. Technol.*, vol. 222, pp. 373–380, 2015.
- [254] A. Bellini, J. H. Hattel, and J. Thorborg, "Thermo-mechanical modelling of aluminium cast parts during solution treatment," *Model. Simul. Mater. Sci. Eng.*, vol. 14, no. 4, pp. 677–688, 2006.
- [255] T. Marusich and M. Ortiz, "Modelling and simulation of high-speed machining," *International Journal for Numerical Methods in Engineering*, vol. 38, pp. 3675–3694, 1995.

Chapter 11: References

- [256] R. A. M. W.T. Wu, S.I. Oh, T. Altan, "Automated mesh generation for forming simulation," in *ASME*, 1990, pp. 507– 515.
- [257] Yeli Traore, "Controlling plasticity in the contour method of residual stress measurement," Open University, 2013.
- [258] T. A. Shiro Kobayashi, Soo-Ik Oh, *Shiro Kobayashi, Soo-Ik Oh, Taylan Altan-Metal Forming and the Finite-Element Method (Oxford Series on Advanced Manufacturing) (1989).pdf*. Oxford Series on Advanced Manufacturing, 1989.
- [259] P. D. G. Nick A. J. Lieven, "Effect of experimental pre-stress and residual stress on modal behaviour," pp. 97–111, 2001.
- [260] B. Denkena and L. De Leon, "Milling induced residual stresses in structural parts out of forged aluminium alloys," *Int. J. Mach. Mach. Mater.*, vol. 4, no. 4, p. 335, 2008.
- [261] SFTC, "Inverse heat transfer coefficient calculation."
- [262] S. International, "Heat Treatment of Aluminum Alloy Raw Materials (AMS2772)," 2016.
- [263] P. Pagliaro *et al.*, "Measuring Inaccessible Residual Stresses Using Multiple Methods and Superposition," *Exp. Mech.*, vol. 51, no. 7, pp. 1123–1134, 2011.
- [264] Helical Solutions, *Machining Guidebook- Quick Reference eBook for CNC Milling Practices and Techniques*. 2016.
- [265] D. Ključanin, "Design of experiment using Taguchi method for milling aluminum via helical ramping entering method," *Int. Res. J. Eng. Technol.*, vol. 4, no. 5, pp. 1147–1151, 2017.
- [266] S. Atlati, A. Moufki, M. Nouari, and B. Haddag, "Interaction between the local tribological conditions at the tool–chip interface and the thermomechanical process in the primary shear zone when dry machining the aluminum alloy AA2024–T351," *Tribol. Int.*, vol. 105, no. October 2016, pp. 326–333, 2017.
- [267] Sandkiv, "Milling formulas and definition," 2019. .
- [268] J. Luo, M. Q. Li, and B. Wu, "The correlation between flow behavior and microstructural evolution of 7050 aluminum alloy," *Mater. Sci. Eng. A*, vol. 530, no. 1, pp. 559–564, 2011.
- [269] B. S. Institution, "BS EN ISO 3452-1:2013 Non-destructive testing - Penetrant testing. General principles," 2013.
- [270] S. P. Siebenaler and S. N. Melkote, "Prediction of workpiece deformation in a fixture system using the finite element method," *Int. J. Mach. Tools Manuf.*, vol. 46, no. 1, pp. 51–58, 2006.

Appendix A: Residual stress simulation of pocketing strategies

The effect of pocketing on residual stress redistribution is shown in Figure A-3 for sequence 1. The initial stresses prior to the pocketing sequence are shown in Figure A-3 (a). The images are taken in the bulk of the billet and illustrate how the maximum and minimum residual stress in the longitudinal direction (X stress) redistributes during the pocketing sequence. During the pocketing sequence, the residual stresses have little redistribution of around 2 – 5 MPa (Figure A-3 (b-i)). The effect of the pocketing sequence is apparent when the part is released with a redistribution of – 53 MPa and 25 MPa (Figure A-3 (k)). Due to this distribution, the distortions are expected to increase by a few hundred μm .

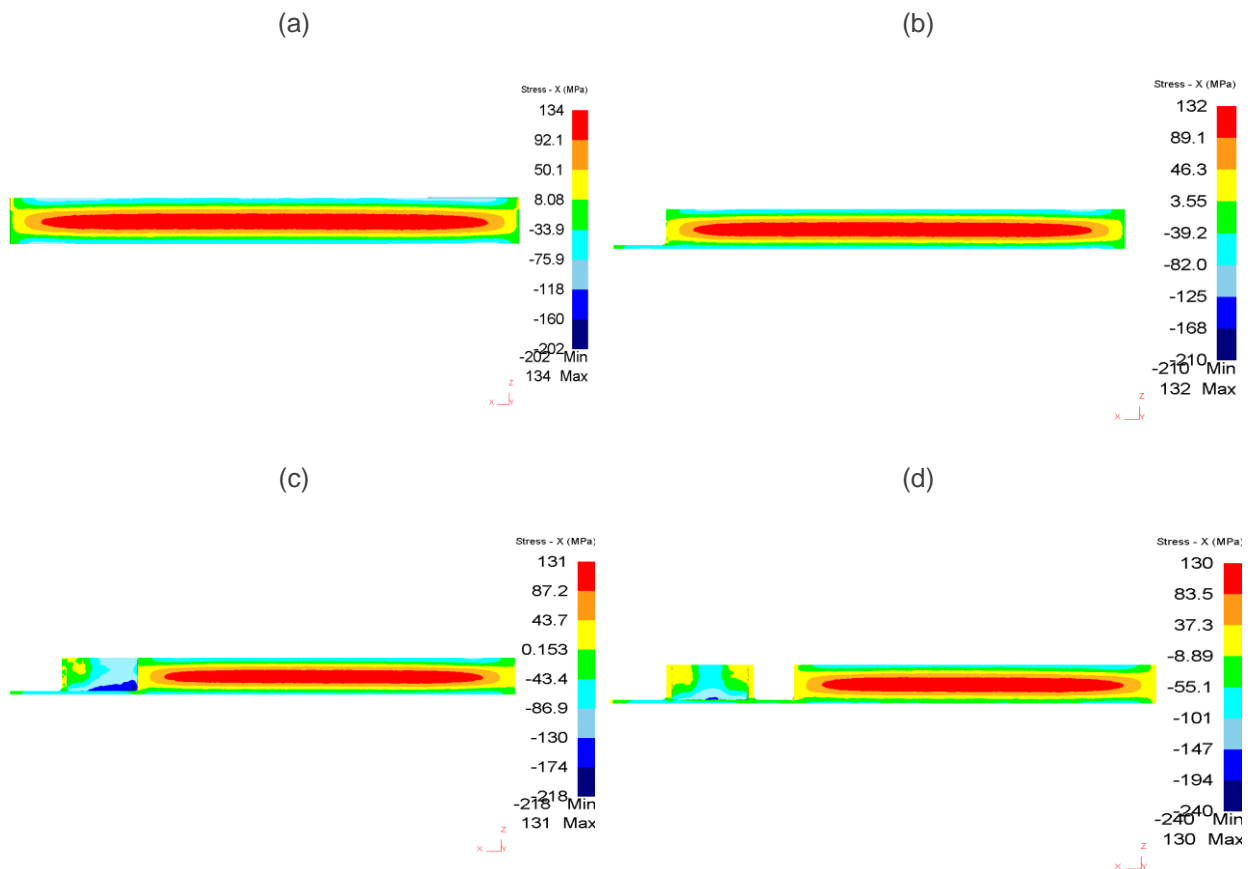


Figure A-1: Bulk residual stress redistribution during pocketing sequence: (a) Quench residual stress condition of the billet, (b) Pocket 1, (c), Pocket 2, (d) Pocket 3.

Appendix A: Residual stress simulation of pocketing strategies

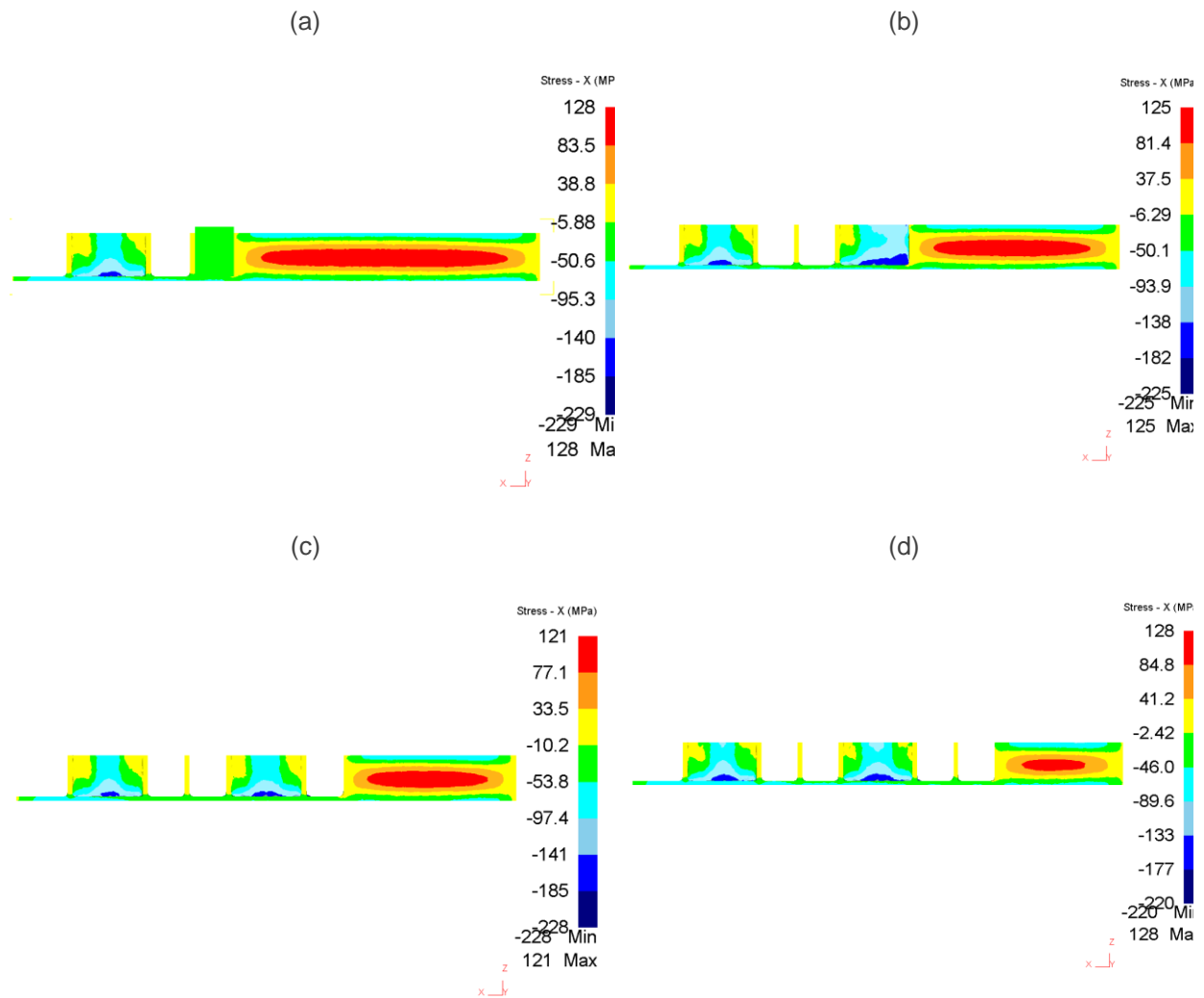


Figure A-2: Bulk residual stress redistribution during pocketing sequence: (a) Pocket 4, (b) Pocket 5, (c) Pocket 6, (d) Pocket 7.

Appendix A: Residual stress simulation of pocketing strategies

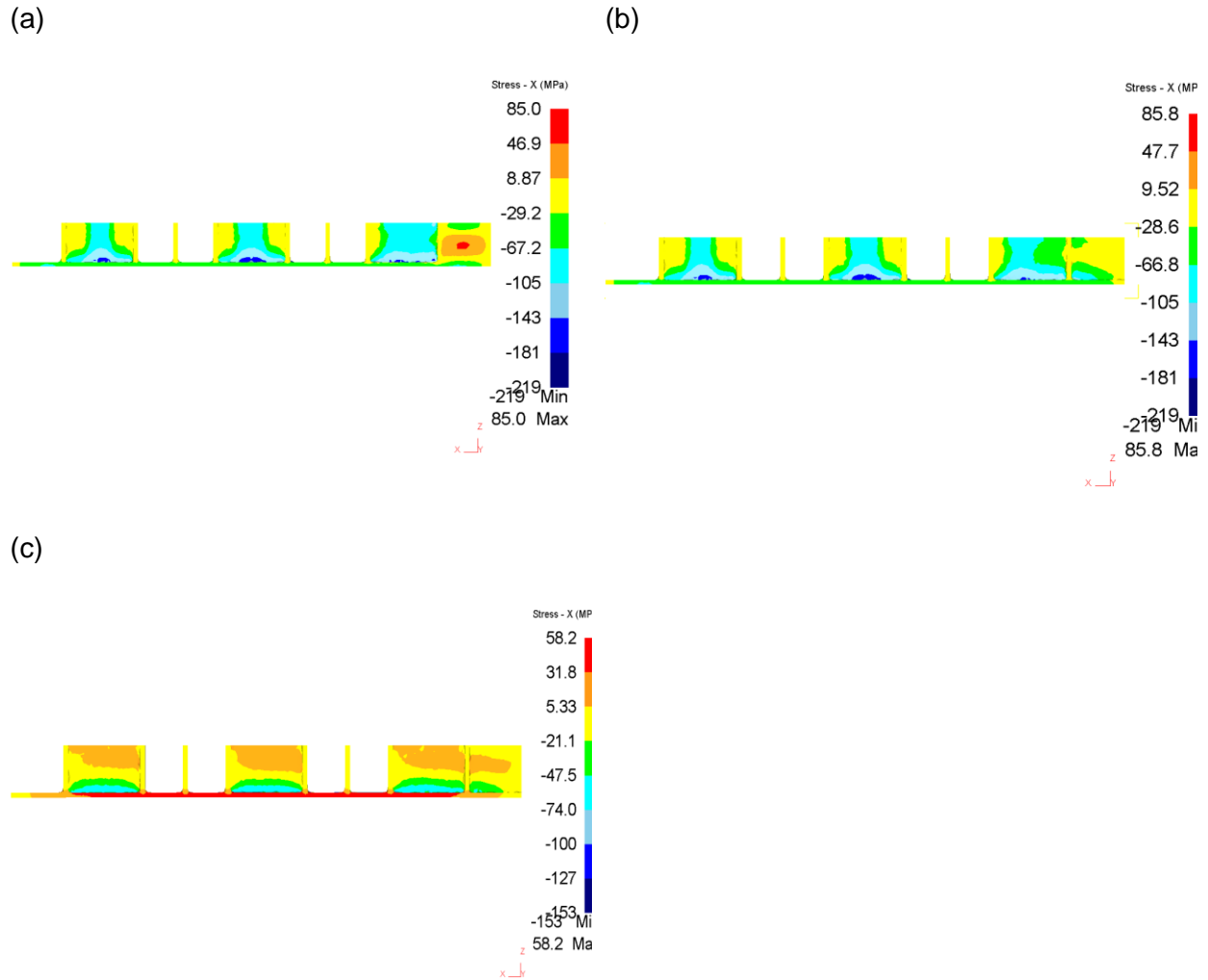


Figure A-3: Bulk residual stress redistribution during pocketing sequence: (a) Pocket 8, (b) Pocket 9, (c) Fixture release.

The effect of pocketing on residual stress redistribution on sequence 2 is shown in Figure A-5. The quench residual stress prior to the pocketing removal is shown in Figure A-5 (a). The images are taken in the bulk of the billet and illustrate how the maximum and minimum residual stress in the longitudinal direction (X stress) redistributes during the pocketing sequence. During the pocketing sequence, the residual stresses have a higher redistribution in comparison to sequence 1 with around 5- 10 MPa (Figure A-5 (b-i)). The effect of the pocketing sequence is observable when the part is released with a redistribution of – 75 MPa and 43 MPa (Figure A-5 (j)). The ratio between the min and max stress is 1.74 comparable to 2.18 for sequence 1, lower in this case; therefore, the distortion will be lower.

Appendix A: Residual stress simulation of pocketing strategies

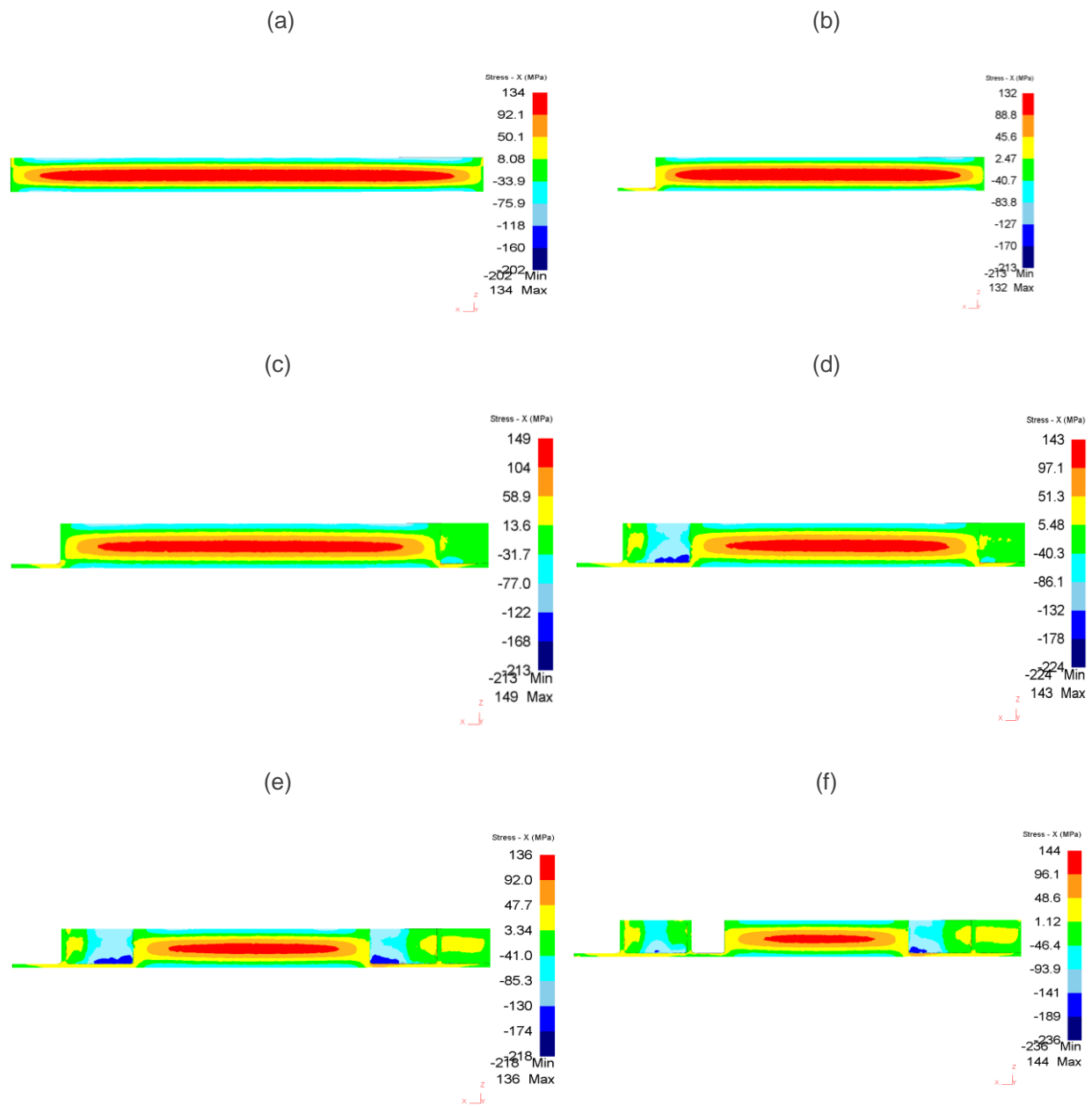


Figure A-4: Bulk residual stress redistribution during pocketing sequence: (a) Quench residual stress condition of the billet, (b) Pocket 1, (c) Pocket 2, (d) Pocket 3, (e) Pocket 4, (f) Pocket 5.

Appendix A: Residual stress simulation of pocketing strategies

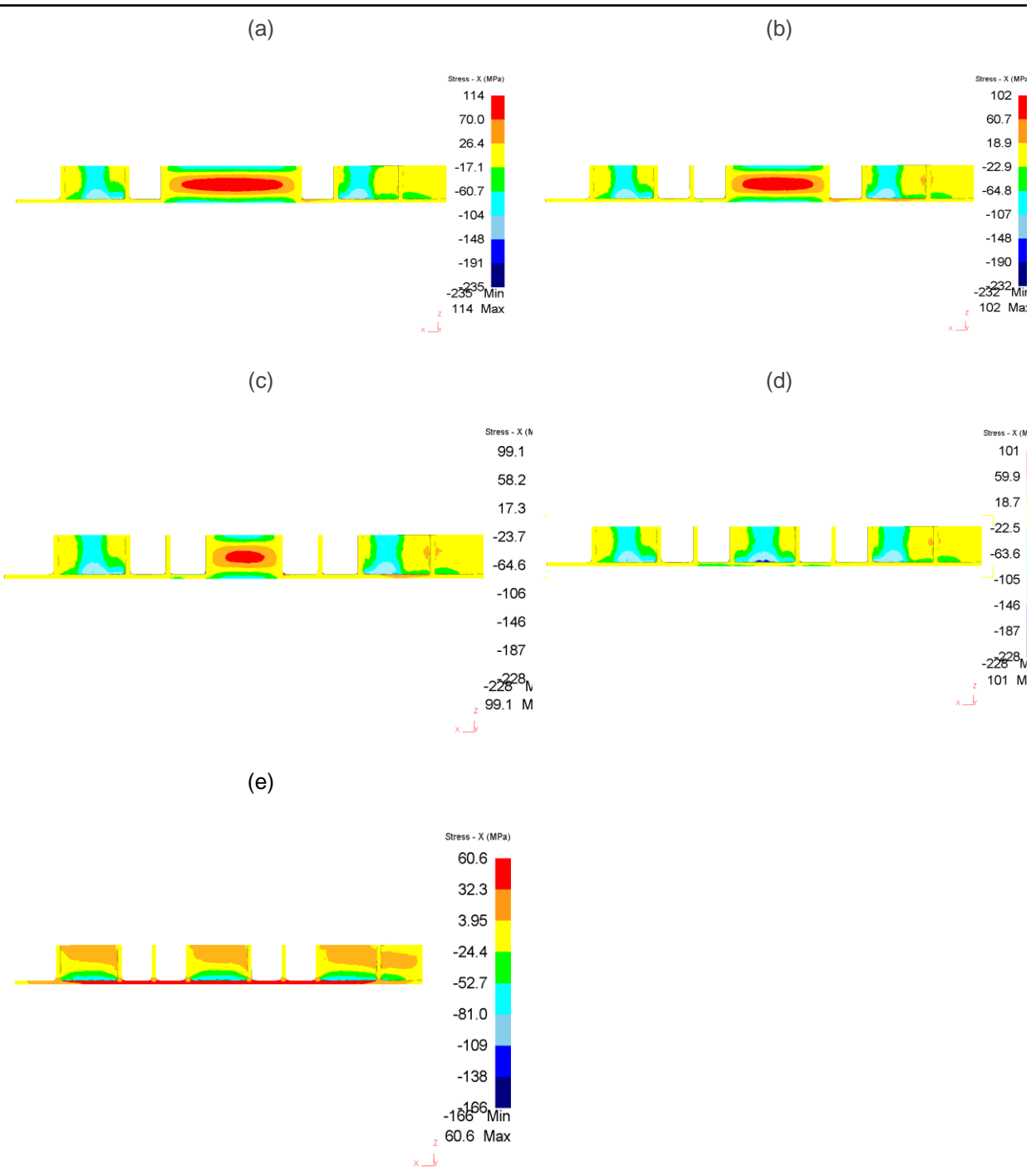


Figure A-5: Bulk residual stress redistribution during pocketing sequence: (a) Pocket 6, (b) Pocket 7, (c) Pocket 8, (d) Pocket 9, (e) Sequence 2 fixture release.